

# Abrasive Machining with MQSL

---

The Development of Minimum Quantity Solid Lubrication

TOM MORRIS

PHD THESIS

SCHOOL OF APPLIED SCIENCES

DEPARTMENT OF MATERIALS

PRECISION ENGINEERING

A thesis submitted in partial fulfilment of the requirements of Cranfield University for the degree of Doctor of Philosophy



CRANFIELD UNIVERSITY

SCHOOL OF APPLIED SCIENCES

Department of Materials

Precision Engineering

PHD THESIS

---

Abrasive Machining with MQSL

TOM MORRIS

SUPERVISORS:

PROF. D.J.STEPHENSON

DR I. WALTON

PROF. J. NICHOLLS

© Cranfield University, 2011. All rights reserved. No part of this publication may be reproduced without the written permission of the copyright holder.

A thesis submitted in partial fulfilment of the requirements of Cranfield University for the degree of Doctor of Philosophy

JULY 2011

---

## Abstract

Grinding and polishing of engineered components are critical aspects of the precision manufacturing of high performance, quality assured products. High process temperatures are, however, a common and for the most part undesirable feature of the grinding process. They increase the likelihood of microstructural change within the immediate subsurface layers with detrimental effects on the strength and performance of manufactured products. Tighter environmental legislation and the need to reduce manufacturing costs are also driving industry to seek innovative fluid application techniques.

In this context, with sponsorship from three industrial partners, namely: Fives Cinetic, Fuchs Lubricants plc and Southside Thermal Sciences Ltd, and the Engineering and Physical Sciences Research Council (EPSRC), this research aimed to compare Minimum Quantity Lubrication (MQL) and Minimum Quantity Solid Lubrication (MQSL) as methods for abrasive machining, with particular reference to the control of surface temperatures. The research also explored the feasibility of an optical method for assessing surface grinding temperature with the intention of constructing a real-time grinding temperature management system.

A range of MQSL lubricants, namely Molybdenum Disulphide ( $\text{MoS}_2$ ), Calcium Fluoride ( $\text{CaF}_2$ ), and hexagonal Boron Nitride (hBN) were compared with a semi-synthetic water soluble MQL machining fluid (Fuchs EcoCool) using a series of Taguchi factorial experimental trials. A thermo-optical sensor, comprising a Charged Coupled Device (CCD), was used to measure emitted light and hence detect surface temperatures during the MQL and MQSL grinding processes. Changes in spectrum patterns were compared with experimental and modelled process temperatures for selected material removal rates.

Specific Grinding Energy (SGE), which corresponds to the energy consumed by the grinding process and its thermal properties, was measured for a range of lubricants. It was found that SGE consumption reduced when MQL water-based flow rates were mixed with increasing concentrations of oil lubricant, confirming the challenge of developing dry abrasives that are energy efficient and heat regulating.

The hBN lubricant produced the lowest SGE and grinding temperatures of the solid lubricants tested, although temperatures were higher than those achieved using the EcoCool control. Microstructural analysis showed that solid lubricants could achieve similar surface roughness and residual stress values to that of the EcoCool oil emulsion. Optical sensing showed that the wavelengths of light from the grinding chips were positively correlated with the temperature of the grinding surface. Variations in

---

the physical and thermal interactions of the tool, the workpiece and the lubricant, were shown to influence the behaviour of the spark spectrum emitted during grinding. The results suggest scope for developing a non-destructive, non-invasive, thermo-optical control system, although careful calibration is required to utilise the predictive modelling capability of a fully automated numerical control system.

The study confirms the potential of MQSL technologies for improved manufacturing efficiency. It also shows the value of collaboration between researchers and industry in pursuit of improvements in material technology and manufacturing machine design.



---

## Acknowledgments

The support and guidance from Professor David Stephenson and Dr Ian Walton is greatly acknowledged. Their encouragement throughout the duration of this research was unlimited and greatly appreciated. Additional thanks towards the resources and contributions provided by Professor John Nicholls.

Acknowledgements to the ESPRC for the research grant and the assistance provided by the sponsoring parties Fives Cinetic, Fuchs Lubricants and STS Ltd. Their time and resources were most valuable towards this study; a special thanks to Ed Brown and Vadim Baines-Jones, Fives Cinetic.

Gratitude is extended towards the academic and technical staff of the Department of Precision Engineering at Cranfield University, for their infinite enthusiasm and unreserved support throughout my time there. To my colleagues in the research group who provided great inspiration. To Andrew Baldwin and Rodger Collins who provided support in the early stages of the research.

I would like to extend a huge thankyou to Brian Atkinson and Paul Wakefield over in Building 57 for their advice, contribution and practical assistance, which were essential for the completion of this project.

Special thanks are due to Julia for her patience, and to my friends and family for their tolerance and good humour.

*“Measure twice...cut once”*

---

## Nomenclature

| Symbol          | Definition                               | Units             |
|-----------------|--|-------------------|
| $a$             | Applied depth of cut                     | mm                |
| $a_e$           | True depth of cut                        | mm                |
| $a_d$           | Dressing depth                           | mm                |
| $A$             | Cross-sectional area                     | mm                |
| $b_d$           | Effective width of dressing tool         | mm                |
| $b_s$           | Wheel width                              | mm                |
| $b_w$           | Contact width                            | mm                |
| $C_p$           | Specific heat capacity                   | kJ/kg.K           |
| $D$             | Diameter                                 | Mm                |
| $D_e$           | Effective wheel diameter                 | mm                |
| $D_s$           | Wheel diameter                           | mm                |
| $D_w$           | Workpiece diameter                       | mm                |
| $e_c$           | Specific Grinding Energy                 | J/mm <sup>3</sup> |
| $e_{ch}$        | Specific Energy taken by chip            | J/mm <sup>3</sup> |
| $E$             | Young's modulus                          | Pa                |
| $f_d$           | Dressing feed rate                       | mm/min            |
| $f$             | Frequency of BN                          | Hz                |
| $F_t$           | Tangential force                         | N                 |
| $F_p$           | Horizontal force                         | N                 |
| $F_Q$           | Vertical force                           | N                 |
| $F_n$           | Normal grinding force                    | N                 |
| $G$             | G-ratio                                  |                   |
| $h_{eq}$        | Equivalent chip thickness                | μm                |
| $h_{pores}$     | Depth of pores                           | Mm                |
| $k$             | Thermal conductivity                     | kW/m.K            |
| $K_0$           | Bessel function of the second order zero |                   |
| $l_c$           | Contact length                           | mm                |
| $l_o$           | Real contact length                      | mm                |
| $L$             | Peclet number                            |                   |
| $m$             | Mass                                     | kg                |
| $m_{lubricant}$ | Mass flowrate of solid lubricant         | g/min             |
| $\dot{m}_u$     | Useful mass flowrate                     | g/min             |
| MP              | Magnetic power                           | MP                |
| $n$             | Shape of heat source                     |                   |
| $n_d$           | Number of dressing passes                |                   |

---

|             |   |                       |
|-------------|---|-----------------------|
| $N_s$       | Revolution speed of grinding wheel          | r.p.m.                |
| $N_w$       | Revolution speed of workpiece               | r.p.m.                |
| $P$         | Grinding power                              | kW                    |
| $P_{Total}$ | Total grinding power                        | kW                    |
| $P_{Spark}$ | Sparkout grinding power                     | kW                    |
| $P_{Net}$   | Net grinding power                          | kW                    |
| $q_{ch}$    | Heat flux partitioned to grinding chips     | W                     |
| $q_f$       | Heat flux partitioned to grinding fluid     | W                     |
| $q_s$       | Heat flux partitioned to grinding wheel     | W                     |
| $q_t$       | Total heat flux                             | W                     |
| $\bar{q}$   | Mean heat flux                              | W                     |
| $q_w$       | Heat flux partitioned to workpiece          | W                     |
| $Q$         | Flowrate                                    | l/min                 |
| $Q_d$       | Supply flowrate                             | l/min                 |
| $Q_{fu}$    | Useful flowrate                             | l/min                 |
| $Q_p$       | Supply pressure                             | bar                   |
| $Q_w$       | Volumetric material removal rate            | mm <sup>3</sup> /s    |
| $Q'_w$      | Specific material removal rate              | mm <sup>3</sup> /mm.s |
| $r_0$       | Effective radius of grit                    | mm                    |
| $R_a$       | Surface roughness - centre line average     | μm                    |
| $R_q$       | Surface roughness – root mean square        | μm                    |
| $R_t$       | Surface roughness – peak-to-valley          | μm                    |
| $R$         | Heat partition ratio                        |                       |
| $R_s$       | Partition of heat energy into the wheel     |                       |
| $R_w$       | Partition of heat energy into the workpiece |                       |
| $R_{ch}$    | Partition of heat energy into the chip      |                       |
| $R_f$       | Partition of heat energy into the fluid     |                       |
| $T$         | Average chip thickness                      | μm                    |
| $T$         | Temperature                                 | °C                    |
| $T_{max}$   | Maximum surface temperature                 | °C                    |
| $u$         | Specific Grinding Energy (SGE)              | J/mm <sup>3</sup>     |
| $u_{ch}$    | Chip SGE                                    | J/mm <sup>3</sup>     |
| $u_{pl}$    | Ploughing SGE                               | J/mm <sup>3</sup>     |
| $u_{sl}$    | Sliding SGE                                 | J/mm <sup>3</sup>     |
| $U_d$       | Dressing overlap ratio                      |                       |
| $v_f$       | Infeed rate                                 | mm/min                |
| $v_s$       | Wheel surface speed                         | m/s                   |
| $v_r$       | Radial feed per unit time                   | mm/min                |
| $v_w$       | Workpiece surface speed                     | m/s                   |

---

|             |                                    |                   |
|-------------|------------------------------------|-------------------|
| $V$         | Velocity of sliding source of heat | m/s               |
| $z$         | Vertical height                    | mm                |
| $\alpha$    | Rake angle                         | °                 |
| $\alpha$    | Thermal diffusivity                | m <sup>2</sup> /s |
| $\beta$     | Thermal property                   |                   |
| $\delta$    | Depth                              | mm                |
| $\theta$    | Temperature                        | °C                |
| $\theta_m$  | Max temperature                    | °C                |
| $\lambda$   | Wavelength                         | nm                |
| $\mu_0$     | Permeability in vacuum             | H/mm              |
| $\mu_r$     | Permeability of the material       | H/mm              |
| $\xi$       | Semi-Infinite body length          | mm                |
| $\pi$       | Pi                                 | 3.142             |
| $\rho$      | Density                            | kg/m <sup>3</sup> |
| $\sigma$    | Electrical conductivity            | 1/Ω.mm            |
| $\emptyset$ | Wheel porosity                     | %                 |

---

## Contents

|  |     |
|--|-----|
| Abstract .....                         | i   |
| Acknowledgments .....                  | iii |
| Nomenclature .....                     | iv  |
| Contents .....                         | vii |
| Table of Tables.....                   | xi  |
| Table of Figures .....                 | xii |
| 1.0 Introduction.....                  | 1   |
| 1.1 Background and context.....        | 1   |
| 1.2 Aim and Objectives.....            | 3   |
| 1.3 Research Structure .....           | 4   |
| 2.0 The art of grinding .....          | 5   |
| 2.1 Overview.....                      | 5   |
| 2.2 Abrasive machining .....           | 5   |
| 2.3 Mechanical Models .....            | 7   |
| 2.3.1 Cutting Mechanics .....          | 7   |
| 2.3.2 Grinding Mechanics .....         | 8   |
| 2.4 Cylindrical Grinding .....         | 12  |
| 2.5 Grinding Modelling.....            | 15  |
| 2.6 Heat Partition Ratio .....         | 16  |
| 2.6.1 Thermocouples .....              | 21  |
| 2.6.2 PVD Films .....                  | 23  |
| 2.7 Super Abrasives .....              | 24  |
| 2.8 Workpiece material .....           | 27  |
| 2.9 Surface Integrity .....            | 30  |
| 2.9.1 Surface Roughness.....           | 31  |
| 2.9.2 Residual Stress .....            | 32  |
| 2.9.3 Microstructure and Hardness..... | 34  |
| 2.9.4 Barkhausen Noise Analysis .....  | 36  |
| 2.10 Grinding Fluids.....              | 40  |

---

|  |    |
|--|----|
| 2.10.1 Environmental implications .....                              | 42 |
| 2.10.2 Minimum Quantity Lubrication and Useful Flowrate Theory ..... | 43 |
| 2.10.3 Solid Lubricants .....  | 45 |
| 2.11 Key Messages .....  | 50 |
| 3.0 Abrasive machining with MQL and MQSL methods.....                | 51 |
| 3.1 Overview .....   | 51 |
| 3.2 EcoCool Oil Emulsion .....                                       | 51 |
| 3.3 Molybdenum Disulphide (MoS <sub>2</sub> ) .....                  | 52 |
| 3.4 Calcium Fluoride (CaF <sub>2</sub> ) .....                       | 53 |
| 3.5 Hexagonal Boron Nitride (hBN) .....                              | 54 |
| 3.6 Development of solid lubrication delivery system.....            | 54 |
| 3.7 Nozzle Design.....   | 55 |
| 3.8 Powder Feeder Mechanism Development.....                         | 57 |
| 3.9 Electrostatic System .....                                       | 58 |
| 3.9.1 Electrostatic application .....                                | 59 |
| 3.10 Light detection instrumentation .....                           | 63 |
| 3.10.1 Spectrometer Information.....                                 | 66 |
| 3.11 Vacuum Shroud .....   | 67 |
| 3.12 Key Messages .....  | 68 |
| 4.0 Experimental Design.....   | 69 |
| 4.1 Overview .....   | 69 |
| 4.2 Taguchi Experimental Design .....                                | 69 |
| 4.3 Structure of experimentation.....                                | 74 |
| 4.4 Machines .....   | 75 |
| 4.4.1 SATurn Machine.....  | 75 |
| 4.4.2 J&S Surface Grinder .....                                      | 76 |
| 4.5 Machine set up and data collection .....                         | 76 |
| 4.6 Labview Signal Express 3.0 .....                                 | 80 |
| 4.7 Thermal Measurement.....   | 81 |
| 4.8 Surface integrity analysis.....                                  | 84 |
| 4.8.1 Residual Stresses.....   | 84 |

---

|       |  |     |
|-------|--|-----|
| 4.8.2 | Surface Profile.....                               | 85  |
| 4.8.3 | Microstructure .....                               | 86  |
| 4.8.4 | Hardness Testing.....                              | 87  |
| 4.9   | Key Messages .....                                 | 88  |
| 5.0   | Thermal modelling.....                             | 90  |
| 5.1   | Overview.....                                      | 90  |
| 5.2   | Method of Analysis.....                            | 90  |
| 5.3   | Geometrical Representation .....                   | 92  |
| 5.4   | Grinding Tool Path.....                            | 93  |
| 5.5   | Thermal Properties of 38MnSiVS6 – AISI 10267 ..... | 94  |
| 5.6   | Chip Shape .....                                   | 95  |
| 5.7   | Thermal Spectrometry.....                          | 95  |
| 5.7.1 | Spectrometer Calibration .....                     | 95  |
| 5.7.2 | Machining with the CCD .....                       | 97  |
| 5.8   | Key Messages .....                                 | 100 |
| 6.0   | Results .....                                      | 101 |
| 6.1   | Overview.....                                      | 101 |
| 6.2   | EcoCool <sub>(MQL)</sub> Trials.....               | 101 |
| 6.2.1 | EcoCool – Power Consumption .....                  | 101 |
| 6.2.2 | EcoCool – Surface Integrity.....                   | 107 |
| 6.3   | MoS <sub>2</sub> (MQL) Trials .....                | 113 |
| 6.3.1 | MoS <sub>2</sub> – Power Consumption.....          | 113 |
| 6.3.2 | MoS <sub>2</sub> – Surface Integrity.....          | 118 |
| 6.4   | CaF <sub>2</sub> (MQL) Trials.....                 | 123 |
| 6.4.1 | CaF <sub>2</sub> – Power consumption .....         | 123 |
| 6.4.2 | CaF <sub>2</sub> – Surface Integrity.....          | 127 |
| 6.5   | Hexagonal Boron Nitride (MQL) Trials.....          | 134 |
| 6.5.1 | hBN – Power Consumption.....                       | 134 |
| 6.5.2 | hBN – Surface Integrity.....                       | 138 |
| 6.6   | Wet and Dry Dressing.....                          | 141 |
| 6.7   | Electrostatic Dry Machining .....                  | 148 |

---

|             |  |     |
|-------------|--|-----|
| 6.8         | Temperature measurements and modelling ..... | 152 |
| 6.9         | Light Detection .....                        | 165 |
| 6.10        | Key Messages .....                           | 175 |
| 7.0         | Discussion .....                             | 177 |
| 8.0         | Conclusions and Recommendations .....        | 192 |
| 8.1         | Conclusions.....                             | 192 |
| 8.2         | Recommendations.....                         | 195 |
| 8.2.1       | Tooling Development.....                     | 195 |
| 8.2.2       | Electrostatic Machining Lubricants.....      | 195 |
| 8.2.3       | Machine Design and Development .....         | 196 |
| 9.0         | References.....                              | 197 |
| 10.0        | Publications and Abstracts .....             | 203 |
| 11.0        | Key References .....                         | 204 |
|             |  |     |
| Appendix A. | Material Properties .....                    | A1  |
| Appendix B. | Temperature Coding .....                     | B1  |
| Appendix C. | Phosphor Thermometry .....                   | C1  |



---

## Table of Tables

|   |     |
|---|-----|
| Table 1 Typical machine parameters for conventional, creep feed & HEDG grinding...                | 10  |
| Table 2 Difference between Diamond and cBN .....  | 25  |
| Table 3 Thermal properties of 51CrV4 steel (SAE 6150) .....                                       | 29  |
| Table 4 Mechanical Properties of 51CrV4 (SAE 6150).....   | 29  |
| Table 5 Composition 51CrV4 steel .....  | 29  |
| Table 6 Process surface roughness values taken from ISO 1302:1992 .....                           | 32  |
| Table 7 Comparison of cooling properties between water and oil.....                               | 42  |
| Table 8 Common examples of solid lubricants.....  | 48  |
| Table 9 Characteristics when selecting suitable solid lubricant.....                              | 49  |
| Table 10 hBN material properties (Matweb, 2008) .....   | 54  |
| Table 11 Basis for Taguchi L8 orthogonal experiment .....   | 70  |
| Table 12 MoS <sub>2</sub> , CaF <sub>2</sub> , hBN and EcoCool Taguchi machining parameters ..... | 71  |
| Table 13 Calculated Useful Flowrates from wheel surface impressions.....                          | 72  |
| Table 14 Nominal dressing parameters.....   | 73  |
| Table 15 Dry dressing wheel parameters .....  | 73  |
| Table 16 The sequence of abrasive machining setups.....   | 74  |
| Table 17 SAT Machine Specifications .....   | 75  |
| Table 18 J & S 540 Surface grinder specification.....   | 76  |
| Table 19 Olympus LEXT-IR Specifications.....  | 83  |
| Table 20 Talysurf 120L Specifications.....  | 86  |
| Table 21 Zwick vickers micro hardness specifications .....  | 88  |
| Table 22 Key messages: L8 machine parameters.....   | 89  |
| Table 23 GUI thermal properties of tool, workpiece and fluids.....                                | 91  |
| Table 24 AISI 10267 Low Alloy Thermal Properties.....   | 94  |
| Table 25 Practicalities of Dry Dressing vs. Wet Dressing .....                                    | 143 |
| Table 26 Mean averaged PVD surface temperatures for CaF <sub>2</sub> and hBN lubricants ....      | 158 |

---

## Table of Figures

|  |    |
|--|----|
| Figure 1 Flow chart illustrating the route to achieve the project objectives .....       | 4  |
| Figure 2 Cutting zone mechanics (Shaw, 2005) a) mechanics b) shear planes .....          | 7  |
| Figure 3 Illustration of (a) rubbing, (b) ploughing, and (c) chip formation phases ..... | 9  |
| Figure 4 Grinding zone mechanics. Undeformed chip structure (surface grinding) .....     | 9  |
| Figure 5 Thermal modelling partition ratios (Comley et al., 2005) .....                  | 11 |
| Figure 6 a) and b) Specific Grinding Energies over a wide range of S.R.R. ....           | 11 |
| Figure 7 Shear planes within abrasive machining (Jackson, 2008) .....                    | 12 |
| Figure 8 (a) and (b). Basic mechanics involved in Cylindrical Plunge Grinding. ....      | 13 |
| Figure 9 Illustration of varying grit height of a plated cBN wheel .....                 | 13 |
| Figure 10 Conventional grinding cycle .....  | 14 |
| Figure 11 Illustration of external cylindrical plunge grinding.....                      | 15 |
| Figure 12 The thermal distribution along the grinding contact length.....                | 16 |
| Figure 13 Energy distribution between workpiece, grinding wheel, fluid and chip. ....    | 17 |
| Figure 14 Heat partition ratios over varying S.R.R.(Jin and Stephenson, Sep 2003) ....   | 18 |
| Figure 15 Circular arc of heat source AFB (Rowe and Jin, 2001).....                      | 19 |
| Figure 16 Dimensionless temperatures on contact and finish surfaces .....                | 19 |
| Figure 17 Maximum grinding zone temperatures.....  | 21 |
| Figure 18 Illustration of the response mode of thermocouple vs. thermal modelling..      | 22 |
| Figure 19 Thermocouple signal demonstrating the time response .....                      | 22 |
| Figure 20 Examples of PVD materials and thermal behaviour .....                          | 23 |
| Figure 21 Example of method of exposing PVD spliced samples to grinding .....            | 23 |
| Figure 22 Images showing isotherms developing away from a ground surface .....           | 24 |
| Figure 23 Illustration of the structure of Diamond and cBN .....                         | 25 |
| Figure 24 Knoop Hardness of various super abrasives.....                                 | 25 |
| Figure 25 Grain identities .....   | 26 |
| Figure 26 Vitrified Bonded wheels and Electroplated Bonded wheels.....                   | 27 |
| Figure 27 Wheel Identities .....   | 27 |
| Figure 28 The temperature heat source movement over X/L .....                            | 28 |
| Figure 29 Minimum Specific Energy vs. Specific Melting Energy .....                      | 30 |
| Figure 30 Layer chip formation and wheel loading in abrasive machining.....              | 30 |
| Figure 31 Schematic description of Surface Integrity (Griffiths, 2001) .....             | 31 |
| Figure 32 Definitions of surface roughness .....   | 31 |
| Figure 33 States of residual stress .....  | 33 |
| Figure 34 Phase transformation diagram for Fe-C .....                                    | 35 |
| Figure 35 Cooling time and hardness of Fe-C alloy .....                                  | 35 |
| Figure 36 Untempered Martensite (UTM) indicating burn .....                              | 35 |
| Figure 37 Transformations involving the decomposition of austenite (Callister, 1997)     | 36 |

---

|  |    |
|--|----|
| Figure 38 The magnetic influence on domain walls.....                                      | 37 |
| Figure 39 Barkhausen Noise detection methods. ....   | 37 |
| Figure 40 Barkhausen Noise signals relating to Residual stresses .....                     | 38 |
| Figure 41 Surface Temperature and BN over wide range of $Q'w$ (Comley et al., 2006).       | 38 |
| Figure 42 Hardness profile of tempered/untempered EN36 200-600 $\mu$ m and BHN .....       | 39 |
| Figure 43 Grinding fluid effects (Brinksmeier et al., 1999) .....                          | 40 |
| Figure 44 Differences in the plastic and elastic zones between the grinding zones ....     | 40 |
| Figure 45 Total cost of workpiece manufacture (Klocke and Eisenblätter, 1997) .....        | 41 |
| Figure 46 Governing bodies of manufacturing and industrial processes.....                  | 42 |
| Figure 47 Arrangement for collecting useful flow.....                                      | 44 |
| Figure 48 Measuring flowrate passing through grind zone (Jackson, 2008).....               | 45 |
| Figure 49 Hydrodynamic forces.....   | 46 |
| Figure 50 An application method of introducing solid lubricants into the grinding.....     | 47 |
| Figure 51 Specific Grinding Energy over a range of infeed speeds .....                     | 48 |
| Figure 52 Grinding Forces and Specific Grinding Energies with a range of lubricants...     | 48 |
| Figure 53 Compounds of a) Graphite, b) $MoS_2$ c) $CaF_2$ and d) hBN solid lubricants..... | 52 |
| Figure 54 Examples of commercially available hBN solid lubricants .....                    | 54 |
| Figure 55 Shoe nozzle arrangement on grinding wheel surface .....                          | 55 |
| Figure 56 Minimum Quantity Solid Lubrication Nozzle design a) front b) rear .....          | 56 |
| Figure 57 MQSL Delivery Nozzle fitted to SAT Edgetek machine.....                          | 56 |
| Figure 58 Fluid flow of nozzle outlet providing fluid pressures and velocities. ....       | 57 |
| Figure 59 Proven lead screw mechanism .....  | 57 |
| Figure 60 Feeder system – encased .....  | 58 |
| Figure 61 Feeder system – expanded.....  | 58 |
| Figure 62 Close-up of 12 volt motor and lead-screw mechanism.....                          | 58 |
| Figure 63 Improved powder feeder mounted into machine .....                                | 58 |
| Figure 64 Charge density over surface profile .....  | 60 |
| Figure 65 Powder Coating system .....  | 60 |
| Figure 66 Electro filter separation of dirty emissions (Jonassen, 1998) .....              | 60 |
| Figure 67 Instance of electrostatics functioning within milling .....                      | 60 |
| Figure 68 The electrostatic lubricant system .....   | 62 |
| Figure 69 Electrostatic powder feeder and corona electrodes.....                           | 62 |
| Figure 70 Electrostatic Grinding Machine Setup.....  | 62 |
| Figure 71 Control of attractive surfaces .....   | 63 |
| Figure 72 Photodiode and Photomultiplier tube construction .....                           | 64 |
| Figure 73 Charged Coupled Device (CCD) Architecture .....                                  | 64 |
| Figure 74 Phosphor Thermometry test bed with detection sensors .....                       | 65 |
| Figure 75 The electromagnetic spectrum .....   | 65 |
| Figure 76 Spectrometer a) CCS100 CCD unit b) 350-700nm Collimator c) CCD circuit..         | 66 |
| Figure 77 Collimator housing illustrating the internal channels for the air-shield .....   | 67 |

---

|   |    |
|---|----|
| Figure 78 Extraction shroud featuring a) vacuum b) catchment plate c) machine.....      | 68 |
| Figure 79 Example of a Minitab worksheet using the L8 experimental design .....         | 70 |
| Figure 80 Unconditioned B216.....   | 72 |
| Figure 81 Conditioned B216.....   | 72 |
| Figure 82 a) SAT cylindrical grinding machine b) cam grinding c) gear production .....  | 76 |
| Figure 83 J&S 540 surface grinder .....   | 76 |
| Figure 84 The machine fluid delivery system, illustrating the Dosatron.....             | 77 |
| Figure 85 The machining fluid system in position .....                                  | 77 |
| Figure 86 Dosatron body with pressure sensor to the right .....                         | 77 |
| Figure 87 Cross section of Dosatron, detailing the operation mechanism.....             | 78 |
| Figure 88 Design 1: The front end of the MQSL delivery system.....                      | 78 |
| Figure 89 Design 2: Development of mechanical feeder .....                              | 79 |
| Figure 90 Design 3: Electrostatic Grinding Machine Setup .....                          | 80 |
| Figure 91 a) DAQ USB unit setup to collect the necessary signal by b) Labview DAQ...    | 80 |
| Figure 92 DAQ terminal configuration from machine sensors .....                         | 81 |
| Figure 93 PVD three segmented films on sample surface .....                             | 82 |
| Figure 94 PVD polish plate and constructed sample bar .....                             | 82 |
| Figure 95 Components of PVD sample bars .....   | 82 |
| Figure 96 Olympus LEXT Con-Focal Microscope .....                                       | 83 |
| Figure 97 Confocal optics 1301nm IR.....  | 83 |
| Figure 98 Con-focal Microscope in action measuring PVD film heights .....               | 83 |
| Figure 99 Average PVD coating height measurement .....                                  | 84 |
| Figure 100 Barkhausen Magnetic Emission detection equipment .....                       | 85 |
| Figure 101 Taylor Hobson 120L Talysurf .....  | 85 |
| Figure 102 Illustrating cross sectioning of samples to investigate microstructure ..... | 87 |
| Figure 103 Finished samples. Embedded in resin body, polished and acid etched.....      | 87 |
| Figure 104 Zwick Vickers Micro Hardness Testing station .....                           | 87 |
| Figure 105 Vickers Micro hardness testing pattern and regime.....                       | 88 |
| Figure 106 Illustrating the systematic modelling approach.....                          | 91 |
| Figure 107 GUI Heat Flux interface window.....  | 92 |
| Figure 108 Illustration of chip volumes created from intersecting grinding tool path..  | 93 |
| Figure 109 Imported iges files to identify tool path.....                               | 94 |
| Figure 110 Volume intersection between wheel and workpiece .....                        | 94 |
| Figure 111 Magnified illustration of chip volumes demonstrating smooth geometries       | 94 |
| Figure 112 Meshing structure focusing on grinding profile .....                         | 94 |
| Figure 113 Idealised cylindrical grinding chip volume .....                             | 95 |
| Figure 114 Idealised cylindrical x-sectional chip shape.....                            | 95 |
| Figure 115 Spectrometer calibration setup.....  | 96 |
| Figure 116 Box furnace images undertaking spectrometer calibration.....                 | 96 |
| Figure 117 CCD analysis of 38Mn Steel (0-1000C) filtered peaks 10nm bandwidth .....     | 97 |

|   |     |
|---|-----|
| Figure 118 CCD positioning on surface grinder a) front view b) rear view .....                | 98  |
| Figure 119 Response of CCD from surface grinding 38Mn steel .....                             | 98  |
| Figure 120 Change in intensity with collimator position (20000ms, 2 gliding average) 99       | 99  |
| Figure 121 Investigation into CCD positioning sensitivity (a - d).....                        | 99  |
| Figure 122 Vs 100m/s, Vw 0.5m/s, Vf 0.03mm/min, Ae=25µm, 10% EcoCool .....                    | 102 |
| Figure 123 Changes in Net Power and SGE over a variation of $h_{eq}$ .....                    | 103 |
| Figure 124 Main effects on Net Power for EcoCool(MQL) input parameters.....                   | 104 |
| Figure 125 Main effects on Specific Grinding Energy (SGE) for EcoCool(MQL).....               | 105 |
| Figure 126 Interaction of all variables on Net Power (kW), EcoCool(MQL) .....                 | 106 |
| Figure 127 Interaction of all variables on SGE (J/mm <sup>3</sup> ), EcoCool(MQL) .....       | 106 |
| Figure 128 EcoCool(MQL) interaction with SGE with respect to $h_{eq}$ .....                   | 107 |
| Figure 129 Trial 2 EcoCool %10 oil Low level combinations of feeds and speeds .....           | 108 |
| Figure 130 Trial 8. EcoCool %10 oil High level combination of feeds and speeds .....          | 108 |
| Figure 131 Trial 4, EcoCool 1%oil .....   | 108 |
| Figure 132 (a) Water only and (b) Dry Trial EcoCool .....                                     | 108 |
| Figure 133 EcoCool(MQL) Surface Roughness Ra .....  | 109 |
| Figure 134 EcoCool(MQL) Surface Roughness Rt .....  | 109 |
| Figure 135 ANOVA EcoCool Surface Measurements Ra.....   | 110 |
| Figure 136 ANOVA EcoCool Surface Measurement Rt.....  | 110 |
| Figure 137 Roundness readouts for EcoCool .....   | 110 |
| Figure 138 Roundness measurements in comparison to water only and dry .....                   | 111 |
| Figure 139 Barkhausen Magnetic Noise EcoCool .....  | 112 |
| Figure 140 Main Effect of 1% - 10% EcoCool in the fluid system.....                           | 112 |
| Figure 141 EcoCool(MQL) BN Readout .....  | 112 |
| Figure 142 Control surfaces; Dry & Burnt Surfaces BMN.....                                    | 113 |
| Figure 143 Mass flowrate and volumetric flowrate of MoS <sub>2</sub> .....                    | 114 |
| Figure 144 Main effects on Net Power for MoS <sub>2</sub> (MQSL) input parameters .....       | 115 |
| Figure 145 Main effects on Net Power for MoS <sub>2</sub> (MQSL) input parameters .....       | 116 |
| Figure 146 Total interactions on Net Power for MoS <sub>2</sub> (MQSL) input parameters.....  | 116 |
| Figure 147 Interactions on SGE for MoS <sub>2</sub> (MQSL) input parameters.....              | 117 |
| Figure 148 Net Power variation with .....   | 117 |
| Figure 149 SGE variation with .....   | 117 |
| Figure 150 The microstructure images showing the width of the 13mm sample .....               | 118 |
| Figure 151 The microstructure along the 13mm sample width MoS <sub>2</sub> .....              | 118 |
| Figure 152 SEM and EDX images investigating surface staining following MoS <sub>2</sub> ..... | 119 |
| Figure 153 MoS <sub>2</sub> Surface Roughness Ra .....  | 120 |
| Figure 154 MoS <sub>2</sub> Surface Roughness Rt .....  | 120 |
| Figure 155 Trial 2 MoS <sub>2</sub> roundness profile .....                                   | 120 |
| Figure 156 Trial 8 MoS <sub>2</sub> roundness profile .....                                   | 120 |
| Figure 157 Under burn cutting conditions .....  | 121 |

---

|   |     |
|---|-----|
| Figure 158 Dry cutting conditions .....   | 121 |
| Figure 159 Variables of significance with respect to the roundness profile MoS <sub>2</sub> ..... | 121 |
| Figure 160 BN Readouts for MoS <sub>2</sub> .....   | 122 |
| Figure 161 Interactions of MoS <sub>2</sub> (MQSL) on BN magnetic power .....                     | 122 |
| Figure 162 Main effects on Net Power for CaF <sub>2</sub> (MQSL) input parameters .....           | 124 |
| Figure 163 Main effects on SGE for CaF <sub>2</sub> (MQSL) input parameters .....                 | 124 |
| Figure 164 Interactions on SGE for CaF <sub>2</sub> (MQSL) input parameters .....                 | 125 |
| Figure 165 Main effects for ESW2 Wheel: B120, Workpiece: 38Mn Steel: CaF <sub>2</sub> .....       | 126 |
| Figure 166 Grinding 38MnSiV6 steel with cBN B90 vitrified bond wheel using CaF <sub>2</sub> ..    | 127 |
| Figure 167 Grinding the harder 51CrV4 steel with cBN B90 vitrified wheel: CaF <sub>2</sub> .....  | 127 |
| Figure 168 Vs=50m/s, Vw=0.5m/s, Vf=0.03mm/min, CaF <sub>2</sub> =18g/min .....                    | 128 |
| Figure 169 Vs=75m/s, Vw=0.6m/s, Vf=0.06mm/min, CaF <sub>2</sub> =18g/min .....                    | 128 |
| Figure 170 Vs=50m/s, Vw=0.6m/s, Vf=0.06mm/min, CaF <sub>2</sub> =41g/min .....                    | 128 |
| Figure 171 Vs=50m/s, Vw=0.5m/s, Vf=0.03mm/min, CaF <sub>2</sub> =18g/min .....                    | 128 |
| Figure 172 SEM investigation .....  | 129 |
| Figure 173 The surface roughness comparison of the 18 g/min - 41g/min CaF <sub>2</sub> .....      | 130 |
| Figure 174 CaF <sub>2</sub> Surface Roughness figures .....                                       | 131 |
| Figure 175 Vickers Micro-hardness testing regime (0-2.25mm depth) .....                           | 132 |
| Figure 176 BN Readouts for CaF <sub>2</sub> Trials .....  | 133 |
| Figure 177 Main effects BN readouts CaF <sub>2</sub> (MQSL) .....                                 | 133 |
| Figure 178 Grinding 38Mn steel with cBN B80 vitrified bond wheel using hBN .....                  | 135 |
| Figure 179 Grinding 51Cr steel with cBN B90 vitrified bond wheel using hBN .....                  | 135 |
| Figure 180 The power and SGE values from the grinding of the softer 38Mn steel ....               | 136 |
| Figure 181 The power and SGE values from grinding the harder 51CrV steel .....                    | 137 |
| Figure 182 Variation of SGE over the ranges of equivalent chip thicknesses .....                  | 137 |
| Figure 183 Barkhausen Magnetic Noise (BN) signal of the hBN trials, on the 51CrV ..               | 139 |
| Figure 184 Averaging Barkhausen Noise with differing lubricants .....                             | 139 |
| Figure 185 Significance of the addition of hBN on the residual stresses .....                     | 140 |
| Figure 186 Overall residual stress effects from the levels of lubricant .....                     | 140 |
| Figure 187 a) Grinding wheel surface wet dressing b) dry dressing .....                           | 143 |
| Figure 188 Diamond dresser surface post dry dress .....   | 143 |
| Figure 189 Dressing wheel surface with added water to the dressing regime .....                   | 145 |
| Figure 190 Dressing wheel surface with no added water to dressing regime (dry) ....               | 145 |
| Figure 191 Cross section of dressing wheel surface after dry dressing .....                       | 146 |
| Figure 192 Illustration of porous volume after adding water to the dressing process               | 146 |
| Figure 193 Confocal surface map of grinding wheel after dry dressing .....                        | 147 |
| Figure 194 Images demonstrating the solid lubricant attraction to the workpiece ....              | 148 |
| Figure 195 Microstructural images from the electrostatic trials. ....                             | 151 |
| Figure 196 Main effects on the surface roughness Ra with the change in CaF <sub>2</sub> .....     | 152 |
| Figure 197 Development of PVD isotherms .....   | 153 |

---

|  |     |
|--|-----|
| Figure 198 PVD Height Con-focal Scan inside step.....  | 153 |
| Figure 199 An image of a PVD sample bar after machining.....                                     | 154 |
| Figure 200 The PVD melt zone for Indium .....  | 154 |
| Figure 201 Confocal Analysis of PVD melting depths.....  | 156 |
| Figure 202 CaF <sub>2</sub> PVD Melting depths and surface temperatures.....                     | 157 |
| Figure 203 hBN solid lubricant surface (finish) temperatures .....                               | 157 |
| Figure 204 PVD Surface Temperatures (Celsius) .....  | 159 |
| Figure 205 Main Effects on Surface Temperature ANOVA CaF <sub>2</sub> .....                      | 160 |
| Figure 206 Main Effects on Surface Temperature ANOVA hBN.....                                    | 160 |
| Figure 207 GUI inputs showing an example of input settings.....                                  | 160 |
| Figure 208 Plotted series of temperatures against experimental SGE with B90 .....                | 161 |
| Figure 209 Transient Heat flux flow – showing depth of isotherms .....                           | 162 |
| Figure 210 Illustration of heat flux application to sample surface .....                         | 162 |
| Figure 211 Burn Threshold Diagram of different lubricant types .....                             | 164 |
| Figure 212 Comparison of the captured light under the calibration conditions .....               | 165 |
| Figure 213 Similar machining parameters under Trial 8 conditions .....                           | 166 |
| Figure 214 Spectral light peak changes over an increase in CaF <sub>2</sub> .....                | 167 |
| Figure 215 Spectral light peak changes over a single Taguchi trial.....                          | 168 |
| Figure 216 Spectral light peak changes over a single Taguchi trial with CaF <sub>2</sub> .....   | 168 |
| Figure 217 Spectral light peaks from Boron Nitride.....  | 169 |
| Figure 218 Simplified shape of the light captured - Using CaF <sub>2</sub> .....                 | 170 |
| Figure 219 Simplified shape of the light captured - Using hBN.....                               | 170 |
| Figure 220 ANOVA main effects analysis on the behaviour of captured light: CaF <sub>2</sub> .... | 172 |
| Figure 221 ANOVA main effects analysis on the behaviour of captured light: hBN ....              | 172 |
| Figure 222 Measured PVD Temperature (Celsius) vs CCD detected peak wavelength                    | 173 |
| Figure 223 Intensity of the grinding sparks against the PVD measured temperature.                | 174 |
| Figure 224 PVD measured temperature vs. modelled temperature .....                               | 178 |
| Figure 225 Illustration of the variation in the model thermal property inputs .....              | 179 |
| Figure 226 Modelled temperatures with measured temperature (Celsius).....                        | 180 |
| Figure 227 Temperatures measured and modelled (Celsius) when using hBN .....                     | 181 |
| Figure 228 Changes in the spectrum measurements when using CaF <sub>2</sub> and hBN .....        | 182 |
| Figure 229 Reduction of power consumption by using MQL of CaF <sub>2</sub> and hBN .....         | 183 |
| Figure 230 Towards a successful implementation of MQL and MQL into industry ...                  | 185 |
| Figure 231 The influence of chip thickness on the application of a solid lubricant .....         | 188 |



---

## 1.0 Introduction

### 1.1 Background and context

Grinding is a fundamental manufacturing process able to produce extremely precise surfaces and geometrical tolerances. As a result, grinding is used within a huge range of engineering applications, including for example; the automotive, aerospace, energy, medical, optical and marine industries. Grinding has existed for hundreds of years and continues to develop in order to enable the machining of technologically advanced materials and to meet the increasing demands of product quality and functional performance.

Grinding however is a highly energy intensive material removal process. The thermal energies associated with grinding are higher than alternative methods such as in metal cutting. Therefore the process temperatures created in grinding have an additional risk of thermally inducing damage, and have a profound influence on the surface integrity of the machined product (Marinescu et al., 2004). Exposure of surfaces to sources of heat particularly throughout the forming and finishing stages dictate; the dimensional accuracy, the material microstructure, the residual stresses and the overall life time performance of the component.

In response to this, traditional grinding methods introduce high-volume or high-pressure machining fluid systems to provide cooling and lubrication between the tool and the workpiece. This provides a measure of control with respect to the thermal behaviour within the grinding zone and enable a general 'bulk' cooling of the grinding process. The machining fluid market is estimated at £16 million a year within the UK however the 'added value' through their functional use is undeniably much greater. Nevertheless the application of fluids account for an extensive proportion of the total manufacturing cost. The costs attributed to the use of machining fluids do not only comprise of the initial purchase and delivery logistics but also the storage, energy consumption, treatment, filtration, and the end of life disposal {{78 Klocke,F. 1997; 66 Brinksmeier,E. 1999}}. The majority of fluids are semi-synthetic soluble oils that also require the use of water. In this respect, industry is required to comply with regulations that control the use and disposal of lubrication materials that are potentially hazardous to, or place unacceptable burdens on natural resources and the environment.

The manufacturing industry is currently facing the prospect of financial penalties and market exclusion (Koc, 2007) if it fails to meet increasing environmental standards with a particular focus on management of chemical wastes (Cheng et al., 2005).



---

Manufacturing companies have responded by developing and adapting alternative production techniques in order to remain legally compliant and competitive in the face of rising costs of natural resources and waste management. The development of Minimum Quantity Lubrication (MQL) techniques is one such response (Brinksmeier et al., 1994). The overall concept of this research study considers the scope for Minimum Quantity Solid Lubrication (MQSL) within the grinding and polishing of manufactured components as part of a broader commitment by industry to achieve more sustainable and environmentally responsible manufacturing.

In this context, there is a clear need to explore the potential for using Solid Lubricants within abrasive machining, developing upon the existing MQL theories in order to establish a stable and reliable grinding process. The ability to control thermal energies through the reduction or elimination of frictional sources is an essential requirement for the practical viability of MQL and MQSL techniques. Therefore this research develops precise methods of application to assess the performance of the solid lubricants and to measure the capability of the solid lubricants to control the thermal environment of grinding. The grinding temperatures were recorded both through empirical measurement and predicted surface temperatures. No system exists in practice that can measure and adaptively control the temperature of the grinding cycle. Therefore this research explores the development of a non-contact non-intrusive thermometry method to provide a real-time measurement of the grinding zone temperatures.

---

## 1.2 Aim and Objectives

The aim of this research was to develop an understanding of Minimum Quantity Solid Lubrication (MQSL) within abrasive machining. This study focuses on the efficiency of the grinding process with respect to the ability to control process energies and suppress thermally induced damage. This study also assesses the principles and the practicalities of delivering solid lubricants into the grinding zone. To achieve this aim the research has four major objectives:

1. Identify the behaviour of MQL machining fluids within the abrasive machining process.
2. Develop an understanding of the implications of MQSL within abrasive machining, involving the development of suitable MQSL feeding mechanisms and compare with use of conventional fluids.
3. Investigate the feasibility of an optical non-invasive method of determining the surface finish temperature, by capturing the emitted energy from the grinding zone.
4. Construct, by combining the previous three objectives, a real-time grinding temperature management system.

### 1.3 Research Structure

The project was systematically designed to progress through the four research objectives, see Figure 1. The colour coded flow diagram identifies the individual research objectives along with their associated decisions and experiments. This systematic approach allows key messages to be carried forward from the completion of each objective in turn, forming the basis of greater understanding until the overall aim of the study was achieved.



**Figure 1** Flow chart illustrating the route to achieve the project objectives (Key: The rounded boxes indicate the objectives, the diamonds indicate decisions and the squared boxes indicate work needed to be done)

---

## 2.0 The art of grinding

### 2.1 Overview

The purpose of this chapter is to review the existing knowledge of controlling process temperatures within abrasive machining, from both academia and industry. The principles of the grinding process were studied along with the identification of gaps in the knowledge to control the thermal aspect of grinding. Various properties of the machining fluids are also explained together with the fundamental reasons for lubricating the grinding process. In general the chapter includes:

- grinding theories, behaviours, and the effect that grinding has on workpiece structure,
- an insight into the roles of machining fluids, advantages and legislation,
- the idea behind Minimum Quantity Lubrication (MQL) including an introduction into Minimum Quantity Solid Lubrication (MQSL).

### 2.2 Abrasive machining

Abrasive machining describes any manufacturing process that involves hard abrasive grits acting against a softer workpiece surface. In general this is known as grinding however it can exist in other forms such as, lapping, and sanding. The interaction of an abrasive grit upon a surface involves the removal of unwanted material through the methods of rubbing, ploughing and cutting, to expose the desired surface geometry.

By definition abrasive machining can be split into two classifications; Stock Removal Grinding (SRG) and Form and Finish Grinding (FFG). SRG focuses on large rates of material removal, for example the rough conditioning of forged components such as crankshaft bearing journals and camshafts profiles. In these situations the undeformed chip thicknesses tend to be relatively large and the wheel-wear comparatively high. Comparisons can also be made between the mechanics involved between SRG and traditional metal cutting methods. On the other hand FFG is concerned with the production of tight tolerances and high workpiece surface integrities, for example the polishing of optical lenses. Removal rates are relatively low and the mechanics of the grinding cycle create small chips and high quality surface integrities (Shaw, 1996).

Abrasive machining generally combines high machine speeds and high specific energy removal rates (Society of Manufacturing Engineers, 1983) that result in high process temperatures increasing the risk of creating thermal stresses that ultimately determine the components surface integrity (Malkin and Guo, 2007). This method of machining however is heavily exploited throughout all major engineering sectors, including the

---

automotive, aerospace, energy, marine and medical industries and continues to develop and compete against traditional turning and milling methods as it has the advantage of producing high surface finishing tolerances (Webster and Tricard, 2004).

The consequence of high process temperatures is the risk of exposing high grinding temperatures towards the machine structure, to the abrasive grits, to the wheel composition and of course to the workpiece. The majority of the mechanical energy input is converted into heat that is divided between the workpiece, chip, wheel, and fluid, with the remainder involved in the surface conditioning and the generation of residual stresses (Brinksmeier et al., 2006). The thermal history, including the thermal stresses, that are introduced through each stage of production will greatly influence work piece functionality, defined by any change in the workpiece properties (Klocke et al., 2005);

- Macro (accuracy in shape and dimension)
- Micro (surface topography)
- Meso (material structure and properties, including residual stresses)
- Nano (tribo-mechanical chemistry)

More specifically it is extremely important, and not just within precision engineering, to consider the functions and properties necessary for the work piece to retain once the machining process is complete:

- Mechanical functions (capability of carrying mechanical loads)
- Thermal functions (heat resistance or temperature conductivity)
- Tribological functions (surface interaction with other media)
- Optical functions (visible appearance, light reflection behaviour)
- Flow functions (influence of the flow of fluids)

Understanding the origins of the heat generation and the flow of thermal energies throughout the abrasive cycle is critical towards the attainment of the desired surface integrity, of the form and of the finish (Comley et al., 2005). Substantial development in grinding modelling and simulation continues to take place intending to help forecast, not only grinding temperatures, but also grinding energies, forces, and machine fluid flow, as outlined in Brinksmeiers review (Brinksmeier et al., 2006). High process temperatures however are not always regarded as being a negative characteristic and in fact heat is desired and required by many manufacturing processes. Take the welding and heat treating of metals for example, here the purpose is to introduce and adapt change of the workpiece material property. By directly controlling process temperatures the opportunity exists to influence the workpiece structure in a predictable manner, such as the inclusion of surface heat treatment cycles (Klocke et al., 2005)(Tönshoff et al., 2002).

## 2.3 Mechanical Models

Initially the mechanics of the abrasive machining process were assumed to be of a scaled down derivative of cutting. However this is not the case and the processes involved are in fact very different, particularly with respect to form and finishing grinding (FFG) (Shaw, 1996).

### 2.3.1 Cutting Mechanics

Metal cutting concentrates the majority of its energy into clearly defined shear planes that propagate from the deepest cutting edge and pass through the workpiece up to the surface, at a shear angle  $\phi$ , demonstrated by Figure 2a and Figure 2b. Deformation ceases once the material is sheared, leading to the separation and production of a chip.

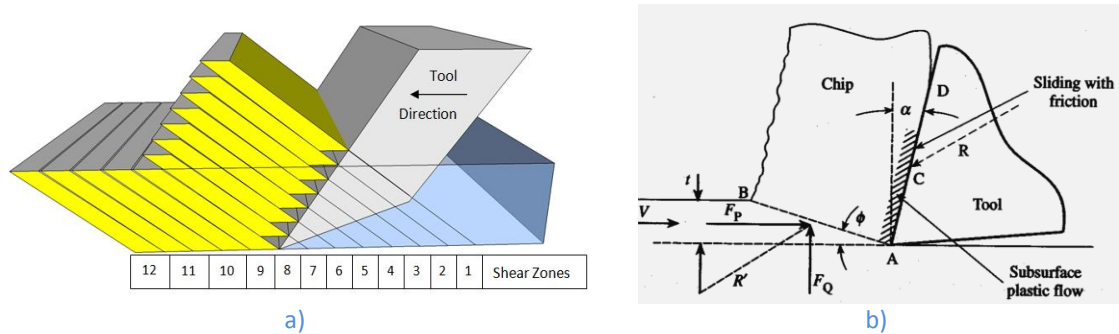


Figure 2 The cutting zone (Shaw, 2005) a) The development of shear planes and, b) the mechanics

The Specific Cutting Energy  $u$  is a functional indicator into the effectiveness and efficiency of this deformation. This value represents the energy required in removing a unit volume of material, with the magnitude allowing for an estimation of the power required from the machining process (Sood et al., 2000). Alternatively this also indicates the amount of energy needed to be removed from the point of cut. In metal cutting the specific energy is defined as;

$$u = \frac{F_p v}{v b t} = \frac{F_p}{b t} \quad (\text{J} \cdot \text{mm}^{-3}) \quad \text{Equation 1}$$

Where  $F_p$  is the horizontal cutting force,  $b$  is the width of cut and  $t$  is the undeformed chip thickness. In the case of metal cutting the specific energy is effectively independent of the cutting speed  $v$ . It changes slightly with rake angle  $\alpha$ , but more importantly it varies inversely with  $t$  (the undeformed chip thickness), and creates what is known as the size effect.

The relationship between the specific cutting energy and temperature is a huge field of study (Shaw, 2005). Subsequent thermal modelling intends to calculate the process temperatures by utilising the machining parameters as inputs into the system, in order to ultimately predict the achievable surface integrity of the component. The

---

dominating feature when utilising single-point cutting methods is the formation and pattern of the shear planes as in Figure 2b. This particular mechanism is outside the scope of this research however it acts as a good origin to appreciate the differences involved in abrasive machining.

### 2.3.2 Grinding Mechanics

Grinding wheels exist in many forms, shapes and sizes, with all wheels being designed and constructed for specific processes. Generally an abrasive wheel includes a randomised pattern of abrasive grit bonded to the periphery of the wheel surface. The nature of the abrasive grit and the composition of the bond needs to be carefully selected in order to provide optimal grinding conditions.

A fundamental distinction between cutting and grinding is noted at the geometry of the tool edge. Grinding has extremely undefined tool edge geometries as the wheels are constructed from many multi-raked and multi-positioned grits in comparison to the well defined point of cutting achieved from a single pointed turning tool. This characteristic of grinding utilises a unique removal mechanism with respect to the creation of the shear planes and the tribological factors involved throughout the contact period of the abrasive with the workpiece, while the thermal behaviour throughout the grinding processing cycle is defined by the shape of the heat source passing across the workpiece surface.

The randomised positioning of the abrasive grits on the surface of a grinding wheel results in the abrasive process having many small points of contact with varying cutting depths at any one time. The number of active cutting points per unit area on the wheel surface is defined as the active grit density,  $C$ . Initially a single abrasive grain will move into the grinding zone, instigate a rubbing motion along the top surface, progressing into a ploughing action before propagating a pathway that eventually develops a shear force and enough deformation to produce a chip, see Figure 3. In effect the undeformed chip thickness increases in size throughout its length, as simplified by Figure 4.

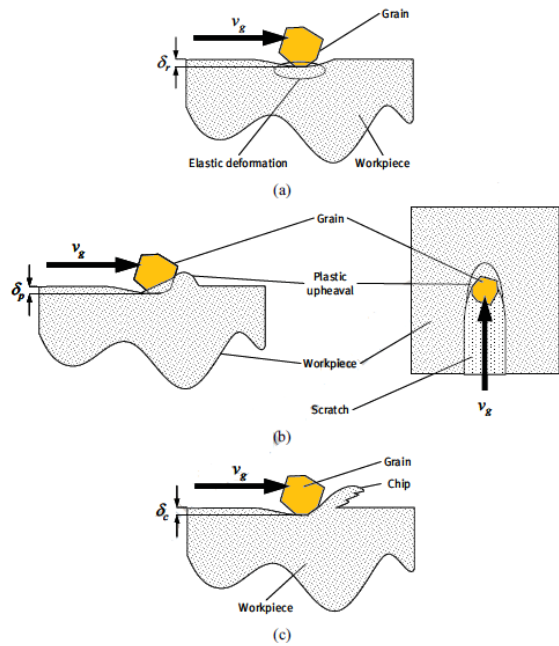


**Figure 3** Illustration of (a) rubbing, (b) ploughing, and (c) chip formation phases of material removal by an individual grain. (Doman et al., 2008)

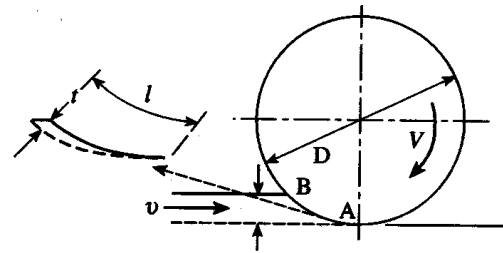


**Figure 4** Grinding zone mechanics. Undeformed chip structure (surface grinding)

The Specific Grinding Energy (SGE) is defined as the energy required in removing a unit of material within the grinding process. Here the normal force is far larger than the tangential force, and the SGE is ultimately described by:

$$u = \frac{F_p v_s}{v_w b d} \quad (\text{J} \cdot \text{mm}^{-3}) \quad \text{Equation 2}$$

With  $v_s$  describing the speed of the grinding wheel,  $v_w$  the horizontal working speed (surface grinding) and,  $d$  the grinding wheel diameter. The differences between the specific cutting energy and the specific grinding are recognised through the energy required to produce a chip. The general association is that abrasive machining involves higher specific energies. Large proportions of this energy will eventually be converted into heat, for example FFG having values 10 to 30 times higher than cutting (Shaw, 1996).

The various forms of energy in grinding include plastic deformation, friction, surface energy, and momentum transfer, however only the first two of these are of real significance (Shaw, 2005). The effective rake angle of an abrasive grain tends to be negative due to the relatively large radius of the grit against the small chip thickness and the volume of the plastically deformed material is estimated to be 75% times greater than the actual volume removed (Shaw, 1995).

In essence the specific grinding energy is a measure of the difficulty of grinding a material under particular conditions (Marinescu et al., 2006). Values of 10-20  $\text{J} \cdot \text{mm}^{-3}$  are typical for easy-to-grind materials with efficient grinding conditions. Values around



200 J.mm<sup>-3</sup> are typical of many finishing operations. High specific energies also indicate high quantities of heat however it is the mode by which the heat is dissipated which is paramount to the surface integrity (Malkin and Guo, 2007). While the surface integrity and heat partitioning is explained in more detail in later sections it is generally accepted that this heat is divided between the wheel, the workpiece, the chip and the machining fluid (Jin and Stephenson, 2006).

The Specific Material Removal Rate (SMRR)  $Q'_w$  is defined as the product of the depth of cut  $a_e$  and the speed of the workpiece  $v_w$ , effectively independent of wheel width;

$$Q'_w = a_e \times v_w \text{ (mm}^3 \cdot \text{mm}^{-1} \cdot \text{s}^{-1}\text{)} \quad \text{Equation 3}$$

Typical values of  $Q'_w$  expected from a variety of grinding regimes are identified in Table 1.  $Q'_w$  is an extremely important factor within the analysis of abrasive machining as depending upon the nature of the grinding process it provides an indication into the likely temperatures and forces introduced into the grinding zone.

**Table 1** Typical machine parameters for conventional, creep feed & HEDG grinding (Comley, 2005)

| Machine Settings  | Grinding Approach |                |                 |
|---|-------------------|----------------|-----------------|
|   | Conventional      | Creep-feed     | HEDG            |
| Depth of Cut<br>$a_e$ (mm)  | Low<br>0.001-0.05 | High<br>0.1-20 | High<br>0.1-30  |
| Work piece speed<br>$V_w$ (m/s)                                     | High<br>1-30      | Low<br>0.05    | High<br>0.5-10  |
| Wheels Speed<br>$V_s$ (m/s)   | Low<br>20-60      | Low<br>20-60   | High<br>80-200  |
| Specific Material Removal<br>Rate<br>$Q'_w$ (mm <sup>3</sup> /mm.s) | Low<br>0.1-10     | Low<br>0.1-10  | High<br>50-2000 |

For extremely low values of  $Q'_w$  the rubbing and ploughing processes dominate. As  $Q'_w$  increases, so does the proportion of energy consumed by the formation of a chip, see Figure 5. Generally the energy consumed through the rubbing and ploughing processes remains relatively constant throughout all  $Q'_w$  values (Marinescu et al., 2006).

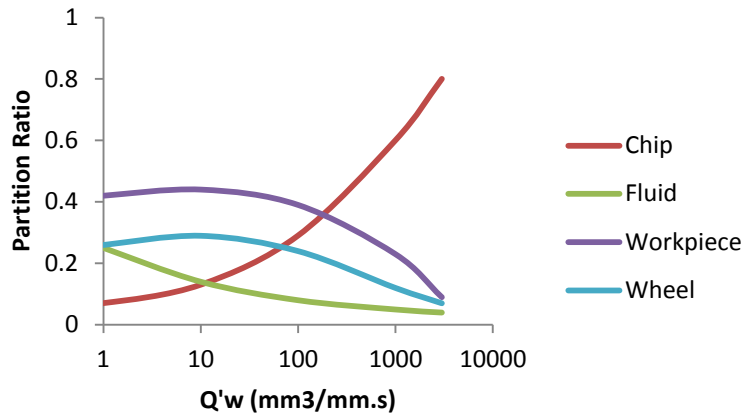


Figure 5 Thermal modelling partition ratios (Comley et al., 2005)

The relationship between the SGE and the SMRR is determinable (Jin and Stephenson, Sep 2003). For example the interaction between these process variables within surface grinding can be found to be;

$$e_c = 70Q'_w{}^{-t} \text{ (J.mm}^{-3}\text{)} \quad \text{Equation 4}$$

Where  $t = 0.24-0.4$ , is calculated from experiment, with the variation of  $t$  shown in Figure 6;

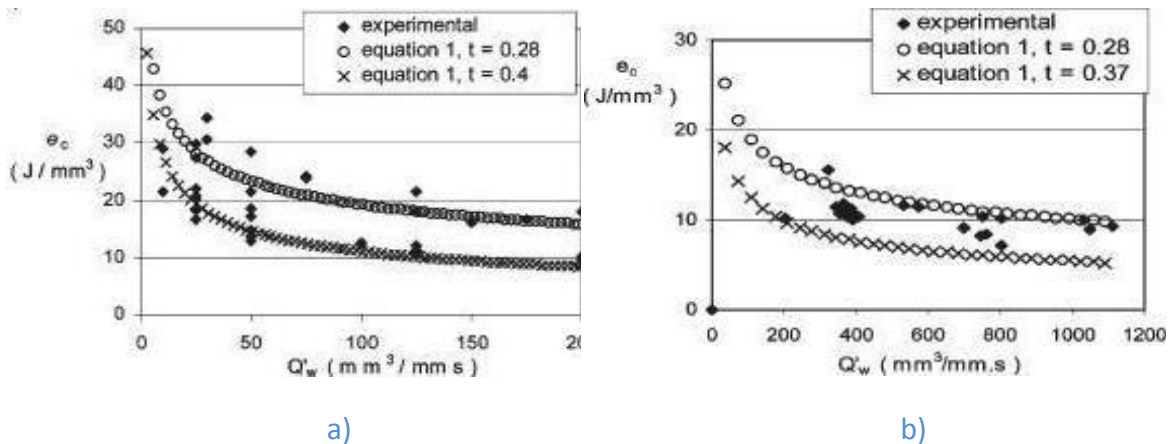


Figure 6 a) and b) Specific Grinding Energies over a wide range of S.R.R.

Equivalent thickness of the contact layer,  $h_{eq}$  is used as a useful comparator of grain penetration aiding the visualisation of process efficiency (Marinescu et al., 2006) otherwise described as the volumetric removal rate per unit depth. Equivalent chip thickness describes the thickness of the layer of workpiece material removed at wheel speed. Generally wheel speeds are in a magnitude of 100 times that of the workpiece speed. Equivalent chip thickness is inversely proportional to the wheel speed.

$$h_{eq} = \frac{a_e \times v_w}{v_s} = \frac{Q'_w}{v_s} \text{ (}\mu\text{m)} \quad \text{Equation 5}$$

As noted earlier the abrasive machining process does not have such a defined point of shear which adds to the complication of modelling, Figure 7. The negative rake angle of the abrasive grain adds a leading zone of compressive forces, whilst a zone of undesirable tension is introduced at the grain tip. Negative rake angles are generally associated with a less efficient means of creating shear zones particularly in comparison to the mechanisms involved in turning and milling, however the high rotating speeds from the interacting grinding wheels promote a more visco-plastic nature of chip deformation through the relatively high process temperatures see Figure 7.

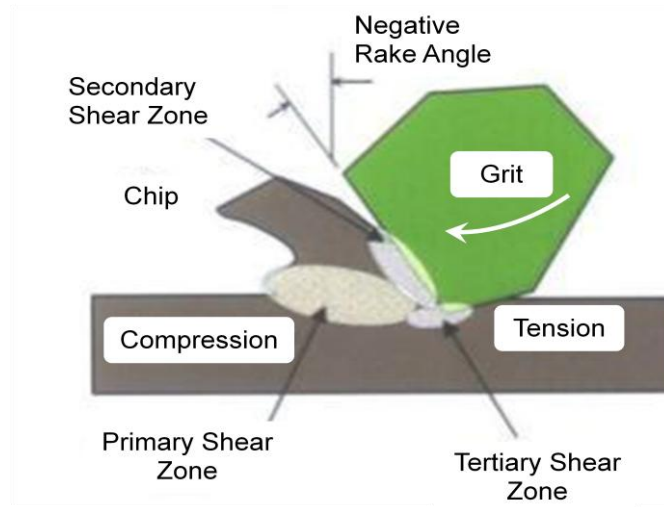


Figure 7 Shear planes within abrasive machining (Jackson, 2008)

The efficiency of an abrasive cycle becomes increasingly difficult to predict as there are many input parameters to be considered. The performance of a machining setup is not only determined through the tooling, the feeds and speeds, the work material, and the machining fluid, but also dependent on the particular type of abrasive machining process selected.

## 2.4 Cylindrical Grinding

Grinding exists in many forms. The types most often found commercially are known as:

- Surface grinding
- Creep grinding
- Internal and External grinding
- Centreless grinding
- Belt grinding
- Lapping and polishing
- HEDG (High Efficiency Deep Grinding)

Surface grinding is by far the most common example of grinding and the simplest to model. However this research focuses on the principles of external cylindrical grinding, more specifically Cylindrical Plunge Grinding, see Figure 8.

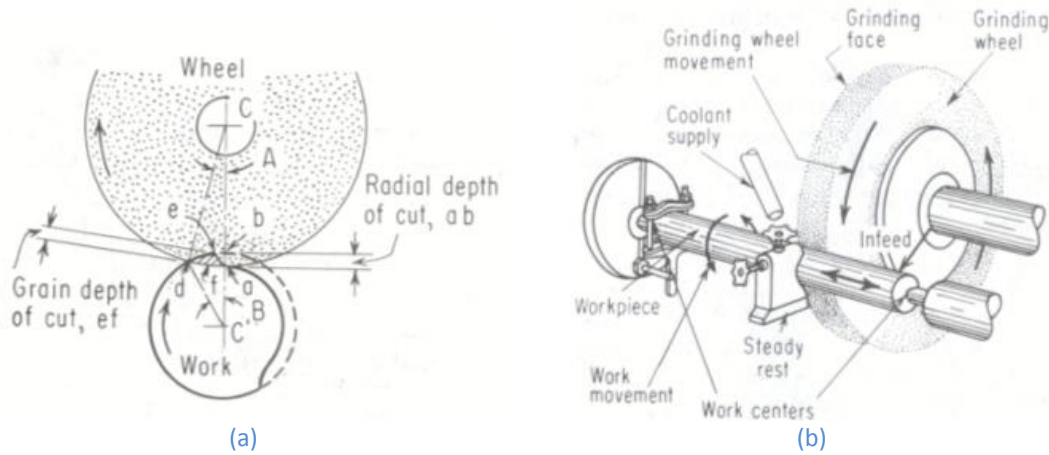


**Figure 8** (a) and (b). Basic mechanics involved in Cylindrical Plunge Grinding. (Society of Manufacturing Engineers et al., 1976)

Plunge grinding refers to the action of uni-axially driving the grinding wheel into the work piece to a required depth of cut ( $d$ ). The depth of cut defined by the radial feed per revolution of the work:

$$d = \frac{v_r}{N_w} \text{ (mm)} \quad \text{Equation 6}$$

Where,  $v_r$  equates to the radial feed per unit time and  $N_w$  the revs per second (r.p.s.) of the work piece.

Varying grit heights come into contact over the width of a wheel on the closer inspection of a single wheel pass, see Figure 9. The surface of a conditioned wheel will commonly contain a mixture of active and inactive grits that physically interact or are made redundant respectively throughout a single pass. Wheel wear and the distribution of the grit also contribute to this grit height variation.

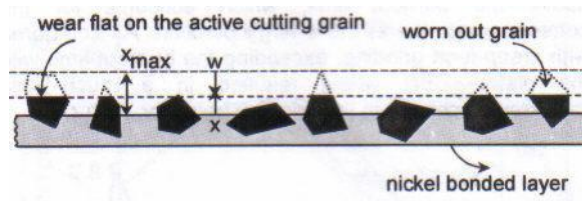


**Figure 9** Illustration of varying grit height of a plated CBN wheel

To quantify the chip height an Average Chip Thickness is used, assuming a mean grit height, and defined as;

$$\bar{t} = \left[ \left( \frac{v_w}{v_s Cr} \right) \left( \frac{D}{l} \right) \right]^{0.5} \quad \text{Equation 7}$$

In the case of cylindrical grinding the wheel and workpiece diameters combine to form an effective diameter  $D_e$ . This effect demonstrates that external cylindrical grinding has a relatively short contact length in comparison with other grinding processes.

$$D_e = \frac{D_s D_w}{D_s + D_w} \quad \text{Equation 8}$$

The contact length of cut,  $l_c$  is a dominant factor in the distribution of energy throughout the machining process. A deeper cut increases the exposure of an abrasive grit to the work piece material. This enhances both the time and the distance of grit contact, greatly influencing the energy partitioning ratio.

$$l_c = \sqrt{(a_e \times D_e)} \quad (mm) \quad \text{Equation 9}$$

A typical external cylindrical plunge grinding cycle involves two defined stages; roughing and spark out, illustrated in Figure 10. The controlled infeed velocity remains constant up until the desired depth of cut. However the actual infeed speed is slightly retarded in its response due to elastic deflection of the system up until the completion of the sparkout phase (Malkin, 1981).

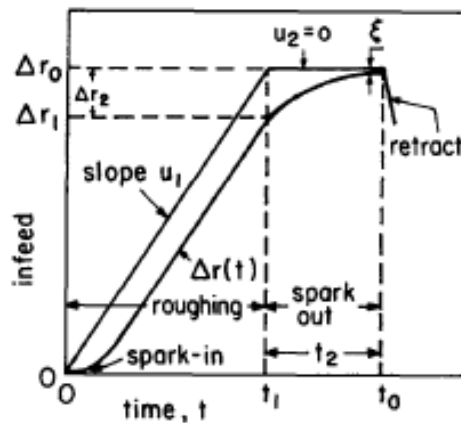
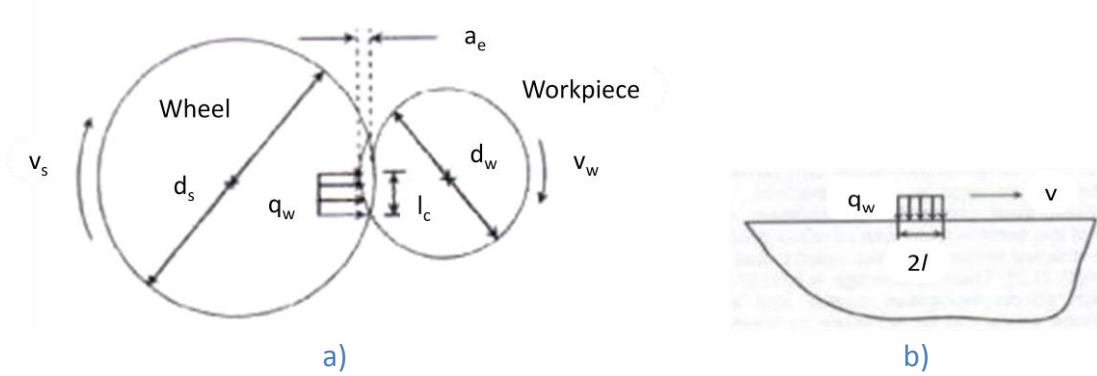


Figure 10 Conventional grinding cycle

An ideal cycle would consist of a fast roughing stage followed by period of zero infeed sparkout. Increased infeed rates and forces throughout the roughing stage increases the likelihood of micro-structural damage, however with suitable understanding of the thermal flows the depth of damaged material can be removed by sparkout (Malkin and Guo, 2007). Surface finish is predominantly determined by the sparkout phase due to surface finishes becoming finer with longer sparkout periods and reduced infeed rates.

## 2.5 Grinding Modelling

The development of grinding models has been directed towards the prediction of grinding forces, thermal behaviours, surface topography and surface integrity (Brinksmeier et al., 2006). Early models were developed using the principles of sliding heat sources (Jaeger, 1942) as a uniform flux of heat moving at a constant velocity over the surface of a semi-infinite solid, under a quasi-steady state heat transfer condition. Since then thermal modelling has progressively developed to equal the accuracy achieved through the enhancement in machine speeds and capabilities. The analysis of heat generation at the grain flats enable an approximation of the maximum contact temperature  $T_{max}$ , also including the temperature just beneath the working surface (Chiu and Malkin, 1993).



**Figure 11** Illustration of external cylindrical plunge grinding with respect to a) the thermal energy source and, b) the thermal sliding source of heat model (Malkin and Guo, 2007)

The temperature rise with respect to Figure 11(b) can be described as:

$$dT = \frac{1}{\pi k} \int_{-l}^l q_w(\xi) e^{-\frac{V(x-\xi)}{2\alpha}} K_0 \left[ \frac{V}{2\alpha} \{(x-\xi)^2 + z^2\}^{1/2} \right] d\xi \quad \text{Equation 10}$$

Where  $K_0$  is the modified Bessel function of the second order zero,  $q_w(\xi)$  is the heat flux distribution at the surface on the semi-infinite body,  $V$  is the velocity of the sliding heat source. The majority of these definitions are derived by the Hahn model. The maximum surface contact temperature is then defined as:

$$T_{max} = \frac{1.595 q_w \alpha^{1/2} l^{1/2}}{k v_w^{1/2}} \quad \text{Equation 11}$$

Where  $q_w$  is the heat flux distribution at the surface of a semi-infinite body,  $k$  is the thermal conductivity,  $\alpha$  is the thermal diffusivity,  $l$  is half of the length of the heat source, and  $v_w$  is the work piece speed (the heat source velocity).

$$l = \frac{l_c}{2} \quad \text{Equation 12}$$

$$l_c = (a_e d_e)^{1/2} \text{ (mm)} \quad \text{Equation 13}$$

Therefore in order to calculate  $T_{max}$  the maximum contact temperature rise we need to find the value of heat flux being introduced into the work piece at the point of grind. Of the total grinding energy only a proportion of heat is conducted directly into the work piece. This fraction  $\epsilon$  is the partitioned heat into the workpiece. The heat flux can be then calculated from the specific grinding energy  $u$ , or power  $P$ , from the cycle;

$$q_w = \frac{\epsilon u v_w a_e b}{l_c b} = \frac{\epsilon P}{l_c b} \quad \text{Equation 14}$$

In actual fact the surface contact zone will experience a flash temperature close to the melting point of the work piece material, see Figure 12. These peaks however are extremely localised and involve microscopic grinding chips. An assumption made throughout thermal modelling of grinding, is to ignore this microscopic behaviour, and focus just underneath the surface with a continuous heating of the grinding zone known as the grinding zone temperature.

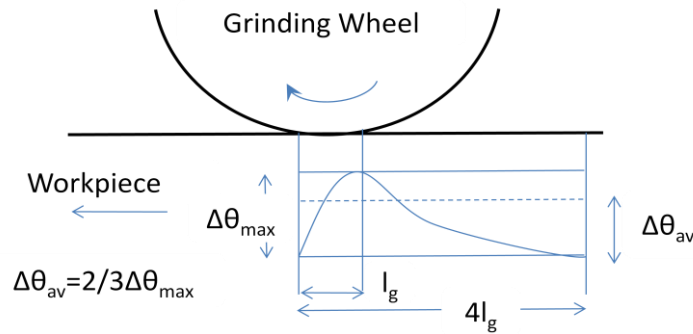


**Figure 12** The thermal distribution along the grinding contact length. The workpiece experiences flash surface temperatures while an average process temperature is calculated from a longer contact length (Rowe et al. 1988).

## 2.6 Heat Partition Ratio

The partition of energy is described as the distribution of specific grinding energy during the three phases of surface deformation; sliding, ploughing and chipping;

$$u = u_{ch} + u_{pl} + u_{sl} \quad \text{Equation 15}$$

The partition of heat is described as the division of the total heat flux between the work piece, grinding wheel, chip and fluid;

$$q_t = q_s + q_w + q_{ch} + q_f \quad \text{Equation 16}$$

This distribution of energy is also described as the Heat Partition Ratio, see Equation 17. The energy sinks are illustrated in Figure 13 (Tawakoli, 1993).

$$1 = R_s + R_w + R_{ch} + R_f \quad \text{Equation 17}$$

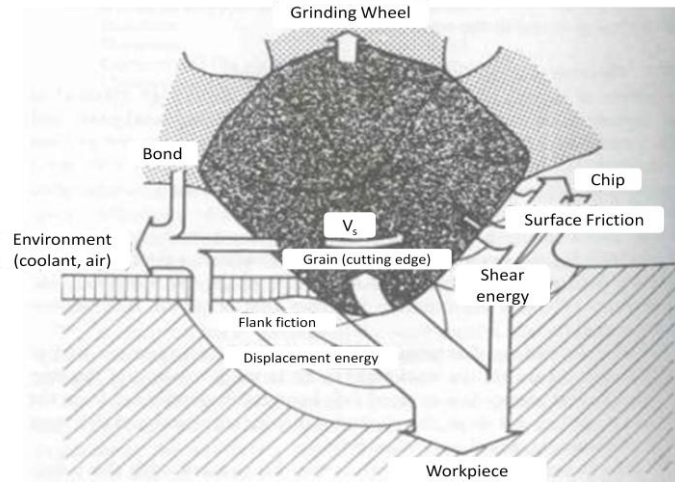


**Figure 13** Energy distribution between workpiece, grinding wheel, cutting fluid and chip.

The division of energy strongly depends on three significant machining parameters; the selected grinding process, the materials involved and the relation between the Specific Grinding Energy (SGE) and the Specific Removal Rate (SRR). As previously noted small SGE values are attained in HEDG grinding due to the relatively large depths of cut and high volume of removed material and the likelihood of high SGE's is more prominent within shallow cut and creep feed grinding.

The total grinding heat flux  $q_t$  can also be calculated if the specific grinding energy is known (Jin and Stephenson, Sep 2003) described as;

$$q_t = \frac{e_c \cdot a_e \cdot v_w}{l_c} \quad \text{Equation 18}$$

The distribution of heat flux is limited by the maximum contact temperature  $T_{max}$ , by the fluid burn-out temperature  $T_b$ , and the material melting temperature  $T_{mp}$ , and can be related though the specific thermal convection factor  $h$ ; (where  $q_w = h_w \cdot T_{max}$ ,  $q_s = h_s \cdot T_{max}$ ,  $q_{ch} = h_{ch} \cdot T_{mp}$ )

$$q_f = h_f \cdot T_{max} | T_{max} \leq T_b \quad \text{Equation 19}$$

Note that once the fluid reaches burn-out temperature its convection factor effectively drops to zero, indicating that there is no more removal of heat by the fluid above this working temperature and is written as;

$$q_f = h_f \cdot (T_b - T_0) \quad \text{Equation 20}$$

Where  $T_0$  is the ambient temperature.

The heat flux that is convected away by the chip can also be estimated as;

$$q_{ch} = \frac{e_{ch} \cdot a_e \cdot v_w}{l_c} \quad \text{Equation 21}$$



Where the energy of the chip is calculated from using the specific heat capacity of the chip  $c$ .

$$e_{ch} = \rho c T_{ch} \quad \text{Equation 22}$$

The proportion of the heat taken by the chip can then be calculated from both the partition of heat flux and the partition of the specific grinding energy taken by the chip;

$$R_{ch} = \frac{q_{ch}}{q_t} = \frac{e_{ch}}{e_c} \quad \text{Equation 23}$$

Figure 14 shows how the partitioning of heat into the chip increases up until the melting temperature.

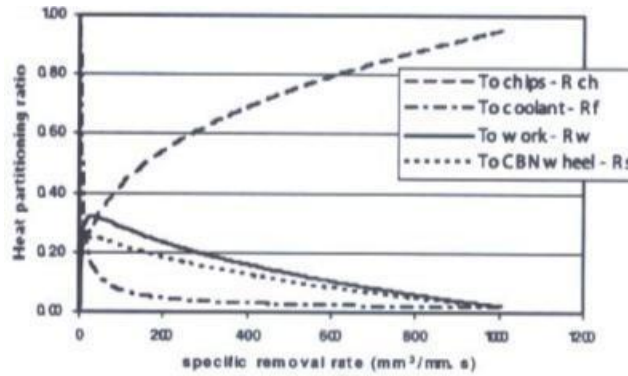


Figure 14 Heat partition ratios over varying S.R.R. (Jin and Stephenson, Sep 2003)

Similarly the work-piece partition ratio is defined as;

$$R_{ws} = \frac{q_s}{q_w + q_s} = \frac{h_w}{h_w + h_s} = \left[ 1 + \frac{0.97 k_g}{\beta_w \sqrt{r_0 v_s}} \right]^{-1} \quad \text{Equation 24}$$

Where  $r_0$  is the effective radius of contact of the abrasive grains on the periphery of the wheel, and  $\beta$  is a thermal property;

$$\beta = \sqrt{k \cdot \rho \cdot c} \quad \text{Equation 25}$$

The shape of the sliding source of heat, with respect to the grinding process, has developed over the years greatly influencing the accuracy of the thermal modelling. The earliest model most commonly referred to is the sliding source of a uniform heat source introduced by Jaeger, before progressing into triangular heat forms, and more recently being established a circular arc of heat model, Figure 15.

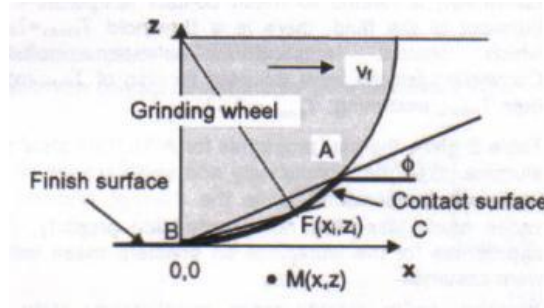


Figure 15 Circular arc of heat source AFB (Rowe and Jin, 2001)

Here the contact length is defined by AFB. But it is possible to recognise the structure of the temperature rise calculation from equation 25, with respect to a point  $M(x,z)$  just beneath the surface;

$$dT = \frac{1}{\pi \cdot k} \int_0^{l_c} q \cdot e^{-\frac{v_f(x-l_i \cos \phi_i)}{2\alpha}} K_0 \left[ \frac{v_f r_i}{2\alpha} \right] dl_i \quad \text{Equation 26}$$

$l_i = d_e \cdot \phi_i$  is the arc length, BF

$\phi_i$  is the contact angle, and  $q$  is the heat flux;

$$q = \bar{q} \cdot (n + 1) \cdot \left(\frac{l_i}{l_c}\right)^n \quad \text{Equation 27}$$

Where  $n$  denotes the shape of source,  $0$  = uniform heat flux,  $1$  = triangular heat flux,  $2$  = square function, and  $\bar{q}$  is the mean heat flux on the surface AFB.

The shape of the heat source creates obvious differences in the thermal model solutions as illustrated in Figure 16. As the capability of grinding machining and tooling has improved, allowing deeper and faster processing, increases in chip thicknesses and length necessitate adaptation of the thermal models to recognize and compensate for the shape of the heat source. This greatly influences the maximum thermal exposure to the surface of the workpiece.

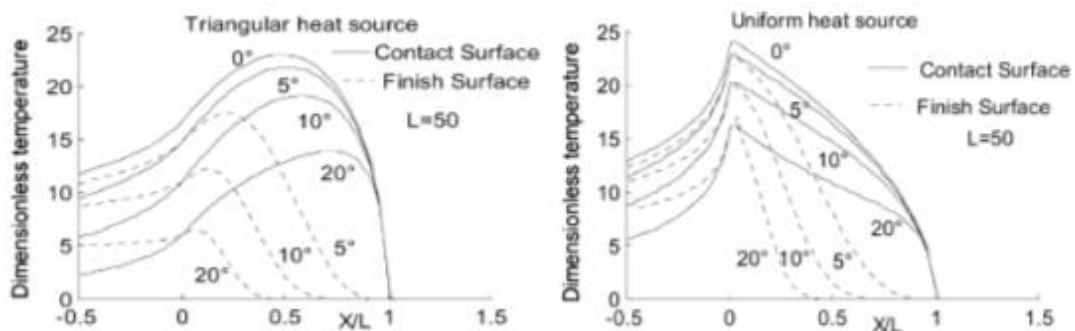


Figure 16 Dimensionless temperatures on contact and finish surfaces illustrating temperature curves relating to shape of source of heat (Jin et al., 2002) ( $X/L$  explained in section 2.8)

Establishing a relationship between the specific grinding energy and the onset of component thermal damage is essential for controlling the grinding process. The exposure of metals to various elevations in temperature increases the likelihood of progressions into tempered, martensitic and austenitic phases. Just how rapidly and how deep the surface energy is taken to really depend upon the structure of the material the temperature particularly with reference to the workpiece thermal conductivity values, thermal diffusivity, density, and specific heat capacity. Therefore a link between the machining parameters and the maximum surface temperature would allow for an optimisation of the material structure post machining.

Developing the ideas of the partition of specific energy (between the wheel, workpiece, chip and fluid) it has been shown, through the use of inverse heat analysis, that most of the grinding energy is dissipated through the actual geometrical contact length, {{149 Kim,N.K. 1997;}}. Where the total energy related to the sliding and ploughing is completely dissipated by the workpiece. A fraction of the energy required to form a chip (~55%) however can be attributed to the thermal environment of the passing abrasive grit. Therefore maximum associated surface temperature is modelled as:

$$\theta_m = \frac{1.13a^{\frac{1}{2}}a_e^{\frac{3}{4}}d^{\frac{1}{2}}}{kv_w^{\frac{1}{4}}}(u - 0.45u_{ch}) \quad \text{Equation 28}$$

The constant value of 1.13 reduces slightly to 1.06 when changing the heat shape from a liner uniform source to a triangular heat source. By rearranging this equation it is then possible to establish a dimensionless representation of the machining parameters and the limits towards surface thermal damage and hence burn.

When,

$$u_o \equiv 0.45u_{ch} \quad \text{Equation 29}$$

and,

$$B = \frac{\theta_m K}{1.06a^{\frac{1}{2}}} \quad \text{Equation 30}$$

Then,

$$u = u_o + Bd_e^{\frac{1}{4}}a_e^{-\frac{3}{4}}v_w^{-\frac{1}{2}} \quad \text{Equation 31}$$

This can then be plotted to identify the division between the good quality grinds to that of burnt and damaged surfaces, see Figure 17. The Burn threshold is then identifiable through the steepness of the gradient, representing the extent of the

threshold temperatures, and the intersection of the specific energy axis which should equal the energy taken away through the forming of a chip,  $u_o$ .

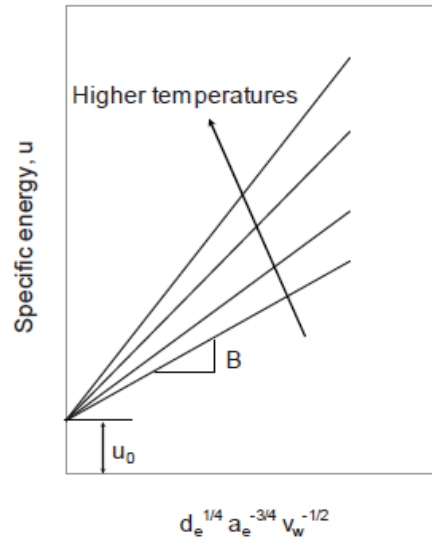


Figure 17 Maximum grinding zone temperatures

Malkin goes on to explain that if there is a known threshold of SGE against the physical grinding parameters of  $f(d_e, a_e, v_w)$  then a measurement of the cycle power would also be able to gauge whether or not thermal damage is or is close to taking place (Malkin and Guo, 2007). The maximum grinding zone temperature is a multiplication of the SGE and the  $Q'_w$ , therefore establishing a threshold power value:

$$P = u_o b v_w a_e + B d_e^{1/4} a_e^{-3/4} v_w^{-1/2} \quad \text{Equation 32}$$

Published experimental data states that the value of the SGE intersect (y-axis intersect) is equal to that of  $U_o$ . If in steels the associated energy required to form a chip is known to be  $U_{ch} \approx 13.8 \text{ J/mm}^3$  then  $U_o$  can be assumed to be equal to  $6.2 \text{ J/mm}^3$  using equation 29.

### 2.6.1 Thermocouples

The ability to model and predict grinding temperatures requires an accurate comparison against empirical temperature data set measurements. Many techniques have been developed to physically quantify the temperatures involved. Thermocouples are well established when demonstrating grinding temperatures however they do not come without their limitations. The rotational nature of the tooling and the workpiece within cylindrical plunge grinding adds an additional challenge of physically connecting any hardware and instrumentation. There is also the general aggressiveness of the grinding process, as an increase in the feeds and speeds increases the disturbance in recorded data signals, especially with respect to the high power consumption effecting the sensitive instruments resulting in poor signal/noise performance.

Thermocouples come in many shapes and forms depending on; the expected temperature ranges, the working environment, and the time response. Earlier research includes the addition of sacrificial thermocouples in order to determine ‘direct’ temperatures at the point of grind. However the resolution can never be guaranteed and the ‘flash’ temperature, seen by the formation of a ground surface, will rarely be recorded. Figure 18 illustrates a typical thermal response from a thermal couple exposed to a passing grinding wheel, while Figure 19 demonstrates the time delay from the creation of a peak grinding surface temperature to when the thermocouple actually records a change. The physical disadvantage of positioning thermocouples into a work zone or workpiece adds to the inaccuracies in temperature readings. Heat flows are greatly affected by machined contours, such as the surfaces created by bored holes for the positioning of the thermocouples. In these instances even the inclusion of a conducting material such as Mica has a limited ability to control any thermal gradients across from the workpiece to the thermocouple.

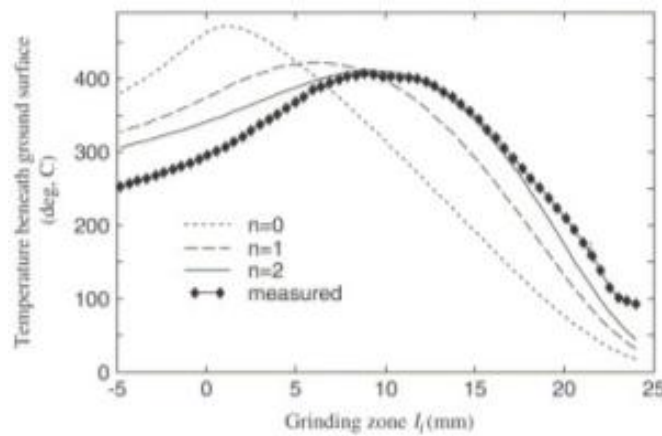


**Figure 18** Illustration of the response mode of thermocouple vs. thermal modelling (Jin and Stephenson, 2006) (Measured and theoretical grinding temperatures beneath the ground surface ( $l_c=24$  mm,  $a_e=2.9$  mm,  $v_w=8$  mm/s,  $q_t=59.77$  W/mm<sup>2</sup>,  $R_w=0.067$ , distance from measuring point to ground surface  $H=1.34$  mm).

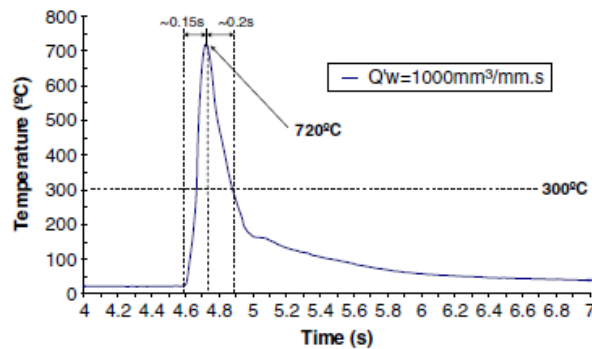


**Figure 19** Thermocouple signal demonstrating the time response after being passed over by a grinding wheel under HEDG grinding conditions. 0.15 second rise to a maximum temperature of 720°C.

## 2.6.2 PVD Films

An effective measuring technique for finding peak surface temperatures was developed by Kato (Kato, 1997). This is however treated as an indirect temperature measurement method but the results that are produced are more or less instantaneous, certainly in comparison to the response modes of the thermocouples that their naturally delaying behaviour.

The key behind the Physical Vapour Deposition (PVD) temperature measurement is in the deposition of a thin layer of metal that has a known low melting temperature. Figure 20 outlines a variety of candidate materials with known properties. The exposure of a sample surface to an elevated temperature will create an isotherm into the depths of the PVD film below the surface of the sample. The leading edge of the PVD isotherm can then be clearly identified as a visual discolouration upon inspection, indicating the depth at which the melting point temperature was experienced by the sample, see Figure 20, Figure 21, Figure 22.

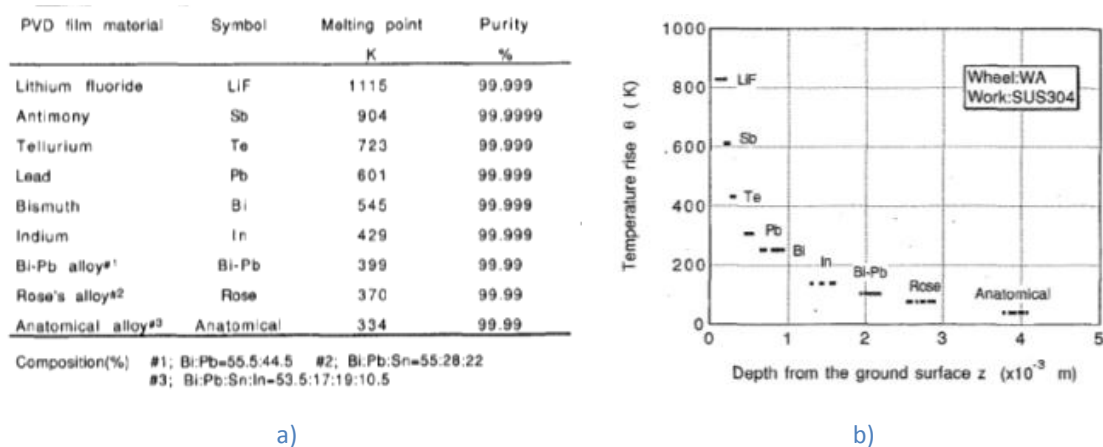


**Figure 20** Examples of PVD materials and thermal behaviour  
a) Elements used as PVD films b) method of tracing isotherms back to surface temperature.

Due to the thickness of the films being relatively small ( $\sim 20\mu\text{m}$ ) no change in heat flow patterns will be seen from introducing a single film between spliced samples. The film thickness is infinitely small in comparison to the size of the heat source.

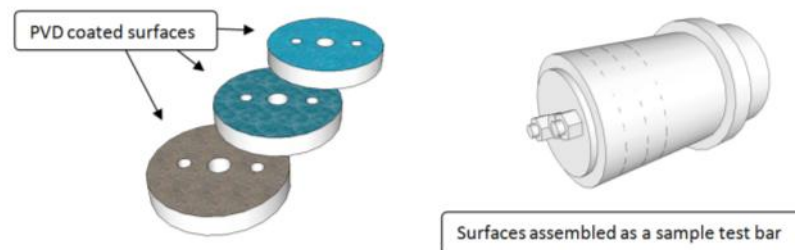


**Figure 21** Example of method of exposing PVD spliced samples to grinding temperatures

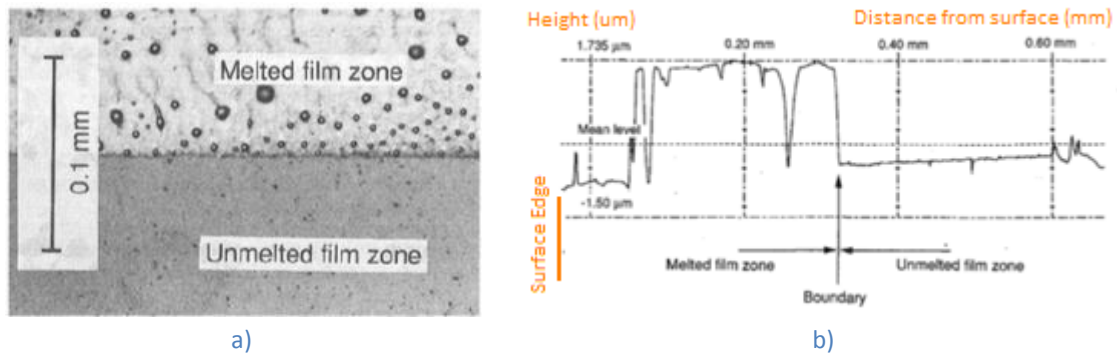


**Figure 22** Images showing isotherms developing away from a ground surface a) digital image illustrating a clear distinction between a melted and un-melted PVD film of Bismuth exposed to a heat source, and b) demonstrating the topography of a melted PVD film (Kato, 1997).

## 2.7 Super Abrasives

Abrasive machining relies upon the abrasive grit being harder than that of the workpiece material (Marinescu et al., 2004). A grinding wheel is considered to have good performance characteristics if the grinding forces, the grinding power, the wheel wear and the achieved surface roughness are low relative to the material removal rate (Shore et al., 2004). Most importantly the grit must be able to retain its hardness throughout the rapid but immense temperature gradient at the point of interaction with the workpiece. The less hard component will normally see the greatest wear.

The Grinding Ratio  $G$ , is defined as;

$$G = \frac{\text{Volume of material removed}}{\text{Volume of wheel wear}} \quad \text{Equation 33}$$

Natural abrasives such as corundum, emery and diamond have almost certainly been replaced by synthetically produced abrasives. (Society of Manufacturing Engineers et al., 1976) Up until this point abrasive materials were limited by mine reserves, involving expensive processing and refining. Manufactured abrasives predominantly include Silicon carbide, Aluminium oxide, Diamond and Cubic Boron Nitride, and more commonly known as Super Abrasives.

Diamond is the hardest of all known elements, a crystalline cubic form of carbon (whilst the allotropic hexagonal form is known as graphite). Diamond is suitable for grinding cemented carbides, ceramics and stone, however not recommended for use with steels. This is due to the oxidation of the carbon, forming  $\text{CO}_2$  and  $\text{CO}$ , instigating tool erosion, along with the tendency of the meta-stable diamond to transform into graphite at relatively low working temperatures.

Cubic Boron Nitride (cBN) on the other hand is chemically resistant against steels whilst retaining a similar structure to that of diamond. Consisting of boron and

nitrogen covalent bonds there are two forms, again allotropic; the hexagon form known as white graphite, hBN, and the cubic form, cBN. The cBN is thermally stable and does not begin to oxidise until 1400°C, in comparison to Diamond at 700°C under dry conditions.

Structures of the strong cBN covalent bonds can be seen in Figure 23 illustrating the similarities between the cubic and hexagon forms of Carbon and Boron Nitride (Metzger, 1986). The hardness and density of cBN is less than that of Diamond. However, as the nature of this research is predominantly concerned with the abrasive machining of steels this review and investigation will focus on machining with cBN super abrasives. Mechanical properties of a variety of super abrasives are also given in Figure 24 and Table 2.

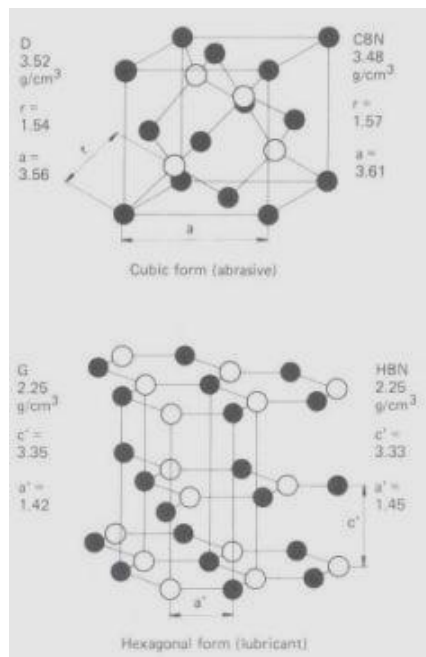


**Figure 23** Illustration of the structure of Diamond and cBN. Cubic and Hexagonal arrangement of covalent bonds demonstrating the allotropic nature of diamond and cBN

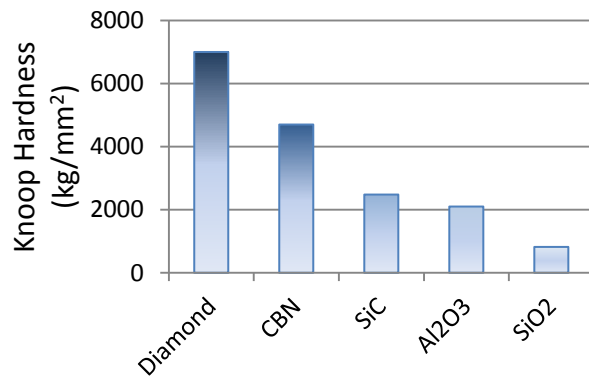


**Figure 24** Knoop Hardness of various super abrasives including mechanical comparison between Diamond and cBN

**Table 2** Difference between Diamond and cBN with respect to their material properties

| Abrasive                     | Diamond<br><i>D</i>                          | Cubic Boron<br>Nitride <i>cBN</i>                                      |
|------------------------------|--|--|
| Density (g/mm <sup>2</sup> ) | 3.52   | 3.48   |
| Thermal Stability (air)      | 700°C  | 1400°C   |
| Chemical behaviour           | Affinity to low carbon steels, oxides in air | No affinity to low carbon steels, reacts with water vapour from 1000°C |

The process involved in synthetically producing cBN is much the same as in Diamond (more detailed information on this can be found in (Metzger, 1986)). However in this instance a boron chloride-ammonia BCl<sub>3</sub>NH<sub>3</sub> is reduced through pyrolysis to gather a hexagonal boron nitride. Lithium nitride is then added as a catalyst to a process that



exposes the white graphite to extreme pressures and temperatures, in the region of 60-200kBars, depending on the required grit size and structure. The combination of the various cBN grain structures together with the selected bonding material are selected by the wheel manufactures to enhance the performance for the grinding of specific materials and predetermined machining regimes. For example large grades of cBN grit combined with electroplated bonding offers a robust stock removal wheel, where the chip size is relatively large and the surface finish is not overly important. On the other hand when surface finish is important then a vitrified bonded wheel is generally utilised in order to provide a multi-direction lay of smaller graded cBN grits. Guidance on the categorisation of abrasive grains is outlined by ISO 6106:2005 identifying the differences in grit shape and form see Figure 25. While Figure 26 illustrates the difference between a multi-layered vitrified resin bonded wheel against that of a single layered electroplated bonded wheel.

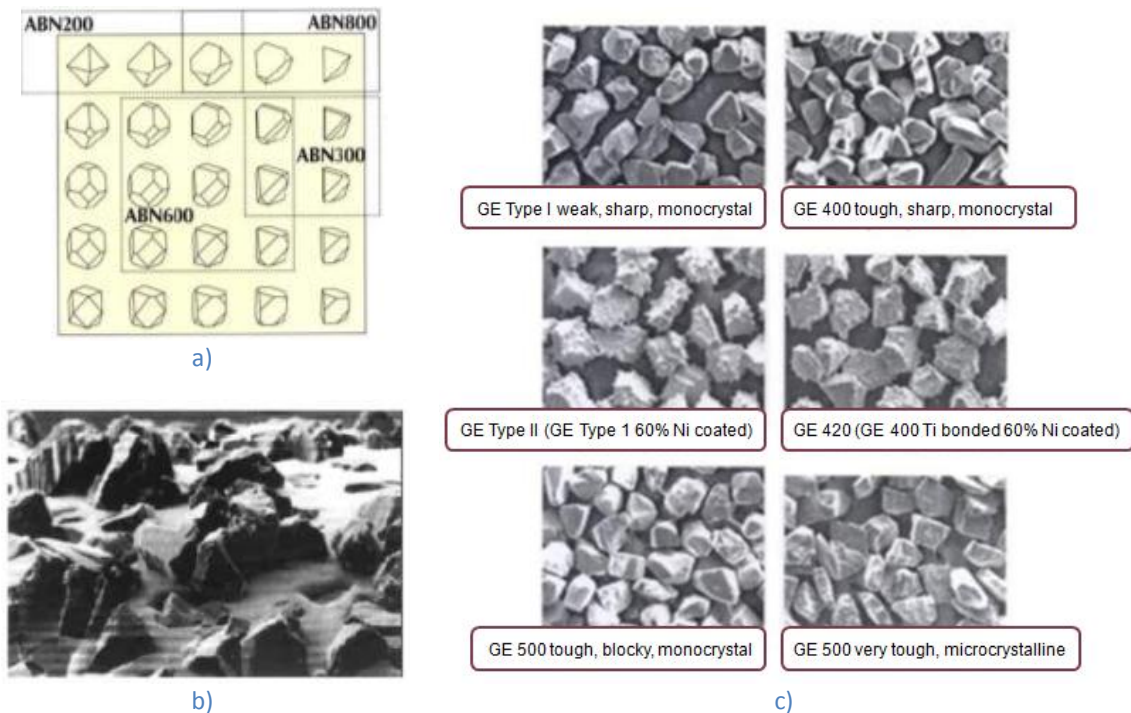


**Figure 25** Grain identities a) cBN grain size and shape configuration, b) cBN grains electroplated bonded to a wheel surface, c) various grain shapes, materials and properties (Metzger, 1986)

Vitrified bonded wheels are extremely brittle in nature. Their ceramic composition ultimately makes them particularly susceptible to damage through impact and shock. Care needs to be taken throughout the handling and processing cycles in order to prevent any undue damage leading to catastrophic failure.

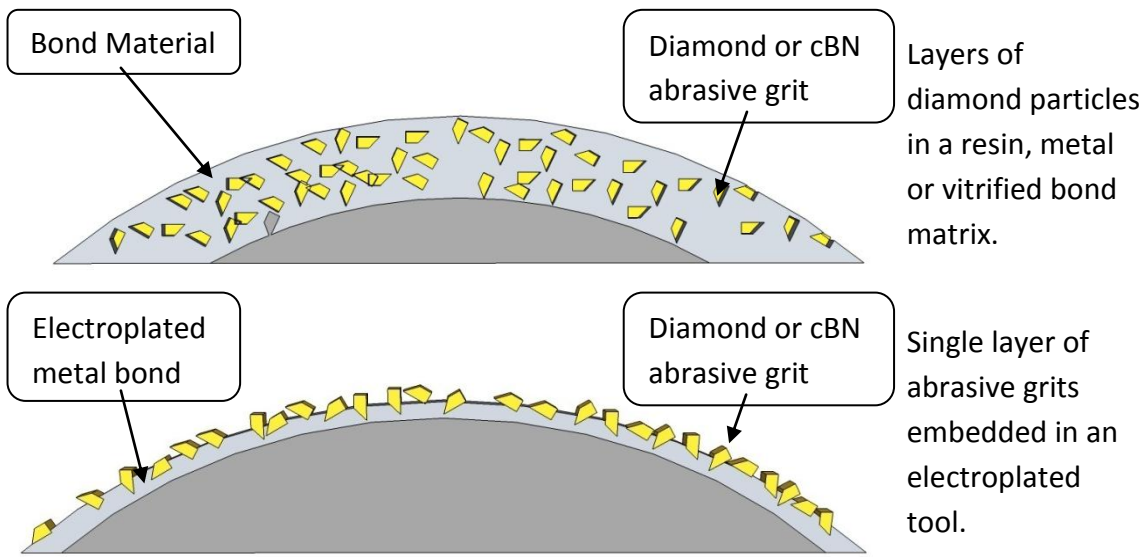


**Figure 26** Vitrified Bonded wheels and Electroplated Bonded wheels

All wheel designs and grit categorisation are standardised by the ISO working group TC 29/SC 5. Figure 27 provides an indication to the system of identification and small selection of wheel types and shapes.

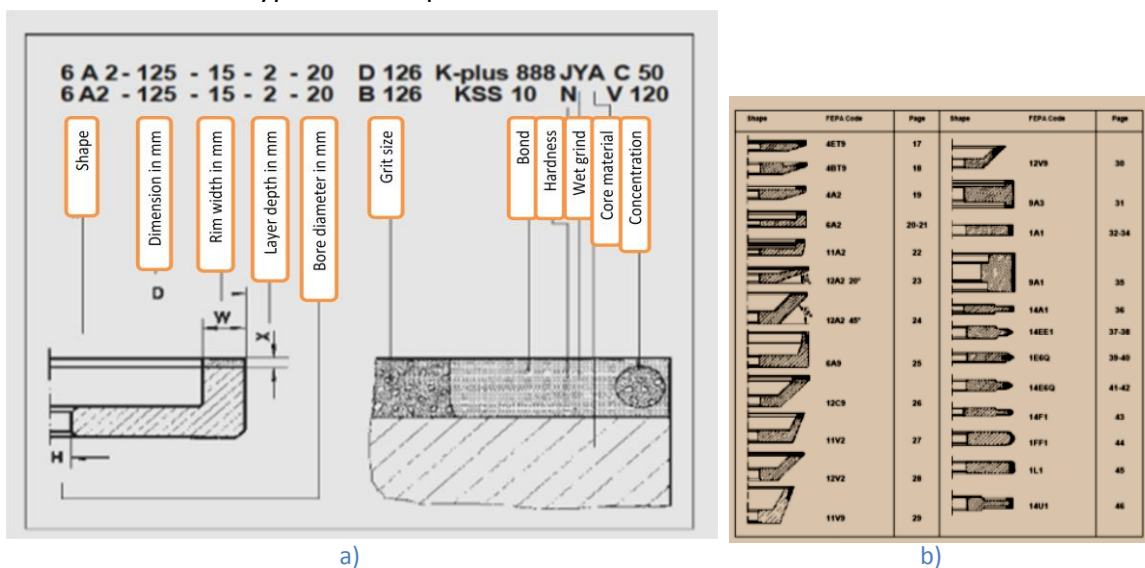


**Figure 27** Wheel Identities a) Wheel specification as outlined in ISO 6106:2005 b) example of wheel geometries

## 2.8 Workpiece material

Of course it is important to carefully select the type of abrasive or coolant within abrasive machining in order to produce the desired and specified finish however it is also critical to consider the composition and thermal characteristics of the actual workpiece material. The movement of the thermally induced energy will depend upon the thermal properties of the workpiece. Thermal conductivity and thermal diffusivity values greatly influence the exposure of newly formed surfaces to microstructural

change and/or damage (Shaw, 1996). This relates closely to the tribological behaviour between the two contacting surfaces with respect to the frictional coefficient, surface condition and material chemistry (Williams, 2005)(Sawyer and Blanchet, 1999). It should be noted that as the workpiece material is exposed to increases in process temperature that variations in the thermal properties occur adding further risk of damage. Thermal diffusivity  $\alpha(\text{m}^2.\text{s}^{-1})$  is a material property representing the effectiveness of movement of thermal energy throughout its body as a function of  $k$  the thermal conductivity ( $\text{W}/\text{m}.\text{K}$ ),  $\rho$  the density ( $\text{kg}/\text{m}^3$ ), and  $C$  the specific heat capacity ( $\text{J}/\text{kg}.\text{K}$ ), defined as;

$$\alpha = \frac{k}{\rho C} \quad \text{Equation 34}$$

A non-dimensional number known as the Peclet number  $L$ , represents the ratio between the advection and conduction of thermal energy. This number signifies the sliding movement of the heat source across a grinding surface with a cut length versus the thermal properties of the workpiece material (Jin and Stephenson, 2008; Jin et al., 2002), see equation 35. The magnitude of the Peclet number indicates the risk of thermally inducing damage into a newly ground surface. Higher Peclet numbers generally demonstrate a reduced ability of a workpiece material to move the heat away from the point of source. If the thermal properties of the workpiece are relatively poor then the likely hood is to have high Peclet Numbers and therefore more susceptible to grinding surface damage.

$$L = \frac{v_w l_c}{4\alpha} \quad \text{Equation 35}$$

The none-dimensional Peclet number can be broken down into its vertical and horizontal components and the shape of the heat source can be seen throughout the duration of the cut length as illustrated in Figure 28;

$$L = \frac{v_f l_c}{4.\alpha}, X = \frac{v_f.x}{4.\alpha}, Z = \frac{v_f.z}{4.\alpha} \quad \text{Equation 36}$$

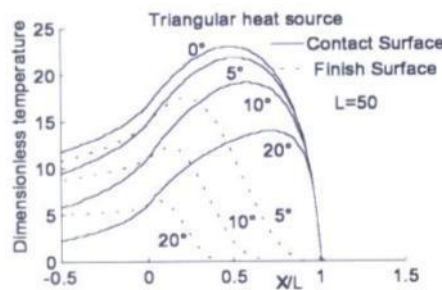


Figure 28 The temperature heat source movement over  $X/L$

As an example 51CrV4 is a medium carbon steel commonly used for environments demanding a combination of high strength, toughness and wear resistance e.g.

crankshafts, camshafts, gears, pistons, shafts etc. 51CrV4 is recognised by the AISI/SAE within the 6150 series, the thermal properties displayed in Table 3, physical properties displayed in Table 4, and the composition of alloying elements presented in Table 5 (Matweb, 2008)(Matweb, 2008) (Callister, 1997). It is worth noting that this particular material responds positively to heat treatment through austenitizing, quenching and tempering giving a clear indication of the influence that thermal energies have on the mechanical properties.

**Table 3 Thermal properties of 51CrV4 steel (SAE 6150)**

| AISI/SAE Number | C, Specific Heat Capacity ( $J/kg.K$ ) | $k$ , Thermal conductivity ( $W/m.K$ ) | $\rho$ , Density ( $kg/m^3$ ) |
|-----------------|--|--|-------------------------------|
| 6150            | 0.475                                  | 46.6                                   | 7850                          |

As a chromium-carbon based steel 51CrV4 possesses a fine grain structure which adds to its abrasive resistance having a machinability rating of 55% (Society of Manufacturing Engineers et al., 1976).

**Table 4 Mechanical Properties of 51CrV4 (SAE 6150)**

| AISI/SAE Number | UNS Number | Tensile Strength $MPa$ | Yield Strength $MPa$ | Ductility % EL in 50mm |
|-----------------|------------|------------------------|----------------------|------------------------|
| 6150            | G61500     | 815-315                | 745-1860             | 22-7                   |

**Table 5 Composition 51CrV4 steel**

| Element | Carbon C | Silicon Si | Manganese Mn | Chromium Cr | Vanadium V |
|---------|----------|------------|--------------|-------------|------------|
| Wt %    | 0.5      | 0.25       | 0.90         | 1.10        | 0.12       |

The minimum specific energy required to remove a chip from the workpiece surface also happens to be directly related to the specific melting energy, see Figure 29. Shear deformation occurs extremely quickly under the influence of grinding and can therefore be assumed to be an adiabatic process effectively resulting in the shearing energy fully converting into actively heating the workpiece material. 75% of the shear energy is understood to be solely utilised in the formation of the chip whilst 25% is expended by friction between the abrasive/chip interactions which of course can be reduced with the inclusion of effective lubrication (Malkin and Joseph, 1975). Figure 30 illustrates the mechanisms involved in the loading of a grinding wheel surface as it is important to recognise that materials with low specific melting energies such as tin, lead and indium, tend to quickly load and clog the grinding wheel surface and are extremely difficult to grind. When machining these types of material the open porous volume of the grinding wheel is rapidly reduced, limiting the wheels effectiveness in creating shear zones.

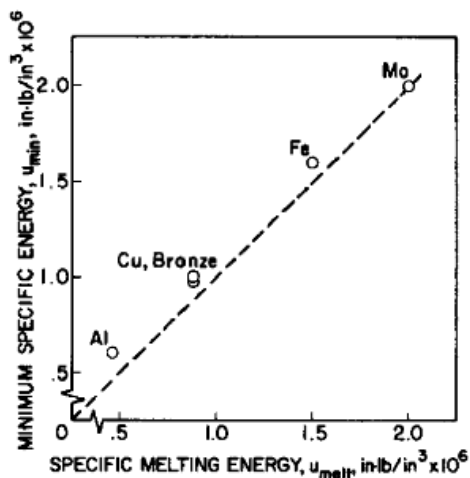


Figure 29 Minimum Specific Energy vs. Specific Melting Energy (Malkin and Joseph, 1975)

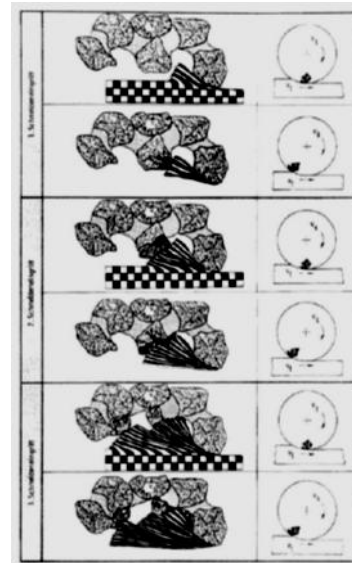


Figure 30 Layer chip formation and wheel loading in abrasive machining (Lauer-Schmaltz and König, 1980)

With the onset of wheel loading the sliding and ploughing energies increasing significantly by an increase in the frictional energy, therefore increasing the specific grinding energy, and eventually leading to surface burn and component damage, not to mention the harmful effects on the actual grinding wheel.

## 2.9 Surface Integrity

The lifetime performance of a manufactured component is greatly influenced from the manufacturing process that brought about its' creation. A precision surface is critical in many respects as this provides the major function within a system or a machine. Examples such as bearing surfaces, optical surfaces, or datum surfaces are all functioning properties of precision manufactured components. The quality of the surface therefore withholds the key in, a components function, the resistance against fatigue, the resistance against the chemical corrosion, and the condition of residual stress; collectively known as the surface integrity (Tonshoff and Brinskmeier, 1980). Abrasive machining is classified as an aggressive machining process as a result of the successive stages of rubbing, ploughing and cutting. As a result, the majority of this energy is converted into forms of heat (see 2.6 Heat Partition Ratio). High grinding temperatures produced as a result of unsuitable grinding conditions is expected to create poor surface performances and high residual stresses, as illustrated by Figure 31 that defines surface integrity throughout various machining conditions. The thermal characteristics of grinding may prove unattractive to many processes however under optimised machining parameters the capability of grinding will undoubtedly impress. The costs associated with grinding as a manufacturing process are very little in comparison to the 'value added' through the manufacture of tight tolerances and high

quality surfaces. This serves to remind us why grinding has existed and will continue to perform as a major machining method in precision engineering.

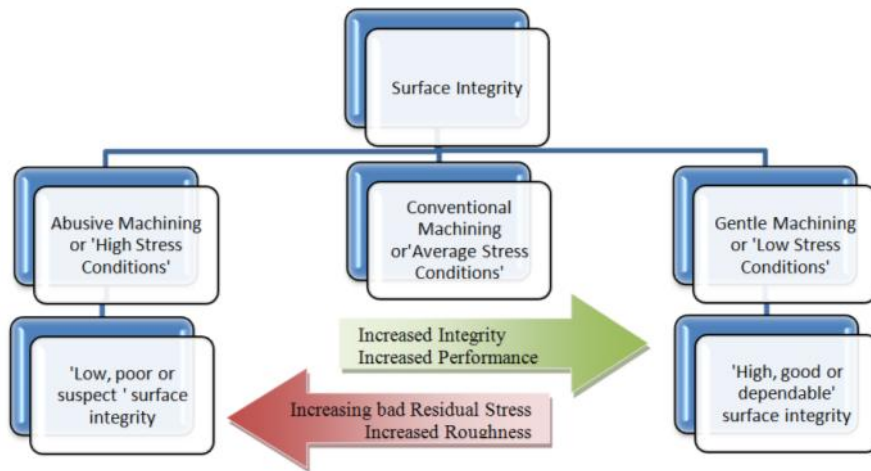


Figure 31 Schematic description of Surface Integrity (Griffiths, 2001)

Abrasive machining can achieve roughness values many times finer than that of conventional milling or turning. Further still the use of multi-orientated abrasive grit within the grinding wheel lay improves the directionality of machined surfaces, particularly in comparison to single point tooling under similar material removal rates. This feature is extremely advantageous in the production of precision surfaces.

### 2.9.1 Surface Roughness

Surface roughness is defined in many ways, but generally it is based upon the statistical height measurement of the surface over a given unit of length. The Centre-line average,  $R_a$ , the root mean square value  $R_q$ , and the peak-to-valley roughness  $R_t$ , can all be determined in a single measurement, however they are calculated quite differently, as illustrated in Figure 32.

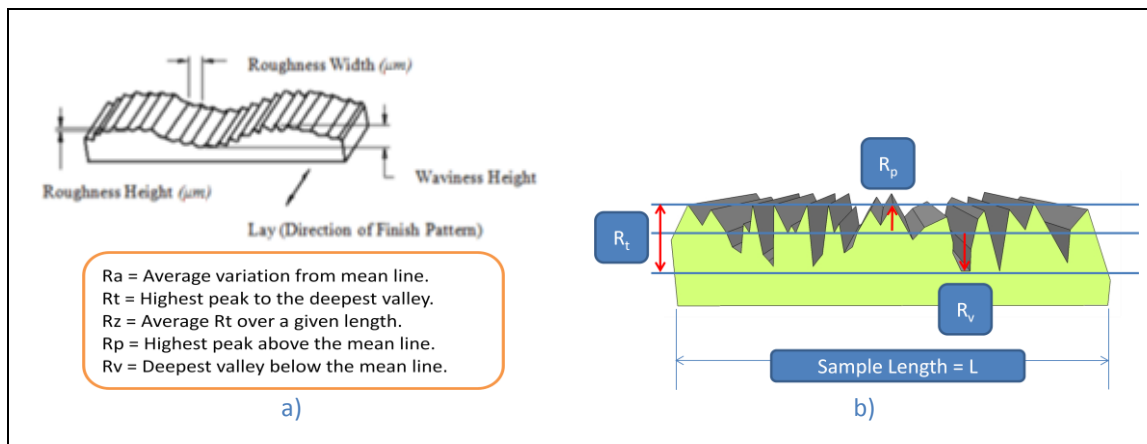


Figure 32 Definitions of surface roughness, a) Roughness and waviness b) Averaging surface lengths



$$R_a = \frac{1}{L} \int_0^L |z| dx \quad (\text{taken over 20 samples}) \quad \text{Equation 37}$$

$$R_q = \sqrt{\frac{1}{L} \int_0^L z^2 dx} \quad \text{Equation 38}$$

$R_t$  = Separation of highest peak and lowest valley

$$\frac{R_t}{R_a} \sim 5 \text{ for grinding, } \frac{R_t}{R_a} \sim 10 \text{ for honing}$$

$R_t$  is understandably related to the undeformed chip thickness (Shaw, 1996) by;

$$R_t \propto \frac{h_{ch}^{\frac{4}{3}}}{a_e^{\frac{1}{3}}} = \left( \frac{V_w}{V_s} \cdot \frac{1}{C.r. \cdot \sqrt{d_e}} \right)^{\frac{2}{3}} \quad \text{Equation 39}$$

The required surface conditions of a machined component should be considered by mechanical designers in many respects. The performance for example of a bearing surface is not only dictated by its load bearing capability. An appreciation of the machining process will consider the implications of the resulting tribological features, and anticipate how the surface roughness contributes to the behaviour of lubricants (Williams, 2005). Typical surface roughness values feature in Table 6, demonstrating the achievable roughness values through abrasive processing.

**Table 6** Process surface roughness values taken from ISO 1302:1992

|              |         |      |              |               |     |     |               |     |               |                |     |     |
|--------------|---------|------|--------------|---------------|-----|-----|---------------|-----|---------------|----------------|-----|-----|
| $R_a(\mu m)$ | 0.025   | 0.05 | 0.1          | 0.2           | 0.4 | 0.8 | 1.6           | 3.2 | 6.3           | 12.5           | 25  | 50  |
| $R_t(\mu m)$ |         | 0.25 | 0.5          | 1             | 2   | 4   | 8             | 16  | 32            |                |     |     |
| N-Grade      | N1      | N2   | N3           | N4            | N5  | N6  | N7            | N8  | N9            | N10            | N11 | N12 |
| Finish       | Lapping |      | Super Finish | Ground Finish |     |     | Smooth Turned |     | Medium Turned | Rough Machined |     |     |

### 2.9.2 Residual Stress

Predicting the behaviour of residual stresses is critical to the estimation of component life (Williams, 2005). Functioning components are normally stressed under operational conditions and are greatly influenced by their internal residual stresses. Components such as bearings, cams, and gears are obvious examples of components experiencing cyclic loading, and therefore cyclic stress. Machining processes also introduce compressive and tensile stresses within newly machined surfaces (Society of Manufacturing Engineers, 1983). If a formed surface is stretched beyond its plastic limit the induced stresses remain as residual stresses, and can penetrate to various depths. Typical residual stresses caused by a selection of manufacturing methods are shown in Figure 33. The type and magnitude of the stress is associated with; the forming temperatures, the process time and the grinding forces. Tensile residual stresses for example, are often a product of abusive and abrasive manufacturing techniques. This generally leads to fatigue failure as the surface is prone to micro cracking.

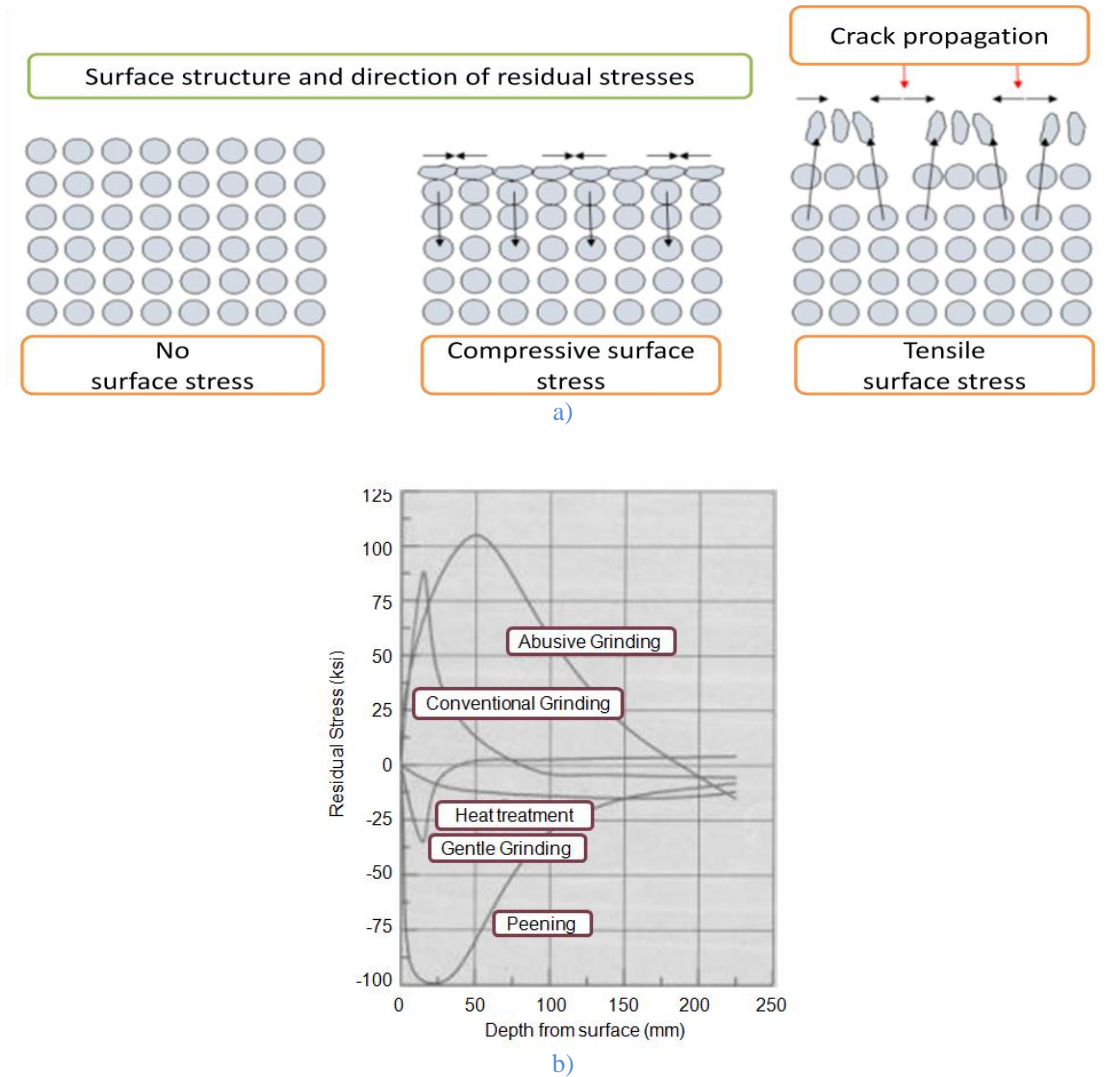


**Figure 33** States of residual stress a) Lattice configuration under various stress states b) Residual stresses vs. processes.(Griffiths, 2001)

Tensile residual stresses are linked to uneven plastic deformation of the surface and high temperature gradients (Malkin, 2007). Therefore through the optimisation of grinding parameters and effective cooling these stresses can be reduced. High temperatures and pressures in the interaction zone between the grains and the workpiece material and the heavy plastic deformation of the surface lead to substantial changes of the physical properties (Brinksmeier et al., 1982). Thus the resulting residual stresses are influenced by the following parameters:

- machining conditions (depth of cut  $a_e$ , speed of workpiece  $v_w$ , cutting speed  $v_s$ )
- topography of the grinding wheel (dressing conditions, wear behaviour)
- specification of the grinding wheel (type and size of grains, structure, bond, hardness)
- cooling conditions



---

Thermal damage leads to many undesired changes to the workpiece, such as burning, phase transformations, softening, re-hardening, cracks and residual stresses. Heat treatment of metals however is an example of where heat is used to improve the performance of a component by transforming the material properties. This enables components to influence the hardness, toughness, and strength. The production of martensite, pearlite, and carbides within the phase of the grain structure are all dependent on temperature, see Figure 34. Depending on the type and depth of the residual stresses, partial stress relief is also possible through the annealing process, where the structure is given the time and the thermal conditions in order to relax. Components are held at elevated temperatures for a determined period of time in order to refine and reduce grain sizes, to produce an even distribution of grains and grain sizes, and equalise the stresses. This highlights the influence that temperature has on microstructure.

Residual stresses can be detected through a variety of methods; such as x-ray diffraction (utilising Bragg's Law), electron diffraction, neutron diffraction, and ultrasonic detection. An effective non-destructive indication of stress type and magnitude however is through a method of magnetic detection. This method takes advantage of the phenomenon known as the Barkhausen Noise Effect, applicable to a range of ferrous materials.

### **2.9.3 Microstructure and Hardness**

The microstructure of a component surface has a higher risk of phase-transforming when it is directly exposed to high proportions of the net grinding energy. This can result through a combination of machining conditions i.e. the material properties, the thermal properties, the machining speeds and quantity of material to be removed. Extreme cases of temperature exposure will lead to burn and to permanent physical damage of the material. It is worth noting that this damage may not necessarily be seen by the unaided eye.

Iron-carbon (Fe-C) phase transformations such as those illustrated in Figure 34 demonstrate that time is also a factor in the phase transitions of carbon steel, mainly due to the diffusion of carbon atoms throughout the solid solution. Grinding however can induce phase transitions in very short spaces of time due to flash temperatures. An analogy of this is made with coffee and sugar (Shaw, 1996) - 'When just adding the sugar the diffusion of the solution is slow, add some physical movement (i.e. stirring a spoon) and the diffusion time is dramatically reduced'.

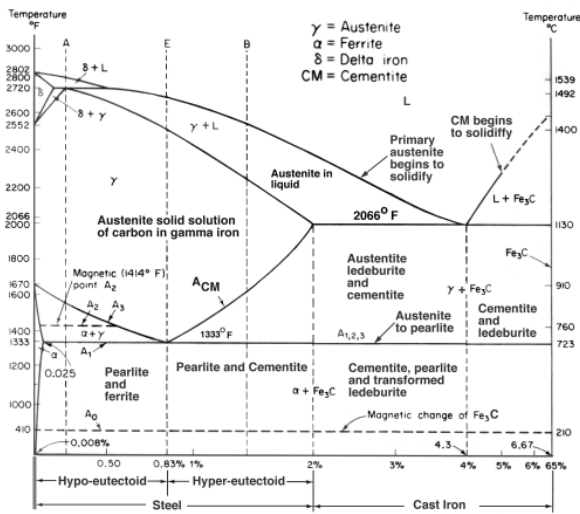


Figure 34 Phase transformation diagram for Fe-C

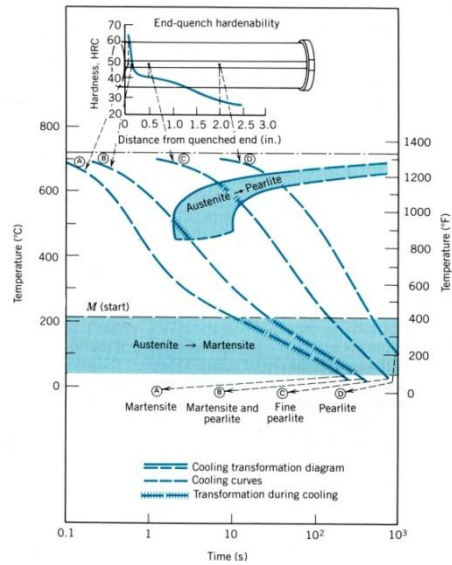


Figure 35 Cooling time and hardness of Fe-C alloy

The ground surface temperature of steel can be elevated higher than the Eutectoid and the  $A_{c3}$ , through localised flash surface temperatures, at which point the formation of the microstructure transforms into body centred  $\gamma$  austenite. Under harsh machining conditions this austenitic microstructure will be effectively frozen in, trapping carbon in a solid solution, known as Untempered Martensite (UTM,  $\alpha'$ ). The rapid cooling is due to rapid energy dispersion between the partitioning heat components. Micro and Macro cracks are common in areas of UTM, with UTM visible as a white layer when the surface is etched with a dilute solution, see Figure 36.

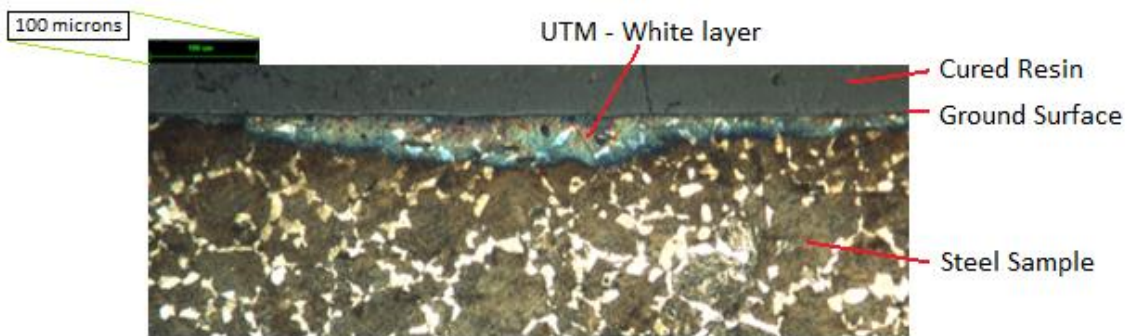
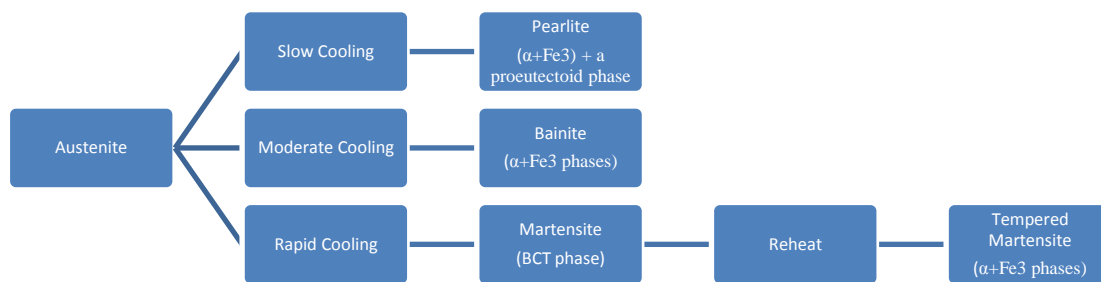


Figure 36 Untempered Martensite (UTM) indicating burn identifiable as a white layer in microscopy analysis

Microstructure formation and the relationship it has on the cooling period are demonstrated in Figure 37. Overtempered martensite (OTM) also appears at elevated temperature where the carbides and precipitates increase in size and spacing. However OTM requires an extended time period to form and generally OTM is softer than the parent metal.



**Figure 37** Transformations involving the decomposition of austenite (Callister, 1997)

Methods to reduce processing temperature continuously evolve with developments in wheel materials, cutting lubricants and cutting regimes. The high thermal conductivity of cBN abrasive grains for example conducts a larger proportion of the grinding energy (Lavine et al., 1989). The research into the chemical and tribological advantages of lubricant additives facilitates the removal of grinding zone heat. Thermal modelling also provides a means of predicting surface temperatures, and the calculation of the heat partitioning. This develops the understanding of the thermal characteristics of selected grinding regimes (Jin and Stephenson, 2008). Extensive developments within this field are continuously producing models with increased accuracy. HEDG (High Efficiency Deep Grinding) is an example of a grinding regime developed with the aid of modelling (Tawakoli, 1993; Jin and Stephenson, Sep 2003; Jin and Stephenson, 2008) preventing thermal damage under extremely large material removal rates.

#### 2.9.4 Barkhausen Noise Analysis

Barkhausen Magnetic Emission is a phenomenon of ferrous materials. This is a magnetic response that is proven to relate to the nature and the magnitude of subsurface residual stresses. It is an important concept and the basis for a non-destructive stress detection method. Professor Heinrich Barkhausen was the first to record a detectable noise signal found from the sudden reversal of the orientation of an electromagnetic signal directed into a substrate material in 1919, and was therefore named the Barkhausen Effect (Zappari and Durin, 2001)(StressTech Group, 2008).

The composition of ferromagnetic materials involves regions known as Weiss domains (magnetic domains). These regions behave much the same as miniature bar magnets and where each is separated by a boundary, known as domain walls. Each domain has an individual magnetic orientation. If an alternating electromagnetic field is pulsed and directed into a newly ground or machined surface then the returned field strength can be detected through a sensory coil. The processing of the detected signal enables an amplified output known as the Magnetic Power (StressTech Group, 2008).

Detection involves capturing the magnetic pulse emitted from the sudden changes in shape of the domain walls, known as Barkhausen Noise Emission. This is physically

detected as the domains spin around in their orientation, emulating that of the direction of the alternating magnetic coil. The ease of their movement, in which the domains are allowed to spin, can be related to the character of the residual stresses found within the components depths, see Figure 39. When applying an external magnetic source in a defined orientation onto the surface of a sample, similarly orientated magnetic domains begin to grow. At the same time any mal-aligned domains are continually reduced in size until a physical flip occurs with the resulting effect of their domains alignment conforming to the orientation of the magnetic field.

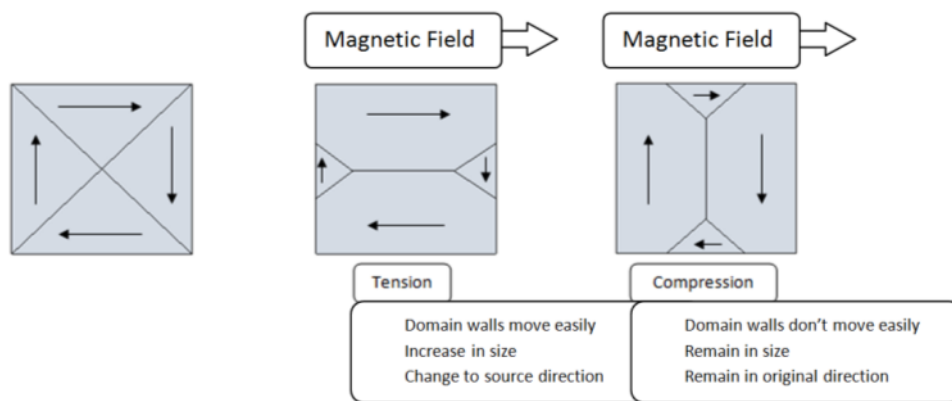


**Figure 38** The magnetic influence on domain walls, illustrating the detectable magnetic-elastic response created by internal residual stresses.

The diverse application of BME is illustrated through the ranges of sensors available, see Figure 39. The geometries of the manufactured component require the sensor to be designed accordingly.

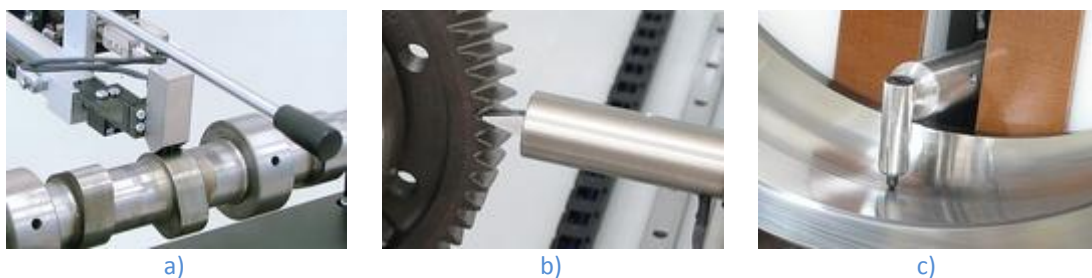


**Figure 39** Barkhausen Noise detection methods. Examples of magnetic-noise detection a) on a cam shaft b) on gear teeth c) on the ID of a bearing race. (StressTech Group, 2008)

The process of machining generally exposes components to stressful environments. Plastic deformation occurs in order to expose new surfaces, or high forming temperatures promoting microstructural phase changes. This results in residual stresses remaining in the components after production (Perez-Benitez et al., 2008). The inter-relationship of stresses and magnetism is known as magneto-elastic interaction (Zapperi and Durin, 2001) and is based around the ability of domain walls to change shape. Under compressive stress conditions domain walls reduce their

ability to move, conversely tensile conditions encourage the movement. Therefore an increase in tensile stresses can be detected through an increased returned magnetic noise signal as shown in Figure 40.

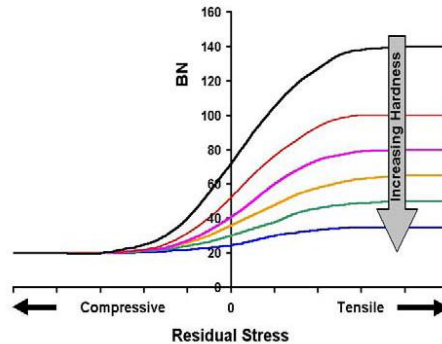


Figure 40 Barkhausen Noise signals relating to Residual stresses {{14 Comley,P. 2005}}

Compressive stresses within the newly formed machined surface are generally preferred due to the benefit that they have towards surface integrity, by extending component fatigue resistance and improving the lifetime performance certainly with respect to the ability to resist the formation of cracks. Surface hardening treatments also rely upon the principle of inducing compressive stresses into the surface such as shot-peening and oil-quenching.

The Barkhausen Noise analysis acts as a non-destructive method of determining microstructural changes and residual stress levels, and is increasingly being utilised in industry for a rapid quality acceptance procedure of newly ground components. Figure 41 demonstrates the relationship surface temperature has on the intensity of BN readouts. Although the amplification of the scale can be altered, the overall shape of the BN curve follows neatly the modelled and measured temperatures.

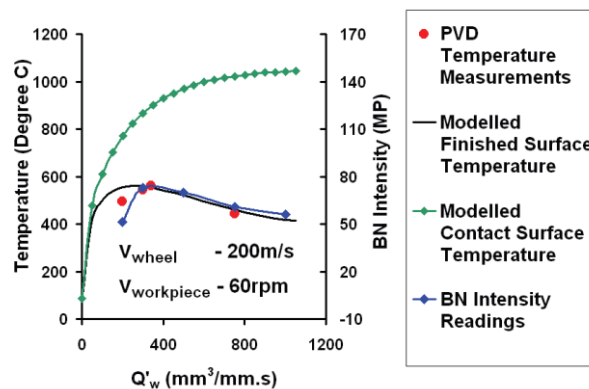


Figure 41 Surface Temperature and BN over wide range of  $Q'w$  (Comley et al., 2006).

However BN does not come without its limitations. Magnetism by its nature is prone to interference and the deeper a source of the signal the more domain walls it will have to pass through. Therefore the depth to which BN measurements can be trusted

is relatively shallow. This results in BN detection being predominantly beneficial on near-surface magnetisation. The electromagnetic field is understood to decay exponentially with the relationship of electromagnetic skin depth  $\delta$  as shown in the equation below (Moorthy et al., 2003);

$$\delta = \frac{1}{\sqrt{\pi f \sigma \mu_0 \mu_r}} \quad \text{Equation 40}$$

Where;

- $\delta$  Depth ( $m$ )
- $\mu_0$  Permeability in vacuum ( $H.m^{-1}$ )
- $\mu_r$  Permeability of the material ( $H.m^{-1}$ )
- $\sigma$  Electrical Conductivity ( $\Omega^{-1}.m^{-1}$ )
- $f$  Frequency of BN

Many material properties have great influence over the production of BN signals. Magnetic eddy currents for example begin to damage the source fields as the interference increases with depth and a size effect exists relating to the grain size of a microstructure. Because of the size effect Barkhausen Noise is not only sensitive to stresses but also to changes in material hardness, for example when analysing case hardened steels, i.e. cam shafts lobes, heat treating providing additional near surface fatigue-resistance against contact wear whilst retaining the comparatively ductile centre. The softening of the sub-surface grains verses the denser near-surface gives rise to an increase in BN signals, Figure 42 (Moorthy et al., 2003), again a restriction in the movement of the grain boundaries.

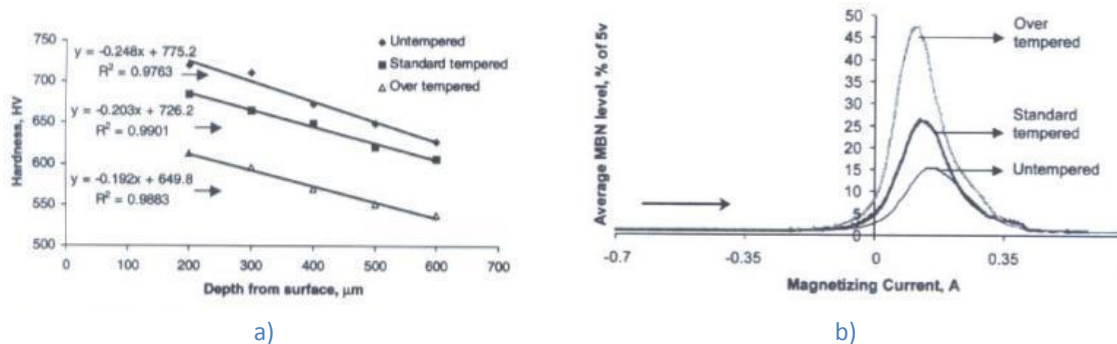


Figure 42 a) Hardness profile of tempered/untempered EN36 200-600 $\mu$ m b) BHN profile

Although BME is used by industry as an effective measure for stress control it should not be taken as an absolute. Therefore careful calibration is required for the magnetic signals to provide accurate measurements of stresses and microstructural change. Calibration, for example, can be matched against the stress analysis from damaged or burn samples and from techniques such as x-ray diffraction stress determination.



## 2.10 Grinding Fluids

Grinding fluids are generally accepted as being critical for the production of quality finished components (Brinksmeier et al., 1999)(Howes, 1990)(Webster et al., 1995)(Society of Manufacturing Engineers, 1983). Tribological effects of grinding coolants are believed to aid in both lubrication and temperature distribution, as illustrated in Figure 43.

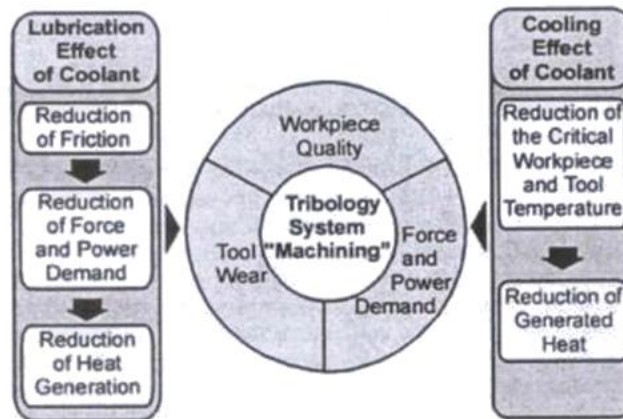


Figure 43 Grinding fluid effects (Brinksmeier et al., 1999)

The fundamental properties of coolants assist in the movement of surfaces contacting between the abrasive grit/workpiece and the chip/workpiece. The use of coolants to reduce friction build-up on the faces of the grit greatly reduces the energy required to form a chip. Shear planes are encouraged to develop more efficiently, that ultimately lead to plastic deformation. The illustration in Figure 44 demonstrates the differences in the deformation zones between an abrasive grit without and with a machining fluid, the later possessing a defined region of shear.

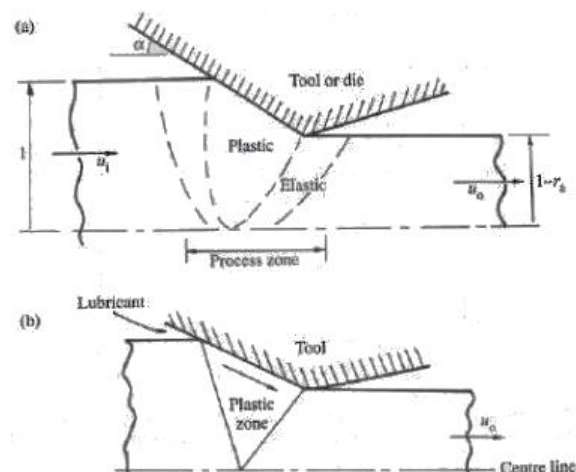


Figure 44 Differences in the plastic and elastic zones between the grinding zones a) without a lubricant and b) with a lubricant

The entire coolant supply system consists of the coolant product (including additives), the storage tank, the delivery pump, the nozzle design, the collection system and the instruments of filtration. As much as 7-17% of the total manufacturing costs can be accounted for when machine fluids are needed, see Figure 45 (Klocke and Eisenblätter, 1997) due to the complete management and disposal necessary under the current legislative climate (Morgan et al., 2008). If suitable process alternatives can be found there is the potential for huge process savings with respect to resources, time and cost. The introduction of additives into the coolants provide particular benefits such as extra lubricity, anti-bacterial agents, anti-foaming agents, tramp oil rejection, chemical stabilisers and corrosion protection (Fuchs Lubricants (UK) Plc, 2007) a chart outlining the most common additives features in the Appendix B (George E. Totten, Steven R. Westbrook, Rajesh J. Shah, 2003).

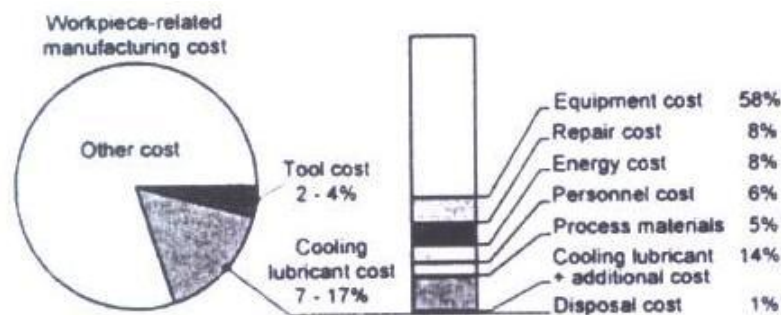


Figure 45 Total cost of workpiece manufacture (Klocke and Eisenblätter, 1997)

An additional cost associated through the use of machining fluids is the loss of geometrical accuracy. The pressure increase by the fluid at the point of abrasive contact introduces hydrodynamic forces that ultimately prevent the workpiece from moving predictably in relation to the grinding wheel (Ganesan, 2001). Previous research has established that greater hydrodynamic forces are experienced through the use of fine grain abrasives due to the apparent smoothness of the wheel periphery. This is a cause for concern when dealing with finer grades of wheels to produce higher tolerance surfaces. The wheel depth of cut, workpiece speed and fluid flow rate are shown as having negligible effects on this force.

Selecting a suitable machining fluid is an intricate and complicated task and only highlights the importance and variation of the lubricant industry. Careful consideration needs to be made with respect into the interaction of tooling and workpiece material properties, such as the chemical compositions and reactions throughout the grinding zone and post processing, the tribological behaviour in terms of the advantages and effects, and an assessment into the actual cooling advantages. The effect of cooling is



believed to be greater in processes that involve low wheel speeds due to the length of time that the coolant is active within in the process zone.

**Table 7** Comparison of cooling properties between water and oil (Kaye & Laby, 2010)(Klocke et al., 2000)

|                        |                   | mineral oil | water |
|------------------------|-------------------|-------------|-------|
| specific heat capacity | $c_p$ [J/g K]     | 1.9         | 4.2   |
| thermal conductivity   | $\lambda$ [W/m K] | 0.13        | 0.6   |
| heat of evaporation    | $r$ [J/g]         | 210         | 2260  |

The cooling effectiveness at higher wheel speeds is also questionable, not just because of the thermal conduction time period, but due to the development of an air boundary around the grinding wheel preventing fluid from attaching to the porous surface (Klocke et al., 2000).

Straight oils are generally regarded as better lubricants reducing friction with effective reductions in grinding energy, certainly in comparison to water based fluids and emulsions. Water based fluids however have better cooling properties since their specific heats are typically two to three times and their thermal conductivities about four times those of oils.

### 2.10.1 Environmental implications

Environmental legislation is demanding a change to modern manufacturing methods, particularly with regards to machining fluids. An early example of industrial change is the move from oil-based fluids to water-based as a means of reducing the amount of hydrocarbon mists produced in work environments. This was known to be hazardous in the form of aerosols, along with the health risks associated with direct skin contact with oils (Rowe, 1982). The use of metalworking fluids (MWFs) further lends itself to the observance of many controlling bodies; The Health and Safety Executive (HSE), The Environmental Agency (EA), The Department of Trade and Industry (DTI) and the European Chemicals Agency (ECHA) with particular emphasis on the recent REACH legislation (European Union, 2007).



**Figure 46** Governing bodies of manufacturing and industrial processes

On top of this, quality requirements from suppliers and clients further necessitate the need for certification of compliance of chemical use, handling, storage and disposal, all

increasing the cost of the manufacturing chains identified in the ISO groups 9000 and 14000 (Edwards and Edwards, 2003). Analysis of the competitive advantage gained by complying with ISO regulations has been outlined by (Koc, 2007) with direct effects of waste and quality management throughout grinding processes (Brinksmeier et al., 1994) highlighting the need not only for industry to develop more efficient manufacturing methods but also for machine and machining fluid manufacturers to develop environmentally reputable equipment and products. There is of course the argument that metalworking fluids (MWFs) do not lose their lubricating properties quite as quickly as anticipated by production planners, however other aspects such as their corrosion resistance properties do begin to fail (Greeley and Rajagopalan, 2004).

### 2.10.2 Minimum Quantity Lubrication and Useful Flowrate Theory

Minimum Quantity Lubrication (MQL) is an alternative approach to traditional flood and high pressure coolant supply, and is a progression towards dry grinding. Extensive work continues to develop this concept within metalworking, as highlighted by (Weinert et al., 2004) with a focus to reduce process costs both financial and environmental. The use of MQL also aims to maintain if not improve the integrity of the manufactured components. The reduction of coolants however is understood to expose the grinding machine, tool and workpiece to; higher process temperatures, elevated forces, increased friction resulting in greater rates of wear, increasing the risk of non-conformances in tolerances, greater surface damage, and not forgetting the problems associated with swarf removal (da Silva et al., 2007). However there is a relatively low understanding on the effects of grinding wheel and MQL oil type in minimum quantity lubrication grinding processes (Tawakoli et al., 2010).

Metzger states that 90-92% of the grinding energy is transformed into heat (Metzger, 1986). However he then goes on to develop a minimum machining fluid flowrate that is able to absorb this quantity of energy away from the tool/workpiece interface. It should be noted that this thermal analysis disregards any fluid dynamics and its possible effect on cooling as it assumes a static layer of coolant between the grinding contact surfaces;

$$Q = \frac{60 \times P_s}{4.184 \times C \times \rho \times \eta \times \Delta\theta} \quad \text{Equation 41}$$

- $Q$  the flowrate ( $l/min$ )
- $P_s$  the spindle power under load ( $kW$ )
- $C$  the heat capacity of the fluid ( $Cal/g^\circ C$ )
- $\rho$  density of fluid ( $g.cm^3$ )
- $\eta$  efficiency of the nozzle
- $\Delta\theta$  maximum tolerable temperature increase ( $^\circ C$ )

Previous models consider fluid dynamics using Reynolds equations, Poiseuille flows and momentum equations. For example Gviniashvili developed an experiment measuring the power consumption through the acceleration of a useful mass flowrate from a nozzle speed to an exit speed, see Figure 47 (Gviniashvili et al., 2004);

$$\dot{m}_u = \frac{P_f}{v_s^2 - v_j v_s} \quad \text{Equation 42}$$

Where  $P_f$  is the power required to cause a rate of change of momentum to the fluid;

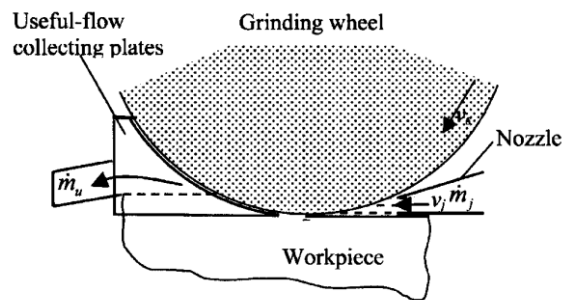


Figure 47 Arrangement for collecting useful flow

This concept is taken further to identify a useful flowrate based around a volume of machining fluid able to pass through the grinding contact zone, as illustrated in Figure 48 (Jackson, 2008). This useful flowrate is physically difficult to establish as many input parameters such as wheel speed and nozzle position contribute to the ability of the wheel to take the fluid into the grinding zone. Four sub-divisions of the useful flowrate are therefore defined;

- Convenient flow which describes the flow that passes through the grinding zone based solely on the topography of the interface.
- Useful flow is defined as the amount of fluid that passes through the grinding contact. This flowrate will always be less than the supplied nozzle flowrate and can be represented as a percentage of supply flowrate, termed the percentage useful flow
- Optimal useful flowrate is the minimum amount of fluid that passes through the grinding contact zone functioning as an effective lubricant and providing sufficient local cooling.
- The achievable flowrate – percentage of convenient flow

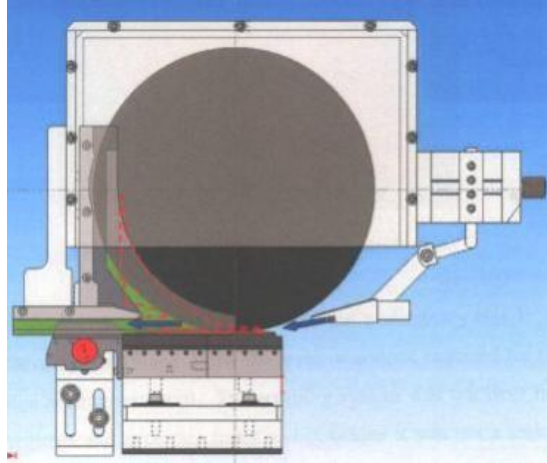


Figure 48 Measuring flowrate passing through grind zone (Jackson, 2008)

Rowe determines a maximum useful flowrate,  $Q_{fu}$ , which can reasonably be achieved. This depends on the porosity of the wheel,  $\phi_{pores}$ , and the mean depth of the pores,  $h_{pores}$  (Marinescu et al., 2004);

$$Q_{fu} = \phi_{pores} \times h_{pores} \times b_s \times v_s \quad \text{Equation 43}$$

This is based around the assumption of a fluid layer thickness which is determined by the topography of the wheel. The useful volume is the porous volume, available to fluid, between the abrasive grains on the wheel;

$$h_{fu} = \frac{Q_{fu}}{b_s \cdot v_s} = \phi_{pores} \times h_{pores} \quad \text{Equation 44}$$

The mean depth of pores is difficult to establish and no clear direct measurement is currently available. With the progress of visualisation and imaging techniques this may well be possible in the future but at present the depth of pore is associated with the average grain diameter  $d_g$ .

The porous nature of vitrified bonded wheels allows higher volumes of fluid to penetrate from the surface particularly in comparison to that of electroplated wheels whose porosity is assumed to be zero. However the depth of penetration is usually small compared to abrasive grain size, which means that the fluid is kept predominantly on the wheel surface (Gviniashvili et al., 2004). It is worth noting that work speed and depth of cut does not affect useful flowrate and that most models are developed around the laminar flow of fluid.

### 2.10.3 Solid Lubricants

The use of solid additives within abrasive machining is not to conduct the generated heat away from the grinding zone but to reduce the frictional energy between the grinding wheel and the workpiece surface. An improvement in the tribological

behaviour such as a reduction in the tangential force will result in a lower specific grinding energy (Malkin, 2007).

The push towards MQL methods within industry is continually progressing in popularity (Weinert et al., 2004). The benefit of MQL however will only be recognised if no detrimental effects on surface integrity are seen. Therefore a combination of both suitable lubricants and application methods, particularly with respect to abrasive machining, will be required to be developed. Their capabilities will then need to be proven over existing techniques. By definition MQL indicates a reduced capability of the machining fluid to remove heat from the process. Much greater premise however is given to the effectiveness of the fluid to reduce frictional heating. The application method is also critical as the distribution of MQL fluids close to the grinding zone is questionable. Effective cooling is generally seen by the bulk of the surrounding workpiece material rather than at the actual point of abrasion (Ebbrell et al., 2000). Therefore the hypothesis of MQL is on its quality (effective lubrication) not its quantity (flood or high pressure coolant flowrates).

Various views exist on the capability of machining fluids to aid cooling particularly at higher wheel speeds. A stiff air barrier builds upon the surface of a wheel and prevents the fluid from entering the grinding arc. Under these conditions the contact time of the fluid within the surfaces of the grind is limited (Batako et al., 2005)(Rowe and Jin, 2001). Hydrodynamic forces within the abrasive work zone have the risk of adding dimensional errors to precision finishing (Tawakoli and Azarhoushang, 2008)(Ganesan, 2001). The incompressibility of fluids tends to initiate additional forces on the workpiece, running the risk of positional inaccuracies within the machining geometry. These forces can be demonstrated through the use of dynamometers, as illustrated by Figure 49. The magnitude of these forces has been shown to be directly proportional to the peak-valley roughness of the grinding wheel.

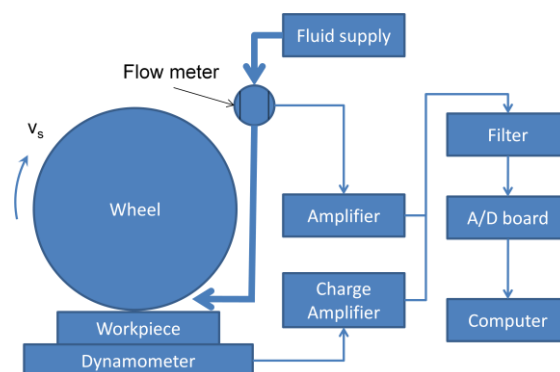


**Figure 49** Hydrodynamic forces. Demonstrated through using a dynamometer, plain wheel at a fixed wheel height

The quantity of the machining fluid flowrate that actually enters the grinding zone is also questionable. This varies on a large number of parameters including fluid flowrate, nozzle position, and grinding wheel speeds (Jackson, 2008). This problem is also relevant with regards to the use of solid lubricants. Previous research includes the addition of graphite into existing machining oils (Shaji and Radhakrishnan, 2002). The graphite/oil was applied with a runner wheel that applied the lubricant paste onto the grinding wheel, see Figure 50. These investigations concluded that the grinding forces and the specific grinding energies were reduced through the increased behaviour of the graphite, see Figure 51. However the performance of the graphite diminishes with an increase in the infeed speed, indicating that the significance of lubrication becomes weaker with larger chip thicknesses. The greatest effects from additional lubrication are found at the slower infeed speeds of the grinding wheel into the workpiece to reach the desired depth of cut. The influence of the dressing stage can also be seen on the specific grinding energy, as shown in Figure 52, demonstrating that the lubrication is more advantageous with finer dressing conditions. The coarse dressing conditions actually promote a more effective use of the dry and normal coolant regimes.

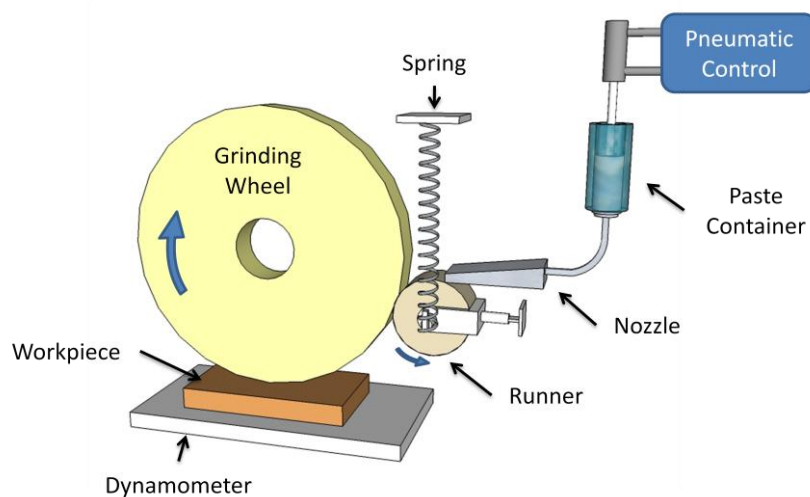


Figure 50 An application method of introducing solid lubricants into the grinding zone {{167 Shaji,S. 2003}}

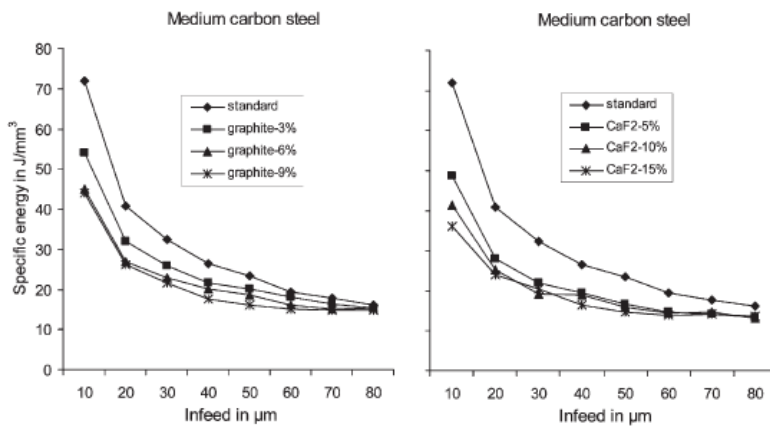


Figure 51 Specific Grinding Energy over a range of infeed speeds with a variation of Graphite and CaF<sub>2</sub> within the structure of the grinding wheel {{168 Shaji,S. 2003}}.

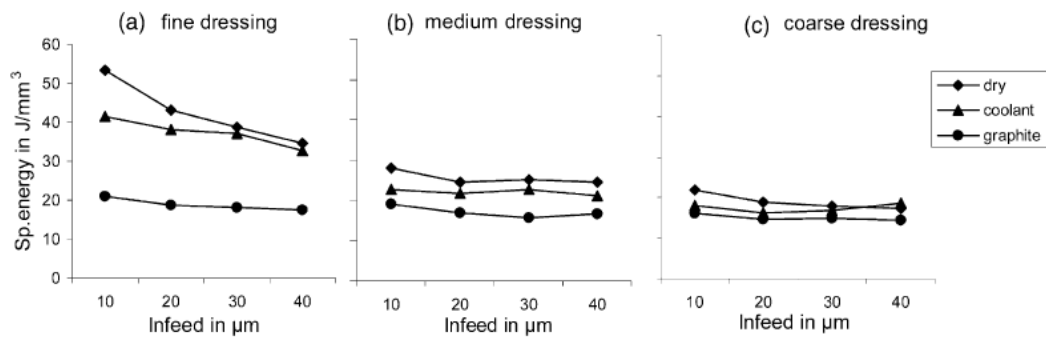


Figure 52 Grinding Forces and Specific Grinding Energies with a range of lubricants {{109 Shaji, S. 2002}}

Lubrication is defined by the ASTM Guide to Friction, Wear, and Erosion Testing as; a low friction substance providing protection of opposing wear counter-faces by the formation of a transfer film (Budinski, 2007). Solid lubrication involves the inclusion, bonding or development of film coatings to separate otherwise interacting surfaces. Table 8 includes examples of materials possessing beneficial properties towards lubrication.

Table 8 Common examples of solid lubricants

| Type of Lubricant         | Examples  |
|---------------------------|---|
| Long chain molecules      | PTFE, FEP, PFA, ETFE  |
| Lamella crystal materials | Graphite, Molybdenum Disulfide, Tungsten Disulfide, Hexagonal Boron Nitride |
| Soft metals               | Brass, Lead, Babbitt  |

Due to the high temperatures and impact forces associated with grinding, compositions consisting of long chain molecules are to be omitted from this research. The melting temperatures are relatively low breaking the molecular bonds, along with damaged bonds through continuous impacting, resulting in tribological losses. Soft metals are also omitted for cost, environmental and chemical stability reasons.

Inorganic solids possessing low shear strengths from their lamellar type crystalline structure provide tribological properties of benefit with respect to boundary and contacting surfaces. Substances such as Graphite (C) and Molybdenum Disulfide (MoS<sub>2</sub>) for example possess these weak covalent bonds. As with all lubricants there are many properties to consider upon selection for optimum performance. Lubricant manufacturing is a standalone industry in its own right with specialised laboratories addressing continuously stringent requirements from clients and legislative bodies (Fuchs 2008). Table 9 highlights a variety of characteristics particularly important when introducing solid lubricants into a system. The grinding environment is particularly turbulent with respect to air movement and poses an elevated risk of flame ignition.

**Table 9 Characteristics when selecting suitable solid lubricant**

| Property                       | Characteristic   |
|--------------------------------|--|
| <b>Thermal Stability</b>       | No undesirable phase and structural changes at low and elevated temperatures.                            |
| <b>Oxidation Stability</b>     | Lubricant resists oxidation over predicted temperature range.  |
| <b>Chemical Reactivity</b>     | Lubricant should form a strong, adherent film on the base material.                                      |
| <b>Melting Point</b>           | Molecular structure is destroyed above the melting temperature rendering lubricant ineffective.          |
| <b>Electrical Conductivity</b> | Machining regimes involving electrical motors or systems need to be protected.                           |
| <b>Volatility</b>              | Lubricant should possess a low vapour pressure due to expected temperature and low pressure environment. |

Solid lubricants are often found in systems when conventional lubricants are not acceptable. For example, in circumstances of:

- Extreme temperatures and pressures
- Inaccessible locations
- Prevention of contamination
- Atmospheric and Environmental protection

The major advantages and disadvantages to solid lubrication being:

- More effective than fluid lubricants at high loads and speeds
- High resistance to deterioration
- Highly stable in extreme temperatures, pressure, radiation, and reactive environments

Whilst the major disadvantages are:

- Poor self healing properties of film structure in comparison to fluids
- Poor heat dissipation

Reference needs to be made to instances of solid lubrication within abrasive machining. Solid lubricant layers have been introduced into grinding zones under



---

particular conditions and with the development of suitable application techniques. Cutting forces and specific grinding energies can be seen to decrease particularly at lower infeed rates. This research even goes as far as to include lubricants into grinding wheel structure however the thermal stability of this development is not yet known. The vitrification process of finishing wheels often involves forming temperatures in excess of 1200°C, a temperature not particularly favoured by solid lubricants, resulting in molecular break down and diffusion into the wheel structure (Tawakoli et al., 2010)

## 2.11 Key Messages

The key messages coming from this chapter are:

- Financial and environmental factors are encouraging metalworking industries to adopt MQL methods in preference to their traditional flood and high pressure machining fluid systems. In particular tighter legislation with regard to the use, the storage and the disposal of chemicals is driving this interest.
- MQL methods will only be accepted if they can maintain the surface integrity of components however a reduction in fluid use is favourable. This is with particular reference to thermal damage and tool life expectancy.
- The use of effective lubrication can potentially control the specific grinding energies. Cooler cutting can be achieved through a reduction in frictional energy, lowering the risk of thermally inducing damage to the surface integrity.

---

## 3.0 Abrasive machining with MQL and MQSL methods

### 3.1 Overview

This chapter explains the development of MQL and MQSL delivery systems used in this research and the practicalities of introducing solid lubricants into an abrasive environment. Minimum Quantity Lubrication (MQL) is process specific depending on the machine setup.

The required quantity of the machining fluid depends on the structural and the thermal interactions between the machine, the tooling, and the workpiece. In abrasive machining, the idea of a 'Useful Flowrate' is an accepted theory of MQL, defined as the most effective volumetric flowrate of machining fluid. Here, the delivered flowrate of the fluid is calculated to match the open porous volume on the surface of a rotating grinding wheel, filling the voids between the grits with a minimum amount of machining fluid. A lower flowrate could increase the probability of burn and surface damage, while an increased flowrate results in an over-use and waste of lubricants as the fluid is splashed or misted without contact with the grinding zone.

This project not only considers the continued use of traditional machining fluids such as emulsified machining oils (in terms of MQL) but also explores the relatively unknown application of solid lubrication (MQSL) within abrasive machining. A selection of solid lubricants was identified through an assessment of their mechanical, chemical and thermal properties. This assessment considered their suitability within abrasive machining, in particular within the application of cylindrical plunge grinding on low carbon steel. The solid lubricants selected for their particular significance and relevance are Molybdenum Disulphide ( $\text{MoS}_2$ ) and Calcium Fluoride ( $\text{CaF}_2$ ) and Hexagonal Boron Nitride (hBN). Alternative mechanical, pneumatic and electrostatic methods for feeding solid lubrication were successively designed and tested.

### 3.2 EcoCool Oil Emulsion

The use of mineral products within machining is increasingly subject to environmental control. MQL methods are able to maintain machining performance while reducing the processing and the waste disposal costs, thereby reducing potential environment impact. One aim of this study is to enhance the performance of an oil emulsion under extreme MQL regimes without detrimental effects on the workpiece components and the environment.

This project uses Fuchs EcoCool oil emulsion as the benchmark MQL fluid against which the performance of other solid lubricants is compared. This particular emulsion

is mixed through a Dosatron cyclic delivery system allowing the oil/water ratio to be precisely controlled.

### 3.3 Molybdenum Disulphide (MoS<sub>2</sub>)

Molybdenum Disulphide (MoS<sub>2</sub>) is a complex material with respect to handling. The lattice structure of MoS<sub>2</sub> provides a tribological advantage of lubrication however also adds a readiness to easily spread. Contamination of the machinery, on personnel, and on processed components is difficult to avoid. As a dark grey compound it is quick to identify and extremely difficult to prevent spreading or remove. MoS<sub>2</sub> is widely used within many commercial products, predominantly as an additive to lubricants, greases and oils.

For this particular application a fine powder of MoS<sub>2</sub> (6µm particulates) was used to allow for the careful mixing and light distribution of an MQL fluid. Suspensions of MoS<sub>2</sub> are commercially available however the comparative water weight of these suspensions is relatively higher than required (predicted to influence the thermal behaviour of the added solid lubricant).

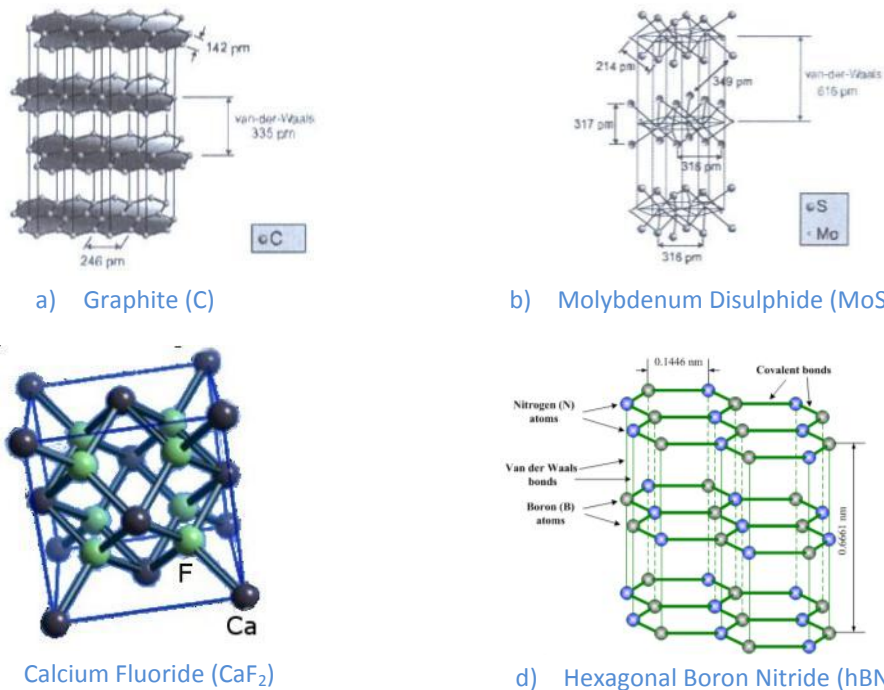


Figure 53 Compounds of a) Graphite, b) MoS<sub>2</sub> c) CaF<sub>2</sub> and d) hBN solid lubricants

The early stages of the investigation focused on the functionality of MoS<sub>2</sub> within the grinding environment. The electrical power consumed throughout a manufacturing cycle ultimately defines the quantity of energy dispersed throughout the entire machining environment. Grinding is classified as an abusive manufacturing process due

---

to the comparatively higher quantities of energy required per unit of material removed, particularly in comparison to metal cutting techniques. The addition of a highly effective lubricant intends to lessen the frictional forces between the interaction of the grinding wheel and the workpiece.

Improving the tribological behaviour between the machining surfaces intends to ultimately result in cooler grinding. The abrasive system energy losses created through the wheel and the workpiece interaction are reduced as frictional energy generally associated throughout the rubbing and ploughing stages of chip creation will be reduced.

Shortening the abrasive grit and workpiece contact time period, with particular respect to the sliding time period, effectively accelerates the formation of shear planes within the grinding zone. Any reduction of SGE lowers the risk of thermal damage for a given  $Q'_w$ , therefore the reduction of the consumption of energy through the sliding and ploughing phases is desired, and under ideal conditions could be completely eliminated.

### 3.4 Calcium Fluoride (CaF<sub>2</sub>)

The use of solid lubricants within this investigation focuses on furthering the knowledge of the tribological interaction between the grinding wheel and workpiece surfaces. This development intends to inform the feasibility of the construction of a real time temperature measuring system. If the structure of the lubricant is seen to remain stable then it may be possible to combine it with phosphorescent materials that possess temperature dependent properties.

The intention would be to pass the phosphors directly through the grinding zone and be thermally excited. Their rapid exit will then allow the surface temperature to be deduced through the collection and interpretation of the phosphor emitted thermo-phosphorescence wavelengths (thermo-luminescence). Additional information is included in Appendix C.

CaF<sub>2</sub> possesses naturally occurring thermo-luminescence properties. If this natural luminescence possesses a life-time decay rate stable enough to calibrate and determine the temperature then the addition of doped phosphors could be excluded. Initially the focus will be on the suitability of CaF<sub>2</sub> as a lubricant. CaF<sub>2</sub> possesses natural lubricant properties and is abundant in supply. Therefore a combination of natural thermo-luminescence and lubrication would prove ideal within the concept of this research. Therefore the effectiveness of CaF<sub>2</sub> application within the grinding environment needs to be determined.

### 3.5 Hexagonal Boron Nitride (hBN)

Hexagonal Boron Nitride (hBN) is an established solid lubricant. As is implied through its pseudo name of 'White Graphite', the lamella structure provides excellent lubrication through the similar structure to that of Graphite. However, it is regarded as possessing superior properties see, Table 10, particularly with respect to its thermal conductivity and chemical stability. Advantages of hBN are:

- Excellent Lubricating Properties due to low Coefficient of Friction at 0.15 to 0.70
- High Temp. Stability, 1000° C in Air, 1400° C in Vacuum and 1800° C in Inert gas
- Low Thermal Expansion
- High Load bearing properties
- Electrical Insulator

Table 10 hBN material properties (Matweb, 2008)

|                        |              |
|------------------------|--------------|
| Density                | 3.49 g/cc    |
| Specific Heat Capacity | 0.793 J/g-°C |
| Thermal Conductivity   | 20.0 W/m-K   |
| Melting Point          | 3027 °C      |
| Maximum Service Temp.  | Air 985 °C   |



Figure 54 Examples of commercially available hBN solid lubricants

### 3.6 Development of solid lubrication delivery system

The MQSL trials required a delivery system to precisely control the volumetric flow rates of the solid lubricants. The lubricants were added to the MQL useful flowrate of water, and in the later stages of experimentation under dry conditions (no water). The lubricants were applied to the surface of a rotating grinding wheel.

The delivery system was developed to locate close to the grinding zone. This was to prevent delivery problems occurring due to extended feed lines. The fluidic behaviour of dry powders was exploited for the delivery systems to function. The delivery systems had to be compact to prevent collision within the machining space, and the control systems were positioned external to the machine for operation and protection from contamination. Details of the development of the experimental equipment feature in the following sections.

### 3.7 Nozzle Design

Critical to the success of the application of MQL/MQSL is the application of MQL fluid onto the surface of the grinding wheel. In order to conform to the useful flowrate theory the geometry of the fluid flow had to be contained. Therefore a nozzle structure was designed and developed by the author for use within the MQL and MQSL trials.

A great amount of research is associated with fluid nozzle design and positioning (Webster et al., 2002). Poor quality nozzle design and fluid delivery pipe systems can result in high jet dispersal, especially at higher jet exit velocities. Changes in pipe diameter and the use of elbows throughout the coolant system cause turbulence within the flow. This action prevents the nozzle from controlling the fluid into a coherent jet and severely restricting the flowrate and pressure available. Shoe type nozzles overcome these limitations providing a large contact area between the wheel and the fluid. This allows for good penetration into the wheel as illustrated in Figure 55a. The motion of the fluid is accelerated and carried into the grinding zone by the topography and the rotation of the grinding wheel, similar in behaviour to that of an external gear pump, as illustrated in Figure 55b. The active grit surface pulls the machining fluid through the grinding zone. However, the shoe nozzle is generally considered bulky for grinding and tooling fixtures. Under the MQL test conditions the gap between the wheel and the shoe is required to remain constant, in order to maintain the pressure and provide the correct geometry.

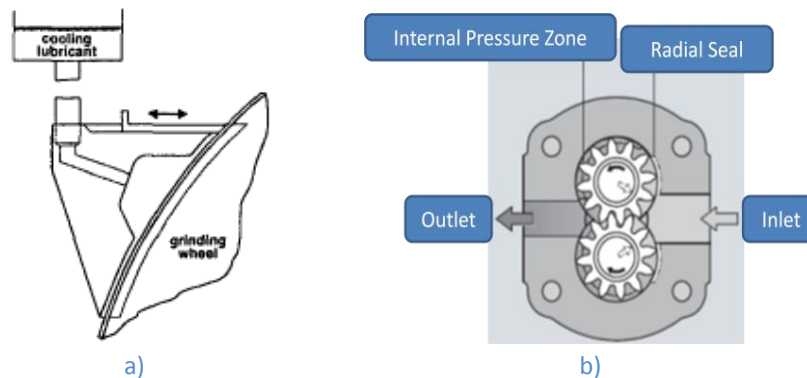


**Figure 55** a) Shoe nozzle arrangement on grinding wheel surface (Klocke et al., 2000) b) showing similarity to gear pump fluid mechanics (Bosch Rexroth, 2004)

A MQL nozzle design was fabricated and installed onto the Edgetek SAT cylindrical grinding machine, Figure 56a. The dominating feature of the nozzle is a graphite face plate that is positioned over the surface of a rotating grinding wheel, Figure 56b. The height and contour of the wheel surface is then replicated into the rear of the graphite nozzle. This geometry maintains the MQL volume, applying a consistent MQL layer directly onto the wheel. The action of a tensioned mount enables the graphite to

maintain its height from the surface of the grinding wheel. The final nozzle assembly was attached to the upper section of the grinding wheel shroud, Figure 57. Fine alignment relative to the grinding wheel was designed to be accessed and adjusted from the front of the machine, allowing for a high degree of monitoring and serviceability.

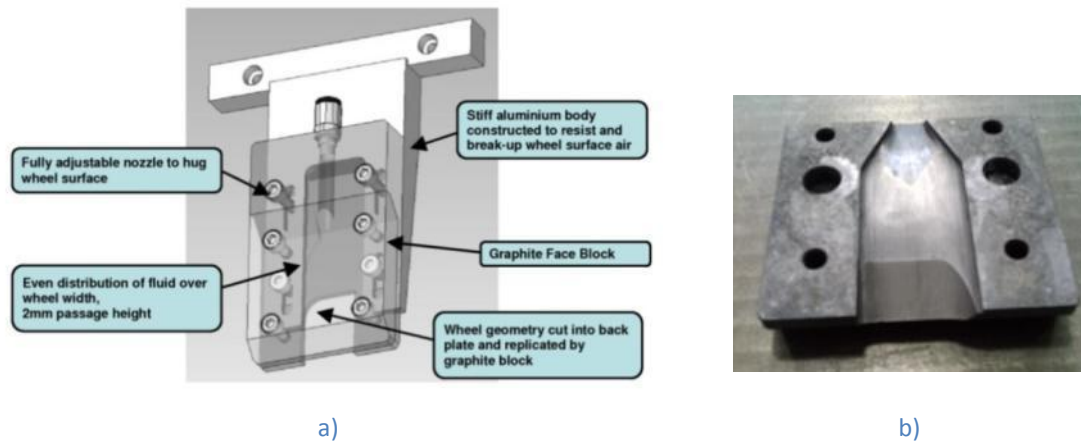


Figure 56 Minimum Quantity Solid Lubrication Nozzle design a) front side b) rear of graphite

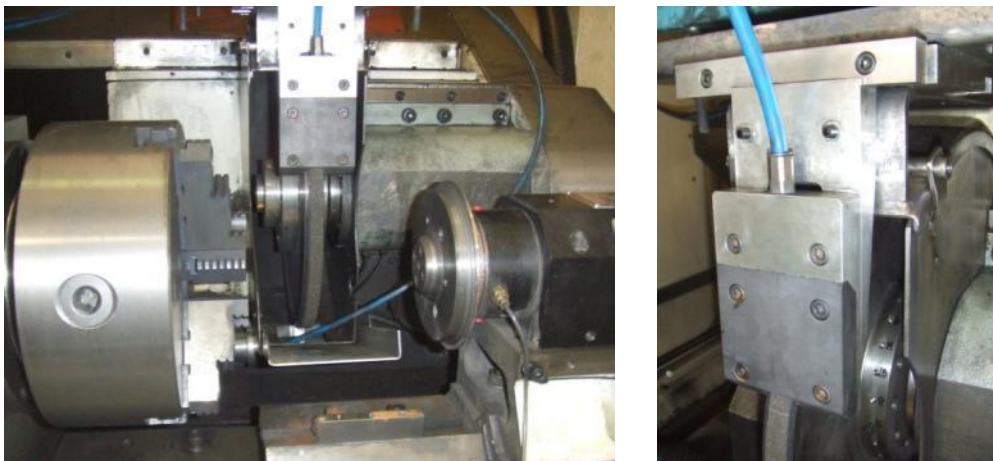
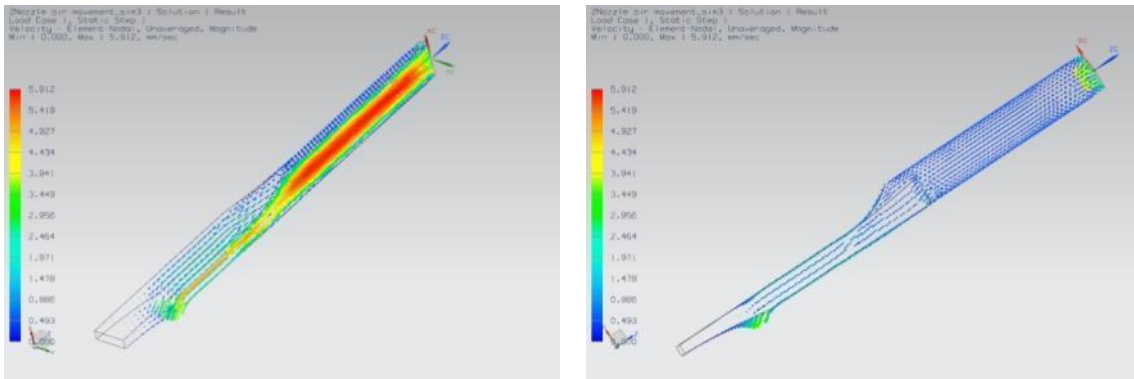


Figure 57 MQSL Delivery Nozzle fitted to SAT Edgetek machine

A stiff air barrier is known to build up on the periphery of a spinning grinding wheel, preventing machining fluids from actually contacting with the wheel surface. The construction of the nozzle incorporates a rigid body back plate, designed to breakdown this air barrier. This encourages the machining fluids to fill the porous surface of the wheel, and to be then carried into the grinding zone. The shoe nozzle design was created with the aid of FEA fluid flow analysis. The cross sectional fluid flow provided an indication of inlet and exit pressure changes through the use of the shoe nozzle see Figure 58. The nozzle channels were then designed to maintain the delivery inlet pressure through to the surface of the wheel.





**Figure 58** Fluid flow of nozzle outlet providing fluid pressures and velocities. Inlet pressure of 2.4bar, max nozzle channel height 1.5mm

### 3.8 Powder Feeder Mechanism Development

The first solid lubrication powder delivery mechanism resembled a pharmaceutical powder-measuring device being adapted and fitted to the grinding machine, see Figure 59. Although large and cumbersome once it was fastened into position above the grinding wheel it proved to be effective.

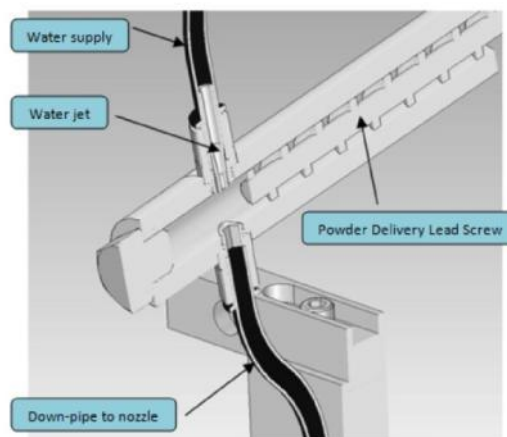


**Figure 59** Proven lead screw mechanism

Developments of the delivery system then began to simplify and reduce the size of the equipment. This was primarily to develop the system into an industrially acceptable machine, see Figure 60 to Figure 63. The feeding control system was also adapted to widen the range of delivery rates. The feeding mechanism provided switches to turn the feeder on and off when the grinding cycle was about to plunge. The unit featured a shorter leadscrew and a method of agitating the powder in the hopper. The variation in the powder delivery rate was determined by the voltage supplied to the D.C. motor. The electrical power unit featured external to the machine ranging from 0-30V. Max voltage of the motor was 12V so care had to be taken not to burn out the brushes.



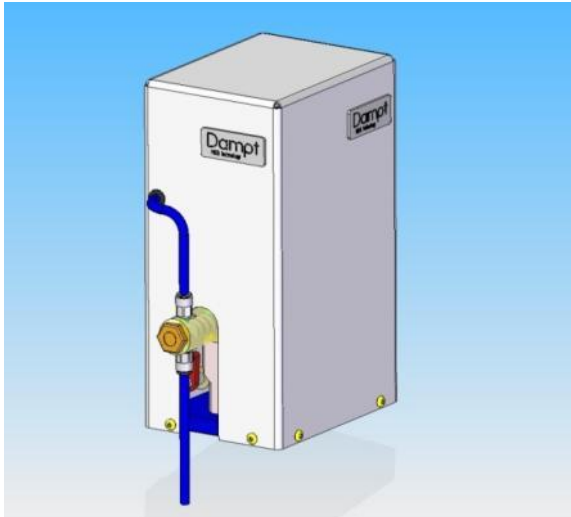


Figure 60 Feeder system – encased

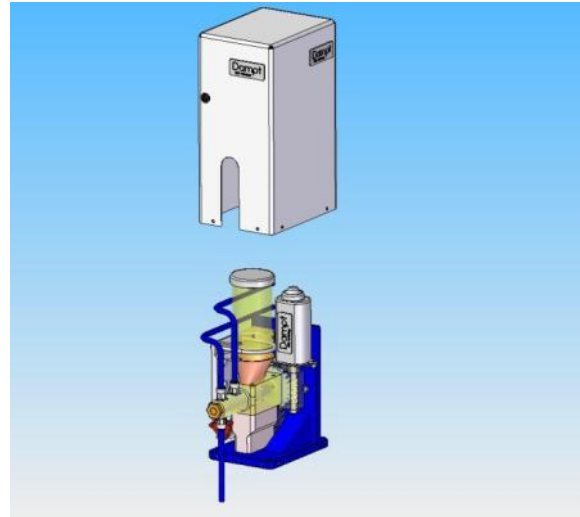


Figure 61 Feeder system – expanded

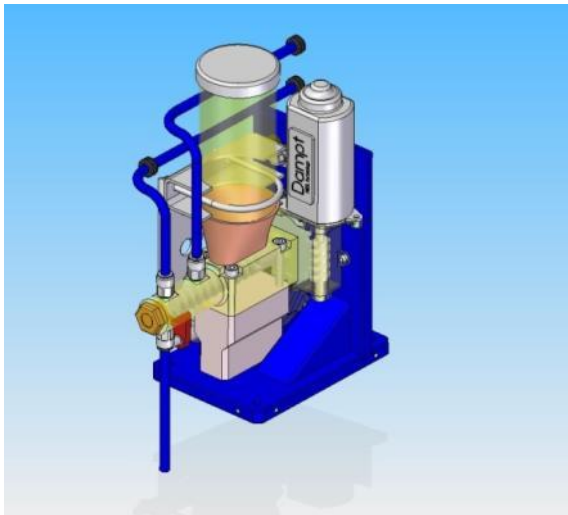


Figure 62 Close-up of 12 volt motor and lead-screw mechanism



Figure 63 Improved powder feeder mounted into machine

### 3.9 Electrostatic System

The powdered lubricant was delivered by a mechanical device in the early stages of development. However this required measured volumes of powder to be collected and carried by a fine mist of oil or water or air, into the grinding zone. Although this method of feed was functional and practical it also posed several potential problems;

- that the carrying fluid may play a significant part in heat partition with respect to thermal conduction and dissipation, and;
- the fluid may be problematic with the operation of thermal spectrometry instrumentation.

---

The use of a fluid is an extremely effective method of carrying and guaranteeing that the solid lubricant is evenly distributed within the grinding zone. However an alternative approach was required to remove these potential issues and provide a more suited setup to analyse the performance of the solid lubricants under dry conditions.

The most engaging solution was to utilise the electrostatic phenomenon of fine particles, where a volumetric feeding system was able to charge the solid lubricant before directing them towards a grounded workpiece. This enables the solid lubricant to be physically controlled upon exiting the nozzle and provides an appropriate method of waste collection once the lubricant has passed through the grinding zone.

### **3.9.1 Electrostatic application**

Incorporated within this research was an exciting alternative approach towards MQL lubricant delivery systems, through the potential of electrostatics. Everyday experiences can confirm how fine particles of liquids and dust become electrically charged resulting in the attraction or repulsion from surfaces. Examples are dust onto electrical appliances such as computer and television screens, the electrical shocks when touching surfaces, seeing fine liquid streams being influenced by charged surfaces, and the signal movements observed by oscilloscopes. Charge is never created, but rather directed or moved which can either be an advantage or disadvantage (Jonassen, 1998).

Early experimentation within electronics investigated how electric fields were able to influence objects passing through them, such as electrode tubes and the capability of electro-motive forces. The principles of electrostatics are well established with significant contributions by Coulomb, Franklin, Edison and Tesla. There are many instances where electrostatic charge is extremely undesired and required to be removed from working systems, such as in fuels lines, storage tanks, and intricate electronic devices where there is the likelihood of dangerously building up static electric charge through either induced or frictional sources. Once elevated to a saturated level the charge will move, often in the form of a spark, over varying distances and provides a potentially devastating point of ignition. There are however many examples where electrostatics is positively exploited. The use of electronic fields allows liquids and gases to be separated and solids to be attracted to particular surfaces. For example dust particulates and toxic contaminants can be removed from industrial emissions through the use of electro-filters that polarise the particulates through the use of high voltage corona electrodes. The ionisation of the undesired compounds results in their attraction to grounded surfaces, where they remain until removal for safe disposal. Corona electrostatics involves the relatively high density of

charge over an electrode surface encouraging the charge to seek a path away from the surface. Sharp pins or needles are particularly useful within the construction of Corona electrodes as the surrounding air can break down as electron avalanches pass through to adjacent particles ionising the air in fractions of a second, see Figure 64. An example of this is on the trailing features of aircrafts, enabling the dispersal of electrical lightening strikes. This type of electrostatics is known as precipitation.

Corona discharge is commonly found in industrial situations such as electro filters, open field ionizers, separating and coating systems illustrated in Figure 65 and Figure 66. The latter two applications are of particular interest with the ability to direct dry powders towards selected (grounded) targets. Heavily utilised in mineral separation electrostatics is used by taking advantage of the composition and conductive nature of differing materials. By agitating and inducing a charge into small particles materials can be separated such as nickel and copper ores, diamonds and silicates.

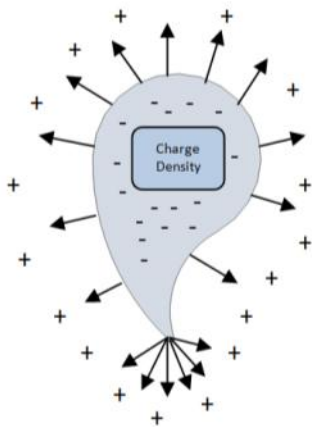


Figure 64 Charge density over surface profile

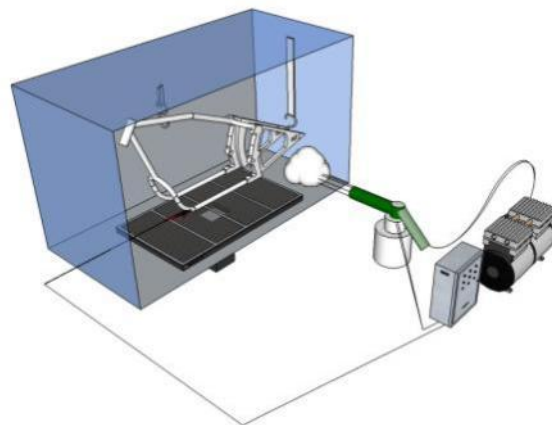


Figure 65 Powder Coating system

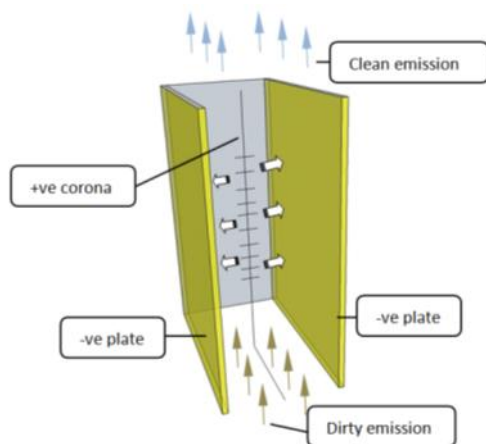


Figure 66 Electro filter separation of dirty emissions (Jonassen, 1998)

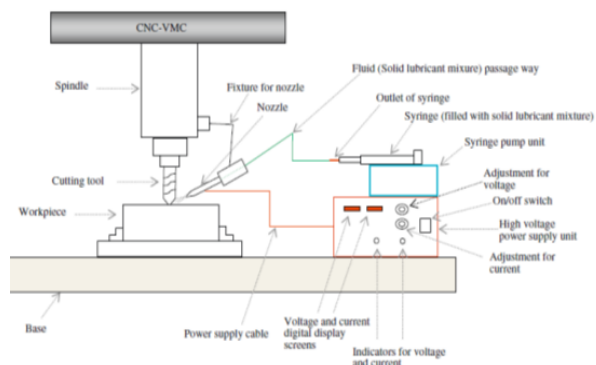


Figure 67 Instance of electrostatics functioning within milling (Suresh Kumar Reddy et al., 2010)

Electrostatic coating systems utilise the attractive nature of fine liquids or solid particles towards substrate surfaces. The benefit of having a concentrated target zone

---

and the minimal loss of process material increases the effectiveness and efficiency of fabrication and are well established in industrial coating systems (Nordson, 2011). Often the substrate is grounded while the paint or powder coating particles are positively charged through a series of corona electrodes providing an evenly distributed layer of paint prior to oven curing. Excessive waste can even be attracted and extracted away to be recycled within the system.

Electrostatic lubrication systems have recently been found to be introduced into instances of milling. However they have not featured within abrasive machining (Suresh Kumar Reddy et al., 2010) see Figure 67. The present research has adapted a commercially available electrostatic paint spraying unit to function within the abrasive machining environment. The corona electrode was positioned directly above the grinding wheel and adds a degree of functionality and serviceability to the system.

The total elimination of an oil or water based machining fluid offers an alternative approach to applying a solid lubricant. One distinct problem when introducing such fine particulates is the ability to control them within the immediate vicinity of the grinding environment, as high air disturbance is found surrounding a rotating grinding wheel. A means of attracting the lubricant into the grinding zone was therefore developed through the introduction of electrostatics. By positively charging the solid lubricant particles close to the work zone a consistent flow of lubrication could be aimed and attracted to a grounded charged substrate, see Figure 68.

Solid lubricant in a powdered form passes through an electrostatic feeder by means of a compressed air line and the Bernoulli Effect. As the air/lubricant mix passes through an electrically conductive passage the particles are lifted into a positively charged state, a triad of corona electrodes aid the charging of the particulates as they exit the electrode tube see Figure 69. Upon exiting the feeder the airflow is directed towards the grinding wheel where the particles are attracted to a negatively charged surface and taken into the grinding zone by the abrasive wheel. The system mounted into the SAT machine is shown in Figure 70.

Controlling the powder before and after the grinding zone is critical to the process and is controlled through switching the negative terminal at a high frequency between the grinding wheel, the workpiece and the vacuum extraction system, see Figure 71. This allows the particles to move around the region of work whilst being released once used. Previous work with solid lubrication noted the continuous build up of solid lubricant material would clog and dull the effectiveness of the grinding wheel. By attracting and repelling the solid lubricant the pores of the wheel are kept open further improving the efficiency of the abrasive process.

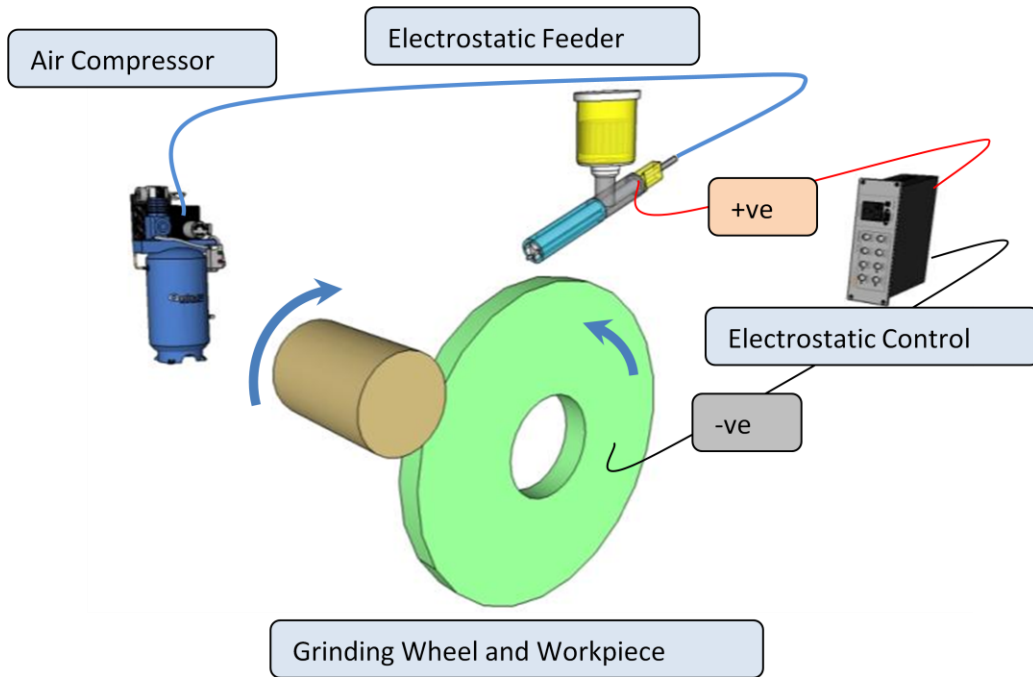


Figure 68 The electrostatic lubricant system

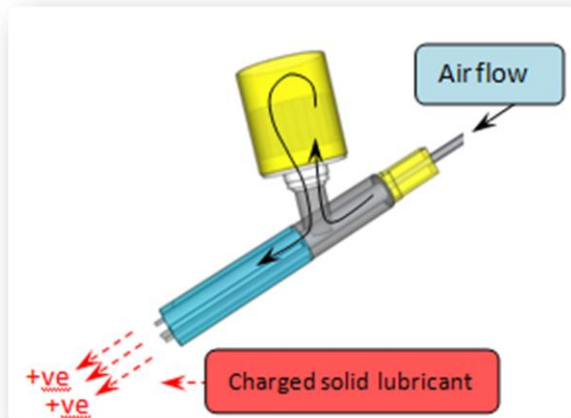
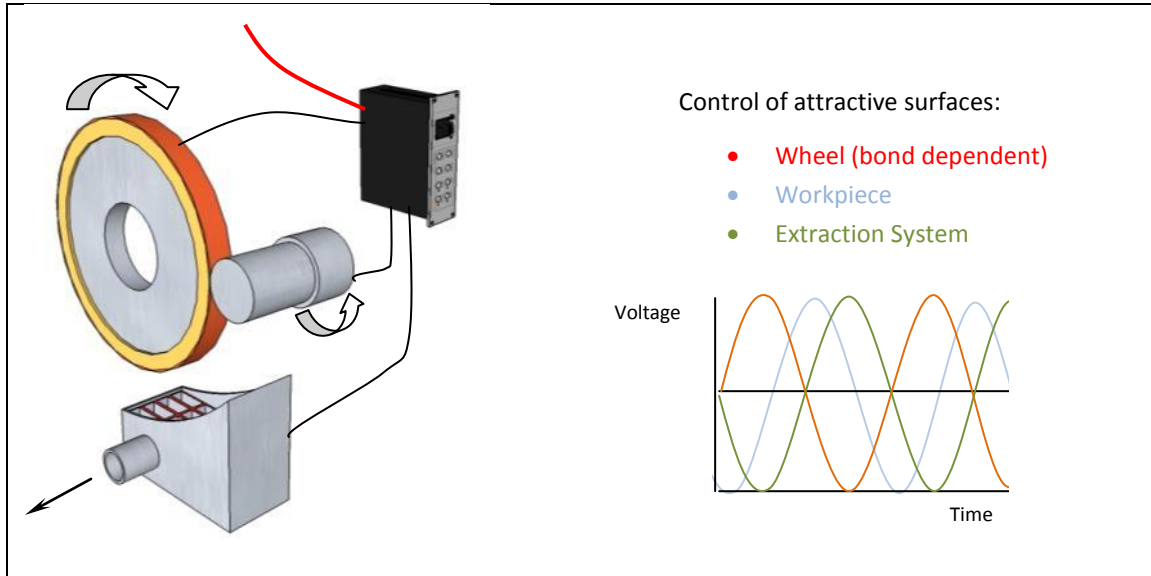


Figure 69 Electrostatic powder feeder and corona electrodes



Figure 70 Electrostatic Grinding Machine Setup



**Figure 71** Control of attractive surfaces demonstrating the alternation of affective surfaces between the grinding wheel, the workpiece and the vacuum extraction system.

### 3.10 Light detection instrumentation

Fibre optics can deliver and return sources of light with very small amounts of interference. They offer the opportunity to relocate delicate instrumentation away from the actual point of interest. This is a great benefit when considering introducing light sensors to the aggressive nature of the grinding environment. Light detection sensors exist in many forms with a variety of methods available to optically observe and image wavelengths and light intensities. These types of sensors also use scanning speeds and possess the resolution necessary for the accurate determination of real-time temperatures.

Photomultiplier Tubes (*PMT*) are a form of point detection and widely used throughout phosphor emission analysis due to their resolution with sensitivity and responsiveness levels allowing response times within 1ns. (Khalid and Kontis, 2008). Photons hit a photo-emissive cathode on entering the tube that accelerate and encourage the impact with sequential dynodes increasing the number of secondary electrons, before finally hitting an anode where the amplified signal can be measured. A single photon is multiplied into  $10^5$  to  $10^7$  electrons.

Photodiodes are semi conductors that have excellent response behaviours to incident light. Their time resolution is slightly slower than that of PMTs however their ability to capture a wide range of wavelengths and compact rugged construction has many advantages. Figure 72 illustrates the physical differences between PMT and Photodiodes.



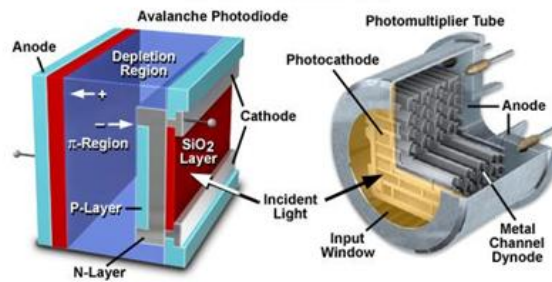


Figure 72 Photodiode and Photomultiplier tube construction

Charge Coupled Devices (CCDs) are another form of solid state imaging where captured photons are converted into an electrical charge. An array of individual pixels provides an area of photon capture allowing for emission images to be established through serial charge transfer conditioning. Interline CCDs include the advantage and increased resolution through parallel charge transfer. Various solid state imaging systems are based upon this principle including Intensified CCDs (ICCDs), Multiport/Multi-gate CCDs, as shown in Figure 73.

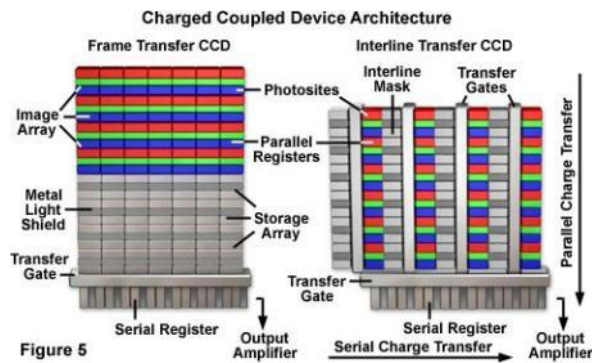


Figure 73 Charged Coupled Device (CCD) Architecture

All light detecting sensors have an inherent vulnerability to noise. Four major noise factors are generally accepted as; Dark shot noise, Photon shot noise, Fixed pattern noise, and electrical readout noise.

Once suitable excitation and detection methods have been selected a complete system can then be constructed an example of which is illustrated in Figure 74. An extremely import feature to consider with abrasive machining is the aggressive motion of the wheel, workpiece, fluid and chips. Phosphor thermometry as a concept is currently being introduced into working gas turbine engines demonstrating the dynamic responsiveness and practicality of such systems. Providing suitable investigation and development is made into suitable fixtures, protection and signal processing it is hoped that phosphor thermometry will be able to determine an accurate working temperature at the point of abrasion.

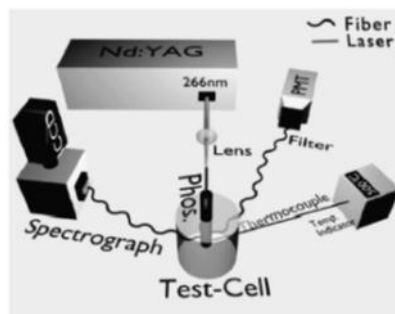


Figure 74 Phosphor Thermometry test bed with detection sensors providing comparators

Thermal spectroscopy involves analysing the electromagnetic wavelength spectra radiated from heated bodies. The fact that heated metal alloys emit such electromagnetic radiation has long been established, and that the visible spectra can also relate to the constituent elements in their alloy compositions. When an alloy is sufficiently heated, each constituent element emits visible light primarily at a characteristic wavelength, i.e., has its own visually observable signature. The wavelength of the emission from each element, at its characteristic wavelength, is relative to the proportion in which that element is present in the alloy being examined.

Generally the colour and the shape of the emitted grinding sparks is an indication of the success of the machining conditions. Early days of machining were often limited to that of skilled individuals who relied solely on personal experience and judgment to produce desired surface conditions, particularly with respect to the recognition of spark and swarf patterns in various metal alloys and difficult to machine materials.

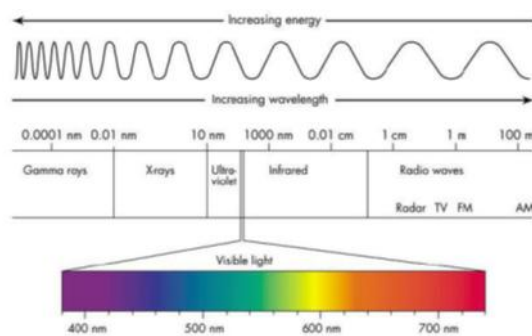


Figure 75 The electromagnetic spectrum

Optically capturing and processing the energy wavelengths emitted from a grinding pass offers the possibility to introduce a real-time monitoring technique. The forming and shearing of sparks from the parent workpiece results in mechanical energy converting from the grinding wheel into bright sparks and elevated surface temperatures. Ultimately the optimisation of the grinding process could develop through the understanding of the division of heat between the chip/wheel/workpiece.



Figure 75 illustrates the electromagnetic range of wavelengths that exist and that possibly offer a detectable and quantifiable relationship to process temperature.

### 3.10.1 Spectrometer Information

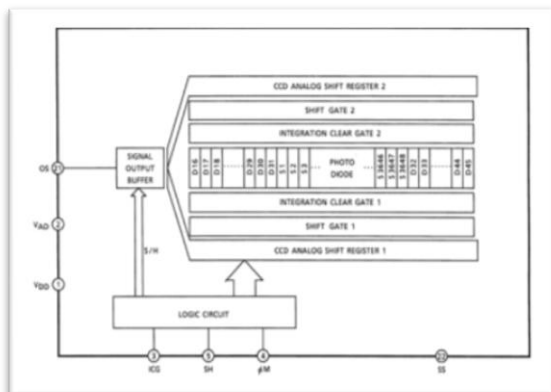
The compact nature of the spectrometer allowed for flexible installation into the grinding environment. The CCD is housed within a rugged casing that was kept external of the machine and away from the abrasive processes, Figure 76a. The light was collected by a banded collimator that was positioned close to the grinding zone, see Figure 76b. The spark light spectrum signal was carried by means of a fibre optical cable towards the CCD sensor. The details of the spectrometer are featured below in Figure 76c.



a)



b)



c)

Thorlabs CCS100 USB CCD spectrometer  
 UV, VIS and IR Spectral Range  
 Czerny-Turner-Spectrometer  
 Size: 30 mm x 120 mm x 80 mm  
 Auto Compensation for Dark Current Noise  
 High Speed USB Connection 200 scans per sec  
 Trigger Input for External Synchronization (TTL)  
 16-bit A/D-Converter  
 3,648 Pixel CCD Line Array  
 No moving parts

**Figure 76** Spectrometer a) USB2.0 CCS100 CCD unit b) 350-700nm Collimator c) CCD circuit array schematic

Fundamental to the success of this system was the distance and orientation of the CCD unit from the grinding zone. The collimator was positioned as close as was physically possible to the point of spark emission. However the grinding environment can be particularly aggressive due to the nature of high speed rotating tooling and rapid material removal processing. The inclusion of an optical detection method was therefore subjected to various interferences in the form of ejected swarf, fluid mist, and grinding dust. These could obstruct a clear line of site to the emitted sparks.

Therefore a protective housing was designed to prevent any obstruction or blockage of the collimator. The collimator is embedded within a hard polyester body see Figure 77, and has a series of air channels integrated into the structure. An air-shield around the front of the housing protects the optics, upon the air exhausting from the channels. This was extremely effective.

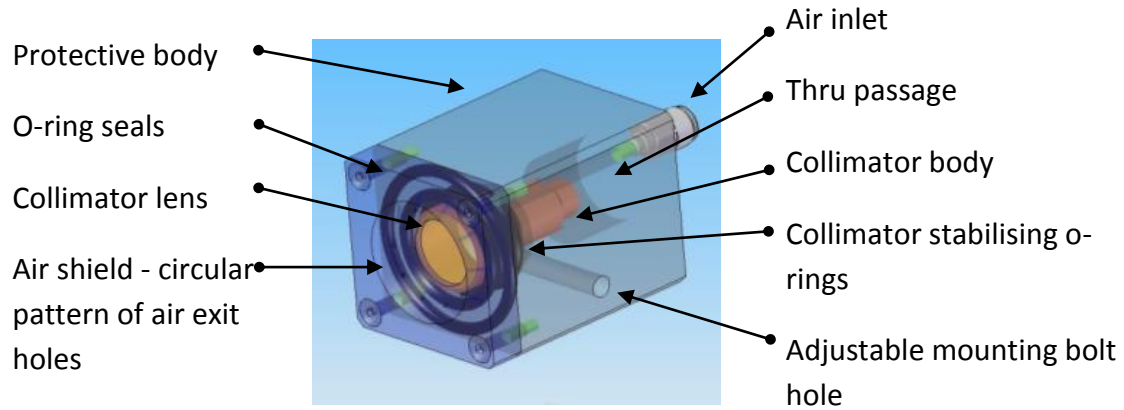


Figure 77 Collimator housing illustrating the internal channels for the air-shield that protects the collimator lens

### 3.11 Vacuum Shroud

Environmental regulation aims to prevent or limit the damage caused by industrial processes. The entire life-cycle of manufacturing needs to be accounted for; including the cost of purchasing, the logistics, the storage, the filtration, the maintenance and ultimately the price of controlled disposal of hazardous materials and chemicals. MQL machining strategies can reduce the total quantity of machining resources required throughout the stages of manufacture. Currently the use of solid lubricants is a 'single-use' resource, however providing a development in the waste collection systems the opportunity exists to filter and reuse MQL materials within long-term production. A vacuum shroud was necessary to prevent any contamination to the machine from the solid lubricants as this would be the first stage in the eventual separation and cleaning of the solid lubricants for re-use. The shroud was positioned neatly below the wheel in order to capture all the process waste while its shape was designed to capture all of the machining fluid expelled throughout the duration of the machining process. The vacuum line ran external to the machine to allow for ease of operation and serviceability, located at the lowest section of the wheel circumference to extract the maximum quantity of process waste, as seen in Figure 78a and Figure 78b.



**Figure 78** Extraction shroud featuring a) vacuum takeoff b) catchment plate c) clean machine

The shroud design incorporates an adjustment in the size of the catchment area and for ease of removal when not required, particularly with respect to the wheel replacement, the wheel balancing and the adjustment of fixtures, Figure 78c. The freedom of the machine axis travel was maintained by positioning the extraction line behind the X-axis table. The tight enclosure of the shroud around the grinding wheel ensured that a strong positive suction prevented process waste from spreading out onto the machine bed through the use of a 1200 Watt wet and dry vacuum system.

### 3.12 Key Messages

The key messages from this chapter are as follows:

- Minimum Quantity Lubrication (MQL) can provide machining conditions for successful chip formations whilst benefitting process costs and protecting the environment.
- Combining the theories of MQL with the advantages and the practicalities of solid lubrication enables the development of Minimum Quantity Solid Lubrication (MQSL).
- The inclusion of solid lubrication into the abrasive machining process can exploit their tribological properties. A reduction in the frictional forces involved in the formation of a chip between the grinding wheel and workpiece reduces the quantity of energy available to be converted into heat. This can minimise the use of machining fluids. .
- The nozzle design incorporates a graphite faceplate to allow the replication of the wheel geometry. This feature maintains the principles of the useful flowrate theory by matching the thickness of the layer of machining fluid to the highest grits on the wheel periphery.
- The development of solid lubricant delivery systems utilises mechanical, pneumatic and electrostatic principles in order to feed precisely the mass flow rates of dry powdered lubricants into the grinding zone.

These key messages from the development of the lubricant delivery equipment were carried forward to inform the experimental design of MQL and MQSL grinding

---

## 4.0 Experimental Design

### 4.1 Overview

This chapter describes the research methods employed to achieve the project objectives. Details of the Taguchi experiments are included. These experiments were designed to identify the performance of MQL and MQSL lubrication on the surface integrity and grinding temperatures, within the context of the cylindrical grinding of low carbon steel. The machining parameters are listed and the specifications of the grinding equipment are included. Specifications of the analysis equipment and details of their operation provide an insight into the determination of the surface integrity and grinding temperatures.

The sequence of grinding trials enabled the practicalities of introducing MQL and MQSL systems into grinding, to be assessed. The duration of experimentation involved the application of EcoCool<sub>(MQL)</sub>, MoS<sub>2</sub><sub>(MQSL)</sub>, CaF<sub>2</sub><sub>(MQSL)</sub> and hBN<sub>(MQSL)</sub> lubricants, into the cylindrical grinding process.

### 4.2 Taguchi Experimental Design

The Taguchi ordered orthogonal experimental design provides a measured and controlled approach to assessing the performance of solid lubrication within the cylindrical grinding abrasive machining environment. The benefit of this statistical method is the identification of the significance of process parameters through a condensed series of trials. The lubricants to be investigated were identified at the early stages of the research. MoS<sub>2</sub> and BN are often found as additives in greases and oils, while the CaF<sub>2</sub> possesses properties of lubrication and tribo-luminescence, which was investigated in the later stages. The performances of the solid lubricants were compared to the results from EcoCool, under similar grinding conditions.

The Taguchi method chosen is formed upon the two-factorial experimental design. In this research the 'factors' are identified as a set of machining parameters, while the 'levels' are a high and a low variation of the factor. The machining parameters that were chosen were thought to be the parameters of most significance with respect to recording grinding power, creating an identifiable difference in the material removal rates, and influencing the temperature of the process. The machining parameters selected were; wheel speed ( $v_s$ ), workspeed rotation ( $v_w$ ), Infeed speed ( $v_f$ ), and the quantity of lubrication. The selection of four factors enabled a full-factorial L8 experimental design and was thought to provide adequate data for the analysis of the effect of lubrication. The factors and the variation of the levels are listed in Table 11. The trials were repeated at least twice to improve the confidence in the analysis.

The use of MiniTab V14 statistical software provided the means by which to collect and analyse the grinding data. An example of the MiniTab interface features in Figure 79, demonstrating the structure of the L8 array. The process outputs include the net power, SGE and the surface temperature. The factorial relationships are then interpreted through an Analysis of Variance (ANOVA) method to identify the significance of the variation of the process parameters. The selected levels of the machining parameters were suggested by one of the industrial sponsors to imitate industrial removal rates, see Table 12. In addition to these trials supplementary sets of control tests were included in order to establish benchmarking samples. These include extreme feed rates with water-only and dry grinding conditions to provide serious burn conditions, for use as a comparative.

**Table 11** Basis for Taguchi L8 orthogonal experiment

| Taguchi Test No. | Wheel speed (Vs) m/s | Work speed (Vw) m/s | Infeed rate (Vf) mm/s | %MQL %MQSL |
|------------------|----------------------|---------------------|-----------------------|------------|
| 1                | Low                  | Low                 | Low                   | Low        |
| 2                | Low                  | Low                 | High                  | High       |
| 3                | Low                  | High                | Low                   | Low        |
| 4                | Low                  | High                | High                  | High       |
| 5                | High                 | Low                 | Low                   | High       |
| 6                | High                 | Low                 | High                  | Low        |
| 7                | High                 | High                | Low                   | High       |
| 8                | High                 | High                | High                  | Low        |

|   | C1       | C2       | C3      | C4          | C5          | C6             | C7          |
|---|----------|----------|---------|-------------|-------------|----------------|-------------|
|   | Vs (m/s) | Vw (m/s) | heq(um) | Vf (mm/min) | EcoCool (%) | Net Power (kW) | SGE (J/mm3) |
| 1 | 75       | 0.5      | 0.0033  | 0.03        | 1           | 0.1001         | 30.8141     |
| 2 | 75       | 0.5      | 0.0067  | 0.06        | 10          | 0.5315         | 81.7659     |
| 3 | 75       | 0.6      | 0.0040  | 0.03        | 1           | 0.1881         | 48.2310     |
| 4 | 75       | 0.6      | 0.0080  | 0.06        | 10          | 0.2178         | 27.9238     |
| 5 | 100      | 0.5      | 0.0025  | 0.03        | 10          | 0.1207         | 37.1247     |
| 6 | 100      | 0.5      | 0.0050  | 0.06        | 1           | 0.5746         | 88.4030     |
| 7 | 100      | 0.6      | 0.0030  | 0.03        | 10          | 0.2515         | 64.4781     |
| 8 | 100      | 0.6      | 0.0060  | 0.06        | 1           | 0.6203         | 79.5297     |

**Figure 79** Example of a Minitab worksheet using the L8 experimental design and variation in the  $V_s$ ,  $V_w$ ,  $V_f$  and quantity of machining fluid/solid lubricant

**Table 12** MoS<sub>2</sub>, CaF<sub>2</sub>, hBN and EcoCool Taguchi machining parameters

| <i>Machining Parameters</i>     | <i>Settings</i>  |
|---------------------------------|--|
| Machine Tool                    | Holroyd Edgetek SAT grinding machine   |
| Work piece material, dimensions | 38MnSiVS6 , 51CrV  |
| Grinding Wheel Type             | TVM B216 Electroplated wheel<br>Winter cBN90 M200 vitrified bonded wheel<br>Asahi B120 Vit. Bond<br>Noritake cBN80 Vitrified wheel |
| Grinding wheel dimensions       | Ø350mm x 20mm  |
| Spindle Power                   | 37kW grinding spindle  |
| Wheel Speeds                    | 75m/s-50m/s, 100m/s-75m/s  |
| Infeed Speeds                   | 3-0.6mm/min, 0.3-0.06 mm/min   |
| Selected Flowrates              | 100%Q <sub>fu</sub> with 5.5-8.3 g/min,3.8-11.3 g/min,18.3-41.3g/min   |
| Width of sample                 | 13mm   |
| Nozzle                          | MQL/MQSL Nozzle  |
| Sparkout                        | 5 Seconds  |

The flowrate of the MQL delivery system was set as the calculated useful flowrate that is particularly dependant on the exposed grit height and on wheel speed. Grit height measurement was undertaken through the aid of microscopy as impressions of the grinding wheel periphery were taken, firstly with a rubber compound to create a negative impression, before being positively cast with an epoxy resin providing a complete moulding of the grains and pores within the surface. The calculated Useful Flowrates feature in Table 13.

An average depth of pore value was determined by measuring many heights of the cBN grains, over a given surface area. Images of the wheel surface clearly demonstrate the varying shapes and heights of the abrasive grains. Examples of worn grains can be seen against untouched grains demonstrating the variance of wheel layup as seen in Figure 80 and Figure 81.

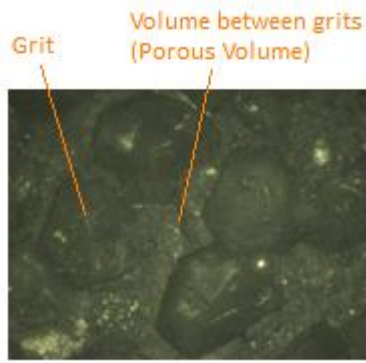


Figure 80 Unconditioned B216.

Average pore depth = 102.68µm

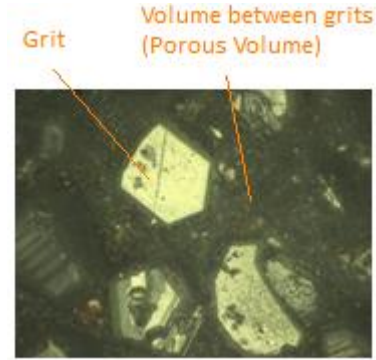


Figure 81 Conditioned B216.

Average pore depth = 89.32 µm

Example 1:

$$Q'_{fu} = \phi_{pores} \cdot h_{pores} \cdot b_s \cdot v_s$$

$$= 1 \times 102.68 \times 10^{-6} \text{m} \times 10 \times 10^{-3} \text{m} \times 100 \text{ m/s}$$

$$Q'_{fu} = 0.000102 \text{ m}^3/\text{s} = 0.102 \text{ l/s} = 6.12 \text{ l/min}$$

Example 2:

$$Q'_{fu} = \phi_{pores} \cdot h_{pores} \cdot b_s \cdot v_s$$

$$= 1 \times 89.32 \times 10^{-6} \text{m} \times 10 \times 10^{-3} \text{m} \times 100 \text{ m/s}$$

$$Q'_{fu} = 0.000089 \text{ m}^3/\text{s} = 0.089 \text{ l/s} = 5.34 \text{ l/min}$$

Table 13 Calculated Useful Flowrates from wheel surface impressions

|                    | CBN EP B216           |                       | CBN Vit Bond B90      |                       | CBN Vit Bond B80      |                       |
|--------------------|-----------------------|-----------------------|-----------------------|-----------------------|-----------------------|-----------------------|
| Average Depth (um) | 89.32                 |                       | 45.16                 |                       | 42.63                 |                       |
| Useful Flow Rates  | $\text{m}^3/\text{s}$ | $\text{l}/\text{min}$ | $\text{m}^3/\text{s}$ | $\text{l}/\text{min}$ | $\text{m}^3/\text{s}$ | $\text{l}/\text{min}$ |
| Wheel Speed (m/s)  |                       |                       |                       |                       |                       |                       |
| 50                 | 0.000045              | 2.68                  | 0.000023              | 1.35                  | 0.000021              | 1.28                  |
| 75                 | 0.000067              | 4.02                  | 0.000034              | 2.03                  | 0.000032              | 1.92                  |
| 100                | 0.000089              | 5.36                  | 0.000045              | 2.71                  | 0.000043              | 2.56                  |
| 150                | 0.000134              | 8.04                  | 0.000068              | 4.06                  | 0.000064              | 3.84                  |

This ranged from 4.02l/min for the wheel running at 75m/s, to 2.68l/min for the wheel running at 50m/s for a grit size of 216cBN. The fluid delivery system included the Dosatron fluid-powered proportional flowrate mixing unit enabling the lifting of EcoCool machining oil in order to produce an emulsified machining fluid to various levels of concentration. Consistent to factorial experimental design the extreme low and extreme high values of emulsion mixture of 1% and 10% EcoCool oil were added respectively. The efficiency of the abrasive regime is therefore determined by the Net power consumed against the volume of material removed while the Taguchi experimental design promoted the collection of maximum data through the minimum number of trials necessary.

The variation in the quantity of lubrication was actually added to an MQL fluid flow (however in the later stages the experiments progressed towards completely dry grinding). The MQL fluid flowrate was based upon the introduction of water under flowrates calculated from the useful flowrate theory. This calculated MQL based upon



the specifications and the topography of the grinding wheels. The average grit-heights of the grinding wheels were measured under the machining set-up conditions. This enabled the L8 experiment to identify the influence of the solid lubricant or EcoCool. The selected levels of the quantity of the solid lubricant were set at extreme values of high and low, and were determined by the capability and capacity of the solid lubricant delivery system at the time.

Before each grinding trial the topological (surface) condition of the grinding wheels were re-dressed. This was important in regards to not allowing the wearing of the grinding wheel to influence the experimental analysis. This was important for the purpose of the investigation, although it would not occur within industrial practice. A diamond dressing wheel was traversed across the width of the grinding wheel to re-form the abrasive surface. A series of grinding wheel plunges took place before any trial was recorded in order to condition the wheel and break away any sharp or loose grit within the surface. Grinding wheels are required to be 'bedded in' before the machining data is trustworthy. A set of dressing parameters were identified to optimise the performance of the grinding wheel, again these were suggested by a sponsoring partner. These dressing parameters were designed for use under normal operating conditions with a fluid to control the temperature of the diamond dressing wheel, and are listed in Table 14. The later stages of MQSL experimentation ventured into dry dressing. Coolant is normally recommended throughout the stages of dressing however the calculated parameters used feature in Table 15.

**Table 14** Nominal dressing parameters

|                      |                                    |
|----------------------|------------------------------------|
| Dressing Wheel       | Dia. 150mm, D40 Metal Bond         |
| Dresser Wheel Speed  | 5480rpm (dia 150mm = 43m/s)        |
| Grinding Wheel Speed | 4093rpm (dia 350mm = 75m/s)        |
| Traverse Speed       | 1650mm/min                         |
| Passes               | 8 passes 0.005mm, 8 passes 0.003mm |
| Coolant              | Water                              |

**Table 15** Dry dressing wheel parameters

|                      |                              |
|----------------------|------------------------------|
| Dressing Wheel       | Dia. 150mm, D40 Metal Bond   |
| Dresser Wheel Speed  | 5480rpm (dia 150mm = 43m/s)  |
| Grinding Wheel       | B90/80 Vit. Bonds            |
| Grinding Wheel Speed | 780rpm (dia 350mm = 14.3m/s) |
| Overlap Ratio        | 3, traverse speed 520mm/min  |
| Passes               | 8 passes 0.005mm, 8 passes   |



|  |         |
|--|---------|
|  | 0.003mm |
|--|---------|

### 4.3 Structure of experimentation

The sequence of experiments followed the use of 4 wheels; a single B216 cBN Electroplated wheel, and three cBN vitrified wheels; B120, B90 and B80. The electroplated wheel was used for preliminary investigations while the vitrified wheels focused more towards the semi-super finishing regimes. MQL and MQSL applications are thought to be of more benefit within the semi-finishing regimes where smaller chip thicknesses are involved. The complete combinations of tooling and workpiece are listed in Table 16, and each experiment was repeated nominally twice. The workpiece material available was a combination of 51CrV4 crank shaft steel and 38Mn low carbon steel.

**Table 16** The sequence of abrasive machining setups throughout the period of experimentation, demonstrating the collection of data necessary for an overall comparison of the performance of the lubricants.

| <i>Wheel No.</i> | <i>Wheel Type</i> | <i>Workpiece</i> | <i>Lubricant</i> |
|------------------|-------------------|------------------|------------------|
| Wheel 1          | B216              | 38Mn             | EcoCool          |
|                  | Electroplate      |                  |                  |
|                  | with Water        | 38Mn             | MoS2             |
| Wheel 2          | B90 Vit Bond 1    | 38Mn             | EcoCool          |
|                  |                   | 38Mn             | MoS2             |
|                  |                   | 38Mn             | CaF2             |
|                  |                   | 38Mn             | CaF2+ Water      |
|                  |                   | 38Mn             | CaF2 + EcoCool   |
|                  |                   | 51CrV            | CaF2             |
|                  |                   | 51CrV            | CaF2+ Water      |
|                  |                   | 51CrV            | CaF2 + EcoCool   |
| Wheel 3          | B120 Vit Bond 2   | 38Mn             | CaF2             |
|                  | Dry               | 38Mn             | hBN              |
|                  | Electrostatic     | 51Cr             | CaF2             |
|                  |                   | 51Cr             | hBN              |
| Wheel 4          | B80 Vit Bond      | 38Mn             | CaF2             |
|                  | With Water        | 38Mn             | hBN              |
|                  |                   | 51Cr             | CaF2             |
|                  |                   | 51Cr             | hBN              |
|                  |                   | 38Mn             | EcoCool          |

The development of the solid lubricant delivery evolved simultaneously with the experimental trials. Three separate designs are featured in this project work. The development of the feeding system allowed for greater range of delivery flowrates,

and aimed at establishing a more acceptable system to be used within an industrial context. The first two designs were similar in the mechanical leadscrew design. The last design used an alternative electrostatic approach. The delivery systems were assessed throughout each trial with respect to their performance that finally led towards the electrostatic delivery system. From a design point of view this incorporates the three model-principle; two developments, and one unique.

## 4.4 Machines

### 4.4.1 SATurn Machine

The majority of the trials were undertaken on a Holroyd Edgetek SATurn Super Abrasive Turning (SAT) machine. The machine is illustrated in Figure 82a. and the specifications are listed in Table 17. This machine was designed for high stock removal grinding to rival traditional hard turning methods. The superabrasive tooling is in the form of cBN electroplated and vitrified grinding wheels engaged in cylindrical and plunge grinding. The SAT machine enables the production of cylindrical forms employed extensively by the automotive, aerospace, and energy industries. The creation of high-precision cylindrical surfaces is critical within the production of components such as bearing races, cam shafts, crank shafts, and turbine blades, (see Figure 82b and c). The tooling industry also requires the grinding of cylindrically accurate tooling for the production of high tolerance tools. The SAT machine possesses a combination of tooling and workpiece rotation speeds, with high frame stiffness and super abrasive technology.



a)



b)

**Table 17 SAT Machine Specifications**

|  |
|--|
| 37kW grinding spindle                        |
| 9,000 rpm spindle speed                      |
| Cutting speeds up to 12,200 metres/min       |
| Wheel speed up to 200m/s                     |
| Wheel diameter 350mm                         |
| Feed rate up to 125 mm/s                     |
| High pressure coolant delivery up to 83 bars |
| 3 axis indexer work head                     |
| Force and power monitoring                   |



c)

Figure 82 a) SAT cylindrical grinding machine b) cam grinding c) gear production

Under normal operating conditions the machining fluid is fed by an external delivery system. This system is able to pump fluid at flowrates of up to 75l/min and up to pressures of 8bar.

#### 4.4.2 J&S Surface Grinder

A variety of smaller trials featured on the industry standard J&S 540 surface grinder, as shown in Figure 83, the specification of which is featured in Table 18. This machine offered a great degree of physical access in order to assess the practicality of introducing the Charged Coupled Device (CCD) sensor. The early stages of development with respect to the thermo-optical instrumentation were achieved on this machine assessing the practicalities and identifying the limits of its operation. Preliminary spectral analysis used a combination of  $\text{AlO}_3$  wheels against 51CrV steel and Titanium for maximum spark output. The surface grinder was used under a variety of wet and dry conditions with a small range of machining fluid flowrates.



Figure 83 J&S 540 surface grinder



Table 18 J & S 540 Surface grinder specification

|                                    |
|------------------------------------|
| 18" x 6" Magnetic Chuck Table      |
| Hydraulic Table Feed               |
| 1.5kW motor                        |
| Min Vertical feed step:<br>0.001mm |
| Min cross table step:<br>0.006mm   |
| Wheel diameter: 150mm              |

#### 4.5 Machine set up and data collection

The MQL delivery system was designed to provide adequate control over the fluid input variables. The water supply was taken from the workshop mains with a nominal pressure of 2.1bar. A series of valves and sensors provided the necessary control and is illustrated in Figure 84. The flow was filtered before passing through a series of flowmeters, a pressure transducer, the Dosatron unit, and exiting at the MQL nozzle. The pressure sensors and flowmeters are positioned in the flow line to provide a precise method of controlling the flow with respect to the useful flowrate theory. All instrumentation, excluding the nozzle is mounted externally on the machine; see Figure 85 and Figure 86. The turbine flowmeters were fitted in the system before and after the Dosatron unit, see Figure 87. A straight section of pipe before the

flowmeters, recommended to be a minimum of 200mm in length, enabled the fluid stream to fully-developed. The chemical analysis of the water is featured within Appendix B.

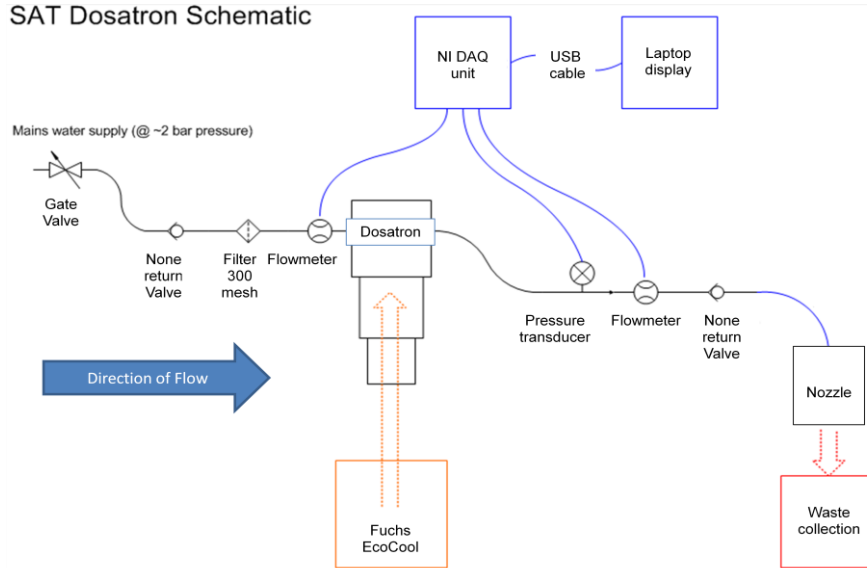


**Figure 84** The machine fluid delivery system, illustrating the Dosatron cyclic oil concentration mixer. The schematic also includes the positions of flowmeters, of pressure sensors and the USB DAQ collection unit directly linked to Labview SignalExpress



**Figure 85** The machining fluid system in position. Water supply in from the rear of the machine under mains pressure. The Dosatron unit picks up the EcoCool oil from below before passing through sensors and fed directly to the nozzle through the side of the machine



**Figure 86** Dosatron body with pressure sensor to the right



**DOSATRON®**

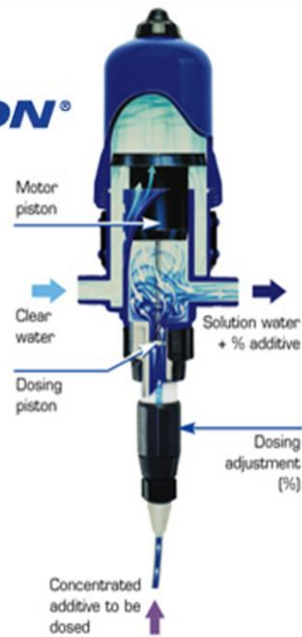


**Figure 87** Cross section of Dosatron, detailing the operation mechanism and the method of adjusting the concentration of EcoCool within the MQL water flow.

The MQSL powder delivery mechanism is sited directly above the grinding wheel, see Figure 88. This is predominantly to reduce the length of the delivery pipe between the nozzle and feeder lessening the likelihood of a build-up of powder. A water jet is positioned directly above the powders exit from the lead screw not only to assist in carrying the powder through the nozzle and onto the wheel but also to maintain a clean and unobstructed delivery passage.

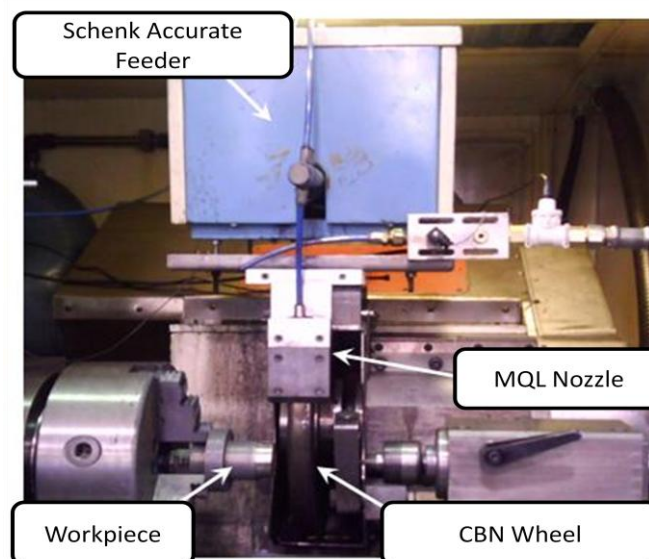


**Figure 88** Design 1: The front end of the MQSL delivery system. The graphite shoe nozzle is positioned directly onto the wheel surface while the powder delivery mechanism sits directly above.

---

The mechanical leadscrew delivery design progressed to a secondary model, see Figure 89. This design increased the accuracy of the mass flowrates by shortening the distance the powder had to travel, reducing the restrictions and likelihood that the powder would compact. A tickling gear was added to agitate the powder and encourage the lubricant to fall into the leadscrew funnel. The hopper was situated above the leadscrew reducing the risk of water and moisture running back into the system.



**Figure 89** Design 2: Development of mechanical feeder to incorporate a shorter lead-screw and achieve higher delivery rates of solid lubricants. The capacity of the feeder was increased however the size was greatly reduced.

The final design of the solid lubricant feeder combined a pneumatic feed with the electrostatic electrode. The graphite nozzle was adapted to accommodate a power-coating unit, see Figure 90. The solid lubricant powder was contained in a hopper directly above the grinding zone. The system was an unobtrusive and robust addition to the machine. An eccentric motor was attached to the hopper to prevent the solid lubricant powders from settling within the feed lines. The air supply was dried and filtered, before adding the lubricant powder within its flow. The workpiece was electrically grounded by means of a spring loaded contact, running upon the surface of the workpiece in a designated groove and aided with electrically conductive copper-slip. These feeding mechanisms were devised by the author to offer exciting and novel approaches to lubricant application.





**Figure 90** Design 3: Electrostatic Grinding Machine Setup. This set-up provided the lubricant to be applied by a pneumatic means, with or without the electrode being charged.

#### 4.6 Labview Signal Express 3.0

A DAQ (Data Acquisition) USB data collection unit was used in conjunction with Labview Signal Express Version 3.0. The National Instruments DAQ unit allowed for several important signals to be digitally recorded. These input signals were calibrated within the Labview Signal Express software capturing and imaging the machine performance through the duration of the trials. The NI 6210 usb unit is extremely versatile allowing for many signal types (analogue, digital, timers, counters) to be recorded simultaneously, and the interface display is shown in Figure 91. The fluid supply sensors were connected to the DAQ unit. Figure 92 demonstrates the termination of the signal devices into the DAQ unit.

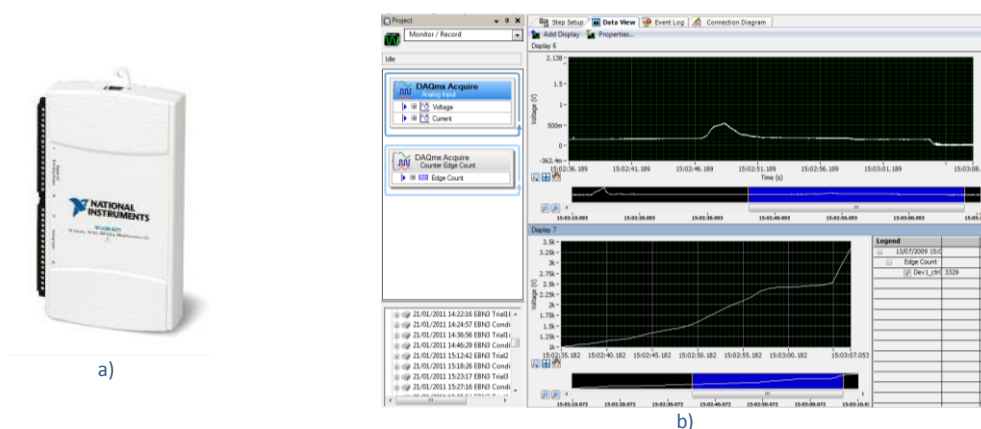


**Figure 91** a) DAQ USB unit setup to collect the necessary signal by b) Labview DAQ Signal Express showing an example of a recording of the Cycle Power and the machining fluid delivery flowrate.

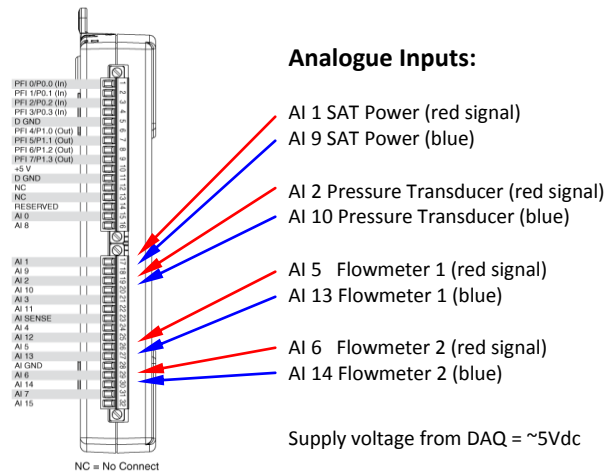


Figure 92 DAQ terminal configuration from machine sensors

All cables were routed external to the grinding environment to minimise the electrical noise often experienced within the workshop. Cables were shielded and the DAQ unit located in dust free enclosure.

#### 4.7 Thermal Measurement

The introduction of Physical Vapour Deposition (PVD) temperature sensitive films enabled the grinding temperatures to be determined. The fundamentals are covered in Section 2.6.2. A novel approach of applying the PVD films used a segmented pattern of differing films, upon the cross sectional surface of the cylindrical steel samples. This enabled three types of PVD material to be subjected the identical conditions, of a single grind. This provides an accurate method of determining the surface temperature throughout the variation of the Taguchi factorial experiments.

This required the careful preparation of 38Mn steel samples to be turned out of similar stock material into long bar sections with an outer diameter of 50mm. The bars were sectioned by EDM wire machining in order to slice them into discs. This guaranteed that the thicknesses of the discs were similar and the surfaces had minimum thermal distortion. The surfaces were then polished to a mirror finish with a 6micron diamond paste and a silica colloidal solution. This quality of surface was required for deposition of the PVD films.

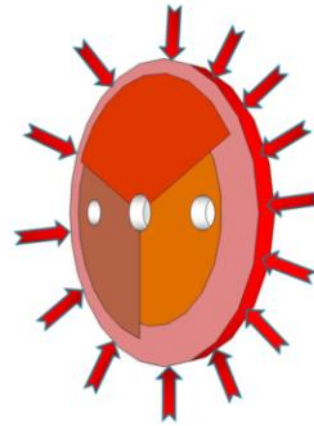
A masking plate was fabricated to expose a single 120 degree segment of the disc. This masking plate contained positions for four sample dices at any one time. The PVD process would then deposit a single film upon the exposed surface. After processing the discs were then rotated by 120 degrees in order for the second PVD film to be deposited, and so forth, until the discs contained three segments of film. Once fully processed the discs appeared to have three segments of coatings, see Figure 93. The samples were then assembled into a bar shaped workpiece. The assembly consisted of



a base section that clamped a series of PVD coated discs, blanks and spacers, as shown in Figure 94 and Figure 95. A single bolt ensured that the assembly was clamped sufficiently and there was no gap or inferences between the PVD surfaces and the blank discs. Two shoulder bolts locked the rotational freedom of the discs and prevented the assembly from moving, due to the tangential action of the grinding wheel.



a)



b)

**Figure 93** PVD three segmented films on sample surface a) pre-ground samples b) heat applied to the surface causing the PVD films to melt and create isotherms



**Figure 94** PVD polish plate and constructed sample bar

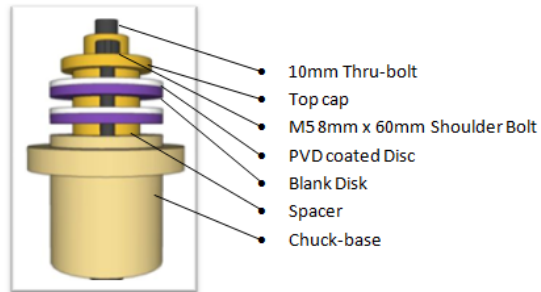


**Figure 95** Components of PVD sample bars

The Olympus LEXT OLS3000-IR confocal microscope provided critical information into surface conditioning with respect to the PVD film heights and melting zone depths. This microscope utilises laser scanning confocal technology with 1301nm wavelengths enabling sub-micron imaging, see Figure 96. This microscope has excellent resolution and extremely accurate three-dimensional measurement, see Table 19 and the inner functioning in Figure 97. Figure 98 show the LEXT in action when confirming the heights of PVD layers necessary for thermal analysis see Figure 99.



Figure 96 Olympus LEXT Con-Focal Microscope

Table 19 Olympus LEXT-IR Specifications

|  |
|--|
| • 3D observation and measurement in real time                                      |
| • Resolution of 0.55um line and space patterns                                     |
| • Magnification from 120x to 12,960x   |
| • No expensive and destructive sample preparation - no vacuum pump-down            |
| • Fast measurement and observation tasks in high volume manufacturing applications |

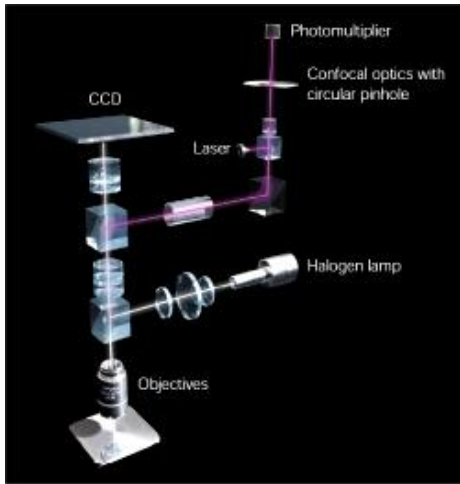


Figure 97 Confocal optics 1301nm IR

**OLYMPUS**

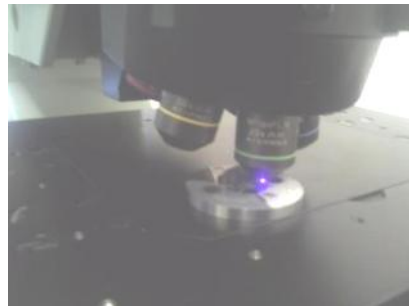


Figure 98 Con-focal Microscope in action measuring PVD film heights

The specified thickness of the PVD film was 20nm film of bismuth, indium and antimony however on receiving the samples the depositions appeared to be bismuth, indium and zinc within a range of 2-15 microns thicknesses. This did not prevent the trials from taking place. However, this must be considered when determining the surface temperature as the thickness may influence the clarity of the isotherms. The gap between the PVD discs and the blanks is assumed to be reliable even with these thicker PVD films, as this will reduce the effects of thermal distortions.

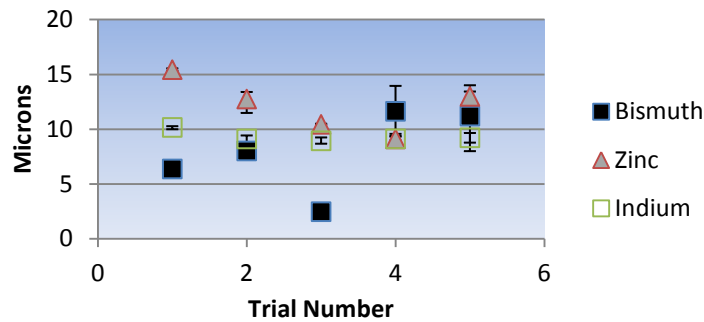


Figure 99 Average PVD coating height measurement

## 4.8 Surface integrity analysis

A series of post machining analyses provided an insight into the integrity of the surface. This involved the surfaces being analysed, partially after the grinding had taken place, and the microstructural investigation after the samples had been sectioned. Details of the instrumentation and methods used feature below, relating to the measurements of the; residual stresses, surface roughness, microstructural form, and subsurface hardness values.

### 4.8.1 Residual Stresses

The Barkhausen Magnetic Emission (BME) measurements were conducted by using a Stresstech  $\mu$ Scan device which consists of; a sensor, electromagnetic generator and a detection unit. The output signals produced were collected by a data acquisition system. A computer was connected to the output device and recorded by StressTech  $\mu$ Scan software. The excitation frequency of the magnetic field was 125Hz. Single signal was set to Channel 1 with conditions of the signal generator; Magnetisation set at 25, Gain set at 50, calibrated against previous work and tested against burnt samples.

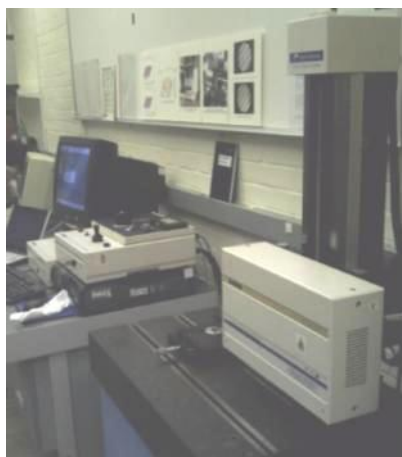
The magnetic responses were recorded over 360degrees of the cylindrical samples. The samples were rotated relative to a floating sensor, see Figure 100a, and the generator is pictured in Figure 100b. The samples had been designed to be wider than the sensor head (10-13mm) to eliminate the ingress of errors due to magnetic edge effects or grinding burrs. Three full rotations of samples (1080degrees) enabled an averaging of the magnetic recordings. Simple mineral oil was added to the surface of the steel samples to prevent the sensor from vibrating or distorting against surface defects, allowing for a continuous resolution of the magnetic signal.



**Figure 100** Barkhausen Magnetic Emission detection equipment the floating cam sensor connected to the magnetic generator and detection unit, Stresstech

#### 4.8.2 Surface Profile

Surface roughness measurements were taken on the Taylor Hobson Talysurf-120L table mounted with a 2 micron radius ruby scanning probe. Talysurfing involves linearly probing over the length of a surface to acquire the nature of the topography. The equipment is illustrated in Figure 101a, with the specifications in Table 20. The samples are placed on a dampened granite table whilst the ruby tipped probe is commanded to find a datum height on the y axis. The probe is then slowly retracting over the surface. The probe utilises a laser interferometer that is aimed at the rear of the probe carriage assembly. This is designed to detect variations in the surface height as the probe emulates the contours. The Talysurf was used for the measurement of the grinding surface roughness as well as determining the PVD film heights, see Figure 101b.



a)



b)

**Figure 101** Taylor Hobson 120L Talysurf

**Table 20** Talysurf 120L Specifications

|                  |  |
|------------------|--|
| Traverse Length  | 120mm  |
| Traverse Speed   | 10mm/sec maximum                               |
| Measuring Speeds | 1mm and 0.5mm/sec $\pm 5\%$                    |
| Gauge Type       | Phase Grating Interferometer 1mN force nominal |
| Measuring Range  | 10mm   |
| Resolution       | 12.8nm @ 10mm range                            |
| Straightness     | 0.5 $\mu$ m over 120mm traverse                |
| Accuracy         | 0.2 $\mu$ m over any 20mm traverse             |

### 4.8.3 Microstructure

Sectioning of the machined MQL and MQSL samples revealed the microstructure of the cross-section of the ground samples. The subsurface layers were prepared in the metallographic laboratory, before digitally imaging the structure of the steel grains. These provided evidence with respect to the thermal conditions of the grinding trials, and identified the influence of temperature on the steel microstructure. It was necessary to acquire the detailed imagery of any phase changes in the metallic structure, to assess the suitability and the limitations of the MQL and MQSL processes.

Figure 102 illustrates the regions of interest upon sectioning the steel. The samples were then set in an epoxy resin in order to regularise them for polishing. Once cured several stages of preparation involved numerous grades of abrasive paper, a 6 $\mu$ m diamond paste, and then a polishing silicon colloidal agent. The samples were polished to a mirror finish, see Figure 103. A 2% Nital solution was used to acid etch the surface for 15 seconds, and then neutralised in cold water. This exposes the grain structure of the steel, necessary for the identification of microstructure change, and recorded by the digital microscopy.

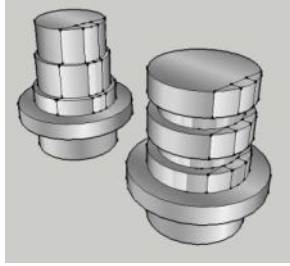


**Figure 102** Illustrating cross sectioning of samples to investigate surface microstructure



**Figure 103** Finished samples. Embedded in resin body, polished and acid etched

#### 4.8.4 Hardness Testing

Vickers micro-hardness measurements were conducted on a Zwick micro-hardness tester. The regime involves applying a force of 4.903N for 10s, see Figure 104. The closest measurable region from the ground surface was 25 microns deep, as edge effects begin to introduce anomalies into the readings. Nine measurements of the micro-hardness indentation (see Figure 105a)) were taken at 25 micron intervals in a staggered array, see Figure 105b). The total depth of measurement amounted to 225 microns. The automated instrument is stated as accounting for a 3% error. This procedure was repeated up to 3 times on each sample to provide a satisfactory resolution within the results.



a)



b)



c)

**Figure 104** Zwick Vickers Micro Hardness Testing station

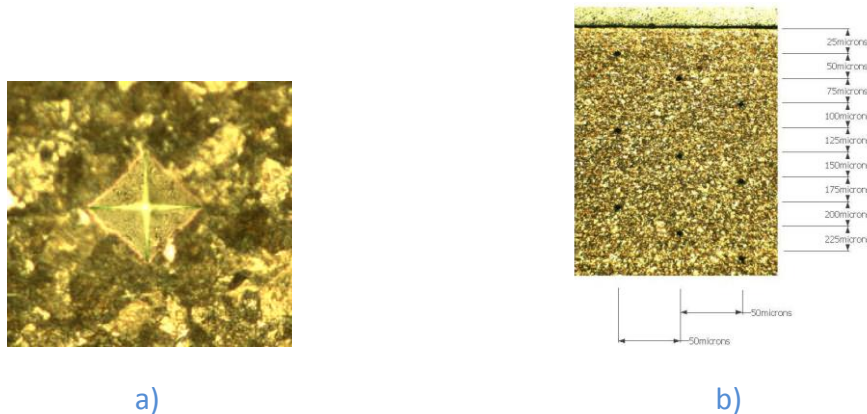


**Figure 105** Vickers Micro hardness testing pattern and regime

The Zwick/ZHV performs micro Vickers hardness tests to ISO 6507, ASTM E92 and certified to UKAS (United Kingdom Accreditation System). Specifications of the instrumentation feature with Table 21.

**Table 21** Zwick vickers micro hardness specifications

|  |   |
|--|---|
| Automatic turret for one-button control of lens/indenter exchange  | Indentec C.A.M.S. Testing System software by Newage TI Inc.           |
| Newage Testing Instruments Controller/Driver   | Automatic conversion to other scales - no conversion tables required. |
| Test scale shown in display  | Manual test weight change   |
| Fully automatic test sequence to predetermined time frame eliminates operator influence during hold time | VMH/HK Knoop hardness   |

## 4.9 Key Messages

The key messages taken from this chapter are:

- MQL and MQSL grinding trials were undertaken using Taguchi factorial designs of experiment. This approach identifies the significance of the machining parameters upon the MQL and MQSL methods through an ANOVA framework (ANalysis Of VAriance).
- At least two repetitions of the trials provide a degree of confidence in the recorded data for use in the analysis of production parameters.
- An L8 orthogonal array was used to explore the variation between high and low levels of 4 machining factors, namely: wheel speed, work speed, infeed speed and quantity of lubricant, as follows.



**Table 22** Key messages: L8 machine parameters

| <i>Factors</i>        | <i>Low</i>                   | <i>High</i>                    |
|-----------------------|------------------------------|--------------------------------|
| Wheel speed           | 75m/s                        | 100m/s                         |
| Work speed            | 0.5m/s                       | 0.6m/s                         |
| Infeed speed          | 0.3mm/min                    | 0.6mm/min                      |
| Quantity of Lubricant | 1% oil or low solid<br>g/min | 10% oil or high solid<br>g/min |

- Labview Signal Express DAQ was used in conjunction with spindle power, fluid flow and fluid pressure sensors to record conditions of the machining process.
- Thermal measurements used PVD coated samples, enabling the isotherm depths to determine the surface temperature of the grinding zone. PVD materials used were; Bismuth, Indium and Zinc metals. They were layered in novel segmented pattern, to simultaneously record the temperatures for a single grind.
- Surface integrity analysis was undertaken including; Barkhausen Noise residual stress detection, surface roughness, microstructure, and hardness.

The key messages from this chapter highlight the parameters associated with the Taguchi experimental method. The collected results from experimental trials and surface integrity analysis are carried forward to inform the development of the tooling and the modelling of thermal behaviour within MQL and MQSL grinding.



---

## 5.0 Thermal modelling

### 5.1 Overview

This chapter describes the modelling approach in the prediction of the final surface temperatures throughout MQL and MQSL cylindrical grinding. These theories link back to the principles explained within Section 2. The thermal properties and machining parameters associated with the machine, the tool and the workpiece are listed as process variables before a complete simulation of the machine tool path is obtained to create the tool-workpiece interaction volumes. A Graphical User Interface (GUI) was created in Matlab in order to process the Specific Grinding Energy of the grinding trials and predict the newly ground finish surface temperature.

A series of ANSYS FEA batch files were written to accept and convert CAD models into volumes for FEA analysis before pre-processing and simulating the thermal patterns of abrasive machining. Grinding wheel tool paths were created in order to realistically predict workpiece interaction ultimately leading to newly formed workpiece component profiles available for thermal loading. The methods of FEA volume creation and meshing are explained, including the settings of the pre-processing thermal loadings.

### 5.2 Method of Analysis

Thermal heat flow predictions were constructed through a combination of Matlab and FEA analysis. ANSYS FEA software is used within this section of research predominantly owing to its industrial relevance, acceptance and commercial availability. However the initial input parameters needed to be defined through Matlab before any analysis could be simulated.

The predictive thermal simulation was refined to be used within an industrial application. This was achieved by developing a fully interactive GUI (graphic user interface) file. The GUIDE interface within the Matlab capability provides a facing window that is able to access to a series of data. By linking the GUI controls to the thermal data tables the surface temperatures and heat flux densities were calculated from existing theory. Several input parameters however needed to be defined in order to successfully run the code, refer to Figure 106.

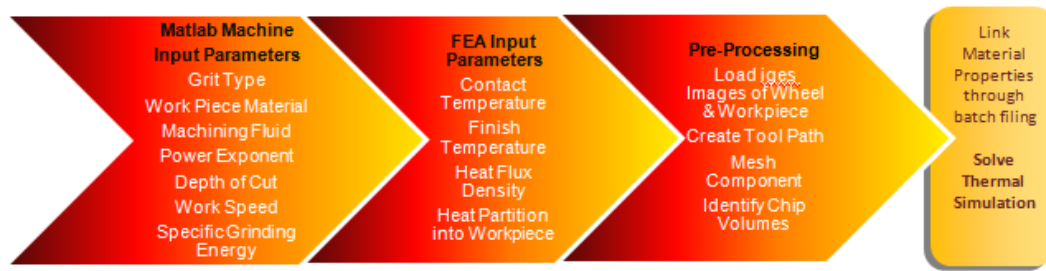


Figure 106 Illustrating the systematic modelling approach necessary for the calculation of the thermal behaviour within cylindrical plunge grinding.

Data sets are accessed by means of a global data system. Material properties such as thermal conductivity, specific heat, density, thermal conductivity and many more are ‘called-back’ and applied throughout the temperature prediction calculations. Table 23 lists the thermal properties established in the GUI global function to be used throughout the thermal simulations.

Table 23 GUI thermal properties of tool, workpiece and fluids (Matweb, 2008; Kaye & Laby, 2010)

| Material               | Thermal Conductivity $k$ | Density $\rho$    |                   | Specific Heat Capacity $c_w$ |        | Thermal Property $\beta$ | Melting Point $T_m$ | Crystal Structure |
|------------------------|--------------------------|-------------------|-------------------|------------------------------|--------|--------------------------|---------------------|-------------------|
|                        | W/m.K                    | g/cm <sup>3</sup> | kg/m <sup>3</sup> | J/g.K                        | J/kg.K | J/m <sup>2</sup> .s.K    | C                   |                   |
| cBN                    | 240/1300                 | 3.48              | 3480              | 0.67                         | 670    | 5.51E+04                 | 3200                | Cubic             |
| Natural Diamond        | 2000                     | 3.52              | 3520              | 0.5091                       | 509.1  | 5.99E+04                 | 3700                | Cubic             |
| 38Mn (low alloy steel) | 46.7                     | 7.83              | 7830              | 0.461                        | 461    | 1.30E+04                 |                     |                   |
| Aluminium Oxide 99.9%  | 46                       | 3.96              | 3960              | 0.753                        | 753    | 1.17E+04                 | 2054                | Rhombohedra       |
| MoS <sub>2</sub>       | 0.23                     | 4.96              | 4960              | 1.7                          | 1700   | 1.39E+03                 | 1185                | hexagonal hP6     |
| CaF <sub>2</sub>       | 9.71                     | 3.18              | 3180              | 0.887                        | 887    | 5.23E+03                 | 1360                | Cubic             |
| Water                  | 0.609                    | 0.998             | 998               | 4.1819                       | 4181.9 | 1.59E+03                 | 0                   |                   |

Figure 107 demonstrates the front face GUI requiring all fields to be entered before initial FEA predictions can be simulated, along with a list of the inputs and outputs variables.

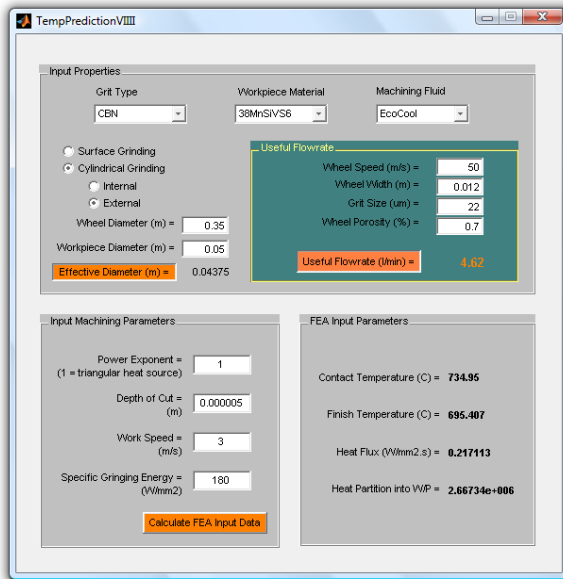


Figure 107 GUI Heat Flux interface window

#### Input Fields of Machining Parameters include:

- Tool;  
Grit type, Dimensions, Speed, Depth of Cut,  
Grit size, Wheel Porosity
- Workpiece;  
Material, Dimensions, Speed, Surface or Cylindrical Grinding (Internal or External)
- Fluid;  
Type

#### Output Fields of FEA Inputs include:

- Effective Diameter
- Useful Flowrate
- Contact temperature
- Finish Temperature
- Heat Flux over chip contact length
- Workpiece Heat Partition Ratio

Once the abrasive machining thermal properties and identities are fully defined from the Matlab this data can be forwarded on to the FEA simulations. Starting with the importation of component geometry through CAD profiles to then simulate and optimise the machining parameters necessary for satisfactory processing.

### 5.3 Geometrical Representation

Original CAD models of the grinding wheel and the workpiece were drawn into a parametric frame work. This allows the geometry of grinding tool profiles to be accurately imaged into Ansys. Ansys does have basic geometrical capabilities to allow shape creation however the inconsistency of lines and arcs can cause severe disruption to loading simulations. Therefore the conversion of CAD files into an Initial Graphics Exchange Specification format (IGES file) provided a more accurate interpretation of the volume of the wheel and workpiece. The script of the lines and the arcs geometries and location was automatically created. Once these were translated the lines, areas and volumes are recognised by the ANSYS FEA, Figure 108.

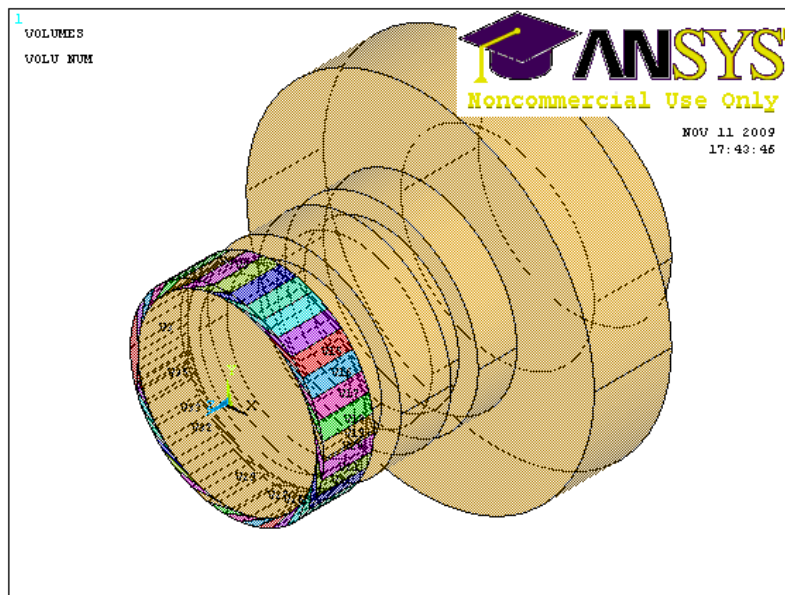


Figure 108 Illustration of chip volumes created from intersecting grinding wheel tool path

## 5.4 Grinding Tool Path

In reality, cylindrical grinding involves the processing of a workpiece about its own central axis. The grinding wheel rotates for cutting and translates relative to a single linear machine axis into the workpiece attaining a depth of cut, creating the final desired geometry. This means that it is difficult and complicated to simulate the grinding process using FEA modelling.

As the workpiece is the focus of the simulation rather than the grinding wheel, a decision was made to lock the rotation of the workpiece and make the grinding wheel move relative to the central axis of the workpiece, Figure 109. Depth of cut per revolution of the workpiece can be included allowing for an accurate chip volume to be created.

The advantage of this approach is to create and capture a series of intersected volumes between the grinding wheel and workpiece that will be identified as removed material i.e. chip formations, Figure 110. The removed chips were then re-pasted, Figure 111, before meshing the volume with transient heat flux values placed upon the workpiece and chip interfacing surfaces, Figure 112.

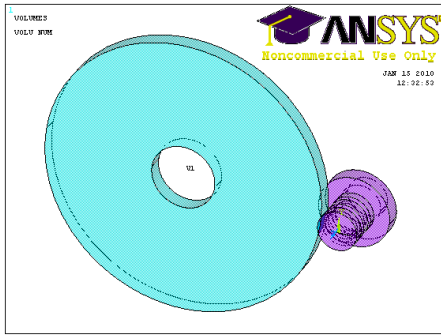


Figure 109 Imported igs files to identify tool path

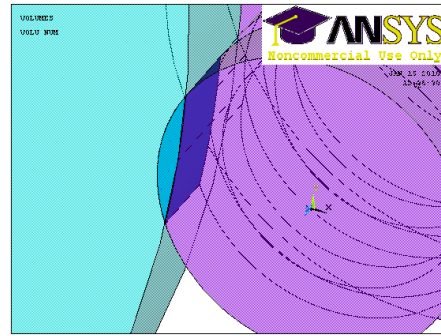


Figure 110 Volume intersection between wheel and workpiece

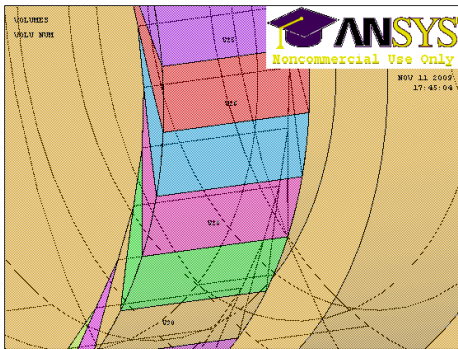


Figure 111 Magnified illustration of chip volumes – demonstrating smooth geometries

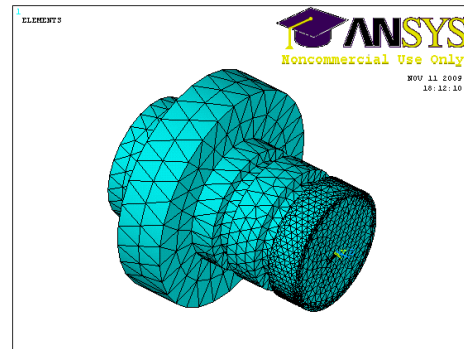


Figure 112 Meshing structure focusing on grinding profile with re-pasted chip volumes

## 5.5 Thermal Properties of 38MnSiV6 – AISI 10267

A set of material properties, and associated units of measurement, were defined in order to combine the CAD data with the ANSYS FEA application. Depending upon the imported scaled conversion of the CAD data the corresponding pre-processing material properties units were matched to the desired scale. Material properties were expressed per metre or per millimetre depending on the scaled image in the ANSYS workspace.

Matching the dimension of the model to the correct material property units dictates the precision of the simulation and is critical to the FEA analysis, see Table 24.

Table 24 AISI 10267 Low Alloy Thermal Properties

| Material Property      | Base SI units           | Technical SI units            |
|------------------------|-------------------------|-------------------------------|
| Modulus of elasticity  | 20.5e10 Pa              | 205000 MPa                    |
| Poisson constant       | 0.29                    | 0.29                          |
| Thermal expansion      | 1.21e-5 K <sup>-1</sup> | 1.21e-5 K <sup>-1</sup>       |
| Density                | 7585 kg/m <sup>3</sup>  | 7.5 e-9 tonne/mm <sup>3</sup> |
| Thermal conductivity   | 46.7 W/m.K              | 46.7 mW/mm.K                  |
| Specific heat capacity | 461 J/kg.K              | 4.61e8 mJ/tonne.K             |

## 5.6 Chip Shape

Grinding chips are rarely wider than the abrasive grains that create them. They are produced in a randomised pattern across the width of the grinding wheel. The FEA simulation however assumes that the chip width is equal to the volume of material removed by a single tool step (the rotational steps of the tool about the workpiece i.e. the iterated tool path), Figure 113 and Figure 114.

At this stage of the research the creation of a generic chip shape is sufficient. However in reality the grain positioning on the wheel periphery removes chips at every stage of the wheel infeed in a randomised pattern. This may be possible to simulate in the future with greater development. This would progress into the Matlab calculated heat flux values to chase the randomly created chip volumes, precisely simulating the abrasive behaviour.

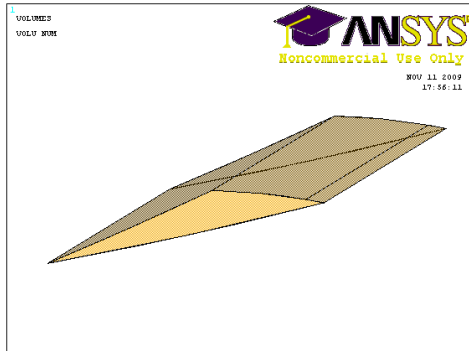


Figure 113 Idealised cylindrical grinding chip volume

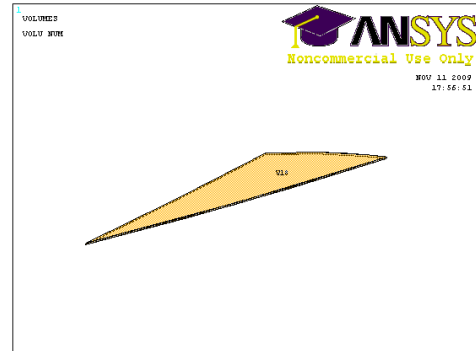


Figure 114 Idealised cylindrical x-sectional chip shape

## 5.7 Thermal Spectrometry

### 5.7.1 Spectrometer Calibration

The spectrometer was verified against the temperature of a steel sample placed inside an oven, see

Figure 115. This was designed to calibrate the optically detectable thermal energy against a series of thermal instruments and equipment.

- The emitted wavelengths of light can be collected by positioning the spectrometer at a sight window on the side of the oven.
- The oven is to be increased over a range from 20-900 degrees Celsius.
- The spectrometer signal is then processed and compared to the temperature readout from the thermostat of the oven, a thermocouple positioned into the core of the sample, and a pyrometer targeted upon the sample surface.



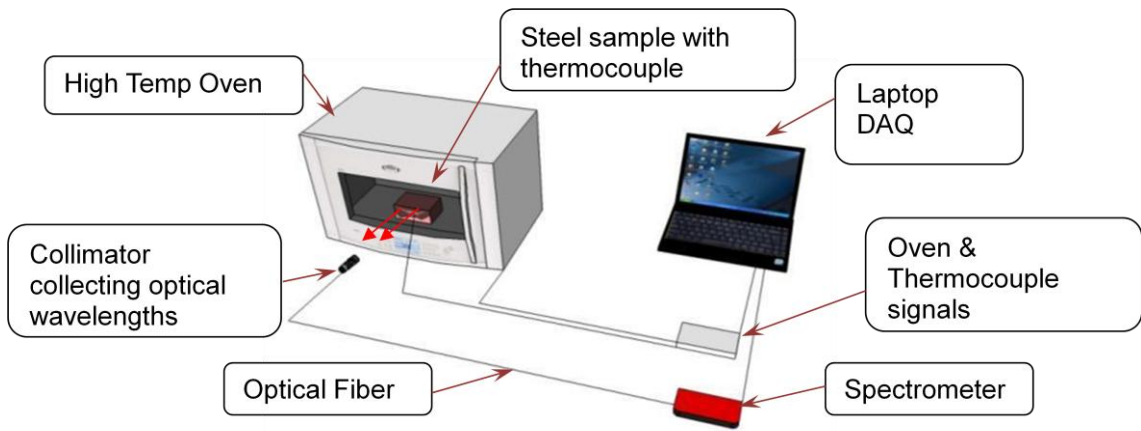


Figure 115 Spectrometer calibration setup

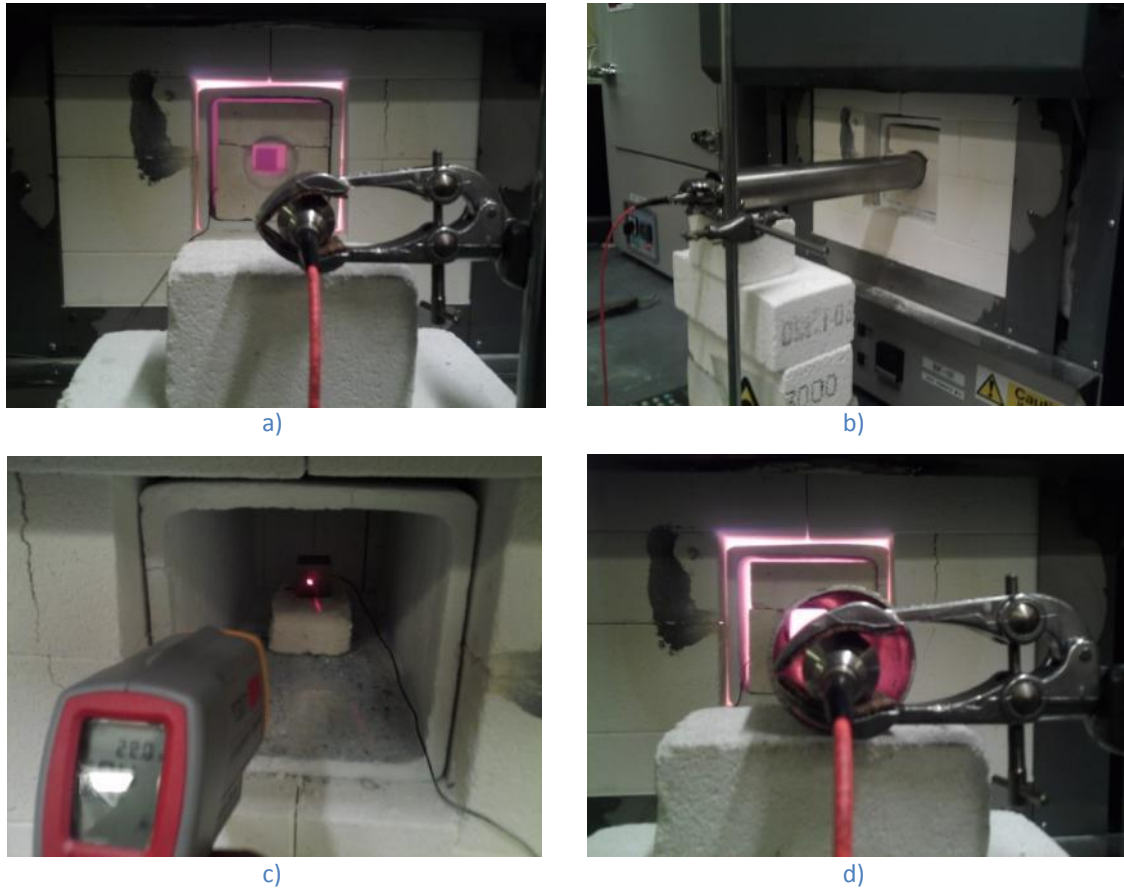


Figure 116 Box furnace images undertaking spectrometer calibration (20-1000 degrees Celsius)

The spectrometer was positioned in front of a box furnace as shown in Figure 116 a) to d). A cube of 38Mn steel (25mmx25mmx25mm) was fitted with a thermocouple and positioned in the middle of the furnace. The temperature of the furnace was gradually increased and the recorded CCD spectrum was mapped against; a signal from the

thermocouple, the thermo couple from the furnace and an additional pyrometer. The CCD device was exposed to the heated steel sample through a “window” in the fire-bricks. This protected the CCD sensor from extended periods of exposure to heat while the temperature of the box furnace was being established. Figure 117 illustrates the spectrum movement around the 500-750nm bandwidth at the elevated temperatures of 900-1000°C. This shift in the peak position with respect to the wavelength and the intensity of the steel reinforced the idea that a relationship could be established between the captured energy from the grinding chip and the finish grinding temperature.

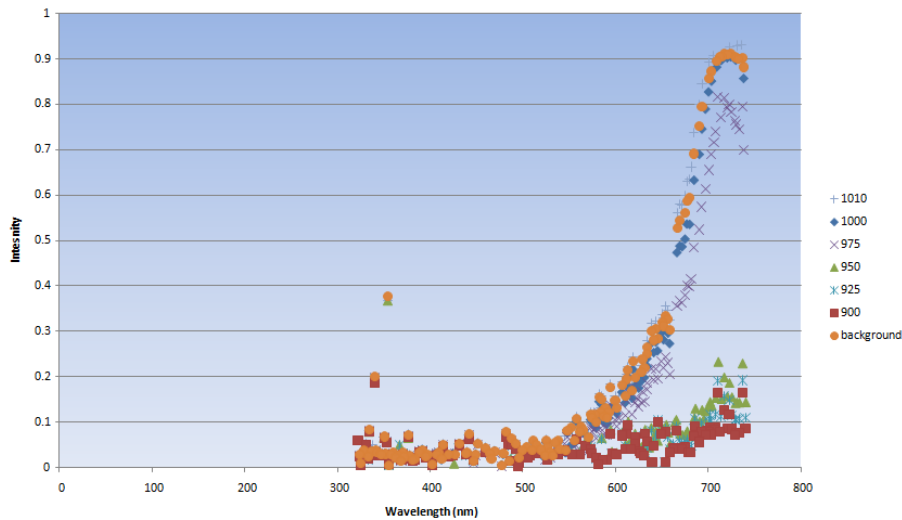
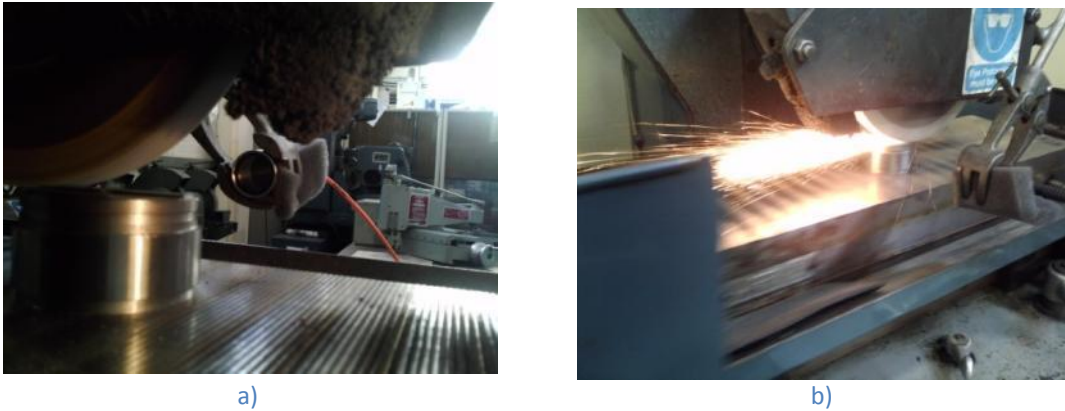


Figure 117 CCD analysis of 38Mn Steel (0-1000C) filtered peaks 10nm bandwidth

### 5.7.2 Machining with the CCD

A prototype CCD setup was installed on the J&S surface grinder in order to establish the CCD device as a practical and beneficial addition to a grinding machine. The surface grinder enabled the easy adjustment of the CCD target position. This identified the limitations of the light capturing instrumentation with respect to the distance and angle of the collimator in relation to the grinding zone. This determined the effective distance needed to capture the energy emitted from the sparks while observing the machine limitations from colliding with the traversing table and providing adequate protection of the lens from encountering molten chips. Figure 118 below illustrates the setup and the intensity of light captured upon preliminary installation.





**Figure 118** CCD positioning on surface grinder a) front view b) rear view

An optical fibre 1m long was used to convey the spark light into the CCD. An example of the CCD reading is illustrated in Figure 119. The greater the depth of cut the more aggressive the conditions producing more heat and therefore hotter sparks. The light intensity can be seen to be growing within the <600nm where the spectrum generally falls within the yellow and red energy wavelengths. This rise in the spectral shape follows from the original findings when comparing against the steel samples in the box furnace and correlates with the expected colours of hot sparks. Figure 119 below shows a clear increase of light intensity captured with the CCD sensor.

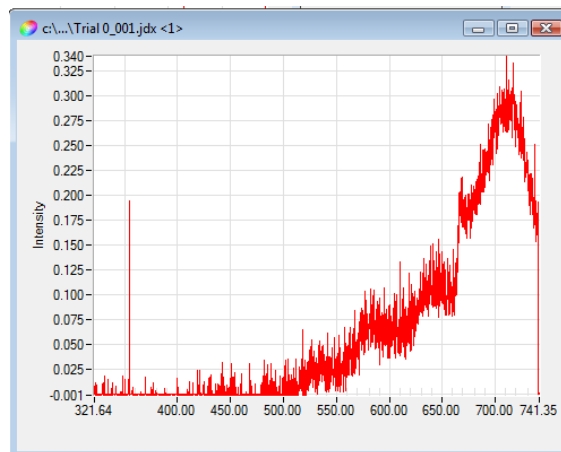


**Figure 119** Response of CCD from surface grinding 38Mn steel ( $a_e = 0.1\text{mm}$ ,  $v_f = 1\text{m/s}$ )

The positioning of the collimator with respect to the trajectory of the spark against the angle of the wheel plane is critical for a successful capturing of the grinding chip energy. To demonstrate the changes in operating effectiveness a surfaces grinds were repeated with various alterations of the collimator angle, see Figure 120. These trials maintained a distance of 100mm from the centreline of the spark trajectory from the grinding wheel. The intensity decreases as the collimator is positioned into a more perpendicular position

with respect to the wheel, Figure 121. Therefore a shallower angle is more desirable upon installation, at least if it is attainable given the existing constraints of the machine (i.e. traverse and crush zones).

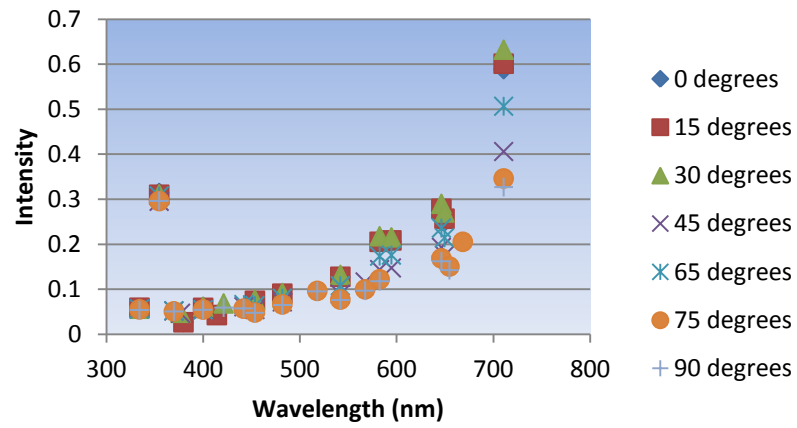


Figure 120 Change in intensity with collimator position (20000ms, 2 gliding average)

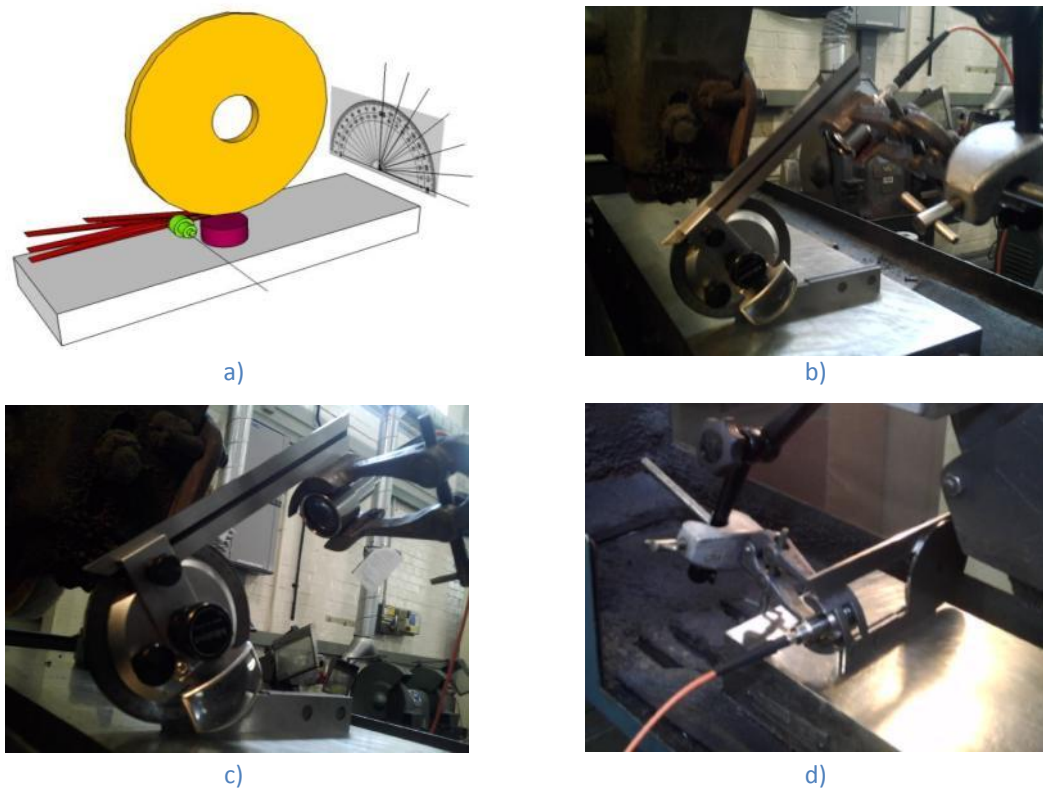


Figure 121 Investigation into CCD positioning sensitivity (a - d)

---

## 5.8 Key Messages

The key messages taken from this chapter are:

- Matlab was used to predict grinding heat flux values based upon grinding thermal theories.
- Data tables are accessed through a Graphical User Interface (GUI). These enabled the structural and thermal properties of the grinding wheel, of the workpiece and of the machining fluid to be selected for simulating the thermal flow throughout the sample depth.
- ANSYS finite element analysis was used to construct the shape of the chips using an idealised grinding chip volume created through a tool and workpiece interacting tool path. The predicted heat flux values from Matlab are then able to be applied to the grinding wheel contact area of the ideal chip volume. Thermal flows originating from the wheel/workpiece contact surface can be simulated by transient thermal flows. This enables the depth of the thermal influence to be measured from the surface. No affect of wheel life and influence by dressing are taken into account when constructing the idealised chip volume.
- Reducing the quantity of fluids within the grinding environment allows the emitted energy from the grinding chips to be detected through a CCD device. The conditions of the grinding process influence the detected peak wavelength and intensity of the chip energy. The detected energy is calibrated as a working chip temperature and is influenced by the positioning of the optical lens and the nature of the workpiece material.

These key messages enable the predicted thermal behaviour within MQL and MQSL grinding to be compared against the experimental results found within the next chapter.

---

## 6.0 Results

### 6.1 Overview

This chapter contains the results and analysis from the MQL and MQSL investigation. The Taguchi experimental method provided a range of output data including the grinding machine power values, the metallographic analysis, PVD isotherm measurement and the optical (CCD device) spectrum recordings (see chapter 4, Table 11 for the Taguchi regimes). The results were interpreted through an ANOVA (Analysis of Variance) method. ANOVA helped to identify the importance of the selected machining parameters with respect to their impact on the performance of the grinding process. The input parameters were assessed through their direct effects and interacting effects on the grinding process. This analysis provides an optimisation of the process parameters of grinding under MQL and MQSL conditions.

The performances of the selected solid lubricants were measured with respect to; the power consumption of the grinding cycle, the Specific Grinding Energy, the surface integrity and temperature of the ground workpiece. The surface integrities were examined and compared with measured and modelled grinding temperatures. This knowledge was carried forward to establish a relationship between the optical grinding energy of the chip and the surface temperature of the workpiece.

### 6.2 EcoCool<sub>(MQL)</sub> Trials

#### 6.2.1 EcoCool – Power Consumption

Preliminary trials established the MQL baseline control data. EcoCool machining fluid was used as the control fluid against which to compare the performance of the solid lubricants. This provided machining results using the MQL Useful Flowrates principles as outlined in Chapter 4,

Table 13. Results were also obtained for specified variations in the percentage of EcoCool oil concentration.

The MQL delivery flowrates are a combination of the EcoCool oil emulsified mixed with the local mains water supply. The water supply was from the workshop main supply pressure and the chemical analysis of the water is shown in the Appendix A – Material Properties. The workshop mains water pressure was 2.1bar. EcoCool is an industrially available machining fluid product that contains no phenols, sodium nitrates and other additives that are potentially harmful to the environment. EcoCool is designed to have a long and effective sump life performance. It is also designed to possess increased lubricity, a property that makes it a suitable machining fluid for the MQL trial.

The grinding power consumption values were recorded directly from the grinding machine, through the use of a Hall Effect device. Figure 122 shows the stability of the machining power curve of a cylindrical plunge grind. This was recorded through the duration of an EcoCool MQL cylindrical plunge with the B80 vitrified grinding wheel and 10% EcoCool oil concentration. The power readout shows the rise in power consumption at the point where the grinding wheel comes into contact with the workpiece. The gradient of the power curve at the first point of contact is a combination of the development of the length of the chip, and a reaction of the machine spindle drive against the inertia of the grind. The plateau of the power curve demonstrates a consistency in the grind that is moving towards ('in-feeding') the desired depth of cut. Once the chip length is established, however, the power required is relatively constant. Initial fluctuations in the power signal are attributed to slightly out-of-roundness of the workpiece. Once the grinding wheel has reached its programmed depth of cut, the grinding wheel is left rotating at the depth for 5 seconds. This dwell period allows the associated power consumed by the machining fluid to be calculated, known as the sparkout power.

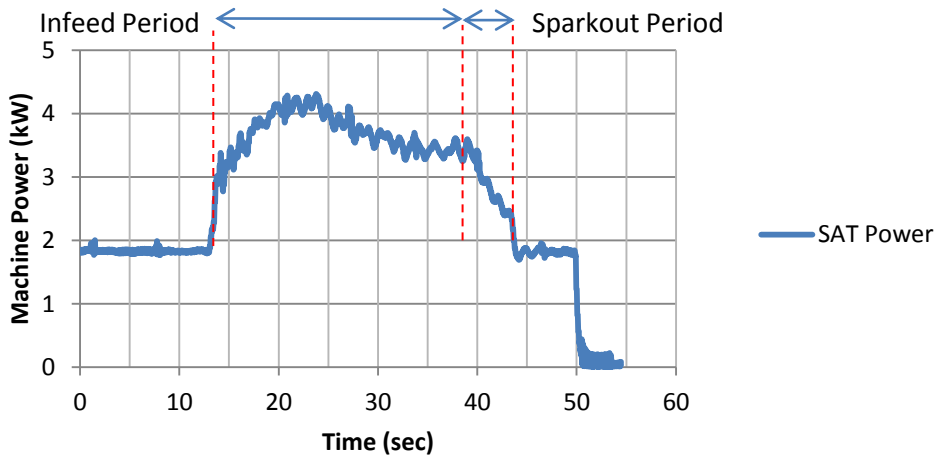


**Figure 122** Vs 100m/s,  $V_w$  0.5m/s,  $V_f$  0.03mm/min,  $A_e=25\mu\text{m}$ , 10% EcoCool Emulsion, 38Mn Steel, B80 Vitrified cBN wheel

The equivalent chip thickness ( $h_{eq}$ ) and the Specific Grinding Energy (SGE) were used as indicators of the efficiency of the grinding process. The  $h_{eq}$  defines the size of the chip and severity of the grinding process. The function of the lubricant was to reduce the specific grinding energy needed to form and release a chip from the surface of the workpiece. An example of the relationship between Net power and SGE with changes in  $h_{eq}$  is illustrated in Figure 123. There is an inverse relationship between chip thickness and specific grinding energy, as more energy is required to produce smaller chips. This confirms the size effect of the chip thickness. The faster in-feed rates ( $v_f$ ) produce larger chip thicknesses, and therefore require more grinding power. Increasing the material removal rate of the workpiece is associated with a reduction in

the SGE. However for a given chip thickness a reduction in the SGE is also associated with a lowering of the risk of thermal damage. Therefore the MQL application of EcoCool achieved its lowest temperatures at the higher chip thicknesses (higher  $v_f$ ). However, the critical aspect of finish grinding, is the ability to control the process temperatures at the smaller chip thicknesses, and therefore control the surface integrity.

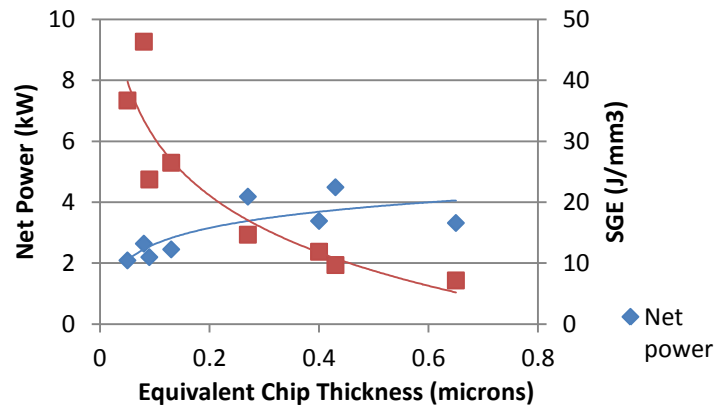


Figure 123 Changes in Net Power and SGE over a variation of equivalent chip thicknesses  $h_{eq}$

The ANOVA main effect charts, plot the gradients between the high and low levels of the machining parameters. The significance of the machining parameter can then be determined by the gradient and position of the ANOVA lines. For example Figure 124 and Figure 125 indicate that the percentage of EcoCool is of a great significance on the net power of a plunge. The ANOVA plots provide the necessary data to begin to optimise the MQL machining process. From the plots below the relationships between the variations in the levels can be selected in order to reduce the SGE values. The 10% oil content decreases the SGE from the grinding cycle, as was expected.

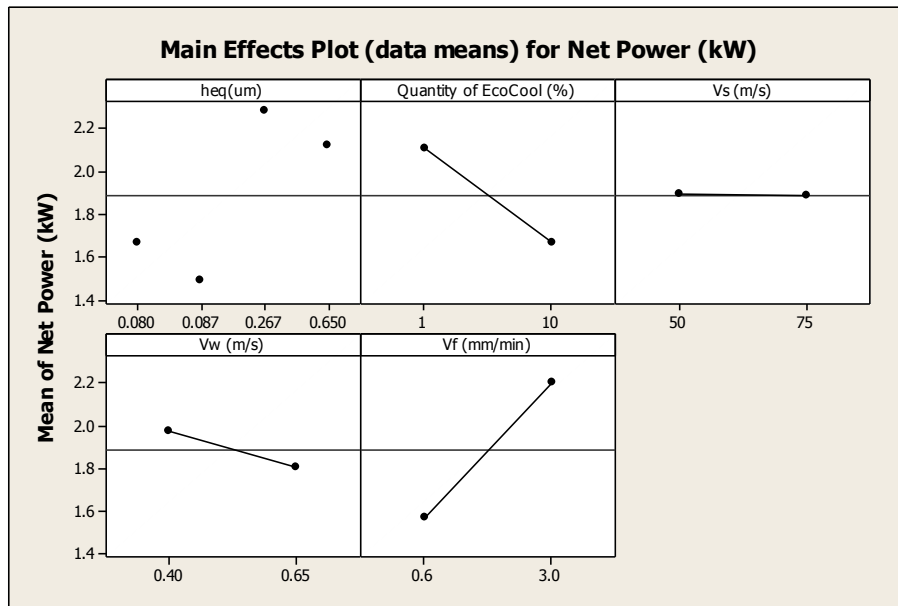


Figure 124 Main effects on Net Power for EcoCool(MQL) input parameters

The conclusion from this is that an optimised selection of machining parameters would include the high levels of; the oil concentration, the grinding wheel speed, the workpiece and the infeed. This suggests that the MQL system with a high quantity of oil operates at its most efficient under large chip thicknesses.

The interaction plots provide an insight between machining parameters. Figure 126 and Figure 127 show the ANOVA interaction plots of the Net Power and the SGE respectively. The ANOVA interaction plots illustrate the relationships between parameters through the direction of the gradients. To verify that the ANOVA analysis was working correctly the ANOVA interaction plot in Figure 126 shows some simple relationships. For example, that there is no gradient and therefore no-dependence between the concentration of EcoCool and the wheel speed ( $V_s$ ). This is known to be correct, as the two levels of oil concentration are completely independent of the wheelspeed.

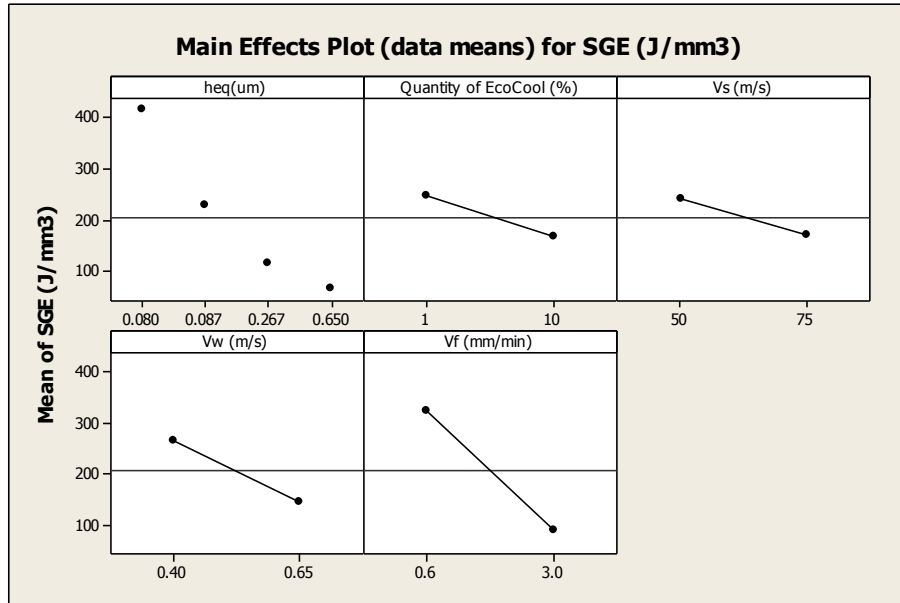


Figure 125 Main effects on Specific Grinding Energy (SGE) for EcoCool<sub>(MQL)</sub> input parameters

A difference in the ANOVA interaction gradients indicates a relationship, no matter how small. For example the concentration of the EcoCool influences the power consumption with respect to work speed ( $v_w$ ). Here a higher percentage of oil (10%) causes a rise in power consumption with a higher work speed. This is attributed to the larger mass of fluid that is required to pass through the grinding zone. Interestingly a 1% oil emulsion with an increase in workspeed reduces the power consumption from 2.4kW to 1.85kW. The concentrations of the oil at both levels consume similar values of power at the higher workspeed. This suggests that at the higher workspeed the 1% oil concentration is the most efficient, which is beneficial towards MQL theory.

The infeed speed ( $V_f$ ) shows a positive interaction with the percentage of EcoCool with respect to SGE however, see Figure 127. This demonstrates that increasing the infeed speed (increasing the chip thickness) responds less to an increase in the concentration of oil. This implies that the factor of lubrication becomes less important at the larger chip thicknesses. The faster infeed relates to the larger chip thickness and results in lower SGE, the principle behind HEDG grinding. The greatest change in power consumption is seen by the variation in equivalent chip thickness against the quantity of EcoCool. This provides some evidence into the smaller thicknesses being assisted by the increased concentration of oil. The increase in chip thickness improves the SGE values, as they fall from  $240\text{J/mm}^3$  to  $175\text{J/mm}^3$  resembling a 28% decrease in SGE, a significant influence on the surface temperature. With respect to the efficiency of the grinding cycle the importance of the oil content is similar to a change both the grinding wheelspeed and the workpiece speed. This suggests that an 10% increase in oil content equates to a 50% increase in wheelspeed (50m/s to 75m/s).



The reduction in the concentration of EcoCool and a reduction in the infeed speed reduce the net power consumption by 22%, from 2.1kW to down to 1.65kW. This is again attributed to the benefit of lubricating the smaller chip thicknesses. Similar trends or influences are then hoped to be achieved through the introduction of solid lubricants.

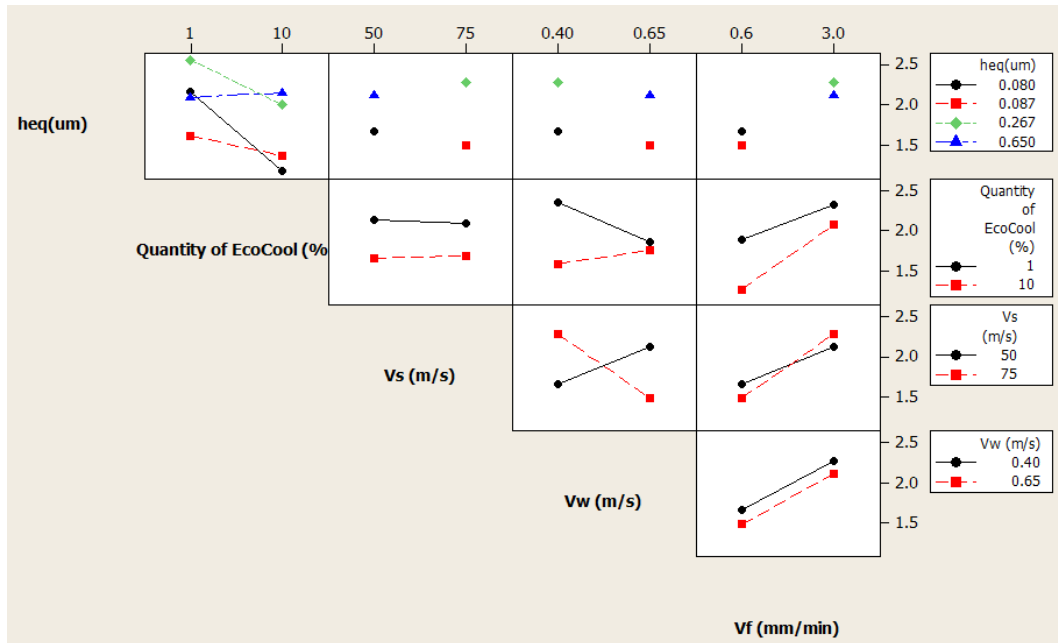


Figure 126 Interaction of all variables on Net Power (kW), EcoCool<sub>(MQL)</sub>

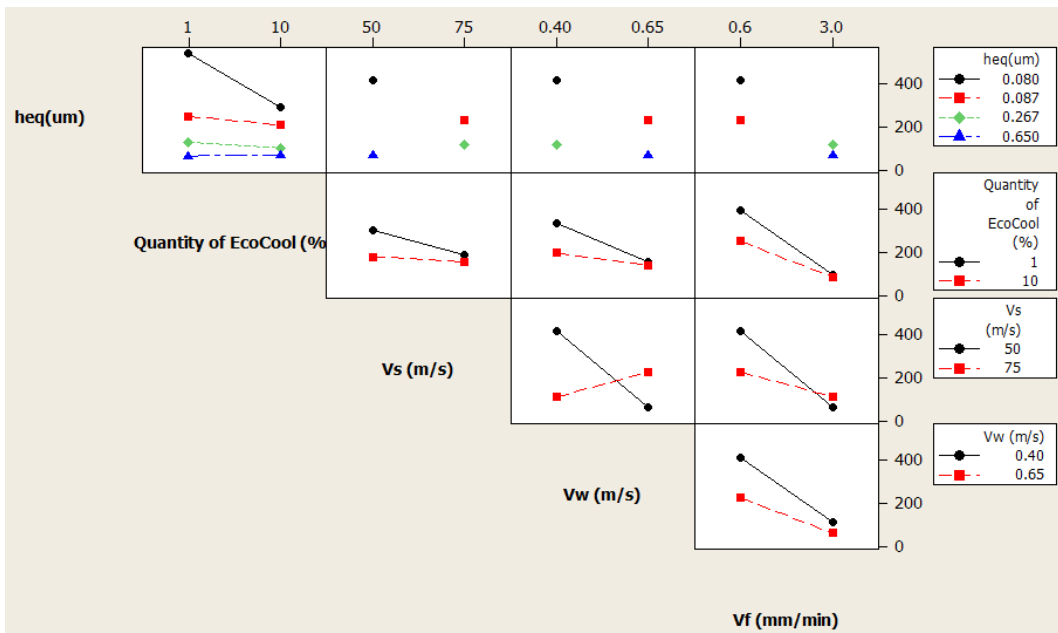


Figure 127 Interaction of all variables on Specific Grinding Energy (J/mm<sup>3</sup>), EcoCool<sub>(MQL)</sub>

Figure 128 is an enlarged interaction plot of the SGE relating to the equivalent chip thickness. This plot highlights the influence that the concentration of oil has on the SGE values, over the range of chip thicknesses. The plots show a tendency for the larger  $h_{eq}$  values to have the lowest SGE values. This is already known to be the case. However the gradient of the ANOVA plot indicates the significance of the lubrication of oil in the smaller chip thicknesses. For larger chip thicknesses the SGE is not sensitive to an increase in oil content. This effect, when varying the concentration of EcoCool oil in the MQL fluid, was consistent throughout the selection of grinding wheels used within this research. Auxiliary results are found in the Appendix section B.

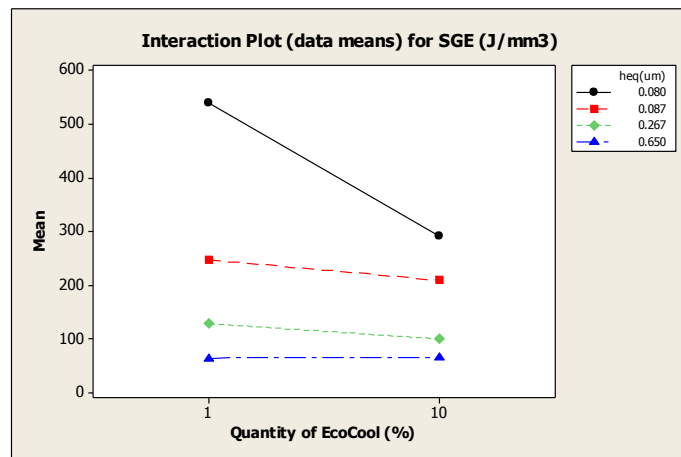


Figure 128 EcoCool<sub>(MQL)</sub> interaction with SGE with respect to  $h_{eq}$

## 6.2.2 EcoCool – Surface Integrity

Microstructural investigation of the samples was required to reveal any damage to the surface caused by an exposure to elevated process temperatures. The selected samples were sectioned, polished and acid etched in order to expose the material grain formations on and under the newly ground profile surface. The key indication of damage to the subsurface layer is if a white layer of untempered martensite is clearly visible upon microscopic inspection once acid etched.

Distinctions can be found when inspecting the samples exposed to the lower levels (1% oil) and higher levels (10% oil) of EcoCool. The Dosatron system had a maximum mixture concentration of 10% oil. The level of 10% oil provided the highest quality from the microscopy images; see Figure 129 and Figure 130. However the purpose of this investigation is to minimise the additives within the machining fluids. Therefore the sample microstructure with a 1% oil mix is of more importance for this research. Figure 131 illustrates that the reduced supply of lubricant or coolant is beginning to promote elevated grinding temperatures on the surface of the sample. A criticism of the Taguchi experimental design at this point recognises that under normal

circumstances the extreme combinations of the machining conditions would not be recommended. The extreme higher levels of the infeed speed and wheel speeds would provide a higher risk process. However for the purpose of research the choice of parameters considers a wide range of operating conditions; providing high quality grinding conditions through to severe burning conditions. As a comparison, trials using the extreme lower levels applying water-only and dry-grinding conditions feature in Figure 132.

Generally the EcoCool maintains a healthy microstructure throughout the various abusive grinding regimes. Certainly with the higher (10%) concentrations of EcoCool there appears to be no thermally induced microstructural damage. The surface is free of burn and the grains appear consistent throughout the depth of the sample. In comparison the lower (1%) concentrations were showing signs of thermal stress, and begin to influence the structure. The 1% EcoCool flow may be too low a quantity of machining fluid to guarantee a stable surface microstructure.

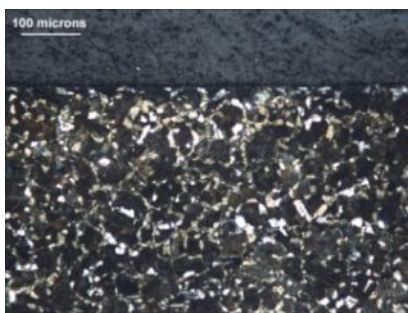


**Figure 129** Trial 2 EcoCool %10 oil Low level combinations of feeds and speeds

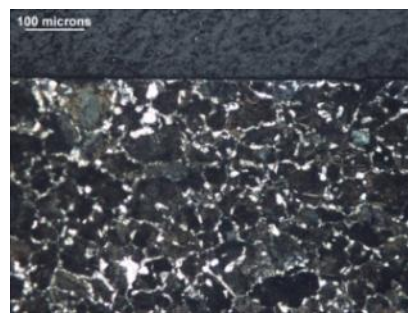


**Figure 130** Trial 8. EcoCool %10 oil High level combination of feeds and speeds

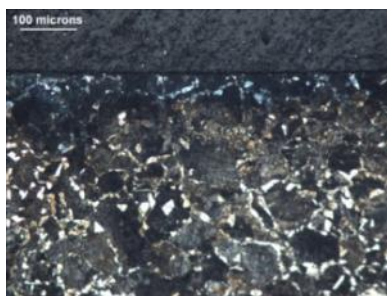


**Figure 131** Trial 4, EcoCool 1%oil

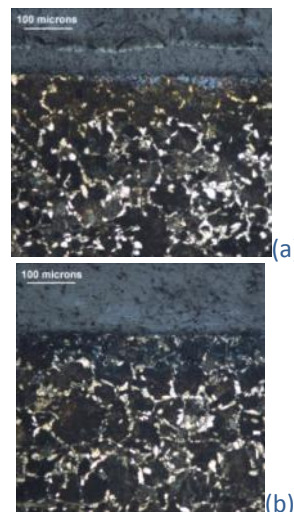


**Figure 132** (a) Water only and (b) Dry Trial EcoCool

Therefore the effectiveness of the useful flowrate theory may need to be adapted to take into account the concentration of machining oil, and not completely depend upon the actual volume of fluid passing through the grinding zone. Oils generally possess reduced viscosities that may also affect the MQL useful flowrate. This is particularly relevant as it may then be possible to achieve flowrates lower than the theoretical useful rate, and achieved through the application of more effective lubricants. However as noted earlier, the action of lubrication is required at the smaller chip thicknesses.

The properties of roughness and roundness are critical to the functionality of most cylindrical components. The intended use for MQL technologies would predominantly be within semi and super finish grinding requiring the use of a finer graded vitrified bonded wheel. Therefore a cBN B90 wheel was used to provide high quality ground finishes between the range of  $0.3\mu\text{m}$  and  $0.5\mu\text{m}$   $R_a$  (centre line average), and looking for results of  $R_t$  (peak-to-valley) between  $2\mu\text{m}$  and  $4\mu\text{m}$  (also known as Grade N4 and Grade N5 surface finishes). Figure 133 and Figure 134 indicate the surface roughness values as an average over the repeated trials. On first impression the results are within the expected ranges. The  $R_a$  values are under control throughout the various parameter variations. The ANOVA plots in Figure 135 and Figure 136 reveal that there is a positive trend between the improvements of the surface roughness values of  $R_a$  with the higher quantities of EcoCool. The  $R_t$  values featured within the desired range of values however they do appear close to the expected limit, and degraded with an increase in the grinding wheel speed. The variation of the chip thickness dramatically affects these readings, so fluctuations were expected. The water only and the completely dry trials provided a comparison showing extreme low values of wheelspeed, workspeed, and infeed speed and feature as trials number 9 and 10 respectively.

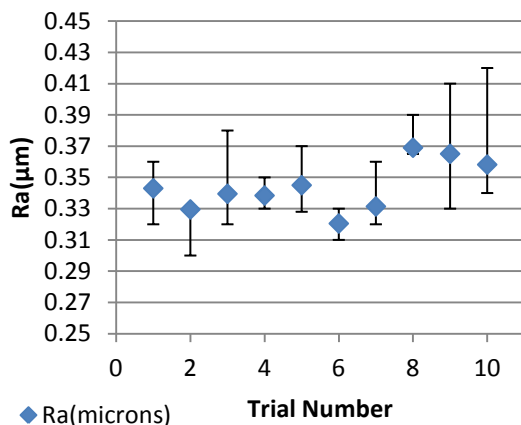


**Figure 133** EcoCool<sub>(MQL)</sub> Surface Roughness Ra, Trials 9 and 10 are the water-only and dry conditions

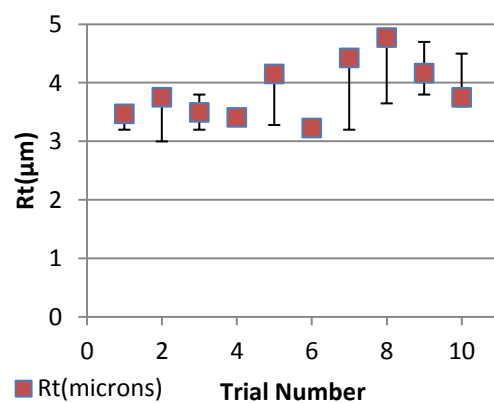


**Figure 134** EcoCool<sub>(MQL)</sub> Surface Roughness Rt, Trials 9 and 10 are the water-only and dry conditions

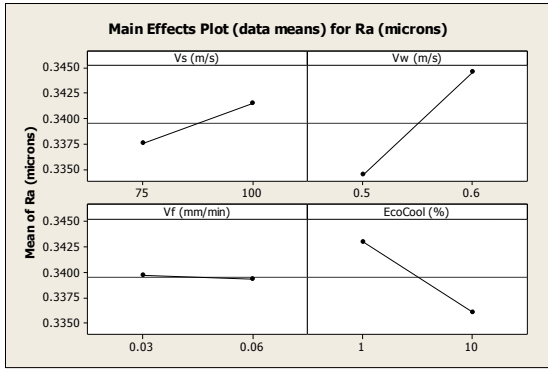


Figure 135 ANOVA EcoCool Surface Measurements Ra

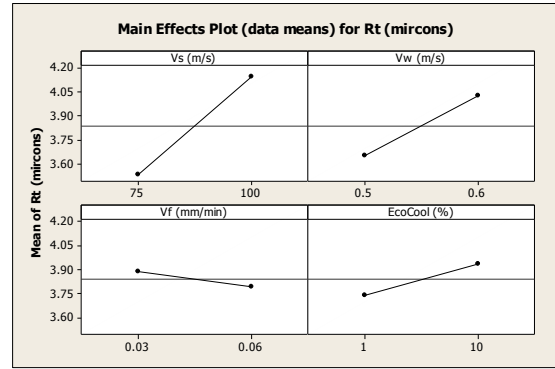
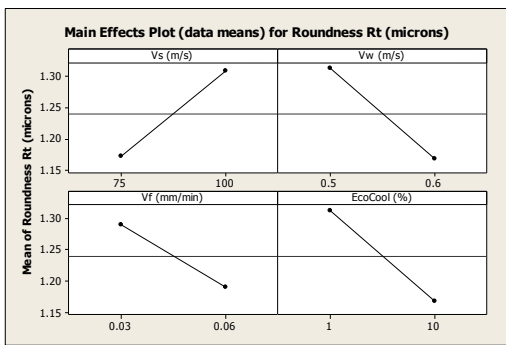
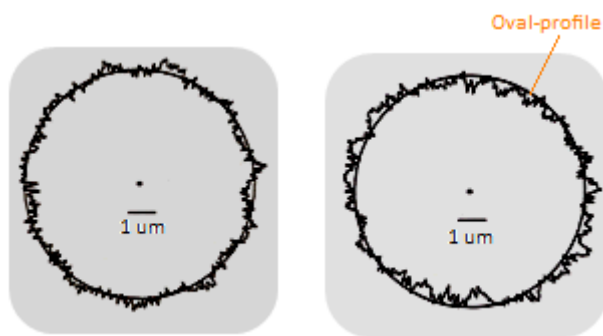


Figure 136 ANOVA EcoCool Surface Measurement Rt

The samples were scanned for roundness on the Talyscenter, prior to sectioning. Figure 137a) illustrates the ANOVA main effects plot illustrating the significance of  $v_s$ ,  $v_w$ ,  $v_f$  and the quantity of lubricant on the roundness. Over the range of chip thicknesses  $h_{eq}$ , an increase in the quantity of emulsified oil to 10% improves the peak-to-valley readout. The roundness analysis improves about 0.15microns  $R_t$ . The added lubrication between the grinding wheel and the workpiece provided by the 10% oil, results in a higher quality surface integrity. In comparison to the water only (zero content of oil) the oil improves the surface roughness  $R_t$  by 14%. Figure 137 b) and c) are examples of the roundness scans. These are from two extreme conditions a) being Low levels of  $V_s$ ,  $V_w$ ,  $V_f$  and high % EcoCool and b) featuring high levels of  $V_s$ ,  $V_w$ ,  $V_f$  with a low % EcoCool. Both produce roundness within the desired range with no damaging indication of loss of form.



a)



b)

c)

Figure 137 Roundness readouts for EcoCool a) ANOVA main effect plot, and examples of extremes; b) Trial 2 Low settings c) Trial 8 High settings (featured scale: 1um)

The data from the roundness measurements feature in Figure 138. This shows the variation in the roundness values between the two extreme trials of 2 and 8. Trial 2 manages to achieve the lowest  $R_t$  value, while the later Trials with increased wheel speeds demonstrate a worsening of the roundness conditions. Included in the chart are the peak to valley measurements for the water only and the dry only grinding

passes of Trial 2, showing the detrimental effect. The increased ‘out-of-roundness’ with the water only is thought to be created by the hydrodynamic effects of a fluid within the grinding zone. Therefore the significance of lubrication on the component form is proven to be more advantageous when; the infeed speeds are low, the chip thicknesses are smaller and the concentration of oil within the emulsion is highest.

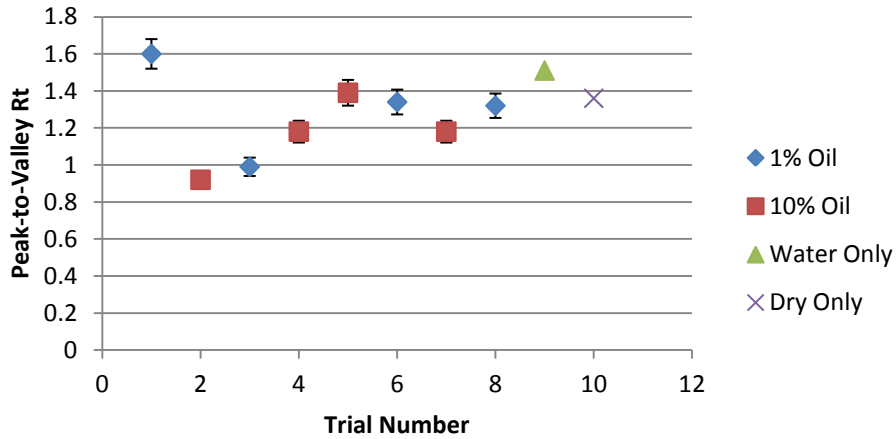


Figure 138 Roundness measurements in comparison to water only and dry conditions

Figure 139 illustrates a complete set of Barkhausen Magnetic Noise (BN) readouts for the EcoCool. The horizontal axis represents a 0-360 degree rotation of the cylindrical surfaces ground by the SAT machine. The gain settings of the magnetic signal generator resulted in the detected BN signals appearing to be relatively close. On closer inspection however the higher quantity of EcoCool added to the emulsion provides a reduced BN signal resulting in a more compressive residual stress. The influence of the emulsified EcoCool oil content is illustrated in the ANOVA main effects plot, illustrated in Figure 140. Out of the four selected machining parameters only one managed to control the residual stress conditions under faster grinding. The magnetic scans from the grinding wheelspeed, workspeed, and infeed speed all indicate that the residual stresses were less compressive with faster conditions. However by increasing the concentration of EcoCool the residual stresses could be made more compressive, which is more desirable with respect to the surface integrity. The interactive plot shown in Figure 141 again implies the chip thickness is the most important parameter with respect to the success of MQL. The relationship between lubrication and the grinding chip thickness became more prominent. The BN scans and the trends in SGE suggest that there may be a link with the chip formation process which may also depend on the open porosity on the surface of the wheel. There needs to be sufficient movement of both the machining fluid and the deformed workpiece material within the gaps between the abrasive grits, in order to achieve a successful formation of a chip.

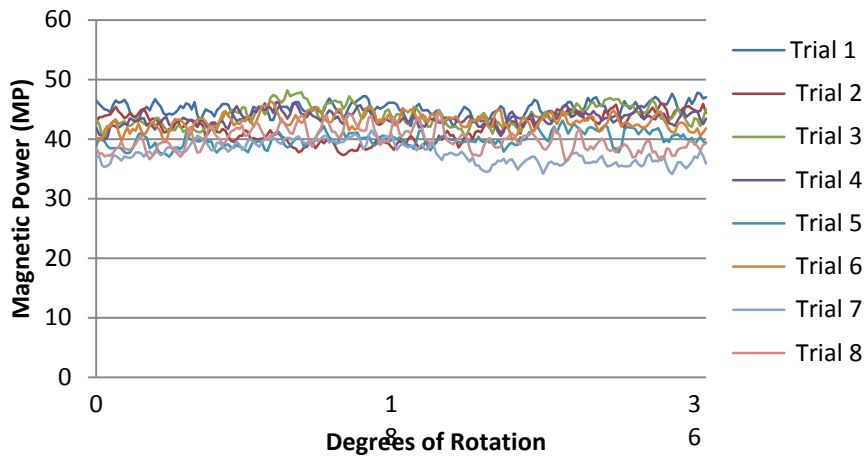


Figure 139 Barkhausen Magnetic Noise EcoCool: Complete Taguchi trial 360 degrees of sample rotation

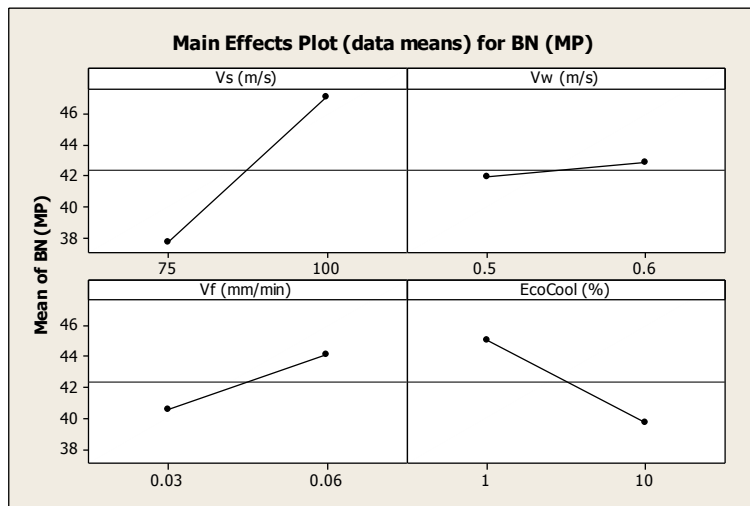


Figure 140 Main Effect of 1% - 10% EcoCool in the fluid system with respect to the surface residual stresses (Barkhausen Magnetic Noise)

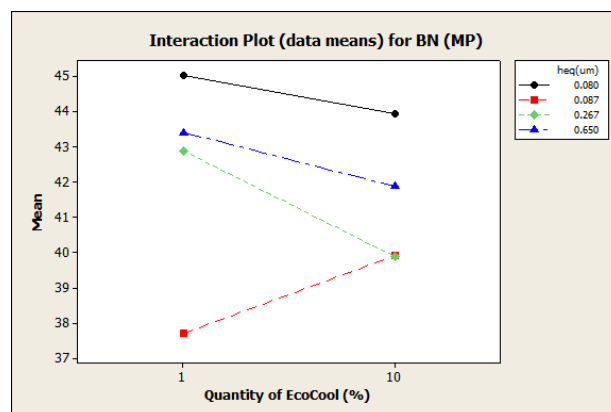


Figure 141 EcoCool<sub>(MQL)</sub> BN Readout

Figure 142 illustrates a series of trials repeating the Taguchi experiment under dry conditions. This trial was a replication of the L8 Taguchi experiment but under

completely dry conditions. In actual fact the test was aborted half way through so not to cause permanent damage to the tool, and to cease burning the sample surfaces. These samples provided the baseline burning conditions for the Barkhausen noise comparison. Large fluctuations in the BN signal indicated the damage to the surface integrity, most likely resulting from the chatter marks influencing the magnetic sensor.

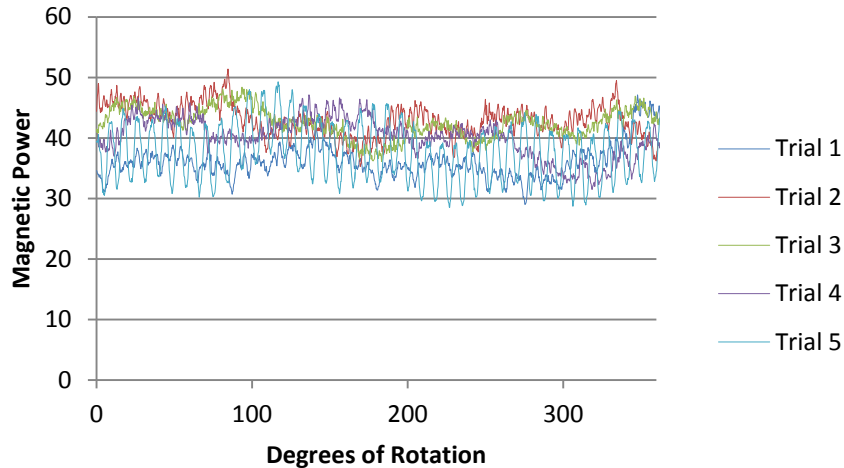


Figure 142 Control surfaces; Dry & Burnt Surfaces BMN

Overall, the EcoCool trials provided the baseline data from which to compare the performance of the solid lubricants. Nevertheless the most important feature from these trials was the link between the chip thickness and the SGE and surface integrity values. This suggests that greater lubrication is required at the smaller chip thicknesses to maintain the surface integrity, that promotes a convincing argument for MQL methods, and which will be beneficial towards the semi-super finishing grinding regimes.

## 6.3 MoS<sub>2</sub>(MQL) Trials

### 6.3.1 MoS<sub>2</sub> – Power Consumption

The experiments progressed onto the MQL trials of MoS<sub>2</sub>. The MoS<sub>2</sub> was carried into the grinding zone by utilising the ‘useful flowrates’ of fluid principle. The ‘Design 1’ solid lubricant delivery system was introduced for the initial MQL experiment setup. The range of the MoS<sub>2</sub> powder feeder was measured for its minimum and maximum flowrates, Figure 143. The MQL values of useful flowrates were matched to the wheelspeed while the concentration of solid lubricant was varied over a range of 0-13.2g/min.



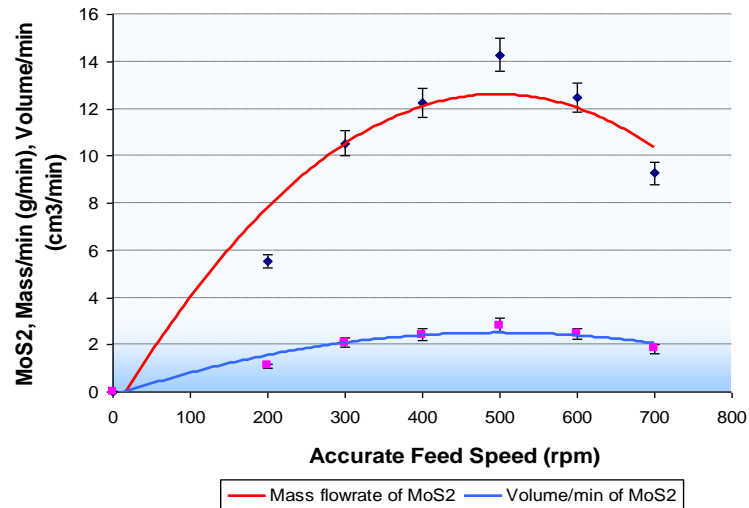


**Figure 143** Mass flowrate and volumetric flowrate of MoS<sub>2</sub>. Demonstrating the maximum mass flowrate at 13.2g/min feed rate. This provided the high level in the Taguchi trials.

An even and consistent distribution of the MoS<sub>2</sub> was visually evident. The useful flowrate of water was silvery in appearance from the combination of MoS<sub>2</sub>. The design of the nozzle allowed a smooth layer to be applied onto the periphery of the grinding wheel. This was recognisable at slower grinding wheel speeds. At the higher wheel speeds it was more difficult to identify but there were no blockages within the working delivery system. This resulted in a successful and well contained supply of solid lubricant. Efficient extraction of the waste lubricant was collected by the encasing shroud, and removed by the vacuum system.

Initial data from the high level values of MoS<sub>2</sub> (13.2g/min) resulted in extremely high recordings of the power consumption, see Figure 144. This was a great disappointment. On closer inspection it was noted that the actual surface of the vitrified bonded cBN grinding wheel was completely layered and clogged with MoS<sub>2</sub>. This proved two things; firstly that the powder feeder was working, and secondly that the extreme ratio of MoS<sub>2</sub> was too high to provide any benefit to the grinding process. A compacted layer of MoS<sub>2</sub> was blocking the abrasives from penetrating the workpiece material. This deemed the wheel ineffective and resulting in abnormally higher specific grinding energies. These higher energies were due to the wheel effectively rubbing the workpiece in order to create the desired geometries. This was creating an increase in thermal energies.

As a consequence, the trial was repeated with a narrower range of MoS<sub>2</sub> flowrates, to prevent the wheel from clogging. The second design of the solid lubricant feeder was installed; Design 2. This was mounted into the machine to enable extremely precise quantities of sold lubricant at the lower mass flowrates of delivery. The useful flowrates of water were applied under the same conditions as before. The reduction in

solid lubricant was to encourage the chips to form and the solid lubricant to be ejected once utilised. This would provide less clogging and result in ‘free’ cutting conditions, whilst enabling the fresh solid lubricant to be taken into the grind zone. This phenomenon suggests the need to establish a maximum volume of powder that the wheel is capable of working with. This would be defined as the ‘equivalent solid lubricant useful flowrate’ that is dictated by the profile and structure of the grinding wheel. It should be noted that the current profile of the wheel was 13mm wide. The profile of the wheel was flat and this investigation assumed complete coverage of the wheel width with the solid lubricant, enabled by the MQSL nozzle. The simple geometry of the plunge grinding wheels remained consistent throughout the trials, enabling a degree of confidence when comparing between the empirical results and the thermal modelling.

Figure 145 shows the main effects of the machining variables produced from the reduced range of MoS<sub>2</sub> levels (MoS<sub>2</sub>, 5.5g/min - 9.5g/min). The conditions of grind were more stable and the wheel was subjected to less clogging at the higher level of 9.5g/min federate of MoS<sub>2</sub>. The interaction of the machine parameters with regards to the power consumption are shown in Figure 146, while a reduction in the SGE can be seen through an interaction effect between the MoS<sub>2</sub> and the variation in the infeed speed  $V_f$ , see Figure 147. The conditions of either high  $V_f$  and high MoS<sub>2</sub> or low  $V_f$  and low MoS<sub>2</sub> indicate a direct dependence on the volume of MoS<sub>2</sub>. This showed that the lower level of MoS<sub>2</sub> was needed to control the SGE against the higher infeed rate  $V_f$ . The higher infeed rates produce higher contact forces between the wheel and the workpiece and the MoS<sub>2</sub> can perform extremely well in high pressure environments. This relationship however demonstrates the ability of the higher level of MoS<sub>2</sub> to reduce the SGEs at the lower infeed. Therefore the effect of additional lubrication is recognised as being more beneficial at the smaller chip thicknesses.

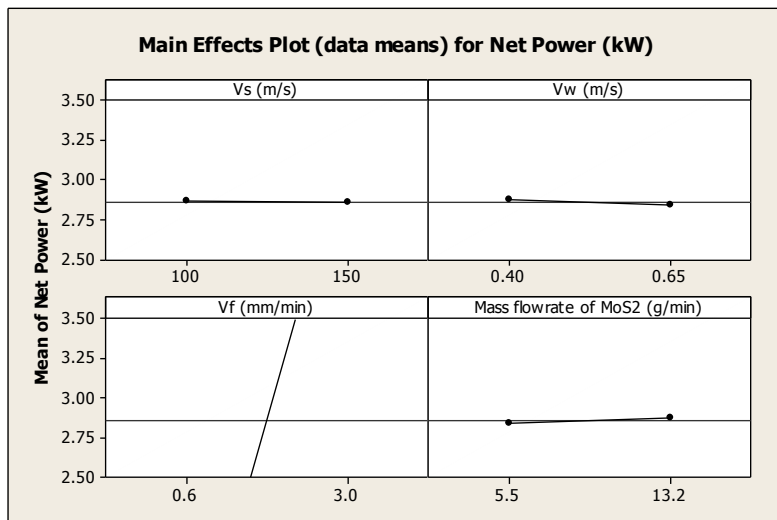


Figure 144 Main effects on Net Power for MoS<sub>2(MQSL)</sub> input parameters (5.5-13.2g/min MoS<sub>2</sub>)

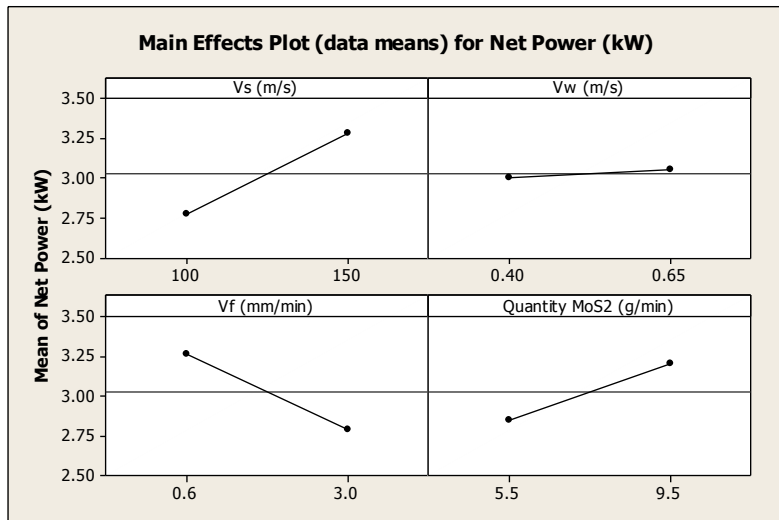


Figure 145 Main effects on Net Power for MoS<sub>2</sub>(MQSL) input parameters (5.5-9.5g/min MoS<sub>2</sub>)

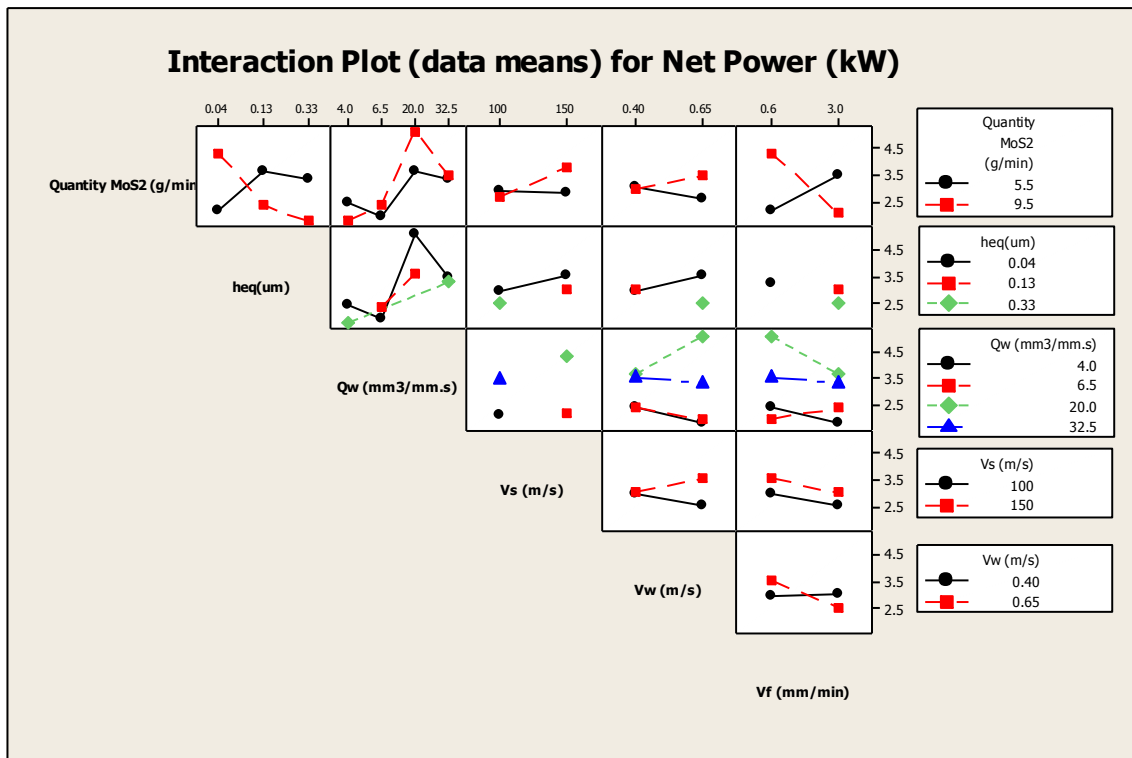


Figure 146 Total interactions on Net Power for MoS<sub>2</sub>(MQSL) input parameters (5.5-9.5g/min MoS<sub>2</sub>)

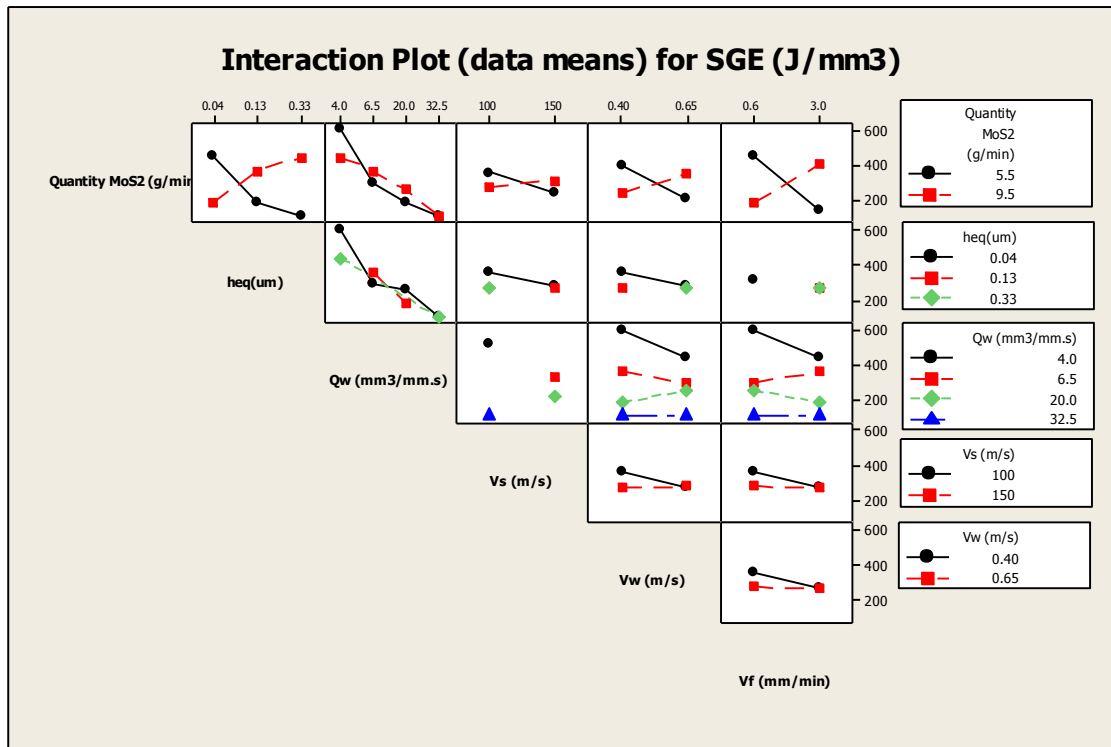


Figure 147 Interactions on SGE for  $\text{MoS}_2$  input parameters (5.5-9.5g/min  $\text{MoS}_2$ )

The behaviour of the  $\text{MoS}_2$  on the smaller chip thicknesses is illustrated by the ANOVA interaction plots between the equivalent chip thickness ( $h_{eq}$ ) and the quantity of  $\text{MoS}_2$ , see Figure 148 and Figure 149. These show the efficiency of chip creation over the range of grinding conditions. The reduction in equivalent chip thickness is known to increase the SGE values. However the interaction plot illustrates that the higher quantity of  $\text{MoS}_2$  has an ability to reduce SGE at the smaller chip thickness. This is a result of additional lubrication in the grinding zone, enabling a reduction in the SGE. This again begins to provide an understanding that the available space between the abrasive grits is critical to create the new chip and successfully introduce the solid lubricant.

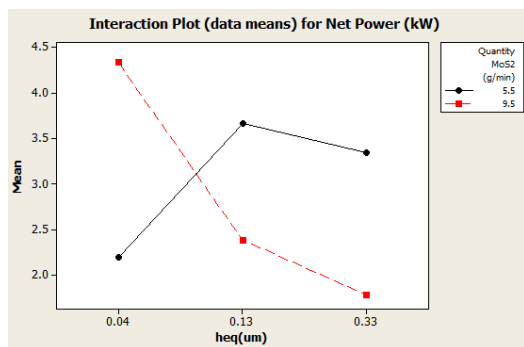


Figure 148 Net Power variation with 5.5-9.5 g/min  $\text{MoS}_2$

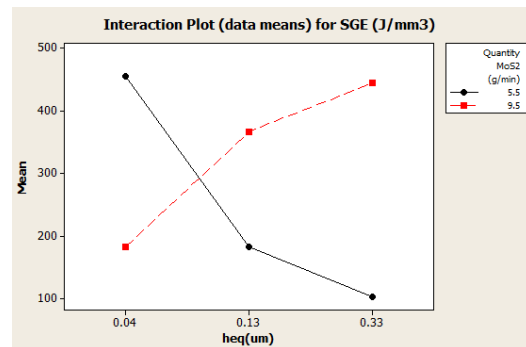
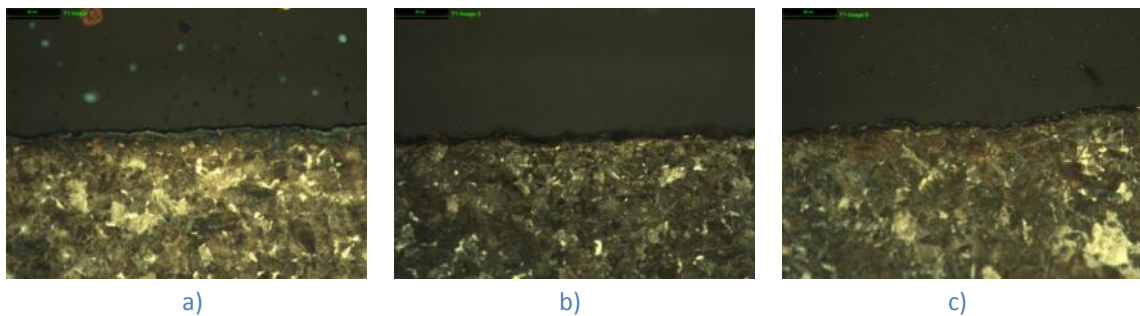


Figure 149 SGE variation with 5.5 -9.5g/min  $\text{MoS}_2$

It is worth noting that physically the plunges appeared to pass smoothly. The sparks were low in volume and brightness. The grinding noise was low and the surfaces appeared clean from chatter or burn. There was however a residue of MoS<sub>2</sub> left upon the workpiece surface. The MoS<sub>2</sub> is difficult to handle with respect to its ability to spread easily, particularly over the machining surfaces, the grinding samples, and the operators.

### 6.3.2 MoS<sub>2</sub> – Surface Integrity

The sample surfaces were analysed for signs of thermal stress and microstructural change. The samples were simple cylindrical sections therefore there were no cam, web or wall geometries to provide positions of stress concentration with respect to residual stresses and thermal conditions. The following selection of images, provide an insight into the post-processed steel surface. Figure 150 and Figure 151 illustrate examples of Trial 2 and Trial 8 from the L8 Taguchi trials. These are the least extreme and the most extreme machining parameters respectively, on 38Mn low carbon steel.



**Figure 150** The microstructure images showing the width of the 13mm sample width from the MoS<sub>2</sub> Trial 2 a) 1mm from the LH edge b) 6.5mm at the middle position c) 12mm from the RH edge

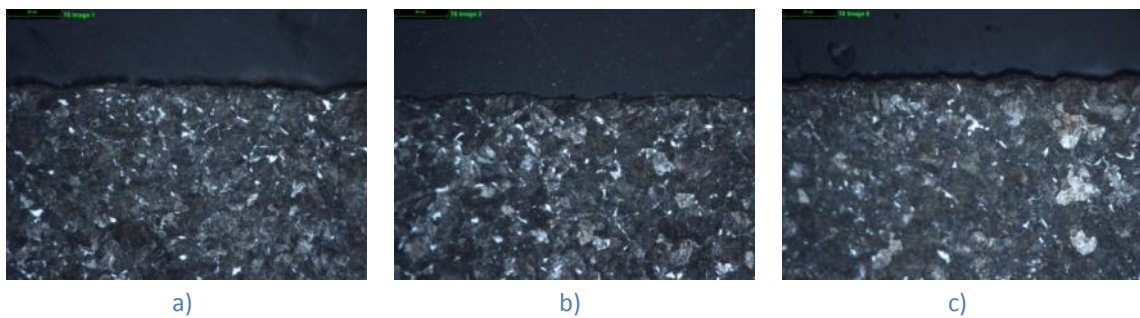


**Figure 151** The microstructure along the 13mm sample width MoS<sub>2</sub> Trial 8 a) 1mm b) 6.5mm c) 12mm

The microstructure from the MoS<sub>2</sub> processed samples appear well structured and free from any thermal damage. The grain formation was constant throughout the depth and there was no sign of any white layering following the Nital etching. There was however some visual tarnishing found upon the surface from what was believed to be the MoS<sub>2</sub> staining and remaining within the ploughed regions of the abrasive grit lay. This was investigated further by SEM imaging, see Figure 152. These images clearly depict the direction of lay and the relatively fine finish to the surface. Inconsistencies

in the lay appear due to the random positioning of the grits on the grinding wheel that briefly interact with the workpiece surface in order to profile the surface. Figure 152 b) and d) show the corresponding elemental scan showing little evidence of impregnation or reaction with Molybdenum. However small captured regions of Sulphur are recognised. Although the actual phase of the elements is not possible to be determine the Sulphur is a cause for concern. The formations of Sulphides on the surface such as iron sulphide would create zones of a brittle nature, extremely undesirable for surface fatigue strength and surface integrity.

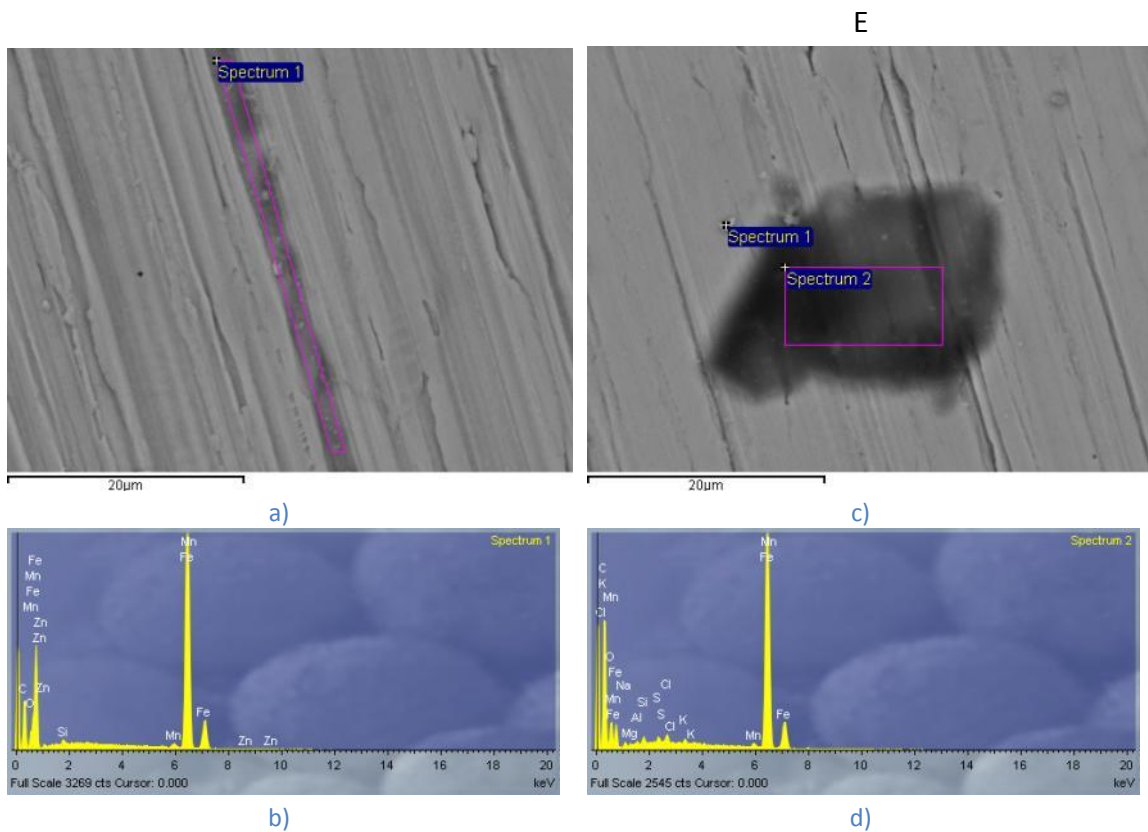


**Figure 152** SEM and EDX images investigating surface staining following MoS<sub>2</sub> processing

Figure 153 and Figure 154 illustrates the  $R_a$  and  $R_t$  surface scans respectively. Comparing these readings to the EcoCool trials there is on average a 20% improvement in surface roughness. This is encouraging and roughness values fluctuate very little over the duration of the Taguchi trials. The control conditions under Trial 2 parameters were repeated using 'water-only' and 'dry-only' appear as trial 9 and 10 respectively, similar as in the EcoCool readings.

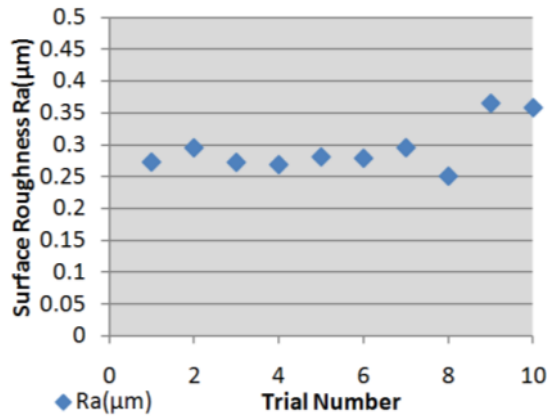


Figure 153 MoS<sub>2</sub> Surface Roughness Ra. (Trials 9 and 10 is water-only and dry grinding respectively)

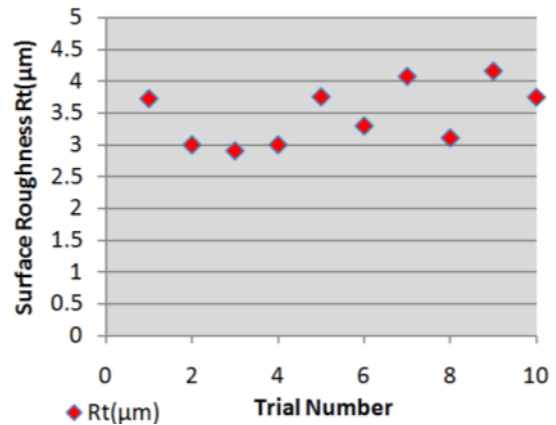


Figure 154 MoS<sub>2</sub> Surface Roughness Rt. (Trials 9 and 10 is water-only and dry grinding respectively)

The roundness profiles in combination with the MoS<sub>2</sub> MQSL are illustrated under the extreme low and high conditions, Trial 2 and Trial 8. The differences in the surface profiles are seen as the fluctuations over the surface contours. These fluctuations are small at the slower wheel speeds, see Figure 155. The extreme high feed rates begin to demonstrate that the process is leading to a state of chatter although the form is generally concentric, as shown by Figure 156. Addition trials were undertaken to expose the workpiece to conditions of burn and dry machining. This provided a comparison for surface form, see Figure 157 and Figure 158 respectively. The occurrence of chatter greatly reduces the surface integrity and is detrimental to the performance and operation of precise mechanical systems. The illustrations identify a range of trial conditions with their corresponding surface profiles. Note the changing of the scaling as the conditions reduce the amount of lubrication.

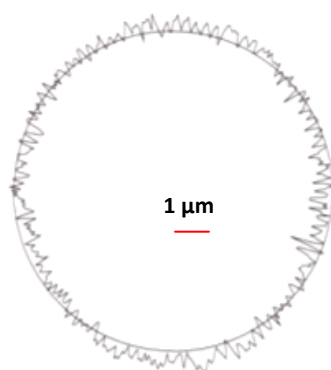


Figure 155 Trial 2 MoS<sub>2</sub> roundness profile

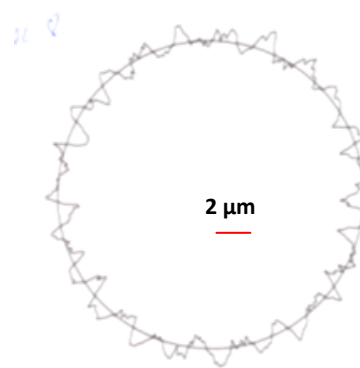


Figure 156 Trial 8 MoS<sub>2</sub> roundness profile

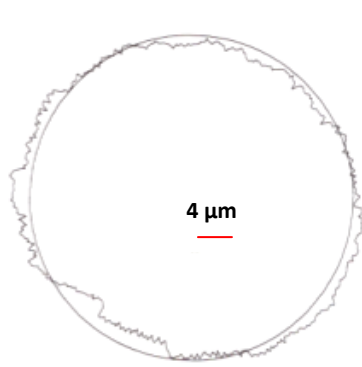


Figure 157 Under burn cutting conditions

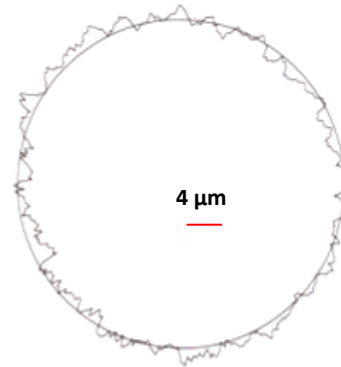


Figure 158 Dry cutting conditions

The results from the form-scans were entered into the ANOVA tables. This provided a visual indication on the effect of the MoS<sub>2</sub> on the roundness, see Figure 159. The improvement over the mean roughness value is very small. Therefore the roughness values are mainly determined by the chip thickness as a combination of the infeed speed, the grinding wheel speed, and the workspeed. The Talycenter was removed from the laboratory shortly after these results were made so unfortunately these were the last sets of roundness scans.

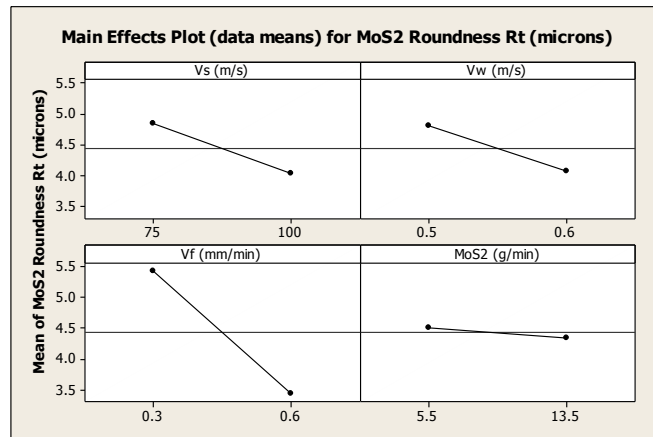


Figure 159 Variables of significance with respect to the roundness profile MoS<sub>2</sub>

The Barkhausen Magnetic Noise surface scan recorded the condition over 360 degrees rotation of the sample see Figure 160. The readings were found to be stable about the circumference of the sample. This fact indicates that the surfaces are free of chatter and other geometrical discrepancies such as edge burrs. The ANOVA interpretation of the effect of the MoS<sub>2</sub> is given in Figure 161. This plots the variation in the input parameters with respect to the condition of the residual stresses.



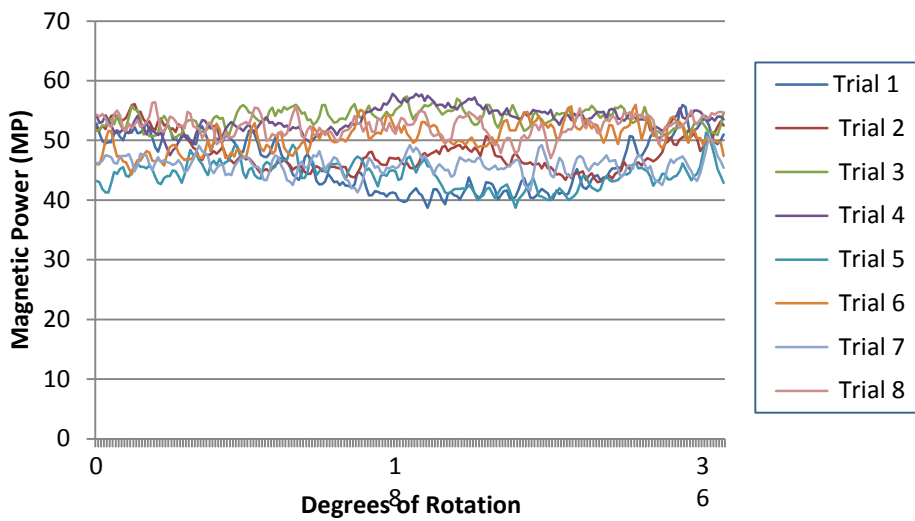


Figure 160 BN Readouts for MoS<sub>2</sub>

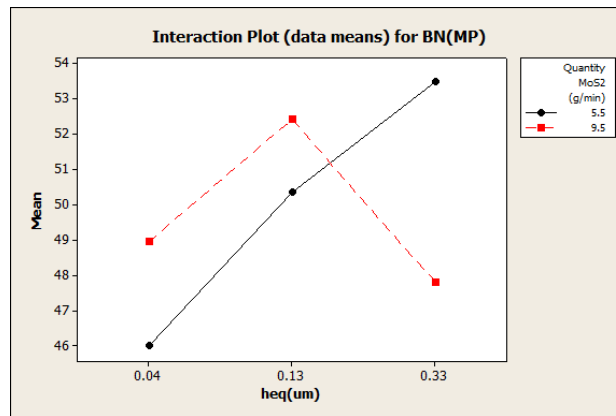


Figure 161 Interactions of MoS<sub>2</sub>(MQSL) on BN magnetic power (5.5-9.5g/min MoS<sub>2</sub>) showing that the larger chip thicknesses respond well to a larger quantity of MoS<sub>2</sub>

The non-linearity of the interaction plots indicates that there is a strong interaction between the two levels of MoS<sub>2</sub> particularly at the higher levels of the chip thickness. The chart suggests that the action of the solid lubricant has less of an effect at the smaller chip thicknesses in comparison to the larger chip thicknesses. Generally small chip thicknesses require more energy per unit volume due to a proportionate amount of energy involved in the rubbing and ploughing stages of grit interaction. The lowest BN level is achieved through a combination of the lower quantity MoS<sub>2</sub> and the smaller chip thicknesses. On the other hand a different approach to the quantity of MoS<sub>2</sub> is needed at the larger chip thickness as a reduction in residual stresses is achieved with higher delivery rates of lubricant. On average a 52% increase in the mass flowrate of MoS<sub>2</sub> added to the useful flowrate resulted in a 10% reduction in the magnetic power signal.

---

## 6.4 CaF<sub>2</sub>(MQSL) Trials

CaF<sub>2</sub> is 2/3<sup>rd</sup>s the density of MoS<sub>2</sub>. For this reason the solid lubricant feeder (Design 2) provided an extremely low mass flowrate of CaF<sub>2</sub>, under the same delivery conditions as the MoS<sub>2</sub> trials. The less dense powder therefore required an alternative approach with respect to the delivery system in order to provide a large enough range between the levels of the mass flowrate to provide any significant conclusive evidence to the MQSL capability of CaF<sub>2</sub>. The Calcium Fluoride by nature is insoluble and tends to collect into small clumps on contact with water, which added to the complications of using water as a carrying medium. The powder would easily collect and conglomerate throughout the length of the lead-screw, eventually mixing into a hardening paste-like-substance. At the exit of the lead-screw and upon the entrance to the nozzle downpipe, the CaF<sub>2</sub> would lodge and obstruct the entire delivery system. The water jet was not strong enough to clear the passage and it would quickly build up and become too thick to break through. To prevent this happening the water jet was positioned half way along the length of the lead-screw. The CaF<sub>2</sub> would move along the lead-screw and the water jet would provide enough dispersion throughout the channel to break the CaF<sub>2</sub> lubricant into smaller particles and provide a more manageable flow. This method evolved through an understanding of particulate mechanics, relying on the agitation of bulk powder grains in order to change the characteristic of their flow from a static to a more fluidic nature. This made a considerable difference to the performance of the feeding mechanism. Once a satisfactory and continuous delivery of CaF<sub>2</sub> was established the experimental design from the MoS<sub>2</sub> trials was repeated. However it was not long before the third and final delivery system was introduced.

### 6.4.1 CaF<sub>2</sub> – Power consumption

The performance of the CaF<sub>2</sub> did not appear quite as effective as the MoS<sub>2</sub>. The Net Power and the SGEs are primarily dominated by the infeed condition; see Figure 162 and Figure 163. On closer inspection there is a slight reduction of Net Power and SGE with the higher level of CaF<sub>2</sub>. The narrow range of CaF<sub>2</sub> delivery mass flow rates probably accounts for this. The two extreme levels of mass flowrate are not wide enough apart to show substantial influence. Analysing the influence of the grinding variables on the SGE values suggests that, other than the infeed speed of the grinding wheel, the grinding parameters had little effect, see Figure 164.

The interaction chart effectively shows that there was very little influence by the CaF<sub>2</sub> over the range of delivered masses (3.5-8.3g/min). The 8.3g/min was the maximum achievable mass flowrate deliverable by the Design 2 leadscrew mechanism. Some reductions in the SGEs are occurring at the higher chip thicknesses but the differences are not sufficiently dramatic to indicate an improvement to the process.

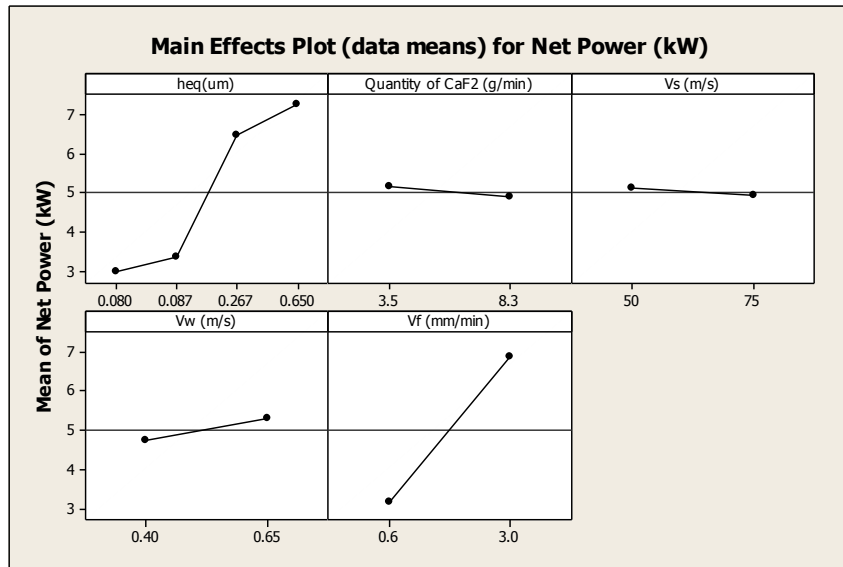


**Figure 162** Main effects on Net Power for  $\text{CaF}_2(\text{MOSL})$  input parameters (3.5-8.3g/min  $\text{MoS}_2$ ). The limited capability of the powder feeder made a non significant contribution to a reduction in the power consumption, particularly in comparison to the infeed speed of the grinding wheel.

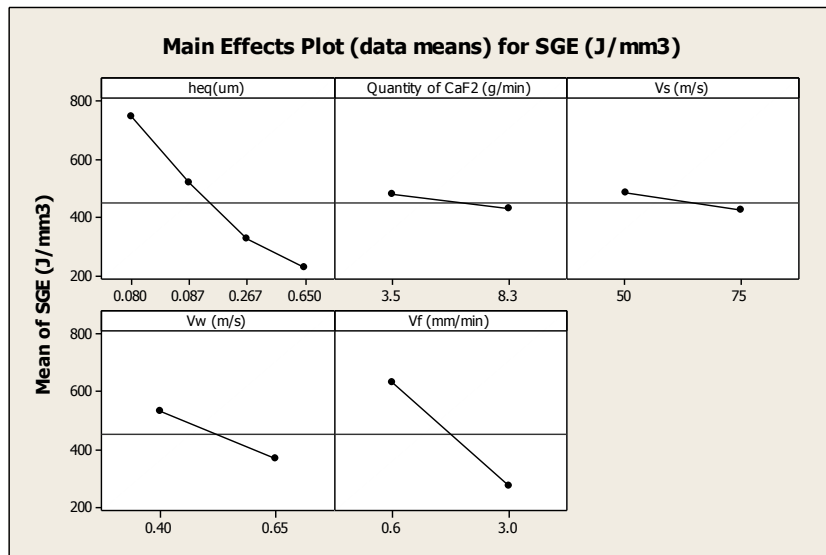


**Figure 163** Main effects on SGE for  $\text{CaF}_2(\text{MOSL})$  input parameters (3.5-8.3g/min  $\text{MoS}_2$ ). The dependence of Net Power on the delivery of  $\text{CaF}_2$  is relatively slight in comparison to the  $\text{MoS}_2$  trials. This was to be expected as the difference in the levels of  $\text{CaF}_2$  masses was not great enough to produce conclusive evidence of influence.

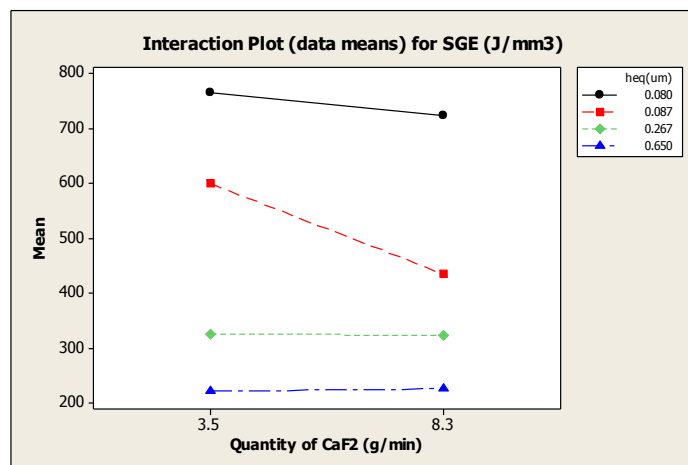


**Figure 164** Interactions on SGE for  $\text{CaF}_2$ (MQSL) input parameters (3.5-8.3g/min  $\text{CaF}_2$ ). A high value of SGE for the grinding of 38Mn steel increased the risk of thermal damage.

Not wanting to discard  $\text{CaF}_2$  however, a wider range of delivery mass levels was required. This would deliver higher mass flowrates of solid lubricant, to assess the lubricity of  $\text{CaF}_2$ . This led to the development of the third solid lubricant delivery system; 'Design 3' which comprised a pneumatic system. The delivery system was able to lift the powder from a sealed pressurised container and direct the solid lubricant through the feed lines. The mixture of air and solid lubricant was then fed towards the surface of the grinding wheel, using the existing shoe nozzle. This greatly improved the delivery mass flowrates of  $\text{CaF}_2$  from a range of 3.5 to 8.3 g/min to a new set of levels of 18g/min and 41 g/min, approximately 5 times the capacity of the previous design. This system also enhanced the reliability and repeatability of delivering the solid lubricant to the grinding wheel. Figure 165 illustrates the main effect and the interaction ANOVA plots following the implementation of the pneumatic powder feeder. These figures indicate that a broadening of the  $\text{CaF}_2$  delivery range resulted in a greater impact on the process conditions.

In comparison to the earlier  $\text{CaF}_2$  results for 3.8g/min to 8.3g/min the new delivery system made a marked improvement with respect to power and SGE values. This implies a cooler grinding process with an identical B120 wheel and 38Mn low carbon steel. For example the (new) higher level of the  $\text{CaF}_2$  reduces the SGE by a considerable  $150\text{J/mm}^3$ . In general an increase in  $\text{CaF}_2$  to 41g/min, resulted in a 33% reduction in average SGEs over the Taguchi levels. This begins to provide evidence that the lubricity of  $\text{CaF}_2$  is more prominent at the higher mass flow rates of feed. However, the introduction of high mass flowrates of a fine powder also has its practical implications; for example the extraction system of the grinding machine has to be able to cope with these greatly increased powder flow rates.

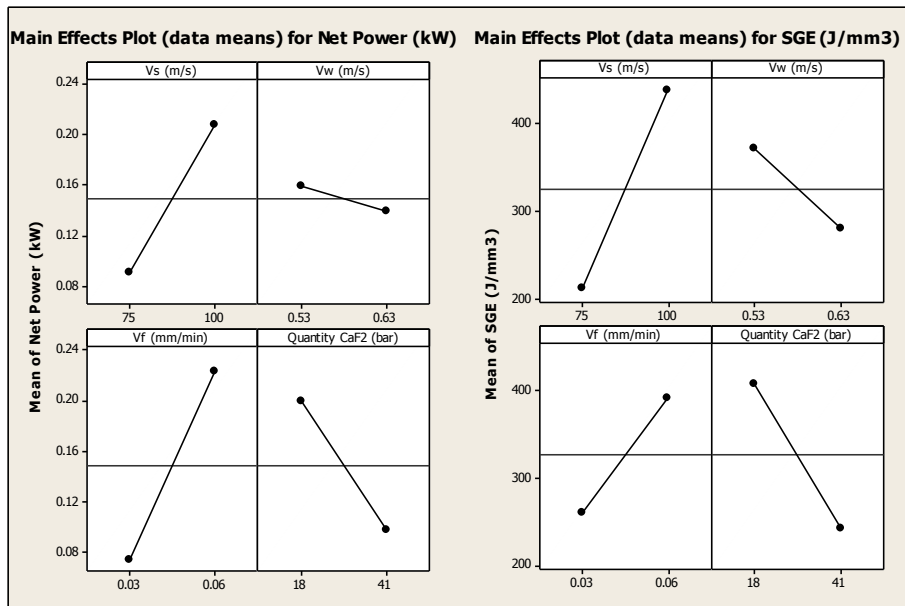


Figure 165 Main effects for ESW2 Wheel: B120, Workpiece: 38Mn Steel, Solid lubricant: CaF<sub>2</sub>

The CaF<sub>2</sub> Taguchi trials were repeated between the B120 and B90 wheels, enabling a degree of comparison between the two wheels. This enabled any differences in power consumption and SGE values to be correlated against the particular wheels. Figure 166 illustrates the B90 values upon the similar 38Mn steel. The first point to notice is that the influence of the CaF<sub>2</sub> on the reduction of the SGE becomes slightly reduced. This suggests the B90 wheel cannot accept the solid lubricant quite as easily. The second is the opposing influence that the infeed speed has on the SGE. This could however be attributed to the relatively new condition of the wheel.

As a result of the CaF<sub>2</sub> reducing the SGEs the workpiece material was changed to the harder 51CrV steel. The Taguchi trial conditions were similar as before. This was done to expose the CaF<sub>2</sub> to alternative grinding cutting conditions generally associated with higher SGEs. Figure 167 shows that the rise in SGE was recorded as over double the average of the grinding of 38Mn steel. The SGE rose to 840J/mm<sup>3</sup> from the 340J/mm<sup>3</sup> recorded previously, and proved particularly undesirable.

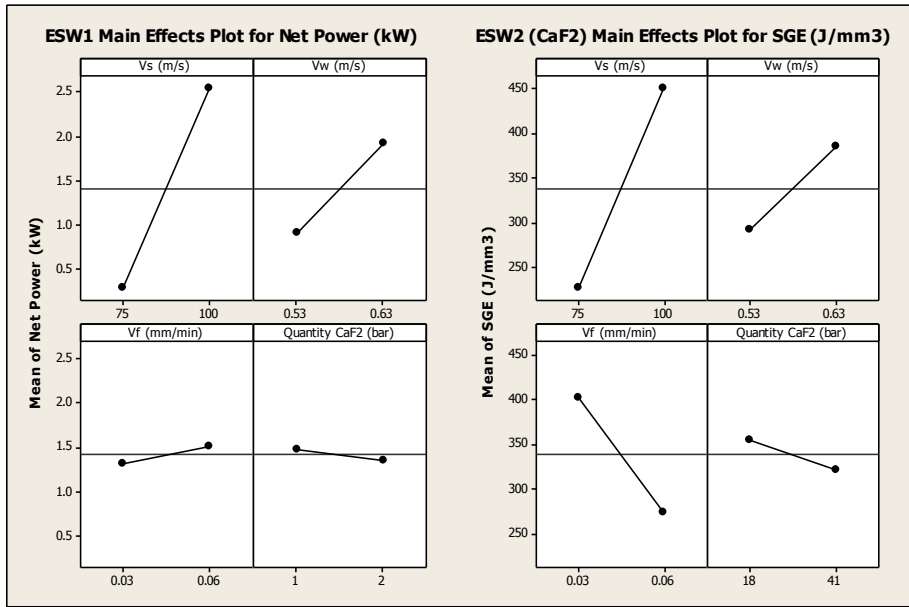


Figure 166 Grinding 38MnSiV6 steel with cBN B90 vitrified bond wheel using CaF<sub>2</sub>

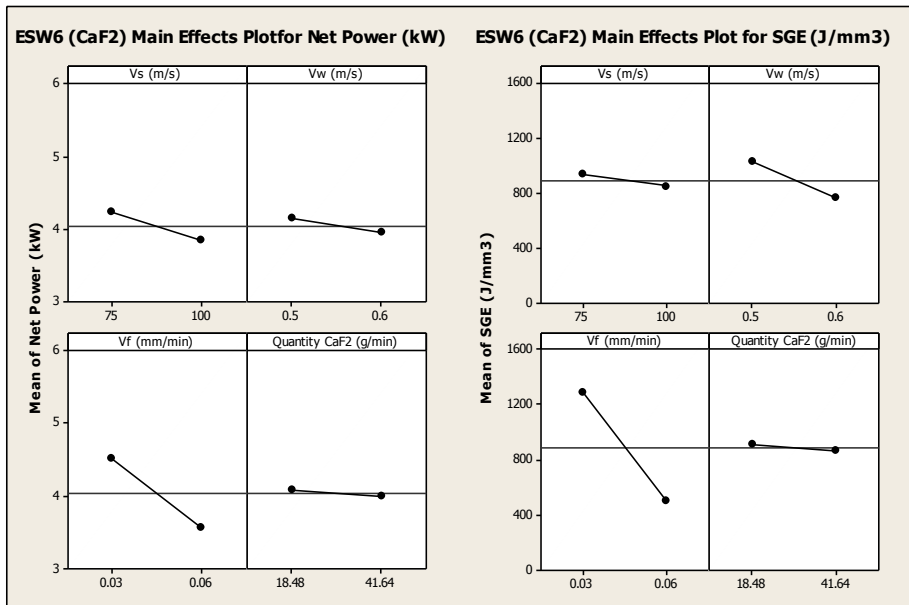


Figure 167 Grinding the harder 51CrV4 steel with cBN B90 vitrified bond wheel using CaF<sub>2</sub>. Demonstrating a rise in the average SGE compared to the 38Mn

### 6.4.2 CaF<sub>2</sub> – Surface Integrity

CaF<sub>2</sub> is much more favourable than MoS<sub>2</sub> with respect to handling. It is much easier to maintain the cleanliness of the machine and the cleanliness of the samples, compared to the silvery-black residue left from MoS<sub>2</sub>. Although not particularly quantitative to the performance analysis of these grinding trials this certainly featured as a practicality. There still remained the possibility that the CaF<sub>2</sub> could influence the

surface composition of the steel, similar to the investigation of the sulphides on the surface of the iron.

The  $\text{CaF}_2$  was still carried into the grinding zone by water which would be providing an aspect of cooling. Therefore heat could be conducted away at similar rates as a conventional machining fluid. These water flow rates however remained at the previously identified useful flowrates, as featured in the EcoCool trials and Chapter 4. Figure 168 and Figure 169 show the 2% nital etched subsurface layer of the extreme cases of machining with  $\text{CaF}_2$ . Figure 170 and Figure 171 illustrate an exposure to a high and low mass flowrate of  $\text{CaF}_2$  respectively showing an loss of integrity with a low level of solid lubricant

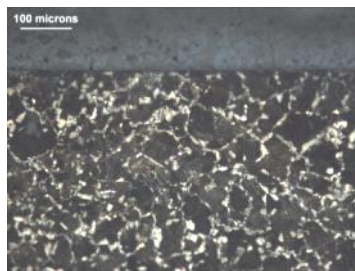


**Figure 168** Machine parameters:  $V_s=50\text{m/s}$ ,  $V_w=0.5\text{m/s}$ ,  $V_f=0.03\text{mm/min}$ ,  $\text{CaF}_2=18\text{g/min}$  Wheel cBN90, workpiece 38Mn Low  $V_s$ ,  $V_w$ ,  $V_f$  and Low  $\text{CaF}_2(\text{MSQL})$

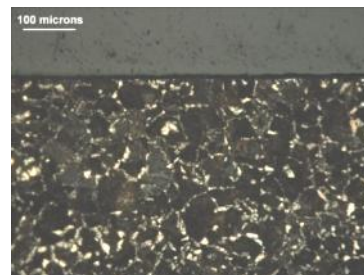


**Figure 169** Machine parameters:  $V_s=75\text{m/s}$ ,  $V_w=0.6\text{m/s}$ ,  $V_f=0.06\text{mm/min}$ ,  $\text{CaF}_2=18\text{g/min}$  Wheel cBN90, workpiece 38Mn. High  $V_s$ ,  $V_w$ ,  $V_f$  and Low  $\text{CaF}_2(\text{MSQL})$

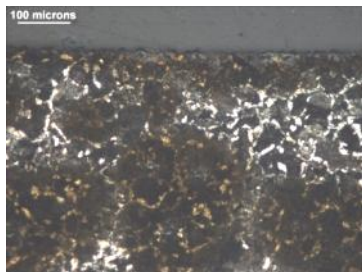


**Figure 170** Machine parameters:  $V_s=50\text{m/s}$ ,  $V_w=0.6\text{m/s}$ ,  $V_f=0.06\text{mm/min}$ ,  $\text{CaF}_2=41\text{g/min}$  Wheel cBN90, workpiece 38Mn.

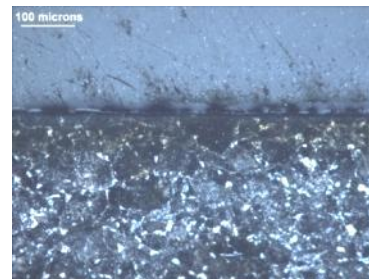


**Figure 171** Machine parameters:  $V_s=50\text{m/s}$ ,  $V_w=0.5\text{m/s}$ ,  $V_f=0.03\text{mm/min}$ ,  $\text{CaF}_2=18\text{g/min}$  Wheel cBN90, workpiece 38Mn showing signs of the onset of microstructural change underneath a slightly chattered surface

The machining parameters were relatively gentle and the range of samples that were processed with  $\text{CaF}_2$  emerged with few instances of damage, shown in the microstructural compositions. To an extent this was surprising as the conditions of the grinds from operators point of view was with bright sparks that would normally suggest tough and aggressive grinding conditions. The formation of white layering was limited, but the onset of chattering was clearly obvious. The brightness of the sparks may however be attributed to the tribo-luminescence of  $\text{CaF}_2$  and will be touched upon in the later chapter of the investigation. Therefore the  $\text{CaF}_2$  held a certain degree

of instability, and not quite as predictable as first envisioned. Although a difference was made by the higher delivery rates of  $\text{CaF}_2$  the subsurface layer was still susceptible to thermal transformation created through elevated SGE values.

Fluoride is one of the most chemically reactive elements in the periodic table which is a reason it is normally found naturally in a combined state, mainly as Calcium Fluoride and Fluorspar. Nevertheless these sources of Fluoride are in contrast extremely stable and insoluble. Under the microscope therefore particular attention was made not only towards the grain structure, but also towards the immediate surface. This was to examine possible reactions with the low alloy steel. Figure 172 demonstrates the SEM investigation where the analysis managed to identify the reminiscence of Calcium and Fluoride upon the surface.

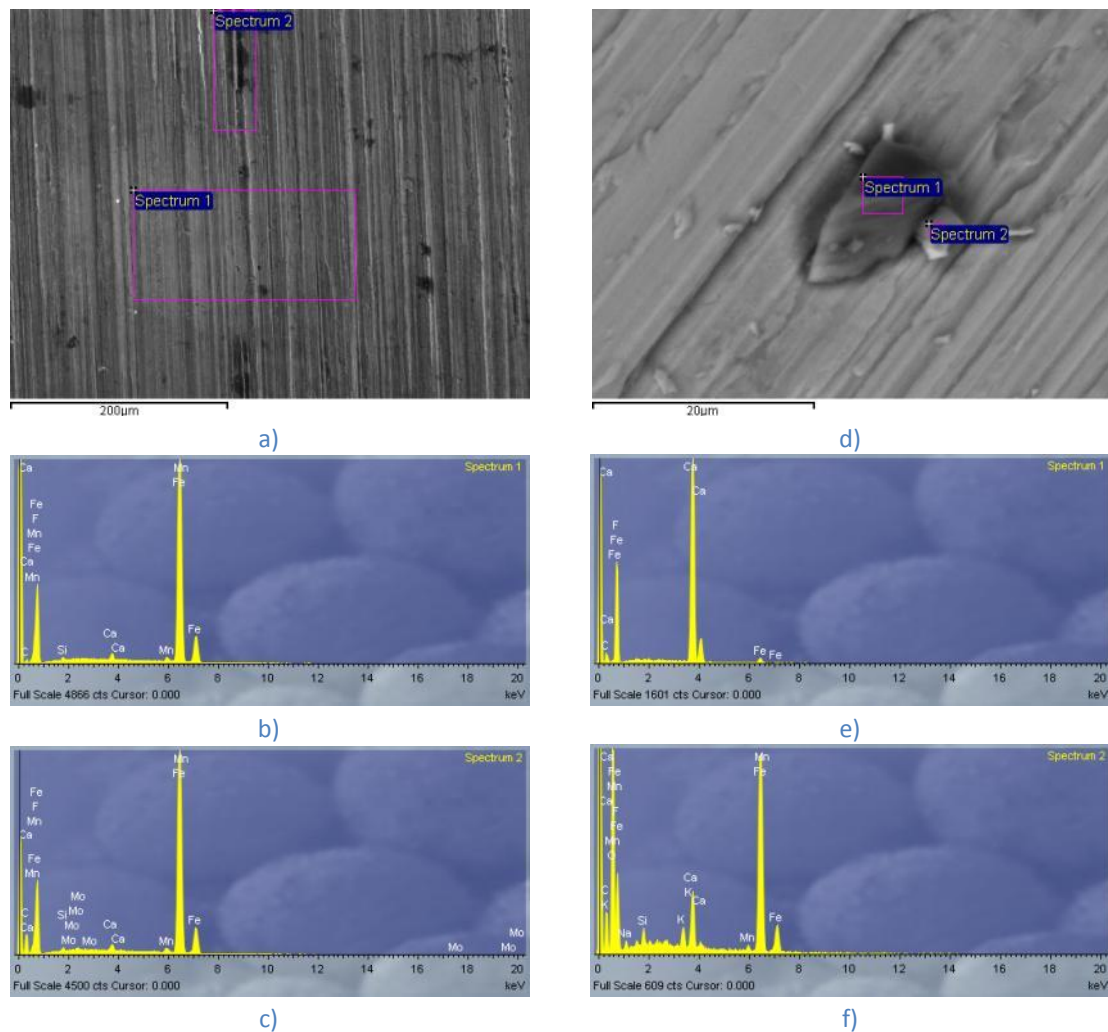


**Figure 172** SEM investigation; a) Trial 2 with the corresponding spectral analysis b) Spectrum 1, c) Spectrum 2 and d) Trial 8 with corresponding spectral analysis e) Spectrum 1, f) Spectrum 2

The direction of the wheel lay can be clearly identified along with certain areas of interest. The corresponding elemental scan enables the detection of not only Ca but



also highlights some Molybdenum which must have been left over from the previous solid lubricant set of trials, therefore a small amount of contamination exists within the system.

The surface roughness of the samples lubricated by CaF<sub>2</sub> showed that the values although acceptable, were not as good a quality as those achieved by the EcoCool oil emulsion, see Figure 173. The flowrate of water was still the same as the useful flowrate providing a direct comparison between the CaF<sub>2</sub> and the EcoCool. The lubricity added by the oil was more beneficial than that of the CaF<sub>2</sub>. However compared to the dry passes (as shown by trial 9) the CaF<sub>2</sub> lubrication helped to make an improvement in surface roughness by a factor of about five. The ANOVA chart identifying the influence of the CaF<sub>2</sub> on the surface roughness is shown in Figure 174. The surface roughness conditions actually begin to deteriorate with an increase in CaF<sub>2</sub> to the higher flowrate of 41g/min. For that reason the physical structure of a large volume of CaF<sub>2</sub> powder proves to be detrimental to the surface condition.

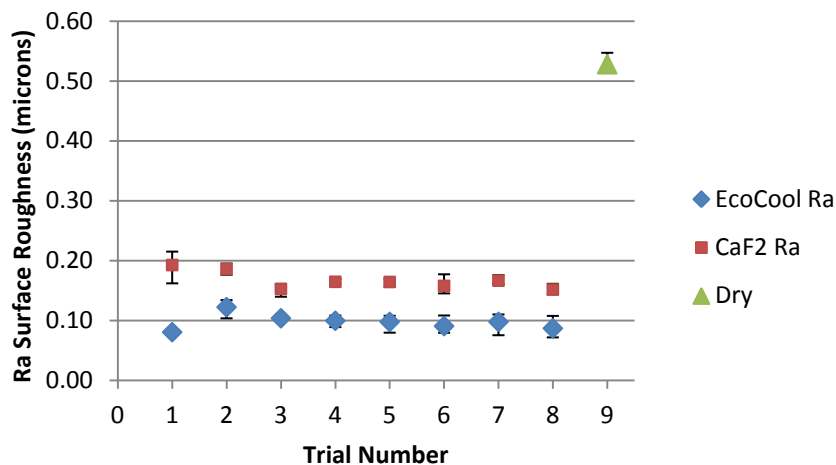
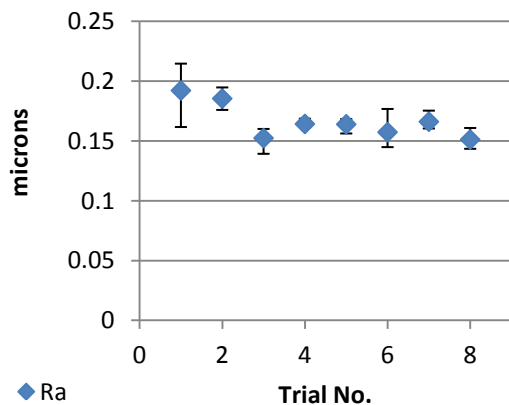
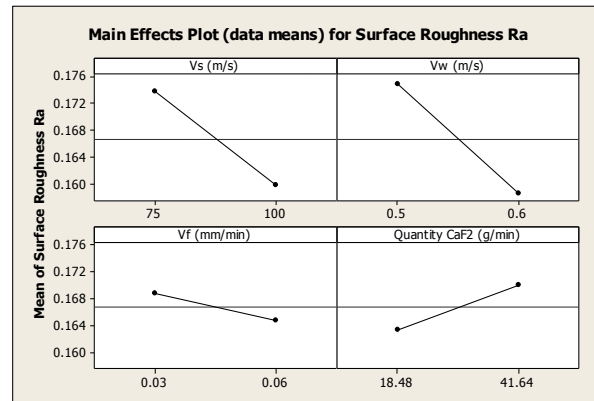


**Figure 173** The surface roughness comparison of the 18 g/min - 41g/min CaF<sub>2</sub> against the 1% - 10% EcoCool Notice the difference of the completely dry (Trial 9) resulting in a nearly 5 times worsening of the surface without any controlling additives to the grinding process.



a)

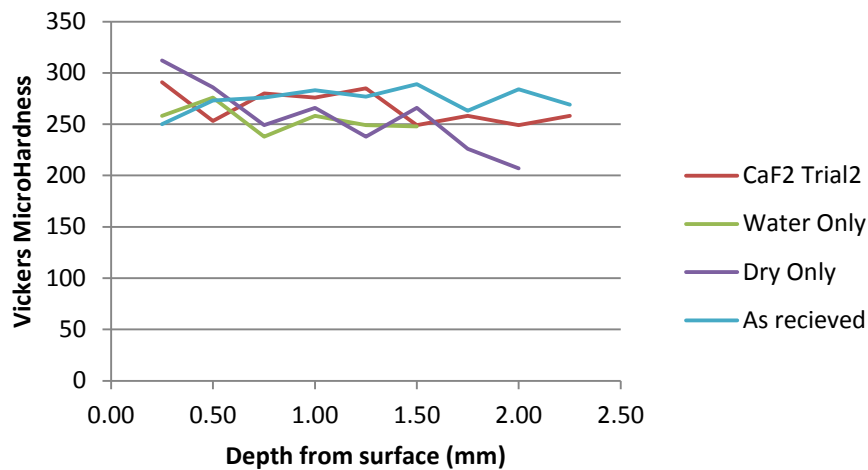


b)

**Figure 174** CaF<sub>2</sub> Surface Roughness figures a) actual Ra measurements b) the ANOVA interpretation of the machining parameters determining that increasing CaF<sub>2</sub> decreases the surface conditions by 0.008microns Ra

Hardness testing reveals changes within the material composition, as a consequence of the grinding process parameters and conditions. Flash process temperatures are likely to occur throughout grinding and often result in the microstructure transforming and cooling into undesired structural formations. The changes in hardness through the sub-surface depth are shown Figure 175 with respect to CaF<sub>2</sub>. There are also comparative results of the control passes of water only and dry conditions. An indication of microstructural damage is the immediate hardening of the surface. The completely dry example below possessed a burnt surface resulting from harsh grinding conditions. Under these conditions the hardness is seen to rise at the surface before falling to a softer structure within the depth. This suggests areas of differing residual stress that could lead to premature failure when in service. Against the water only control passes the hardness of the material remains relatively consistent showing signs of stability at 250 MHV. The hardness of the CaF<sub>2</sub> features at a slightly elevated 260MHV but also remains at a consistent value throughout the sample. This indicates that the residual stresses are in a balanced composition within the substructure.

In general the hardness testing gave indications that subsurface residual stresses should be stable with the use of CaF<sub>2</sub>. The hardness testing showed that the use of CaF<sub>2</sub> created relatively little movement in the hardness values. Therefore the CaF<sub>2</sub> generally maintained stable hardness values throughout the depth. On the other hand, under dry conditions the hardness value is seen to fluctuate, suggesting a hardened surface and a softened core, an indication of residual stress.



a)

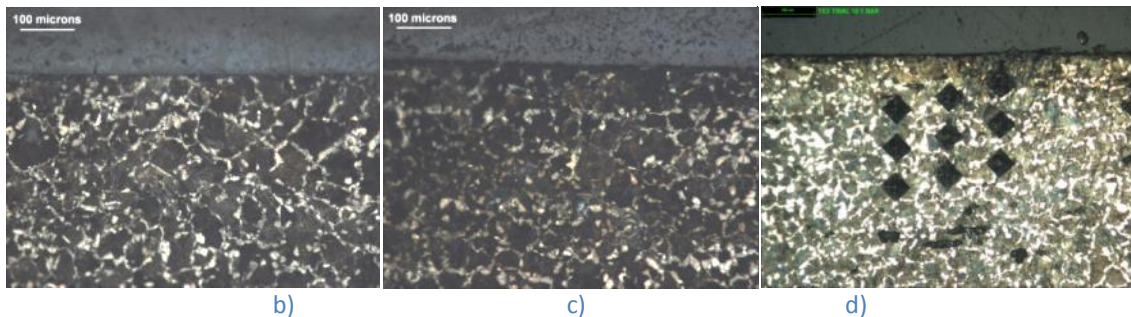


**Figure 175** Vickers Micro-hardness testing regime (0-2.25mm depth) and the corresponding microstructure image b) CaF<sub>2</sub>(1) Trial 1 c) Water only d) Dry Conditions (all the same scale: 100micron scale bar)

A selection of Barkhausen Noise analysis scans feature in Figure 176. What transpires is that the lower grinding wheel speeds, and therefore the reduced MQL fluid flowrates, possess considerably lower BN emission signals from even the MoS<sub>2</sub> trials. Not only are the signals lower but they are also demonstrating well formed responses throughout the rotation of the samples surface, no extreme oscillation. This becomes increasingly apparent in contrast to the higher grinding wheel speeds of 100m/s. The instances of the chatter lines become more defined at the higher wheel speeds indicating a drop in performance, and an elevation in tensile residual stresses. The average magnitude of the higher wheel speed signal is approximately 10MP higher, and the fluctuation in the surface condition would not be acceptable to industry.

The Barkhausen Noise signals are interpreted by the ANOVA and shown in Figure 177. An increase in the CaF<sub>2</sub> shows an increase of the Magnetic Power reading, resulting in a more tensile residual stresses within the immediate surface. The importance of the CaF<sub>2</sub> on the residual stress is less than the influence of the wheel and work speed.

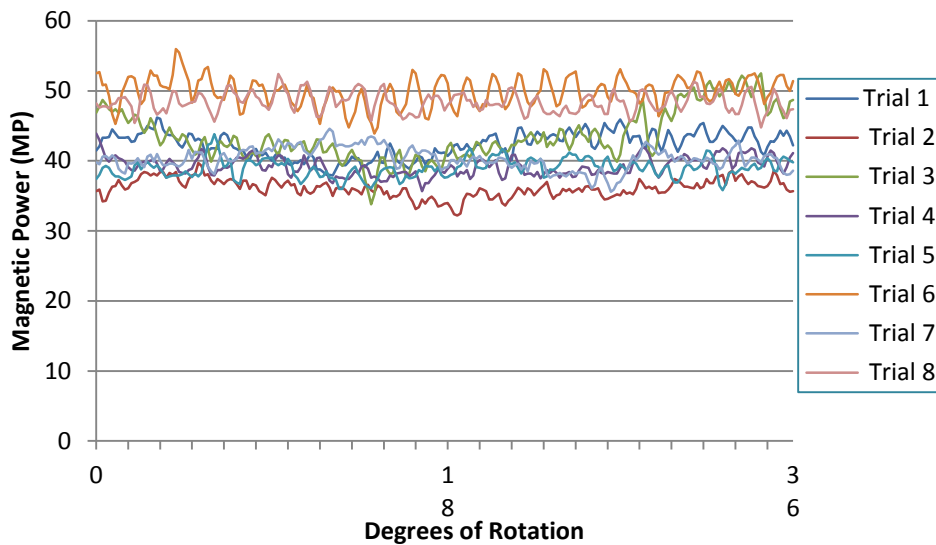


**Figure 176** BN Readouts for CaF<sub>2</sub> Trials. Notice the oscillation of the higher magnetic signals, these are occurring under faster wheel speeds and although not shown to be burnt, they do indicate signs of chatter.

The CaF<sub>2</sub> manages to reduce the nature of the stresses by a recorded 3MP (3%), compared to a 5MP (12%) reduction by reducing the grinding wheel speed and an 8MP (18%) reduction by increasing the workpiece rotational speed. An improvement to the residual stress conditions of the subsurface layer is reduced when applying CaF<sub>2</sub> in comparison to the residual stresses recorded in the EcoCool trials. Therefore in general this assessment indicates that the CaF<sub>2</sub> under these selected mass flowrates produce higher levels of SGEs in comparison to the MoS<sub>2</sub> and EcoCool. This is detrimental to the thermal conditions of the grinding operation. The residual stress scans provide evidence that the thermal conditions are hotter and the tensile stresses are higher when applying an increased mass flowrate of CaF<sub>2</sub>.

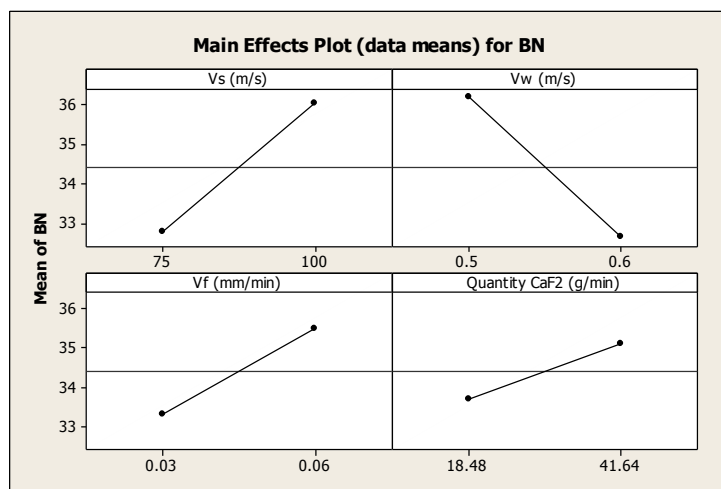


**Figure 177** Main effects BN readouts CaF<sub>2</sub>(MQL)

---

## 6.5 Hexagonal Boron Nitride (MQSL) Trials

Hexagonal Boron Nitride was introduced as the last solid lubricant within the scope of this research. At this point in time the machine was set up with the pneumatic powder feeder (Design 3). This was originally designed to be used with the  $\text{CaF}_2$ , with higher mass flowrates of solid lubricant. The density of hBN is much the same as the  $\text{CaF}_2$ , (hBN = 3.49g/cc,  $\text{CaF}_2$  = 3.18g/cc), so the feed system remained on the SAT machine in order to provide a direct comparison to the previous set of trials.

### 6.5.1 hBN – Power Consumption

Figure 178 features the B80 vitrified bond wheel showing a reduction of the SGE over an increased delivery of hBN into the system. This appeared to be similar in comparison to the application of  $\text{MoS}_2$ . Similar instances of the solid lubricant clogging and loading also became apparent on the surface of the grinding wheel. The characteristics of  $\text{MoS}_2$  and hBN are very similar particularly with respect to the lamellar crystalline structure therefore clogging was an expected issue.

The power and the SGE values recorded from introducing Boron Nitride as a solid lubricant are shown in Figure 178 and Figure 179. These figures identify the variation in power consumption and SGEs from the abrasive machining of 38Mn and 51CrV steels respectively. The most positive indication that the hBN is improving the cycle is seen by a reduction in the SGE as the quantity of hBN is increased. Under identical grinding trial conditions as the  $\text{CaF}_2$  the hBN shows a 75% drop in the mean SGE value from  $340 \text{ J/mm}^3$  to  $88 \text{ J/mm}^3$ . Although still higher than the EcoCool trials (at  $58 \text{ J/mm}^3$ ) the hBN values were a lot more comparable with the SGE values achieved by the traditional machining fluids. By doubling the quantity of hBN the SGE was lowered by 10% from  $92 \text{ J/mm}^3$  to  $83 \text{ J/mm}^3$  that provides a clear indication that the hBN is interacting with the grinding zone. The grinding wheel speed was the most important parameter with respect to influencing the SGE values. At the higher wheel speeds there was an increase in the flowrate of water, as a result of matching the useful flowrate theory. However this higher quantity of fluid did not result in a significant reduction in SGE. Therefore the improvement in the lubrication must be related to addition of the hBN.

The trials were repeated using the harder 51CrV low carbon steel as the workpiece material. The sample dimensions were identical. Harder materials are associated with higher SGEs for chip formation and removal. An increase in the hBN mass flowrate reduced the SGE values as shown in Figure 179, over the given machining parameters. The mean average of the SGE value resides around  $112 \text{ J/m}^3$ . Overall a 9% reduction of the SGE is achieved over the range of hBN flowrates. Therefore there is a similar achievable reduction in SGE between the two workpiece materials. Therefore the use of the hBN is demonstrating a positive influence on the grinding process.

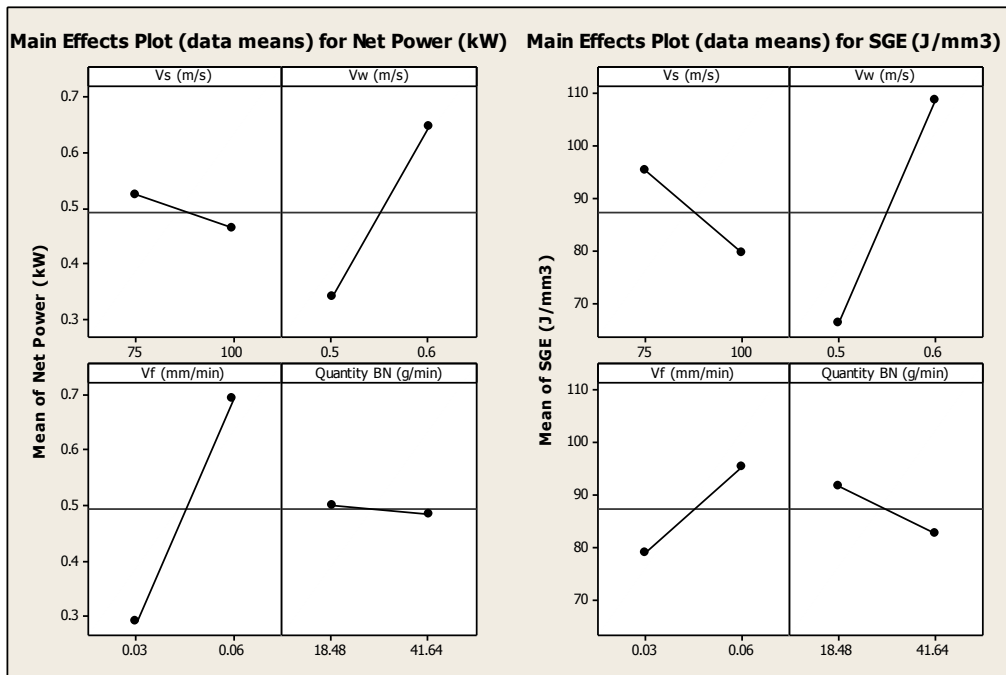


Figure 178 Grinding 38Mn steel with cBN B80 vitrified bond wheel using hBN

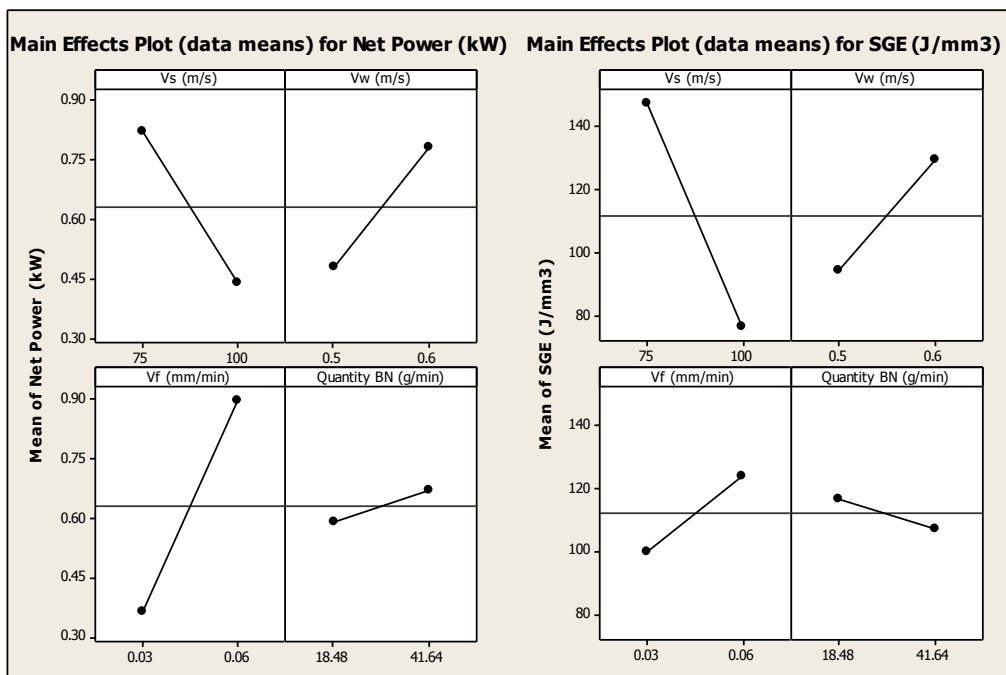
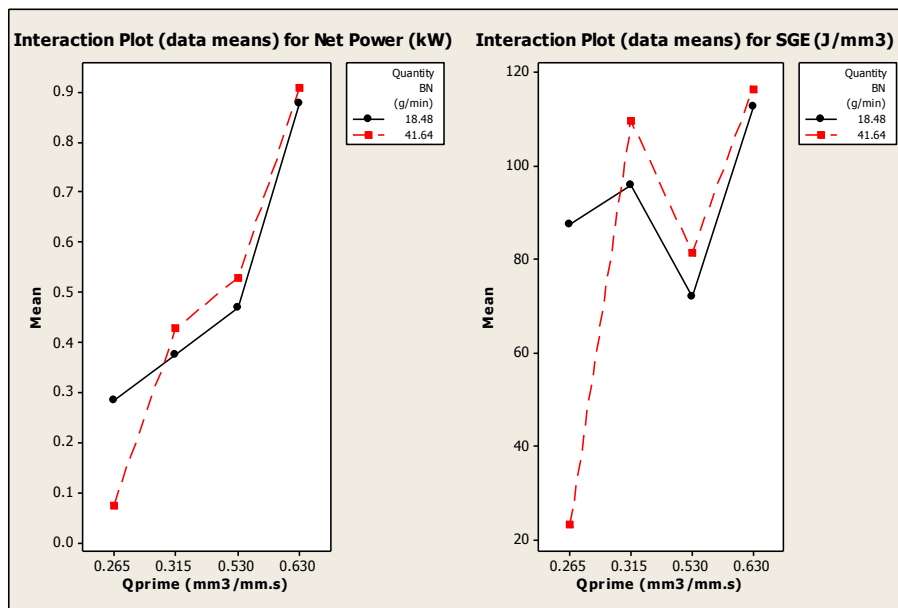


Figure 179 Grinding 51Cr steel with cBN B90 vitrified bond wheel using hBN

The interactions in Figure 180 and Figure 181 are of a particular interest. The two illustrate the variation of the net power and SGE for both the 38Mn steel and the 51CrV steel respectively with  $Q'_w$ . The influence of the hBN is noted over a variation of  $Q'_w$  values (specific material removal rate). A reduction in the SGE is noted at the

lower  $Q'w$  values. In the case of the softer 38Mn steel the influence of hBN is seen to reduce the SGE quite significantly at the lower  $Q'w$  23 J/mm<sup>3</sup> in comparison to the 87 J/mm<sup>3</sup>. The larger  $Q'w$  values tend to possess similar responses throughout the selected trials. The relationships for both the low and the high hBN levels produce similar SGE values at the higher material removal rates. This indicates that the larger material removal rates would be just as effective with lower levels of hBN, and promote the use of less machining fluid or lubricant. This is beneficial towards the MQSL application method as it indicates an improvement in performance with a reduced mass flowrate a machining lubricant.



**Figure 180** The power and SGE values from the grinding of the softer 38Mn steel with cBN B80 vitrified bond wheel shown against the  $Q'w$  values.

The SGE values are higher for the grinding of 51CrV steel. However, the use of a harder material reduces the influence between the levels of hBN. In fact the lower level of hBN begins to show signs of a more effective relationship. The hBN can be seen to make an influential difference with higher rates of powder delivery particularly at the mid ranges of equivalent chip thicknesses. In this region the SGE is greatly influenced and it is anticipated to be the point at which the hBN begins to reduce the rubbing and ploughing effect and encourage a cooler cut.

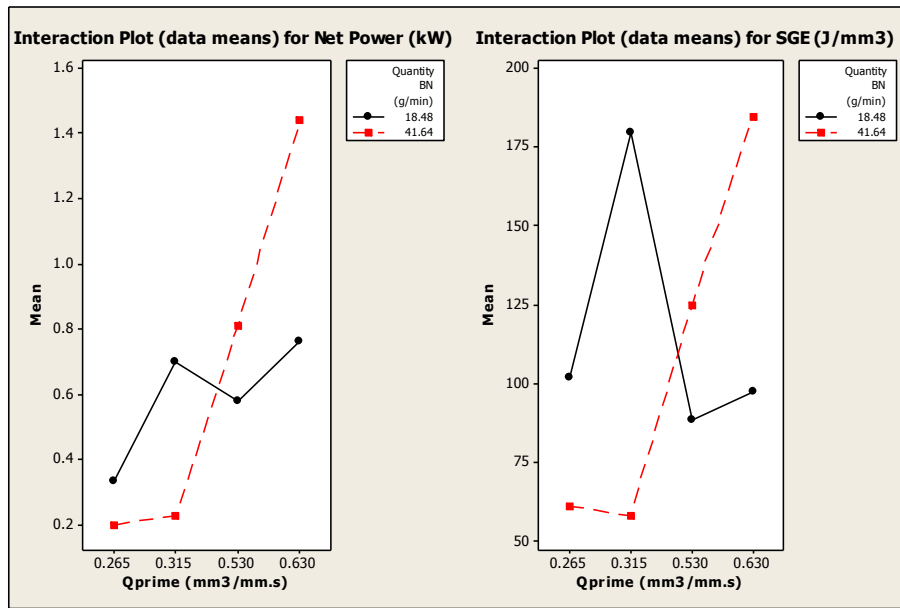
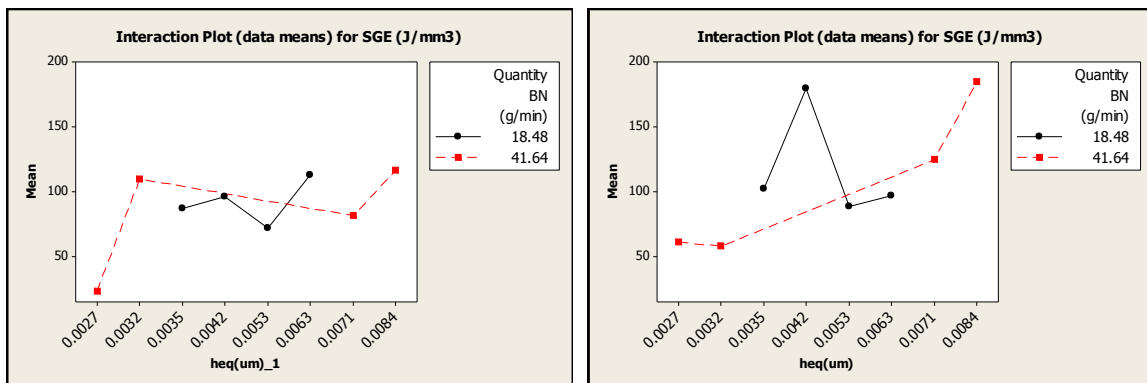


Figure 181 The power and SGE values from grinding the harder 51CrV steel with two levels of hBN (18.4g/min and 41.84g/min) in comparison to the Qprime leves using a cBN B80 wheel.

The influence of the hBN at the lower chip thicknesses is shown in Figure 182. The SGE values at the smaller chip thicknesses when using the EcoCool were previously shown to increase. The behaviour of the hBN suggests otherwise. The higher level of the hBN mass flowrate has a positive gradient. This indicates that the hBN solid lubricant was more influential at the smaller chip thicknesses, and provides evidence that the wheel needs to maintain small chip thicknesses in order to utilise the lubricity of the solid lubricant.



a)

b)

Figure 182 Variation of SGE over the ranges of equivalent chip thicknesses. a) is the 38Mn steel and b) the 51CrV steel. The two levels of hBN mass flowrate are shown. The higher flowrate enables lower SGE at the smaller chip thicknesses

The optimal settings to provide the lowest SGE values, and therefore an anticipated reduction in temperature is seen when; the wheel-speed is high, the workpiece speed



---

is low, the infeed is low, and the quantity of hBN is high. This was true for both the 38Mn and the 51CrV workpiece material.

### 6.5.2 hBN – Surface Integrity

The effect on the BN magnetic readouts from varying the grinding wheel speed was immediately recognised. Increasing the wheel speed from 75m/s to 100m/s resulted in an increase from 50MP to 65MP Barkhausen Noise signal respectively, as shown in Figure 183. The higher grinding wheel speeds also resulted in a slight occurrence of chatter, which was also detected by the magnetic scan. To visualise the performance of the hBN, a series of Water only and EcoCool 5% oil concentrations were added under the control conditions. The water only trial resulted in higher than average Magnetic Power detected signals. The fluctuations in the signal particularly for the water only, give cause for concern as they suggest a degree of chatter and hence non optimal grinding conditions. The inclusion of a 5% oil mixture provided the necessary lubricity and cooling to reduce the MP signal by approximately 7MP. The lower hBN delivery rate created more compressive residual stresses and less oscillation in the magnetic signal. A longer wavelength in the magnetic signal indicates a certain loss of cylindrical form that could be attributed to the reduction of machining fluid. As consequence the hydrodynamic influence from flood and high pressure systems was removed. This was intended to provide a stiffer machining process that was thought to be more advantageous. This should be looked into in the future.

The comparison of the EcoCool, CaF<sub>2</sub> and hBN lubricants feature in Figure 184. The resulting fall in the MP values at the lower wheel speed provide a degree of confidence that the action of the hBN is making a difference. In comparison with the oil the hBN was seen to make a dramatic difference. In general, over the range of machining parameters, the hBN was seen to achieve more compressive residual stresses in the subsurface layers.

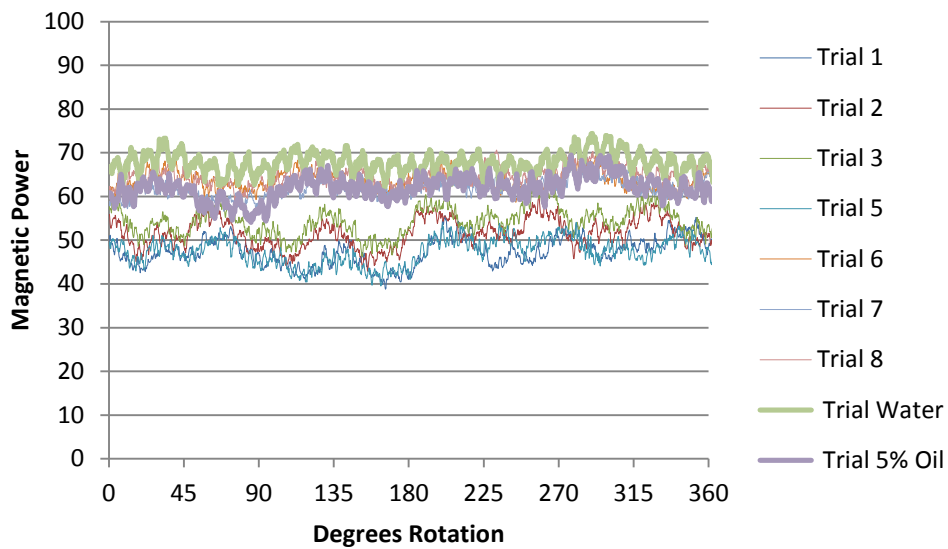


**Figure 183** Barkhausen Magnetic Noise (BN) signal of the Hexagonal Boron Nitride (hBN) trials, on the 51CrV steel

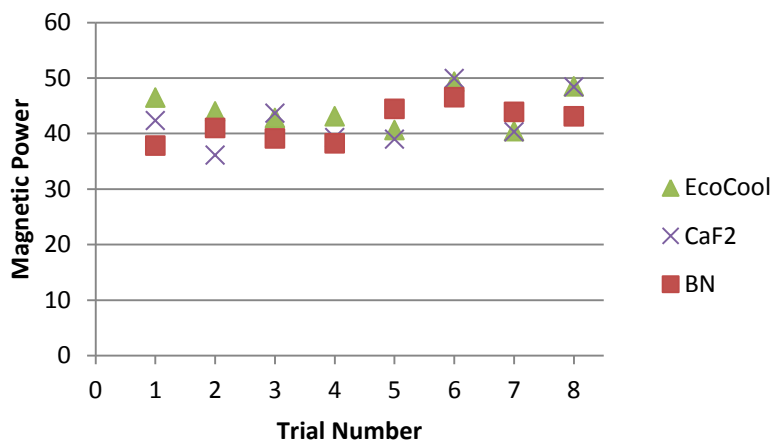


**Figure 184** Averaging Barkhausen Noise with differing lubricants between the 38Mn steel samples

The ANOVA main effect plot identifies that the mass flowrate of the Boron Nitride is very important in determining the residual stresses. The grinding wheel speed is again the most influential as shown in Figure 185. This is an encouraging outcome indicating that a higher quantity of hBN lubricant is managing to maintain more compressive residual stresses within the subsurface layer. The Barkhausen Noises results from the EcoCool, CaF<sub>2</sub> and the hBN over the same trial conditions and with the same workpiece material of 38Mn are shown in Figure 186. This shows that the EcoCool was able to achieve the lowest residual stresses over all, with the higher level of a 10% oil concentration. The CaF<sub>2</sub> resulted in a more tensile residual stress as highlighted by the elevated readings (the Barkhausen Noise axis values on the figures are identical). The hBN on the other hand managed to maintain magnetic signals that were of a similar level to the EcoCool. The mean value was similar but the actual level of influence was

slightly less. The EcoCool possesses a strong negative gradient implying a good capability to reduce the residual stresses, while the solid lubricants indicate a slight positive gradient. This positive nature is related to the difficulty that the wheel has in removing the waste solid lubricant from the pores of the grinding wheel surface. The microstructural analysis indicated that the condition of the workpiece surface was very similar to that produced by the EcoCool trials.

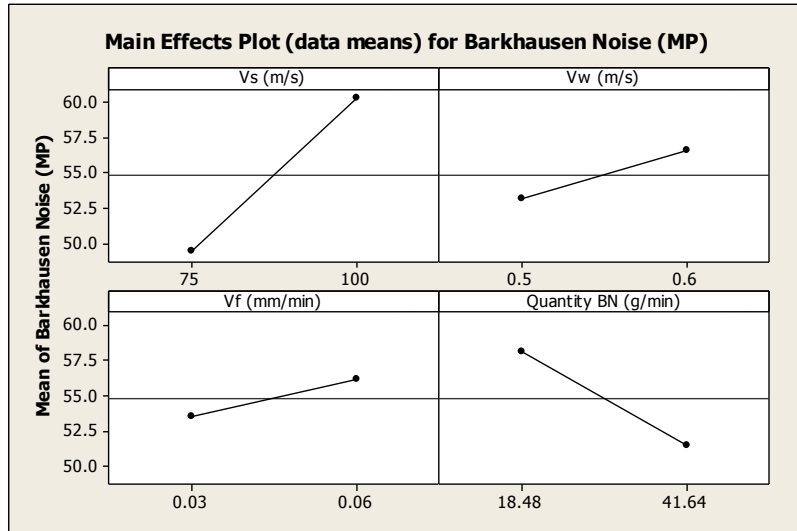


Figure 185 Significance of the addition of Hexagonal Boron Nitride on the residual stresses using factorial levels of BN of 18.4g/min and 41.6g/mi

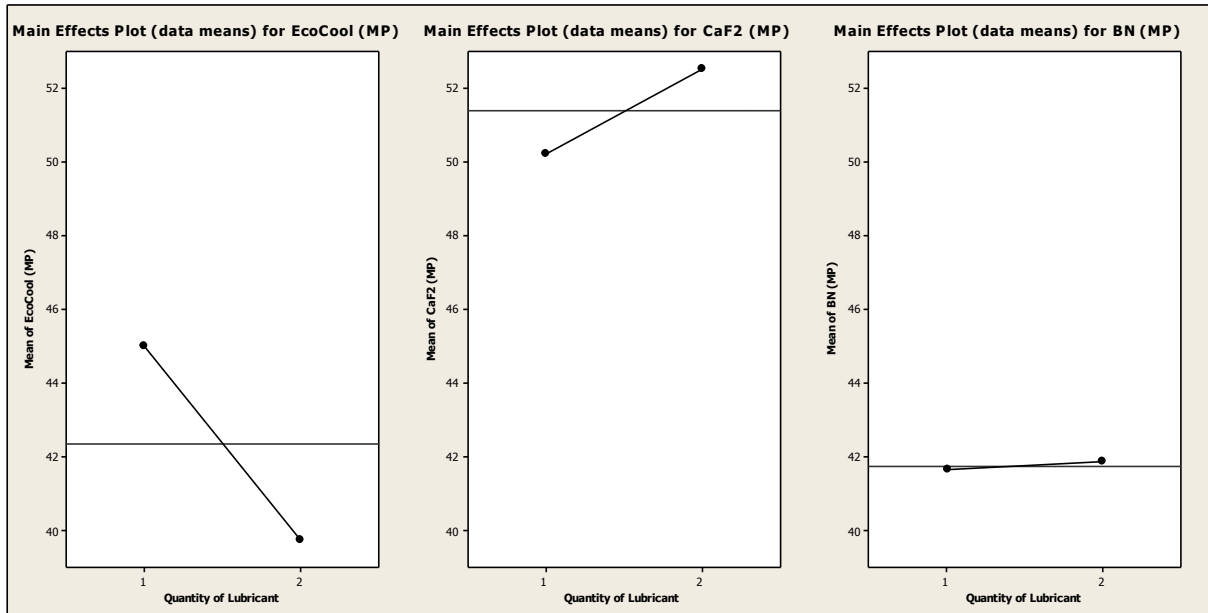


Figure 186 Overall residual stress effects from the levels of lubricant added into the grinding zone.

---

## 6.6 Wet and Dry Dressing

This section includes an analysis with respect to the preparation of the grinding wheels. The introduction of MQL useful flowrates required the careful monitoring of the condition of the grinding wheel surface. The topography of the wheel required constant dressing to guarantee similar wheel conditions for each plunge. Although some grinding regimes do utilise continuous dressing techniques it was acknowledged that this amount of wheel wear would be avoided by industry. However, for the purposes of this research this frequency of dressing was deemed acceptable.

The development of the electrostatic delivery system initially suggested a move towards the total elimination of machining fluids. There were two motives to remove the fluid within the grinding machine; to prevent large losses of the electrical forces to be conducted away through moisture, and to progress towards dry grinding. The implications are also beneficial towards reducing the financial burdens of the use of fluids within industry. In industry the dressing fluid flowrates normally remain similar to those of the grinding operations, as this simplifies the production process; saving time, equipment and programming. The eventual application of dry powders through the electrostatic process however, would require both the dressing process and the grinding trials to be dry.

This section investigates the implications of dry grinding with a solid lubricant. The grinding wheels were dressed and conditioned as listed in the methods Chapter 4.0. However, as noted within the literature review the machining fluids provide many necessary and functioning attributes throughout the grinding process. These included; cooling, lubricating, flushing, and protecting the workpiece from corrosion. Initial stages of dry dressing indicated that the dresser was able to penetrate the grinding wheel, to provide a clean dress. The surface of the grinding wheel appeared unloaded and open. The dressing wheel was acknowledged as contacting the surface of the grinding wheel though the helical witness lines upon the traversing motion of the dresser. However the audible conditions and the rotational speed of the dressing spindle would quickly indicate that the dressing process was unstable. The dressing wheel spindle would speed up to a high audible frequency each time the dresser contacted the grinding wheel. This suggested that the grinding wheel was speeding up the dressing wheel, effectively matching the outer periphery speeds. Therefore no active dressing was taking place under dry dressing.

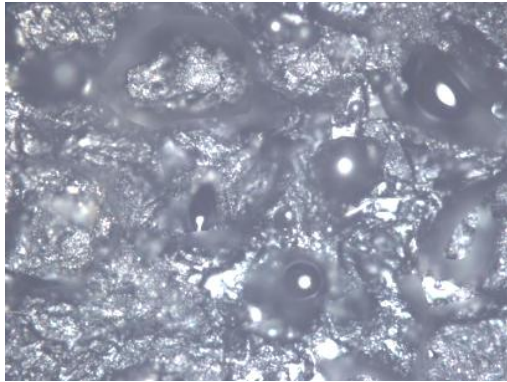
Machining fluids are traditionally delivered throughout the stages of dressing in order to encourage stable conditioning of the grinding wheels, throughout various stages of production. This is predominantly for the cooling effect. The diamond dressing wheels are exposed to extreme temperatures when opening and forming a grinding wheels

---

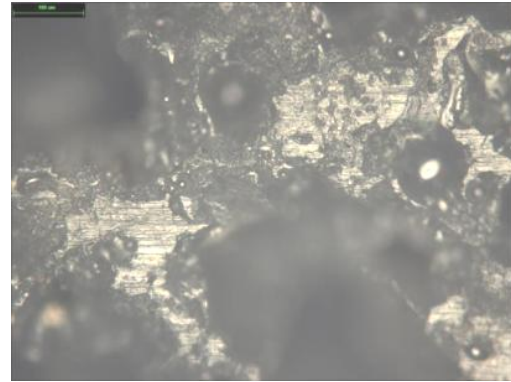
surface. The structure of the dressing wheel began to transform under higher thermal loads. The metal bond material (used to secure the diamond) began to soften with the higher thermal conditions, and as a result the diamond grit was pushed into the bond. The resulting loss of diamond from the immediate surface reduced the free cutting action of the dressing wheel. At this point the dressing wheel surface had become clogged and smeared. As a consequence both the grinding wheel surface and the dressing wheel surface were damaged beyond practical use. The grinding wheel required an extremely deep dressing pass with cooler running parameters in order to regain an open and sharp surface. The dressing wheel on the other hand needed to be rebuilt.

Figure 187 illustrates an example of the major differences attained through the delivery of a machining fluid to the dressing regime. They show the surface conditions of the same B90 vitrified bonded grinding wheel under the two instances. The addition of the fluid can be clearly seen to allow the grinding wheel to maintain open pores between the grits as seen in Figure 187a. The fluid exposes the abrasive grits, removes debris, flushes away the swarf and clears any redundant bond. This exposure of fresh grit and new abrasive surfaces encourages a more successful abrasive penetration into the substrate, in order to remove material.

At the other extreme, the completely dry dressing parameters caused quite some problems generally associated with the grinding wheel loading up. Figure 187b is an impression of the grinding wheel made just moments before the diamond dresser exploded under stressful conditions. The analysis of the bond indicated that the bond began to soften due to the lack of fluid. Not only did the lack of fluid increase the thermal stresses due to a lack of cooling but the grinding wheel had little resistance to clogging as there were no means to be cleared or flushed out. The horizontal tool forces were also increased by the traversing path of the dressing wheel. The grinding wheel loading began to peel the diamond dresser metal bond away from the dresser's steel body. The thermal energy was then conducted into the depths of the metal bond resulting in the diamond grits being forced down into the surface. This effectively lost the dressing wheel any cutting capability and that eventually led to the failure of the bond under brittle fracture. Figure 188 illustrates an example of the diamonds being depressed down into the metal bond matrix of the dressing wheel effectively hiding from any contact with the grinding wheel surface before the forces become increasingly difficult to withstand when traversing across the width of the wheel. The observations from dressing the wheel under these conditions is listed in Table 25.



a)



b)

**Figure 187** a) Grinding wheel surface post wet dressing, open wheel b) Grinding wheel surface post dry dressing, closed and clogged wheel surface (same scale)

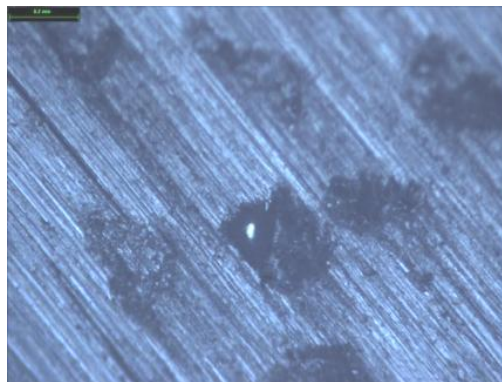


**Figure 188** Diamond dresser surface post dry dress. Diamond is removed or depressed into the softening metal bond.

**Table 25** Practicalities of Dry Dressing vs. Wet Dressing

|   |
|---|
| <b>Dry Dressing</b>   |
| <ul style="list-style-type: none"> <li>• Not practical to Dress dry – Clogged Vit Wheels &amp; Damaged Dressing Wheels</li> <li>• Extremely hazardous to only provide dry powder:               <ul style="list-style-type: none"> <li>• Fine particle dust; H&amp;S intensive.</li> <li>• Light dust covers machine components inc. Lens, contacts,</li> </ul> </li> <li>• No wheel cleaning occurring</li> <li>• Swarf and powder building up in machine</li> <li>• Large volume of wheel periphery removed through dressing</li> </ul>             |
| <b>Wet Dressing</b>   |
| <ul style="list-style-type: none"> <li>• Dressing wet – Maintains condition of diamond and dresser bond</li> <li>• Conditioning wet – To ease clogging of the wheels</li> <li>• Water supplied with Solid lubricant powder:               <ul style="list-style-type: none"> <li>• Less particle dust; H&amp;S friendly.</li> <li>• Fluid weight is easier to control i.e. Clear the lens</li> </ul> </li> <li>• Wheel self cleaning</li> <li>• Flushing of the chips from machine</li> <li>• Less grinding wheel wastage through dressing</li> </ul> |

---

Confocal images of the D40 dressing wheel surfaces after dressing with and without a fluid (water) are shown in Figure 189, Figure 190 and Figure 191. These demonstrate the extent to which the active diamond grit concentration has been lost due to high thermal stresses in the metal bond. Under the dry dressing conditions there are less visible signs of the diamond grits. This indicates that they have either been pushed into the surface, or pulled out. Nonetheless they are made inactive by the metal bond smearing over the dresser surface. The extent of the physical and thermal interaction in dressing is enough to destroy the composition of the dressing wheel, making the diamond redundant. The grinding wheel began to grind away the dressing wheel, rather than the other way round. The resulting topography of the grinding wheel under these dressing conditions is shown by Figure 192 and Figure 193. These images are from dressing the wheel with and without water under identical dressing parameters as listed in Chapter 4. The scaled area of these images is identical, enabling the difference between the two topological conditions to be observed more easily. The images demonstrate the capability of the dressing process. Under normal operation the dressing wheel was able to 'open' the grinding wheel. On the other hand the dry dressed wheel indicated an extreme degree of loading. The dry dressed wheel appeared to be loaded to a consistent height with very few inter-grit spaces. The surface void depths are shown to be approximately 4 times deeper with the fluid than that of the dry conditions. The deeper voids indicate a more effective surface for an efficient formation of a chip.

The dressing parameters were adjusted to enable stable conditions, and the metal bond of the dressing wheel was re-designed with a new composition to withstand high thermal conditions. The use of dry dressing however remained too unstable to continue as part of this research as the limited supply of dressing wheels were beginning to show signs of stress, losing diamond grits, and one particular dresser exploding within the machine.

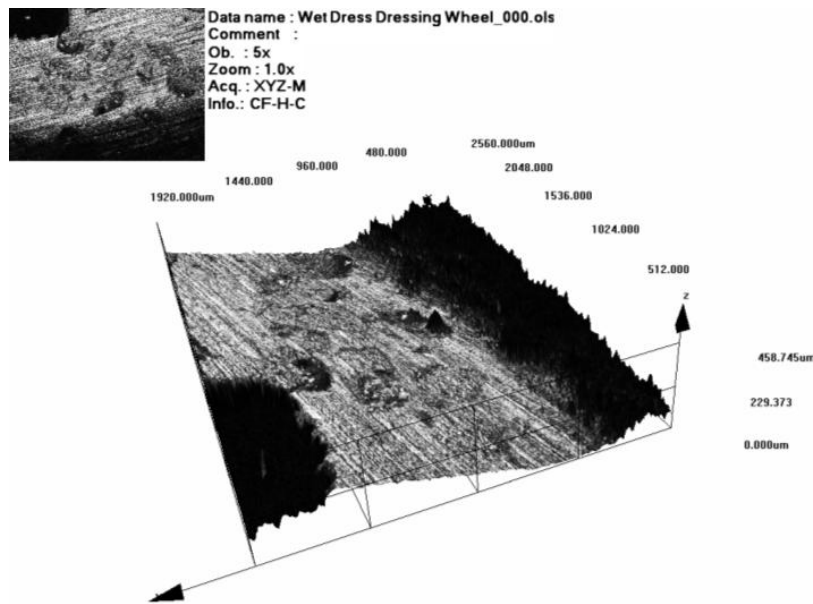


**Figure 189** Dressing wheel surface with added water to the dressing regime. Exposure of the diamond grit remains intact and the active cutting provides successful dressing to the vitrified bonded wheel.

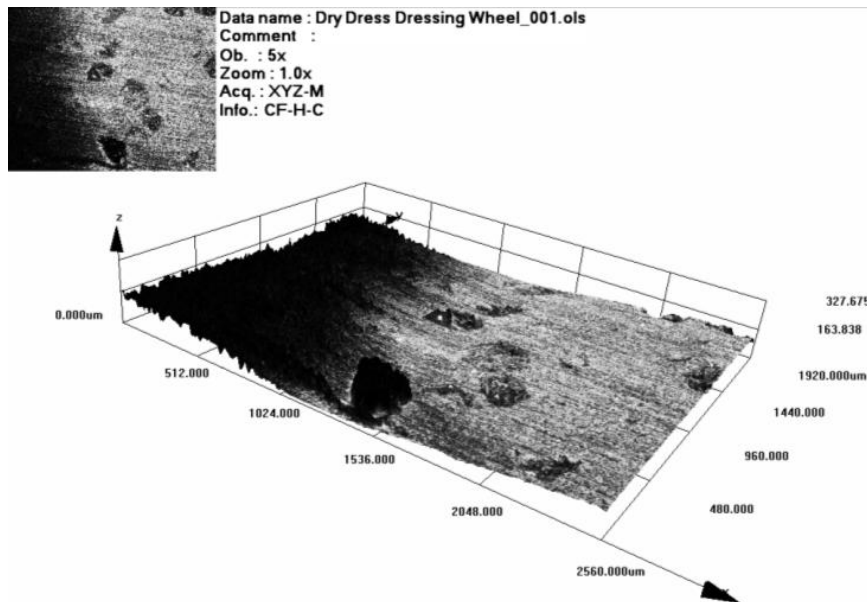


**Figure 190** Dressing wheel surface with no added water to dressing regime (dry). The contour of the dressing wheel is particularly flat indicating a loss of active diamonds. On inspection it appears that the diamond has been pushed into the metal bonded surface (take note of the z axis scale, also shown in ) through an increase in thermal exposure when interaction with the grinding wheel.



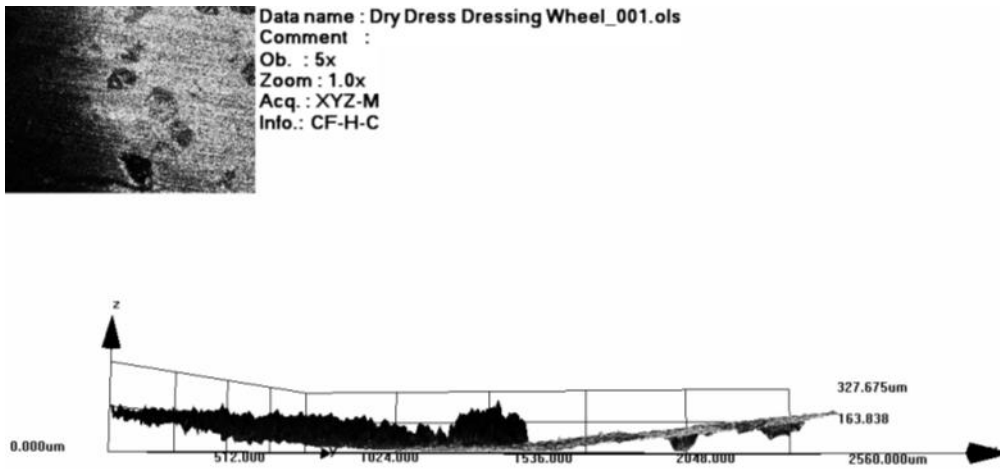


**Figure 191** Cross section of dressing wheel surface after dry dressing. The right hand side of this figure demonstrates the smoothed surface of the dressing wheel resulting in a loss of free cutting diamond.

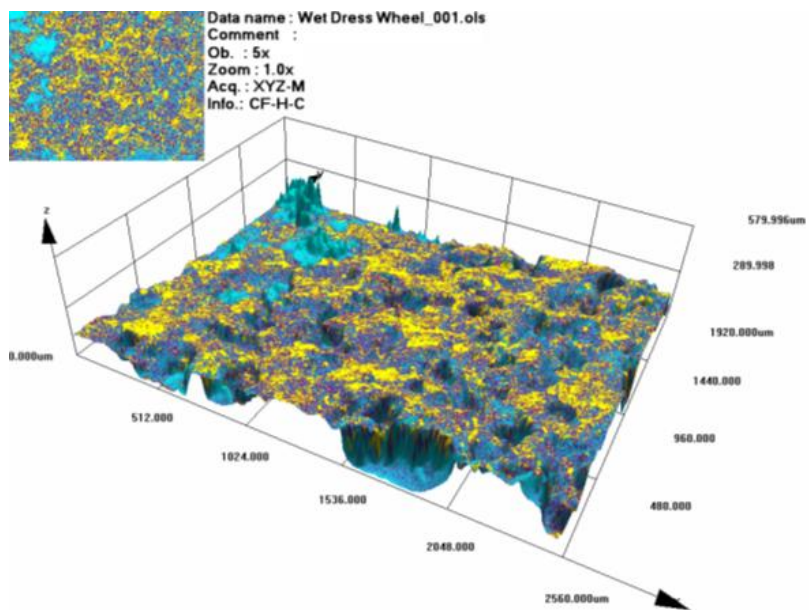


**Figure 192** Illustration of porous volume after adding water to the dressing process. A Confocal surface map illustrating the open porous volume of a successfully dressed wheel through the use of water. The colours and scales are identical to that of Figure 193.

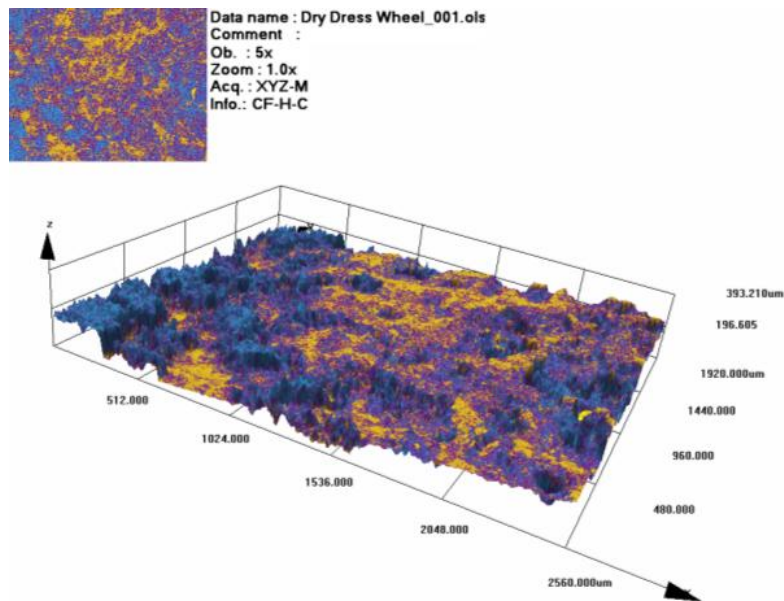


**Figure 193** Confocal surface map of grinding wheel after dry dressing under identical conditions. The grinding wheel surface is clearly loaded showing a no obvious signs of grits or porous volumes. The diamond dresser was unable to penetrate the  $\text{CaF}_2$  bond wheel in order to remove clogging and expose useful cBN grit.

The observations made between the water only and the completely dry dressing showed an inability to introduce dry dressing. A development of the dressing tooling and an understanding of the dressing technique are needed in order to successfully establish dry dressing. Attempts to cool the diamond were made with a compressed air jet, in order to maintain a moisture free environment. The jet was directed towards the dresser surface when contacting the grinding wheel, but this appeared to make no noticeable difference. A secondary air jet was also used to scrub the grinding wheel surface, to encourage the release of swarf and bond out from the wheels surface, but this too made little difference in exposing fresh grit.

Due to the issues associated with dry dressing the dressing parameters were re-assessed. The dressing and grinding wheels were degrading too quickly under these extreme conditions. In order to progress with the experiments it was decided to dress the wheels under wet conditions. This was to prevent unreasonable waste and destruction of the diamond dressers. Once dressed the wheels were then conditioned in order to settle in the active grits and remove any friable pieces, and stabilise the performance of the grinding wheels. This enabled the experiments to continue under the MQL, MQSL and dry grinding conditions.

---

## 6.7 Electrostatic Dry Machining

The electrostatic delivery system was installed on the SAT machine. As noted before the intent was for the system to function under a moisture free environment. This would enable the true determination of the effectiveness of the dry solid lubricants and avoid any conduction of heat likely to occur with fluids. The practicality of the electrostatic delivery system would also be tested. The reason for reducing the moisture was to eliminate any diverting conducting bodies for the charged particles. This would weaken or distract the electrostatic attraction between the positively charged solid lubricant particle and the grounded workpiece body.

An example of using the electrostatic delivery system is illustrated below in Figure 194 with an application of  $\text{CaF}_2$ . The workpiece was insulated in the headstock of the machine, in order to prevent any loss of attractiveness from the charged solid lubricant. The grounding rod was spring loaded and positioned onto the sample close to the headstock, away from any obvious zones of mechanical conflict. A small amount of copper-slip was added between the rod and sample, to maintain the metallic contact as the headstock rotated.

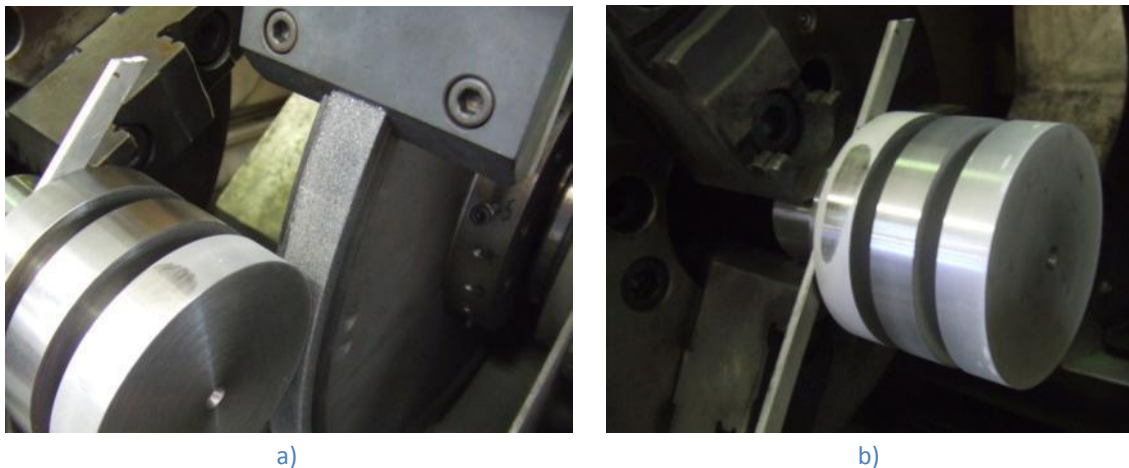


**Figure 194** Images demonstrating the solid lubricant attraction to the workpiece and grounding rod (notice the finger marks on workpiece surface)

The preliminary trials of this system were encouraging. The machine had previously been dried to ensure it was moisture free in order to avoid interference. The grinding wheel was spun at 100m/s after each dressing pass for 2 minutes in order to remove any fluid from the porosity of the wheel. The sample was checked for electrical isolation against the rest of the machine before establishing a stable grounding position. The grinding wheel was always made to spin before the feeding mechanism was turned on, in order to prevent possible clogging of the nozzle passages. The lubricant flows easily out of the tight opening of the shoe nozzle when the wheel spins.

---

There was a high amount of air disturbance from the rotating wheel however the shoe nozzle enabled the lubricant to be accurately targeted towards the grounded sample. The CaF<sub>2</sub> was attracted to the surface of the workpiece with a film of lubricant. The CaF<sub>2</sub> was completely covering the surface of the rotating sample. All the necessary system controls were kept outside of the grinding environment while the power and air supply lines feed into the rear side of the SAT machine.

A series of trials was undertaken using dry grinding conditions with the CaF<sub>2</sub> solid lubricant (zero machining fluid). In the interest of managing the tool life expectancy of the grinding wheel, the machining parameters were maintained at the lower levels from the Taguchi trials. The test then randomly varied the quantity of the CaF<sub>2</sub> solid lubrication between the ranges of 0 to 4 bar pressure under the pneumatic system. This air pressure feed system equates to a range of 0g/min to 78g/min of CaF<sub>2</sub>. The purpose of this trial was to establish the effectiveness of the electrostatic attraction against the air disturbance generally associated with a high speed rotating grinding wheel. . The electrostatic feeder relies upon the pneumatic flowrate to determine the mass flowrate of the solid lubricant that is then collected and directed through the electrode. The pneumatic nature of the delivery system could also influence the ability of the charged lubricant to stay coupled to the workpiece surface.

The results from this trial feature in Figure 195 and illustrate the SGE against the increase of CaF<sub>2</sub>. The CaF<sub>2</sub> was charged as it passed the electrode. The shape of the curve suggests a possible relationship between feed pressure and the success of applying a lubricant into the grinding zone. At the zero feed pressure (0 bar) of CaF<sub>2</sub> the SGE are found to be at a high level, indicating dry conditions. A small mass flow of the CaF<sub>2</sub> is added (0.5 bar at 9 g/min) and the SGE values drop by approximately 18J/mm<sup>3</sup>, a 22% reduction, a considerable difference. Over the range of mass flowrates of CaF<sub>2</sub> the SGE values are seen to respond in an explanatory manner. The dressing and the conditioning stages of the experiment were identical. The influence of the CaF<sub>2</sub> depends upon the pressure of the feed system. This indicates that an optimum mass flowrate for the feeds and speeds of this regime must exist. The lubricant supply rate must be carefully identified. The saturation point of the CaF<sub>2</sub> in the grinding zone is about the 27g/min (1.5 bar) feed rate. The lack of fluid in the system creates a complication in the wheels ability to self cleanse as the less dense powder begins to compact into the periphery up to a point of 79g/min (4bar) at which point the machine was so heavily filled with powder that it was almost impossible to imagine that the lubricant was not entering the grinding zone. The implication of the higher mass flowrates was that the CaF<sub>2</sub> was managing to find itself everywhere; in the grinding zone and in the atmosphere of the workshop. Therefore the higher level of CaF<sub>2</sub> is functional, however also highly impracticable. A selection of

---

microstructural images are shown in Figure 195. The highest SGE value was found when applying a 2.5bar pressure supply of  $\text{CaF}_2$ . This was beginning to put intense thermal conditions into the machining process causing damage to the surface and subsurface layer of the samples. The visual inspection of the freshly ground sample bars showed that the surface appeared to have a varying degree of chattering, These related closely to the conditions of the recorded SGE values. The high SGE values revealed a degree of white layer below the surface, indicating a hardening and a transformation of the microstructure. The degree of burn that occurs at the 2.5bar feed pressure indicates that the combination of the high flowrate of air (from the the pneumatic feeder) reduces the ability of the  $\text{CaF}_2$  to maintain its electrostatic attraction, on the surface of the workpiece. The air movement and turbulence around the region of the work zone was too great. This results in the  $\text{CaF}_2$  being lost in the system and the grinding condition is left effectively empty of lubricant, shown by the highest recordings of the SGE value. The air pressure at this point is thought to be too high to be of benefit. The high air pressure is too aggressive and although it remained effective in feeding the powder into the nozzle, the airflow was too high and overcame the electrical attraction of the grounded workpiece.



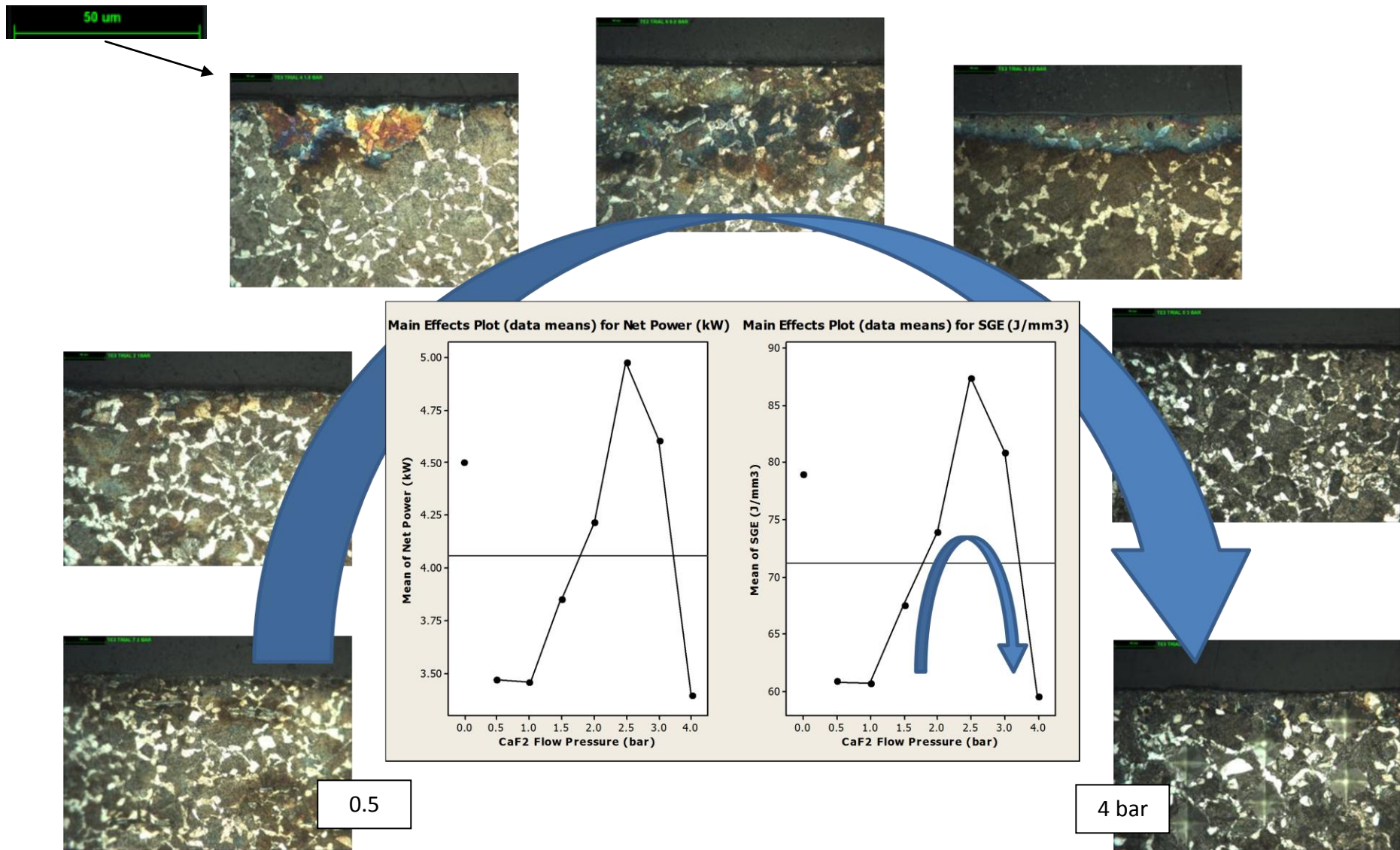
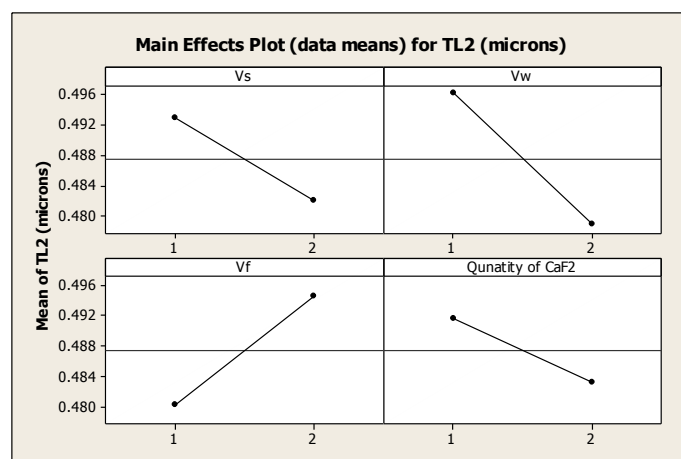


Figure 195 Microstructural images from the electrostatic trials, illustrating the subsurface conditions resulting from a variation of charged CaF<sub>2</sub>, from 0 bar pressure to 4 bar air pressure (clockwise from left to right).

The trends in the subsurface damage appears to be linked to the recorded SGEs. This conforms with existing theories. The energy required to form a new surface must be partitioned between the wheel, the workpiece, the chip and the grinding fluid. In this instance there is no fluid to conduct the heat away. However the results show that the SGE can be controlled though maintaining a suitable quantity of lubrication on the surface of the workpiece.

The surface roughnesses were recorded over the Taguchi variatons in the mass flowrate of the CaF<sub>2</sub> see the ANOVA plot in Figure 196. A positive trend is shown between the quantity of lubricant and the surface roughness values. Increasing the CaF<sub>2</sub> provided a small reduction in surface roughness. The CaF<sub>2</sub> however produced surface roughness values that were approximately twice as bad as the EcoCool and the hBN under the MQL conditions. This implies that the conditions of the dry grinding with solid lubricant are damaging to the surface integrity. The use of CaF<sub>2</sub> was earlier noted to be detrimental to the surface roughness. However, the later investigation into the tribo-luminescent properties of CaF<sub>2</sub> was the main reason for using it as a solid lubricant at this stage.



**Figure 196** Main effects on the surface roughness Ra with the change in level of CaF<sub>2</sub> introduced under the electrostatic delivery system. An increase in the mass flowrate of the solid lubricant is seen to improve the actual surface finish. However the average roughness still remains relatively poor in comparison to when using any fluid.

## 6.8 Temperature measurements and modelling

The depth measurement of the PVD film isotherms enabled the maximum finish surface temperatures to be determined. The depths were measured by a combination of microscopy and confocal analysis. The melting temperatures of Zinc, Bismuth and Indium typical examples are shown in Figure 197. These images demonstrate the typical developments of the isotherms, as they regress from the source of heat provided by the grinding cycle on the surface. Once the depths are measured they are plotted against the melting temperatures. The thermal trends are then traced backwards to the zero depth position, thus determine the surface temperature.

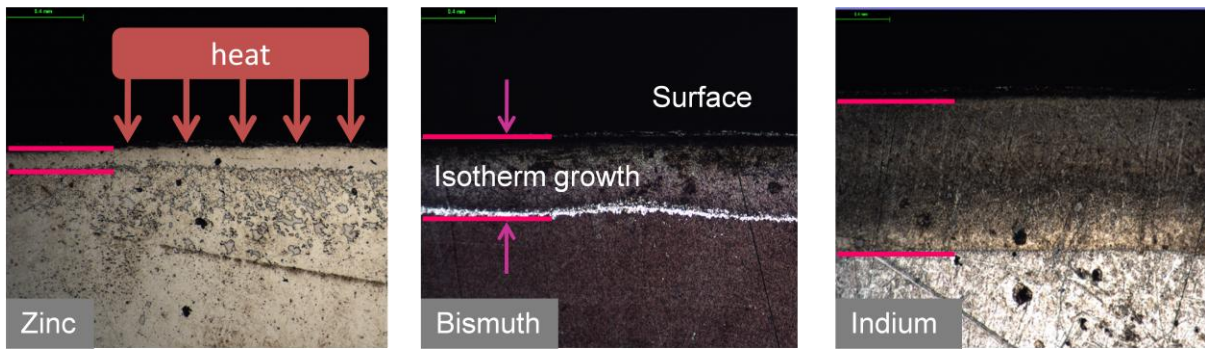


**Figure 197** Development of PVD isotherms after surface exposure to cylindrical grinding. (Scale bar = 0.4mm)  
 (Left to Right) Zinc with a melting temperature ( $T_{melt}$ ) of 419°C, Bismuth  $T_{melt}$  271°C and Indium  $T_{melt}$  155°C

The PVD films were deposited onto the pre-prepared polished surface of the 38Mn steel sample slices. Figure 198 illustrates the measurement of the thickness of the PVD layers. The film heights were scanned to determine the PVD film thickness, providing a confidence in the films ability to perform under the expected grinding conditions. This image shows the cross-sectional height of the Zinc PVD film. Several height positions are recorded to determine the mean value.

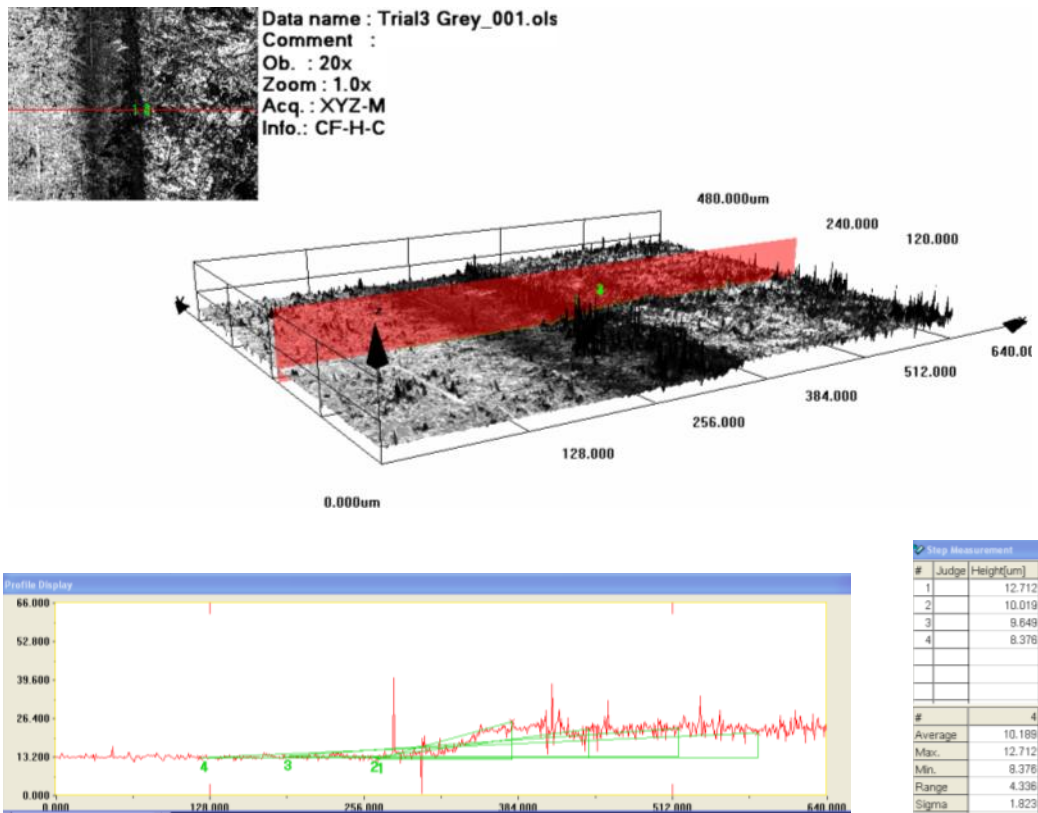


**Figure 198** PVD Height Con-focal Scan inside step

The PVD sample bars were assembled before the Taguchi trials. The PVD coated discs were clamped together with identical blank discs, replicating the cylindrical steel samples that were used in the previous MQL trials. The PVDs were then subjected to the heat source of the grinding process. Figure 199 shows a fully assembled PVD sample bar shortly after being

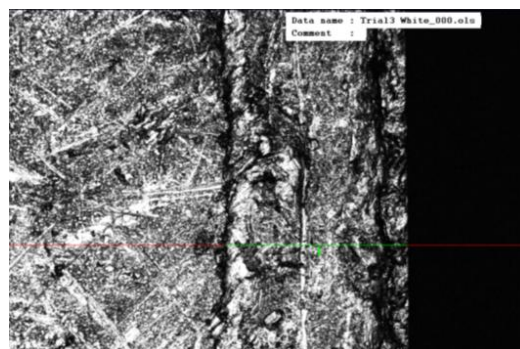


exposed to a hBN solid lubricant trial. The surface of the steel appears untarnished and the dividing surfaces between the PVD discs and the blank discs are not visible.

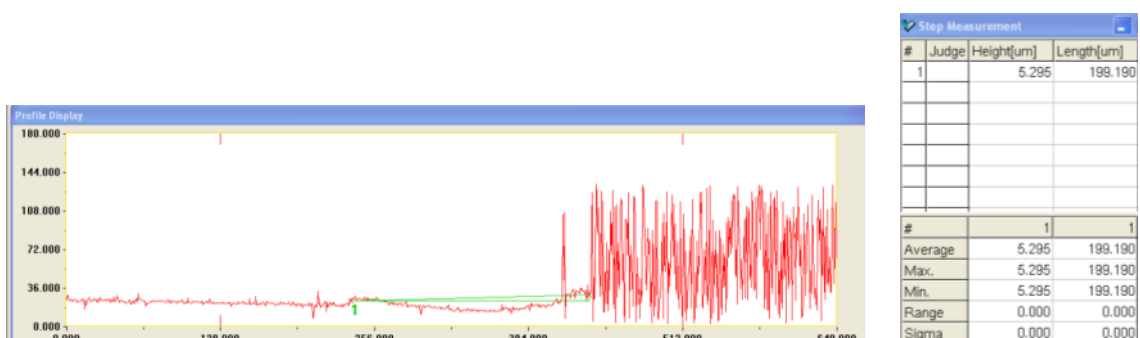


**Figure 199** An image of a PVD sample bar after machining.

The sample bars were then disassembled, carefully avoiding interference or damaging the melted isotherms of the PVD films. They were then promptly analysed to avoid any errors occurring through the onset of corrosion or oxidation on the surfaces. The outer surface of the samples revealed the melted zones immediately below the newly ground surface. Examples of the con-focal imagery used to measure the isotherm depths can be seen in Figure 200 and Figure 201. At least 10 depth measurements were taken for each sample to provide confidence in the temperature determination.

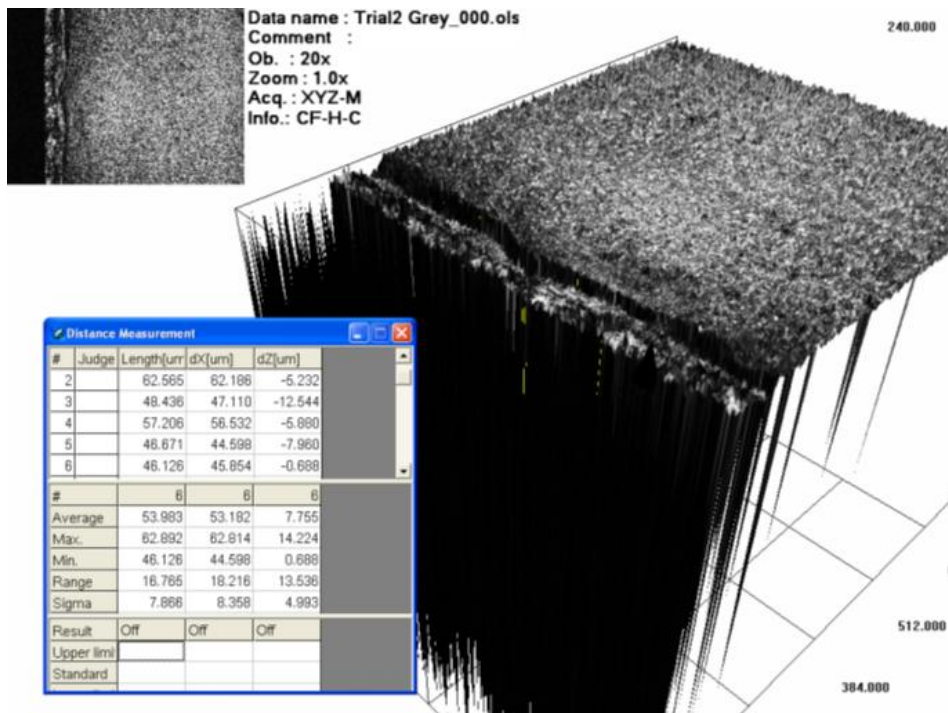


a)

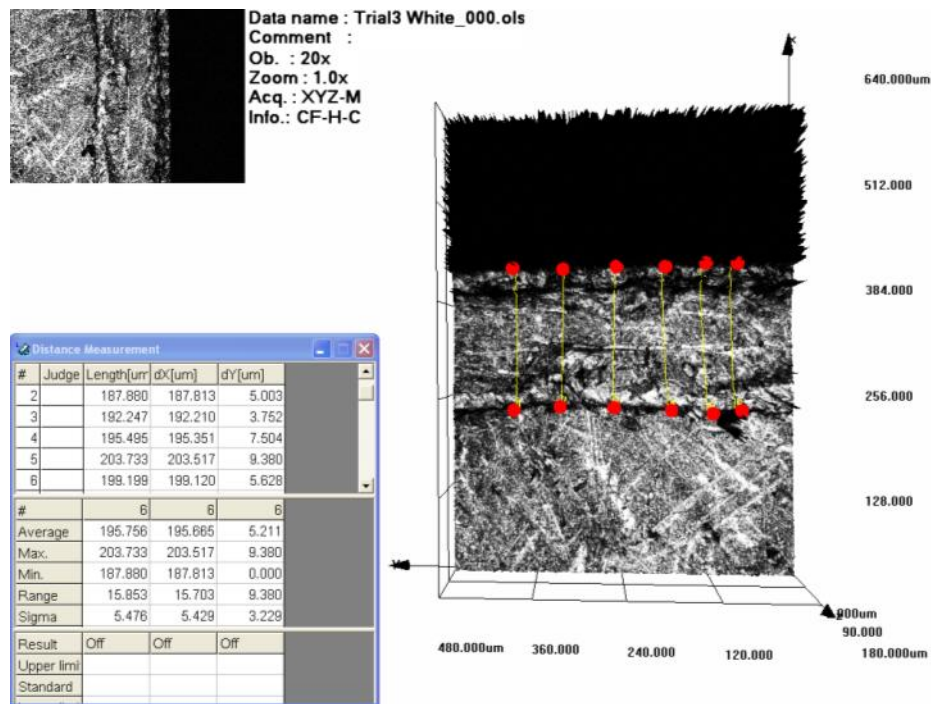


b)

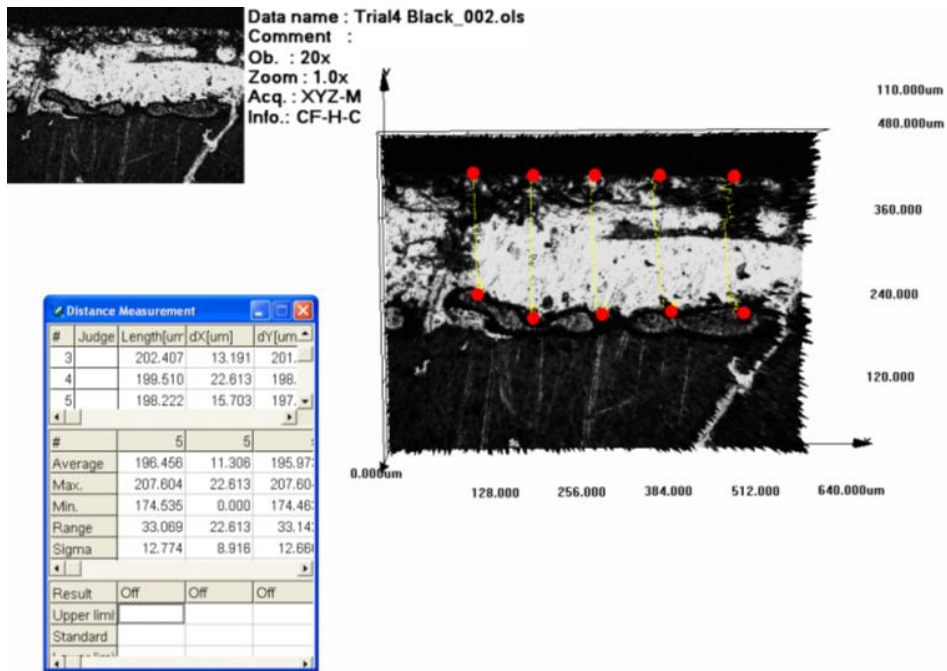
**Figure 200** The PVD melt zone for Indium a) overhead image showing the isotherm melting away from the newly ground surface b) the confocal cross-section of the melt zone from the newly ground surface showing the isotherm distance from the edge of the sample (microns).



a)



b)



c)

**Figure 201** Confocal Analysis of PVD melting depths (microns) showing the differences in the depths of isotherm of a) Zinc (without sharp edge filtering) b) Indium (filtered) c) Bismuth (filtered). The contour of the melt zone is detectable both from microscopy above and through con-focal surface height measurement.

The melting depths were plotted against the melting temperature values as seen in Figure 202 illustrating the PVD isotherm depths of CaF<sub>2</sub>. The surface temperature was established by tracking towards a zero melt depth, and is identified as the y- axis intercept. This was repeated for both the CaF<sub>2</sub> and the hBN trials, allowing a comparison between the two solid lubricants. The most extreme combination of the machining parameters trial appeared in trials 2 and trials 8. Under CaF<sub>2</sub> the difference in surface temperature between these two cases is separated from 428°C to 510°C, an 82°C difference. Figure 203 on the other hand illustrates the temperatures associated with Boron Nitride indicating a 412°C -471°C range, a difference of 59°C. The actual values of the surface temperatures feature in Table 26.

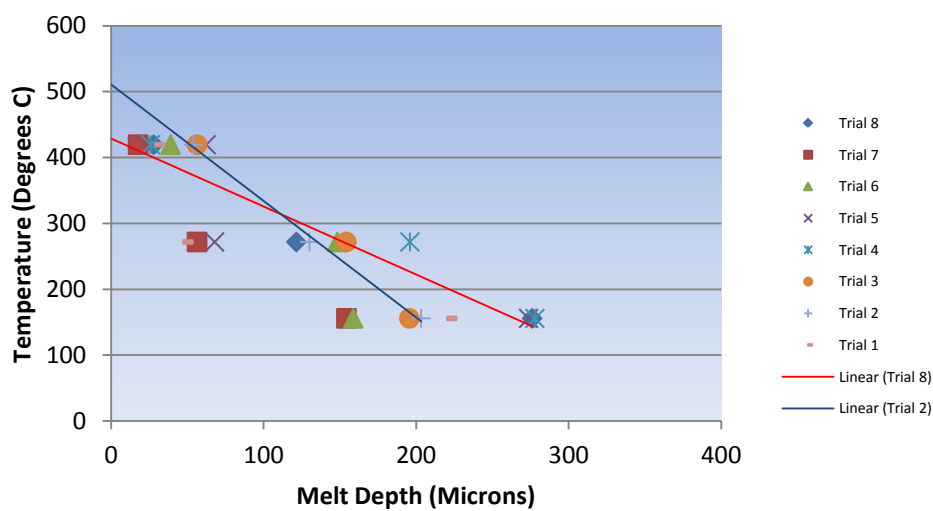


Figure 202 CaF<sub>2</sub> PVD Melting depths and surface temperatures (Example surface temp. of Trials 2 and 8)

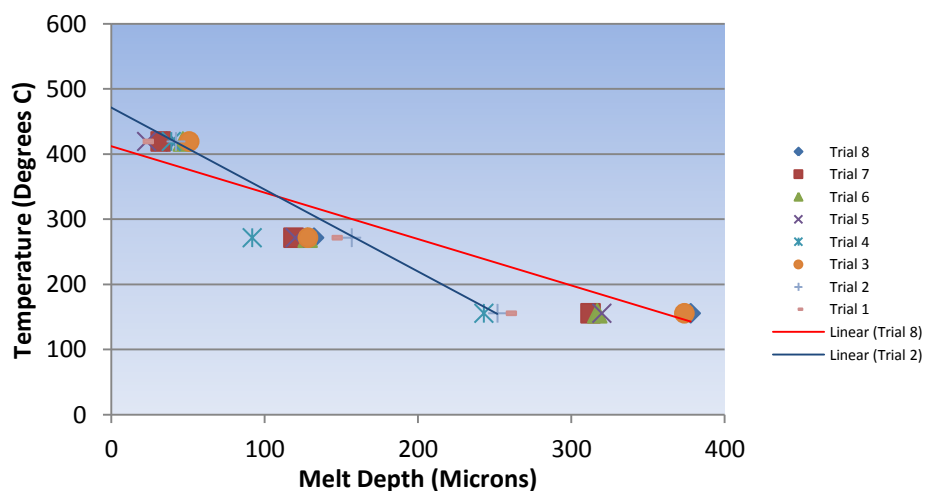
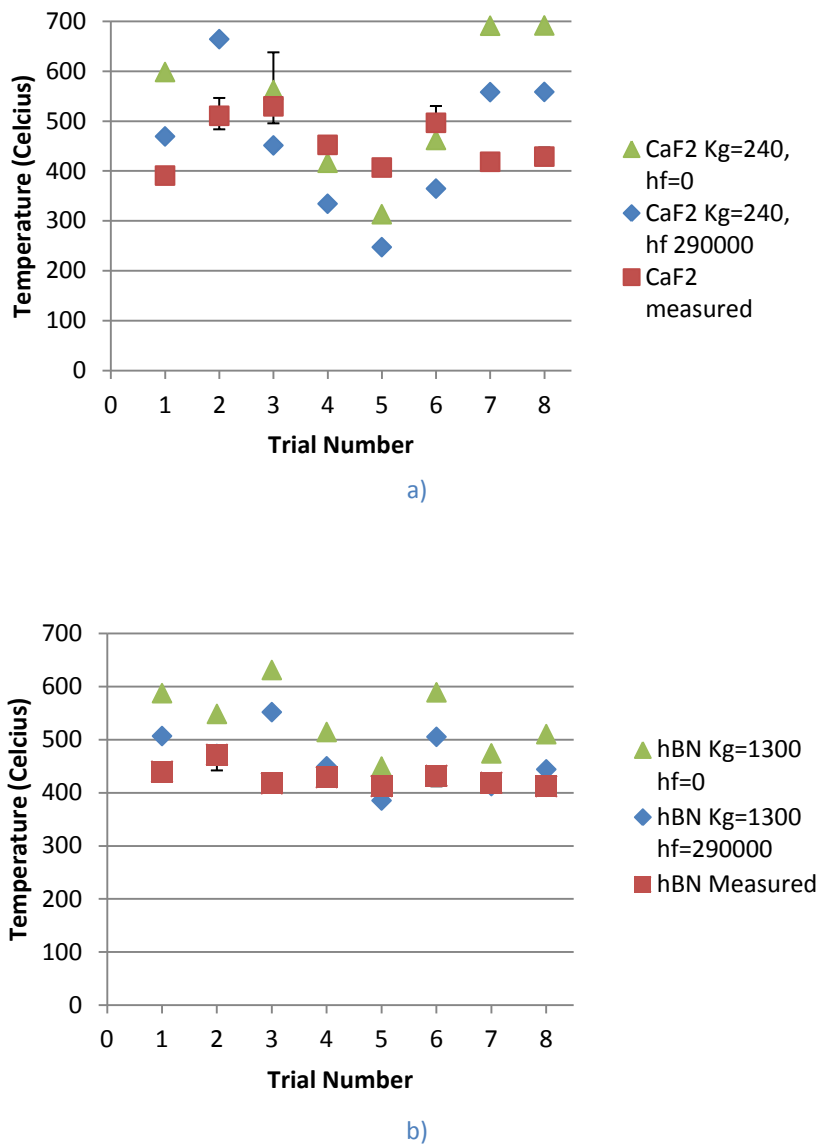


Figure 203 hBN solid lubricant surface (finish) temperatures (Example surface temp. of Trials 2 and 8)

**Table 26** Mean averaged PVD surface temperatures for CaF<sub>2</sub> and hBN lubricants

| Trial No. | Gradient<br>CaF <sub>2</sub> | Surface Temp (C)<br>CaF <sub>2</sub> | Gradient<br>hBN | Surface Temp (C)<br>hBN |
|-----------|------------------------------|--------------------------------------|-----------------|-------------------------|
| T1        | -1.0952x                     | + 390.70                             | -1.1150x        | + 439.60                |
| T2        | -1.7669x                     | + 510.59                             | -1.2587x        | + 471.44                |
| T3        | -1.8249x                     | + 529.60                             | -0.7334x        | + 417.46                |
| T4        | -1.0194x                     | + 452.26                             | -1.1774x        | + 429.05                |
| T5        | -0.9236x                     | + 406.84                             | -0.8421x        | + 412.24                |
| T6        | -1.8550x                     | + 496.50                             | -0.9123x        | + 431.83                |
| T7        | -1.7844x                     | + 418.34                             | -0.8833x        | + 418.79                |
| T8        | -1.0312x                     | + 428.70                             | -0.7127x        | + 412.08                |

Figure 204 plots the CaF<sub>2</sub> and hBN against that of the circular arc of heat thermal model relating the SGE values from the trials. The predicted range of temperatures calculated by the model relate very well to those that were measured by the PVD approach. The measured finish temperatures fall within the 400C-530°C band while the model has a band of 400C-600°C. Therefore the use of solid lubricants enables a cooler cutting than otherwise predicted by the model, particularly in the later trials with the higher wheel speeds. The model temperatures were calculated under the assumption that the thermal conduction capability of the solid lubricants was zero. The application of the MQSL therefore was seen to control the grinding temperatures through the improvement in lubricity. The thermal conduction taking place between the grit and the particles of lubricant is thought to be insignificant in comparison to the lubricative nature of the MQSL material. The Boron Nitride maintains relatively stable conditions throughout the range of machining parameters. This reflects the ability of the hBN to perform under increasingly stressful machining conditions.



**Figure 204** PVD Surface Temperatures (Celsius) shown against the model predicted temperatures for a) CaF<sub>2</sub> and b) hBN with dry conditions (hf = 0 W/m<sup>2</sup>K) and with the water carrying fluid (hf = 290000 W/m<sup>2</sup>K).

The MQSL materials of CaF<sub>2</sub> and hBN are then compared using an ANOVA main effects plot. This assesses the significance of the MQSL compounds with respect to the ability of the MQSL in controlling the thermal nature of the grinding regimes. The ANOVA main effects plots are illustrated in Figure 205 and Figure 206.

The machining parameters of the Taguchi trials were entered into the circular arc of heat model enabling the thermal properties of the tool, the workpiece and the MQL lubricant to be assessed. The front face of the GUI allowing for input parameters to be entered is shown in Figure 207a). A selection of output charts produced through the GUI coding features in Figure 207b) and c). These demonstrate a range of temperature values over a range of wheel speeds, chip thicknesses, and infeed speeds.

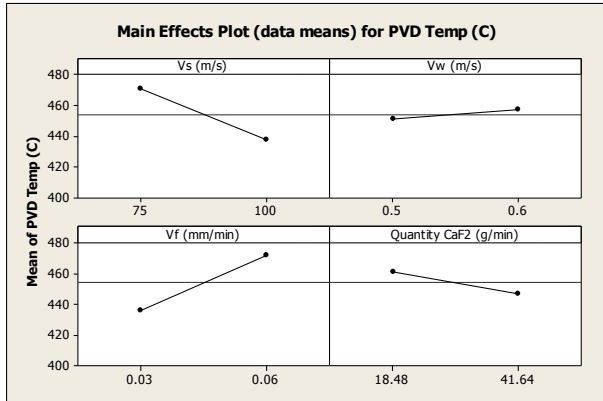


Figure 205 Main Effects on Surface Temperature ANOVA CaF<sub>2</sub>

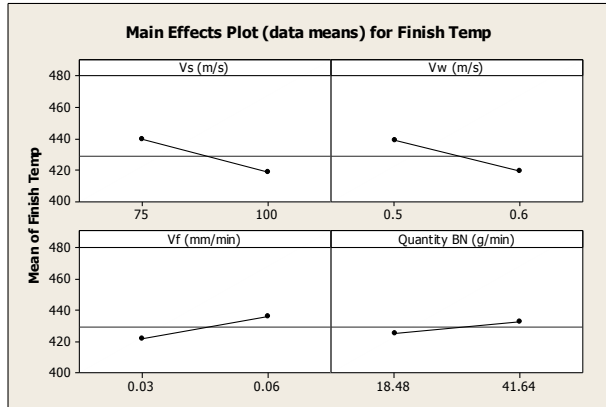
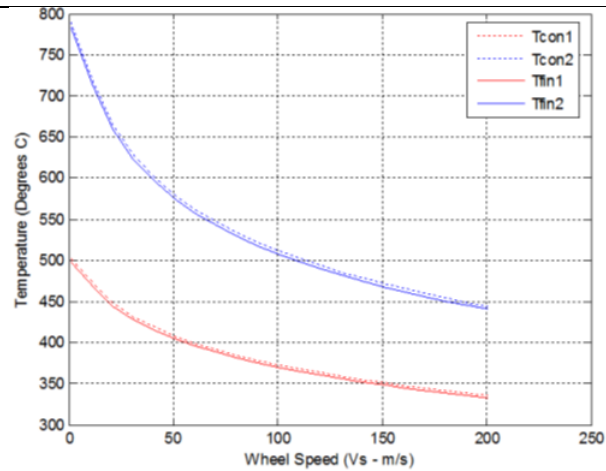


Figure 206 Main Effects on Surface Temperature ANOVA hBN

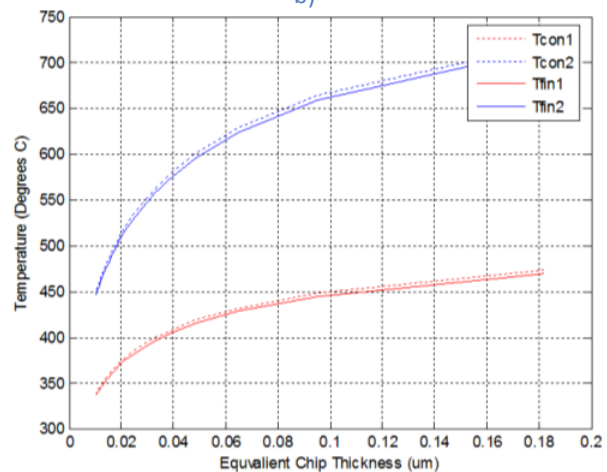


a)

Grit: cBN  
 Workpiece Material: 38Mn  
 Lubricant: CaF<sub>2</sub>  
 Wheel Speeds: 0-200m/s  
 Equivalent Chip Thickness: 0 – 0.2microns  
 Resulting temperature range:  
 Contact/Finish Temp  
 with effective cooling: 340-475 C  
 Contact/Finish Temp  
 without effective cooling: 450-725 C



b)



c)

Figure 207 a) GUI inputs showing an example of input settings linked to graphical outputs b) Wheelspeed vs. Temp, showing the trend of decreasing surface temperatures with increased wheel speed and c)  $h_{eq}$  vs. Temp, showing how at the temperatures are linked to equivalent chip thickness and the difference between cooled (red) and un-cooled (blue) predicted temperatures.

The experimental data was then entered alongside the predicted temperatures to show the correlations, an example of which is illustrated in Figure 208. This illustrates a range of specific grinding energies against the predicted finish surface temperature. There is a positive relationship between the two parameters, the higher the SGE the higher the surface temperature. Two separate lines of the predicted model surface temperature is shown offering no-cooling, or a degree of cooling from the solid lubricant respectively.

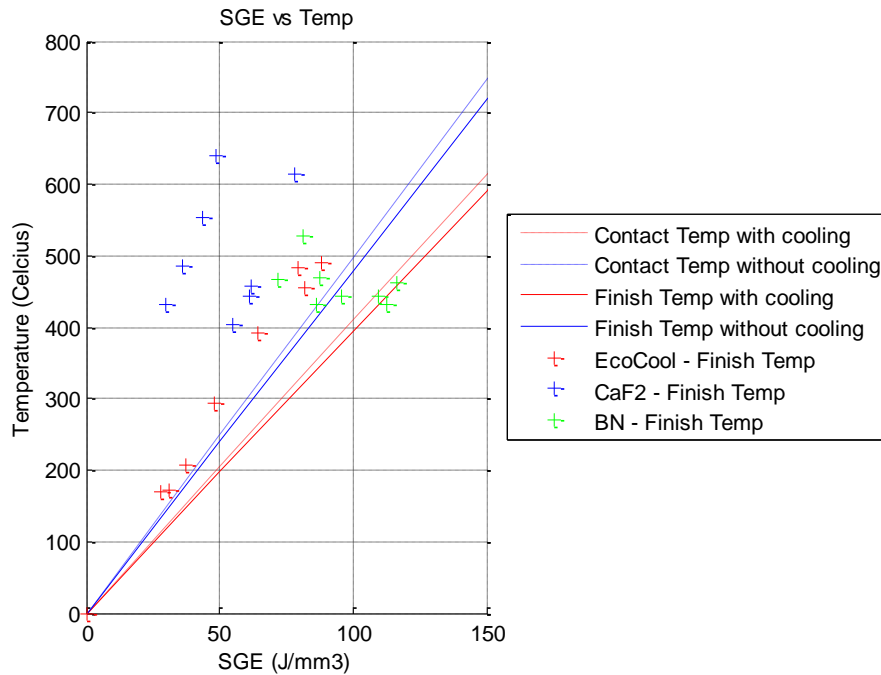


**Figure 208** Plotted series of temperatures against experimental Specific Grinding Energies with B90 wheel, 38Mn steel workpiece, using EcoCool, CaF<sub>2</sub>, and hBN lubricant.

The linear relationship shows the predicted temperatures using a high thermal conduction Kg 1300W/mK with the heat transfer of water ( $h_f = 290000 \text{ W/m}^2\text{K}$ ) and under dry conditions ( $h_f = 0 \text{ W/m}^2\text{K}$ ). The CaF<sub>2</sub> achieves lower SGE values with respect to the EcoCool however the measured PVD temperature ranges between 400-650°C. The hBN on the other hand demonstrates a small increase in the SGE values and manages to suppress the thermal conditions, ranging 400-500°C. The increase in the SGE values was attributed to slight loading of the wheel. The added benefit of the lubricant however suppresses the surface finish temperature from experiencing high process temperatures.

In addition to the temperature calculations ANSYS FEA was used to simulate the growth of the isotherms. The workpiece was modelled in SolidEdge and reconstructed with the newly identified chip volumes. The heat flux values from the Matlab GUI were then applied to the deepest chip surface that was representative of the newly ground surface. This model then calculated the thermal gradients by using a transient solver, enabling the heat flux to rise and dissipate over a given contact length. The movement of the heat on the finish surface then provides an impression of the isotherms to be seen when the grinding wheel comes



into contact with the workpiece, see Figure 209 and Figure 210. The benefit of this approach enabled the temperature distributions throughout the cross-sectional depth of the workpiece, visualising changes such as the wheel contact temperature and the depth of isotherms. The illustrations show a quarter rotation of the workpiece with respect to the action of a cylindrical grind, the symmetry of the cylindrical sample enabled a reduced period for computation. The heat flux applied to the surface was calculated using a sample processed with EcoCool resulting in a 156°C finish surface temperature that would only melt the Indium PVD. The temperature gradients are shown to move up to 12mm from the sample surface under MQL conditions. This expansion of the thermal modelling intended to provide a comparison to the PVD isotherm depths. The depths of grind of 25microns that were utilised throughout the grinding trials caused some difficulty in accurately applying the heat flux values. The principle of operation with larger depths of cut however is able to provide a clear distinction between the partition of heat between the workpiece and the chip.

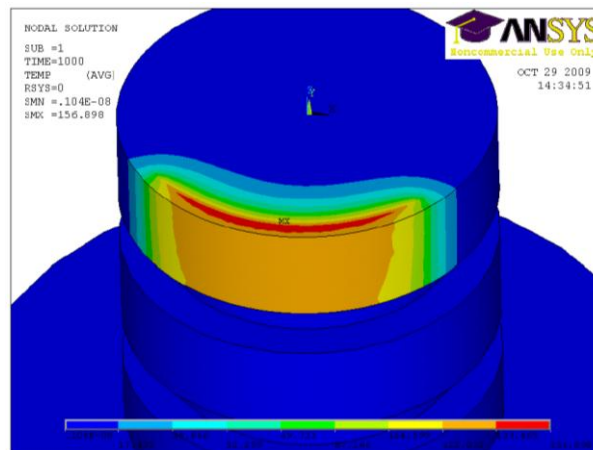


Figure 209 Transient Heat flux flow – showing depth of isotherms from newly created surface

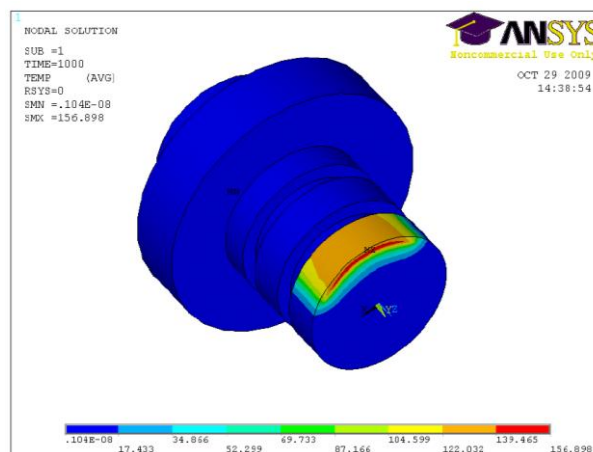


Figure 210 Illustration of heat flux application to sample surface

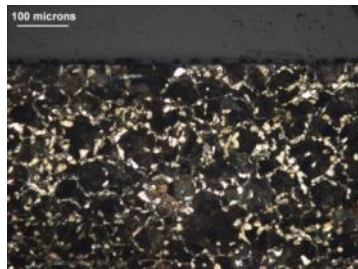
The burn threshold diagram plots the SGE of the grinding process against a function of the process parameters  $f(d_e^{1/4} a_e^{-3/4} v_w^{-1/2})$  as described in Chapter 2.0, Figure 17. Figure 211 illustrates the burn threshold diagram containing experimental trial data from the EcoCool,

---

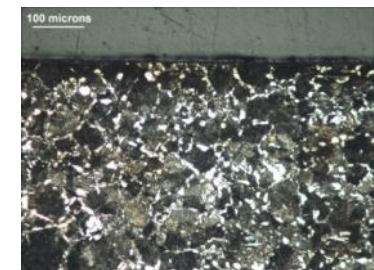
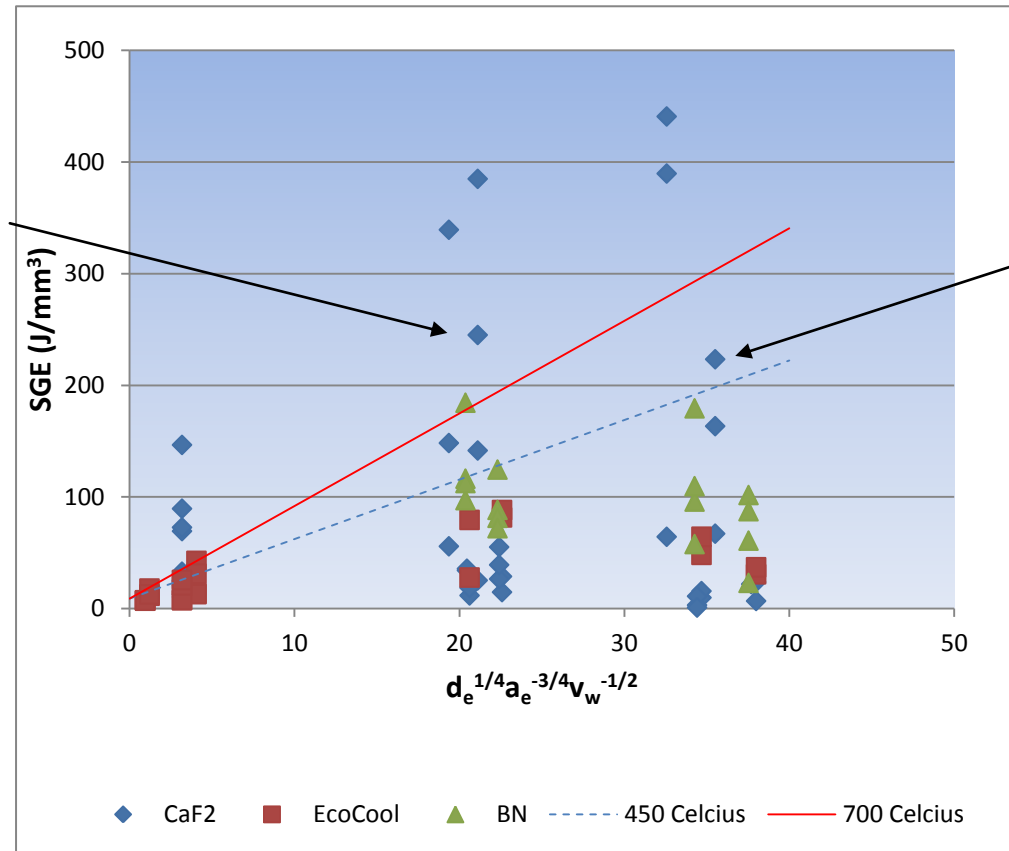
CaF<sub>2</sub>, and the hBN trials and was able to identify thermal regions from the grinding process. The figure illustrates a series of gradients relating to the surface temperature. Under well lubricated conditions the resultant position of the chip thickness and the SGE value feature below the thermal transition to burn around the 700°C region. The 700°C trend-line represents the calculated position that the microstructure of the steel begins to transform, resulting in a hardening of the surface. The temperature region of 450°C provides the thermal region associated with detrimental stress conditions where the residual stresses begin to deteriorate into a more tensile nature. The effect of introducing the various lubricants was then identified with respects to the position above or below the 700°C temperature line. The EcoCool for example manages to maintain surface temperatures well below any effects of residual stress are likely to take effect, while the hBN manages to maintain temperature below 450°C and the CaF<sub>2</sub> demonstrating an extremely wide range of SGE values. This plot therefore illustrates the influence of the lubricants on the SGE values. In order of performance; the EcoCool maintains the lowest SGE, the hBN results in slightly higher values, and the CaF<sub>2</sub> was the least performance enhancing lubricant. Therefore, as a recommendation, the hBN would be the most suitable solid lubricant to utilise within industrial applications. Combining this with the residual stress scans provides evidence that the hBN solid lubricant is beneficial within the grinding zone.

The wide range of SGE values for the CaF<sub>2</sub> originates from the change in the coefficient of friction around 450°C and the variation of the quantity of lubrication. Upon exposure to this condition the CaF<sub>2</sub> breaks down from the cubic form and enables the surfaces to slide. At the same time however there must be a sufficient quantity of CaF<sub>2</sub> to provide a frictional difference when it does begin to break down.

Samples produced under dry grinding conditions provided evidence that unsafe machining conditions involving surface chatter and poor surface integrity existed below temperatures of 450°C. This was credited to the onset of wheel clogging and poor control over the frictional sources of heat from an inefficient chip formation. Once again the SGE values were difficult to stabilise under these conditions.



CaF<sub>2</sub> T<sub>5</sub>



CaF<sub>2</sub> T<sub>3</sub>

**Figure 211** Burn Threshold Diagram of different lubricant types shown against calculated surface temperatures

## 6.9 Light Detection

An optical collimator was positioned behind the grinding zone. A Charged-Coupled-Device (CCD) sensor was then linked externally by a fibre optic cable. The mounting position of the collimator was limited by the physicality of the grinding machine, and the requirement to retain a target 'line-of-sight', derived from previous work. This target was identified as the optimal point of thermal interest, being 2.9cm below the actual grinding zone. This position captures the maximum concentration of grinding sparks. Positioning the detector closer than this increased the risk of damage to the lens and introducing disturbance due to the air flow from the protective air shield. The lens was kept clean by a compressed air shield and periodically inspected for dust and contaminants. The calibration and surface grinding passes, as mentioned in section 5.7.1, provided an optimal setting of 20000ms and 4 iterations for the CCD exposure. The Splicco licensed software then allowed a recording of the captured light emissions. Figure 212 illustrates a direct recording from the CCD device. . This image demonstrates the change in light pattern between the background light from within the grinding machine, and an initial stage of investigation in the J&S surface grinder. This was grinding 38Mn steel under dry conditions with an  $\text{AlO}_3$  wheel. Comparative recordings can be layered in order to provide a visual indication of changes in spectrum peak positions and intensities.

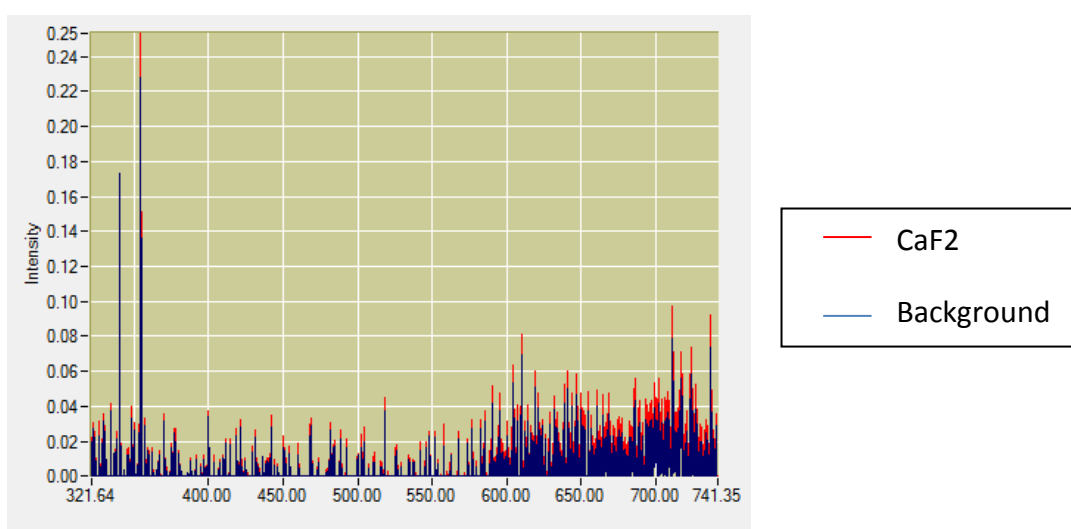


**Figure 212** Comparison of the captured light under the calibration conditions involving the ambient light within the machine and workshop (Blue) against those captured from a Trial 8 involving  $\text{CaF}_2$  (Red). Illustrating the differences recognized at the 600-740nm range of the spectrum.

The CCD device recorded spark light from the solid lubrication experiments. The light was captured when investigating the use of  $\text{CaF}_2$  and hBN as solid lubricants, and also the EcoCool as a control. Figure 213 shows the difference between similar machining conditions and the implementation of Trial 8 in the Taguchi trial. The chip thicknesses used throughout these trials was regarded as ineffective in removing a large proportion of the grinding

energy, compared to the behaviour of the chips found in HEDG grinding. Therefore the assumption was made that an increase in the detected chip energy directly relates to an increased temperature of the finish surface. The detected spark light peaks showed that differences in the wavelengths and the intensities of the chip energy could be recognised, particularly in the longer wavelengths of the spectrum. The finish surface temperatures were determined by the PVD isotherms and then compared to the energy recorded by the CCD device.

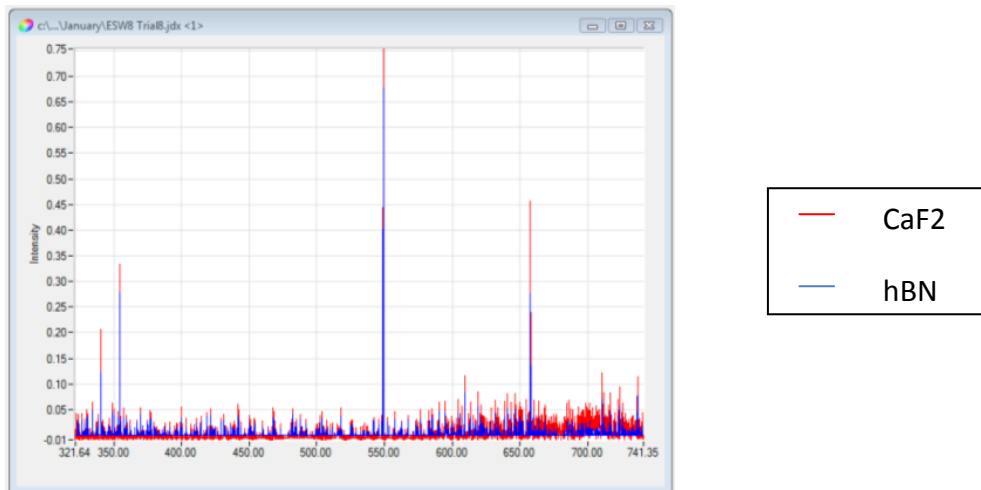


**Figure 213** Similar machining parameters under Trial 8 conditions, alternating between the solid lubricants of CaF<sub>2</sub> to hBN. The 600-750nm region continues to show a movement with respect to the spectral peaks.

The Calcium Fluoride possesses the potentially useful property of luminescence. The premise behind introducing CaF<sub>2</sub> into the grinding zone was to provide a method of lubrication and a source of luminescence that would be indicate the thermal conditions. The particular material property that the CaF<sub>2</sub> is known to possess is ‘tribo-luminescence’, the light being created from the induced energy from the interaction of two surfaces. Grinding creates a large amount of energy due to the interaction of the grinding wheel on the surface of the workpiece. The CaF<sub>2</sub> potentially could convert this energy into a source of luminescence that is captured by the CCD device. Figure 214 shows the CCD spectrometer light detection with an increase in the quantity of CaF<sub>2</sub>. The grinding conditions are similar with only a variation in the CaF<sub>2</sub> feeding pressure. From this plot the variation in the spectrum peaks with a bandwidth of 10nm are filtered and plotted together for comparison. These show that differences in the spark light intensity can be identified and correlated against the finish surface temperature of the grind. Increasing the mass flowrate of the CaF<sub>2</sub> reduced the intensity of the detected chip light, and this reduction was confirmed visually. The less bright indicating an improvement in the lubricity of the grinding zone and a degree of control with respect to the grinding temperature.

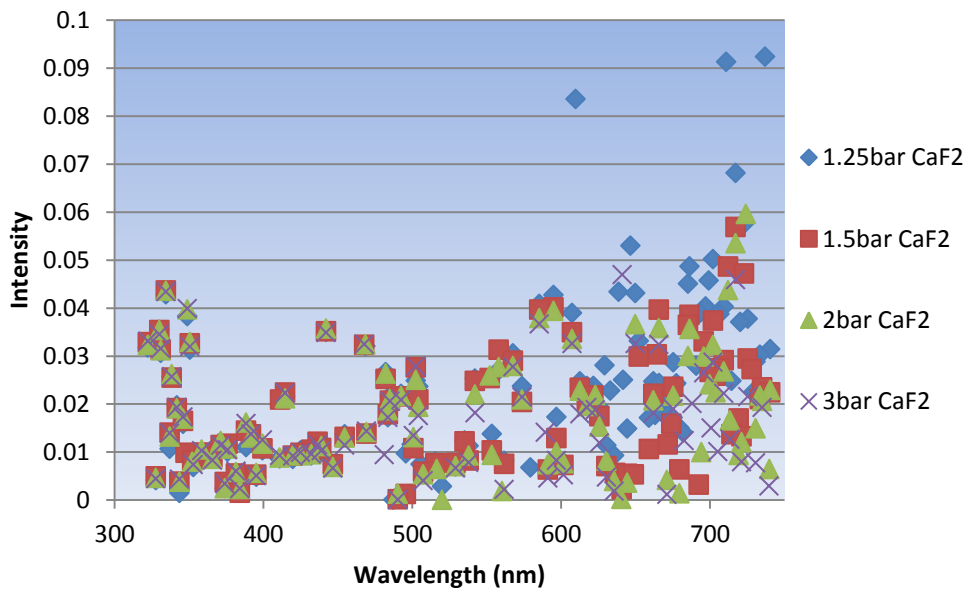


**Figure 214** Spectral light peak changes over an increase in CaF<sub>2</sub>: captured emission spectrum ESW3 Vs = 75m/s, Vw=0.53m/s, Vf=0.03mm/min, CaF<sub>2</sub> 1.25bar -3bar delivery

The spark light intensity was influenced by many factors and required further analysis by considering the CCD sensor results of the Taguchi trials. The following charts provide a visual indication of the changes throughout the spark spectrum profile. Figure 215 illustrates the CaF<sub>2</sub> with the B80 wheel and the 38Mn workpiece with the MQL flowrate being applied as outlined in Chapter 4. The peak positions of the spectrum were filtered to a minimum band width of 10nm, and then plotted. Shifts in the wavelength and the intensities between the trials indicate that a correlation between the process temperature and the spark energy could be found.

As a comparison Figure 216 includes the spark light captured from the grinding trials of water-only and dry plunges. These control plunges featured the lower level grinding wheel speed and the slower work speed rotation that is indicative of creating high SGE values. These addition trials were included to provide a maximum range of spectral peaks. As is shown the higher SGE values result in higher intensity of sparks. This indicates that the system is sensitive enough to detect the changes in the conditions of the grinding process.

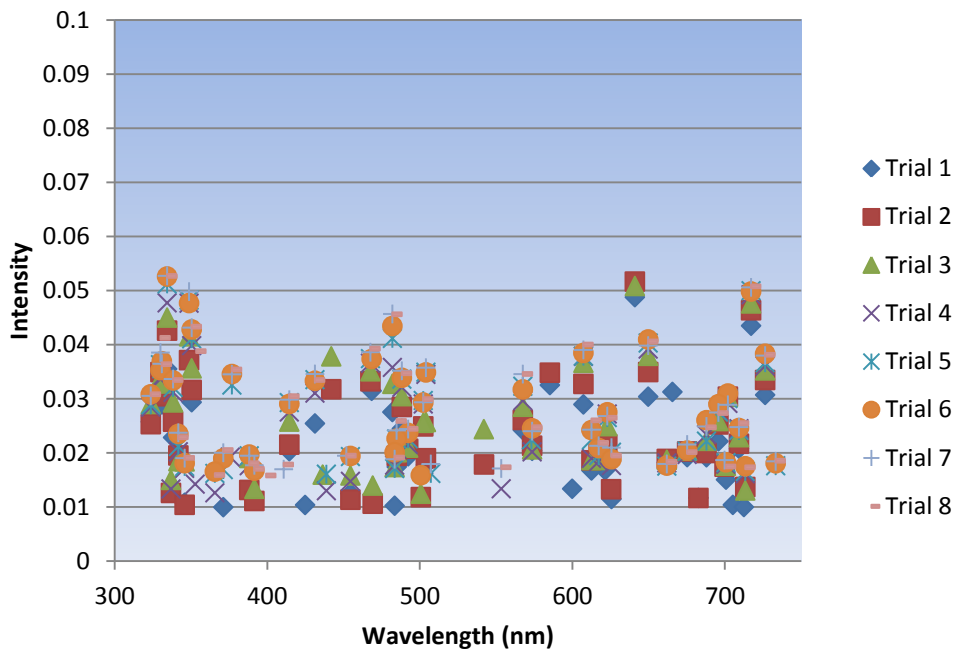


Figure 215 Spectral light peak changes over a single Taguchi trial with CaF<sub>2</sub>: Light Intensities

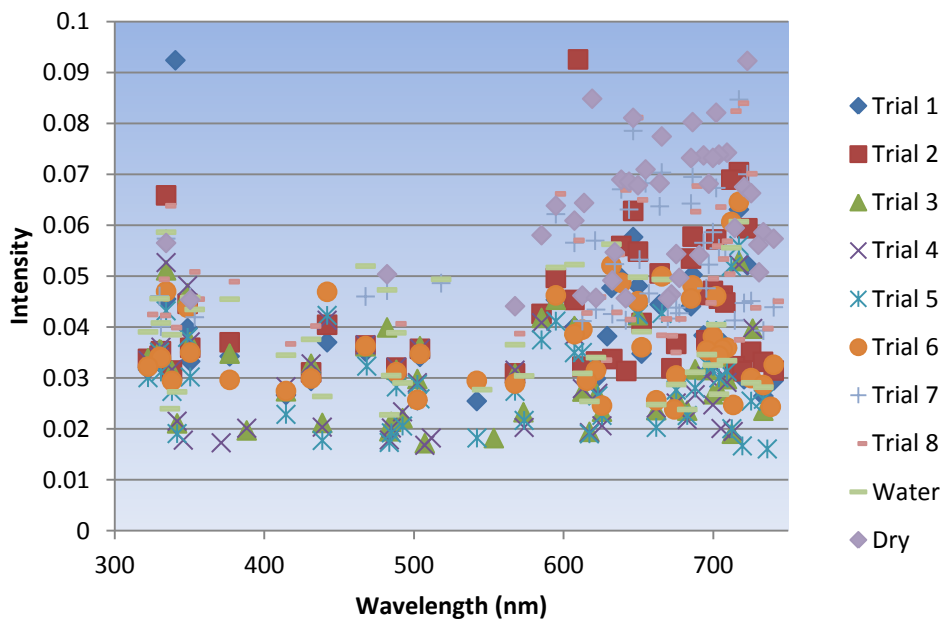
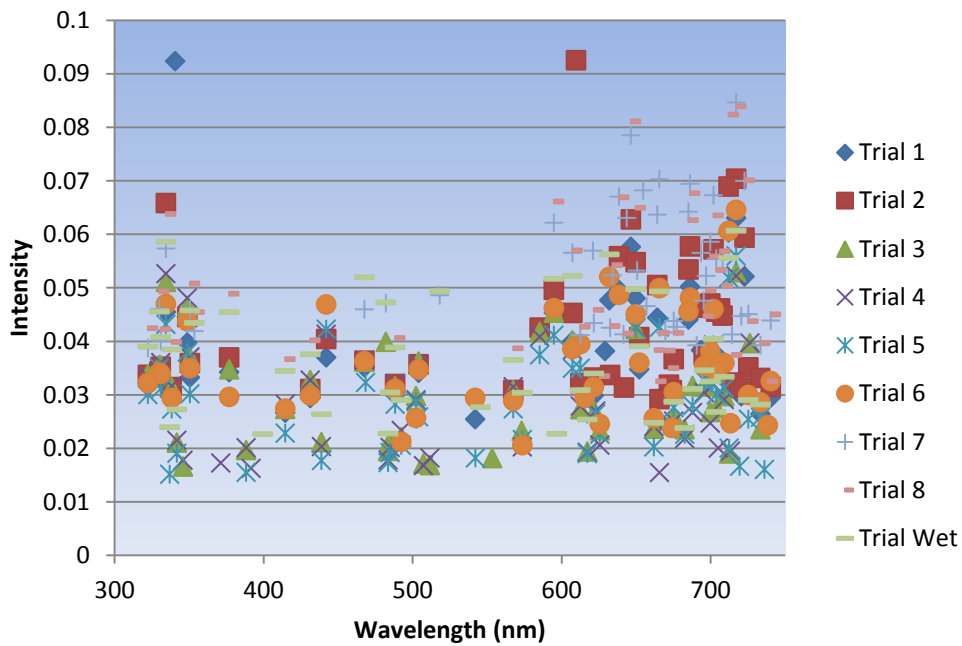


Figure 216 Spectral light peak changes over a single Taguchi trial with CaF<sub>2</sub>: plotted against a dry plunge grind illustrating the difference in captured light.

The CCD recordings from a hBN Taguchi trial are plotted in Figure 217. Movements in the intensity values were beginning to show, as well as small shifts in the peak wavelengths. The grinding conditions were similar to the CaF<sub>2</sub>. At this stage the ANOVA method would be difficult to implement with respect to establishing a link between the captured spark light and the surface temperature. The movement of the longer wavelengths and the shape of the rising intensity in the longer wavelengths however, prove useful in monitoring the grinding conditions.



**Figure 217** Spectral light peaks from Boron Nitride introduced into the grinding zone under the Taguchi regimes.

The movement in the spectrum in the longer wavelengths enabled a method of interpreting the emitted energy. Ideally there would have been a particular wavelength to provide the link to the grinding chip temperature however there was no obvious peak to select. Therefore the spectrums were filtered in order to identify a general shape, constructed from the peak positions of wavelength and intensity, and re-plotted as a dataset. The rising spectrum towards the longer wavelength identifies a curve that provides a process wavelength and a maximum intensity of the emitted chip energy. This pattern provides the link between the spark intensity detected light spectrum over the visible light spectrum of bandwidth 300-750nm. Each grinding trials possessed a different shape with respect to the intensity and wavelength that was then matched to the measured PVD temperatures. The curves and equations were produced for the  $\text{CaF}_2$ , the hBN and the EcoCool water soluble oil. The curves that feature in Figure 218 and Figure 219 show the differences in the light captured from the  $\text{CaF}_2$  and the hBN trials.



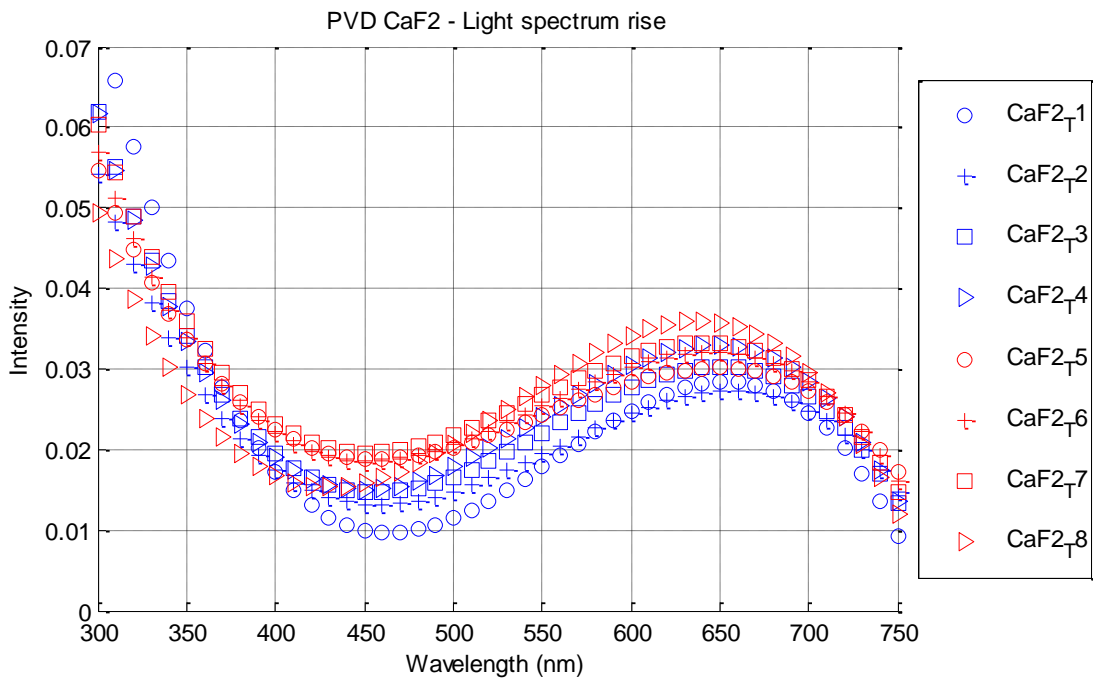


**Figure 218** Simplified shape of the light captured allowing differences to be calculated to be compared to the finish surface temperature - Using  $\text{CaF}_2$

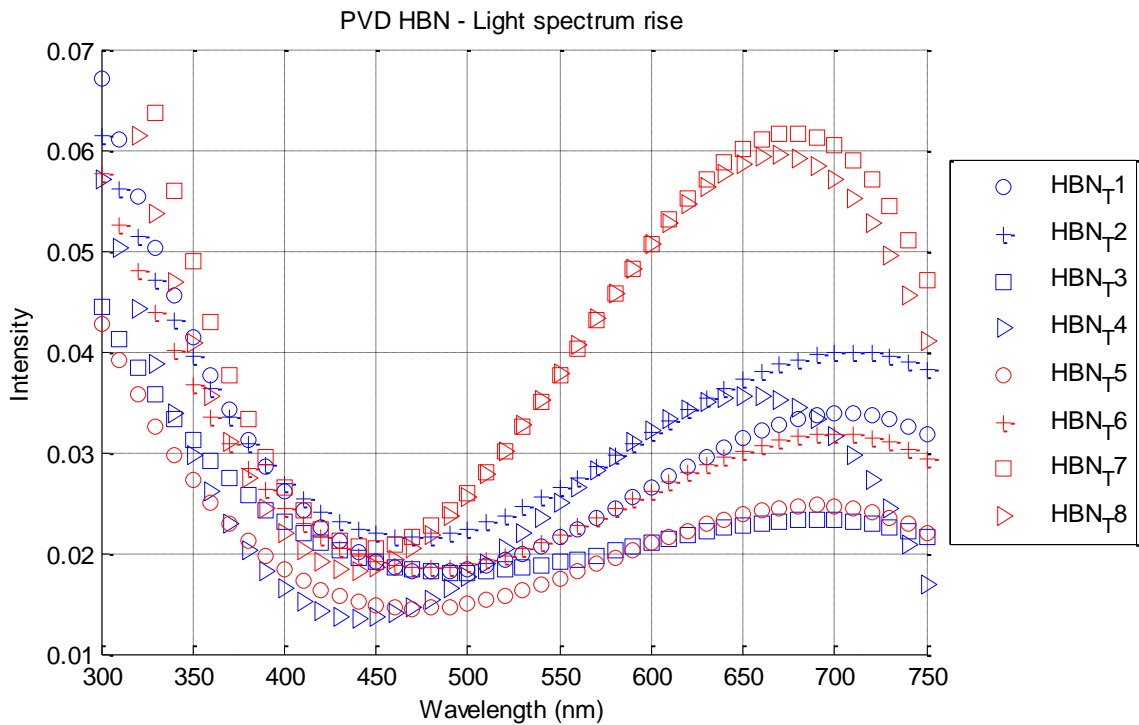


**Figure 219** Simplified shape of the light captured allowing differences to be calculated to be compared to the finish surface temperature - Using hBN

---

CaF<sub>2</sub> is known to possess naturally occurring fluorescent properties and as a consequence is alternatively named Fluorite or Fluorspar. The exact wavelength of CaF<sub>2</sub> fluorescent activity can vary over a wide range of wavelengths therefore the next stage was to determine to what extent the CCD device was able to capture the tribo- excited luminescent CaF<sub>2</sub>, and if was it possible to relate it to a finish grinding temperature. The identification of any obvious tribo-luminescent behaviour however was difficult to determine. Nonetheless the ANOVA analysis was used to assist in the recognition of any relationship between; the SGE, the finish ground temperature, and the position of the peak intensity and the peak wavelength around the 500-750nm range. The main effects from the variation in the quantity of CaF<sub>2</sub> and hBN are shown in Figure 220 and Figure 221.

The effectiveness of the solid lubricants to remove heat through thermal conduction and dissipation was unknown. Traditional machining fluids have their greatest influence at small Q'w values, as the fluids are able to flow into the grinding zone and surround the tool and freshly ground surface. On the other hand the opposite is known to be true were the machining fluid becomes less important in HEDG as the chip removes the larger proportion of heat due to the higher Q'w rates. If this is indeed the case then the optically detectable energy from the chip may well be directly relating to the workpiece finish surface, a hot chip means a hot finish surface. Under conditions of low thermal conduction the formed chips may be forced to conduct a higher proportion of the grinding energy at the low Q'w values. The calibration of the system will be specific depending on the thermal properties of the tool, the workpiece and the lubricant. The ANOVA showed a general trend between the energy of the spark and the finish surface temperature in that the brighter the sparks indicated a hotter finish surface. The chip thicknesses were very small indicating that under normal machining fluid application conditions the majority of the heat would be conducted by the workpiece. The reduction in machining fluid results in a larger proportion of the heat being conducted by the grinding chips. Therefore the chip energy has a direct relationship to the finish grinding temperature.

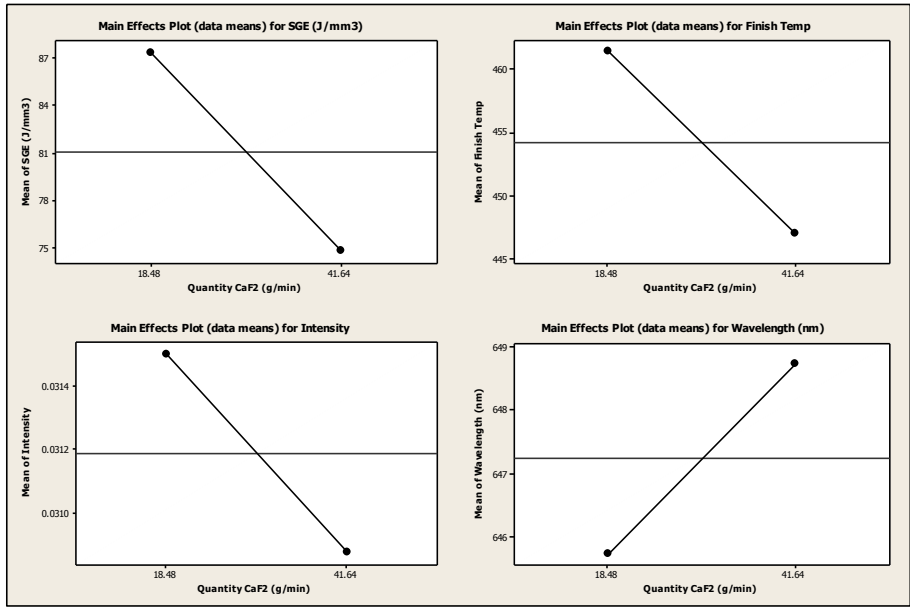


Figure 220 ANOVA main effects analysis on the behaviour of captured light from emitted grinding sparks cBN 80 wheel 38Mn workpiece solid lubricant: CaF<sub>2</sub>

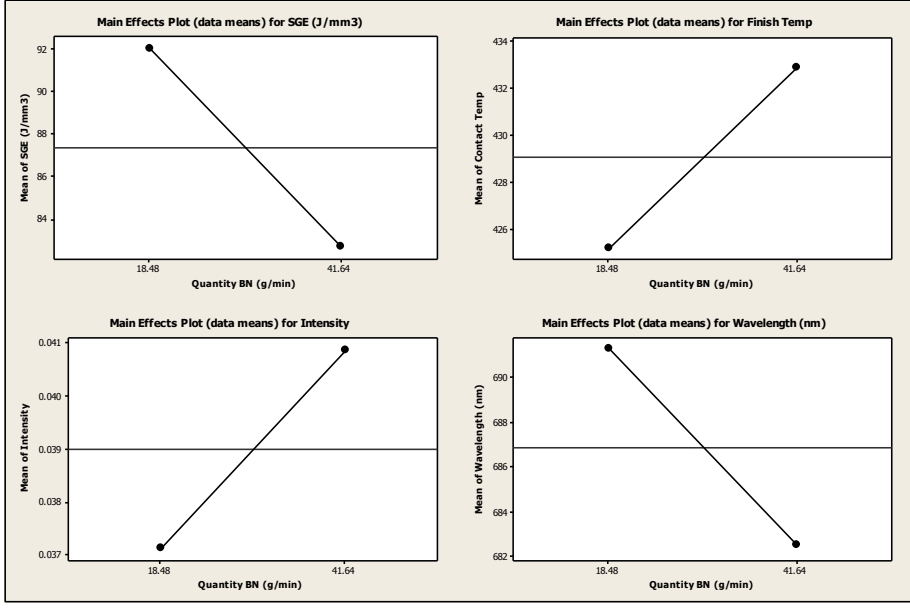


Figure 221 ANOVA main effects analysis on the behaviour of captured light from emitted grinding sparks cBN 80 wheel 38Mn workpiece solid lubricant: hBN

The CaF<sub>2</sub> on average had the highest mean temperature of 454°C in comparison to the hBN of 429°C, a 25°C difference. The coefficient of friction is known to change around the 450°C region which most likely accounts for the wide variation in the SGE values. The hBN was calculated to achieve the lowest surface temperature of 425°C at the lowest level delivery rate however the risk of loading the wheel caused higher SGEs at the higher delivery rates.

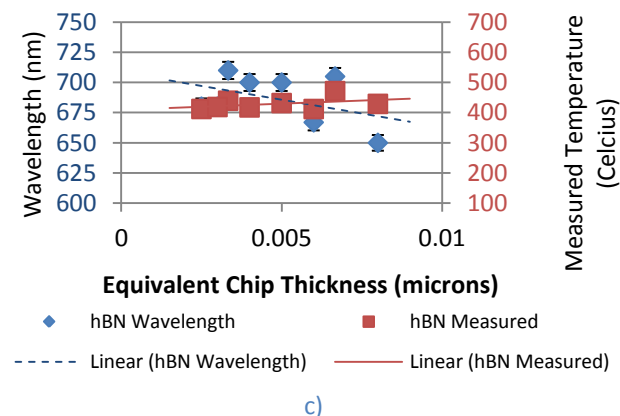
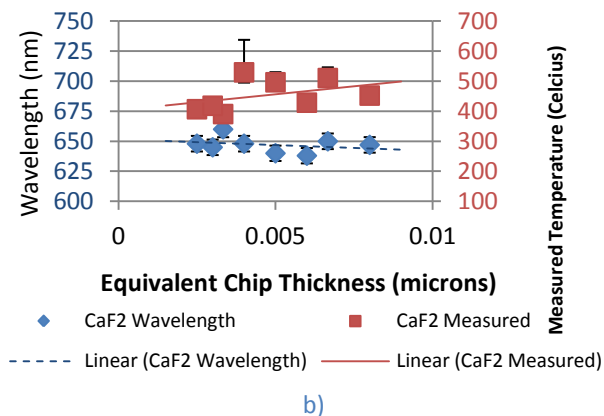
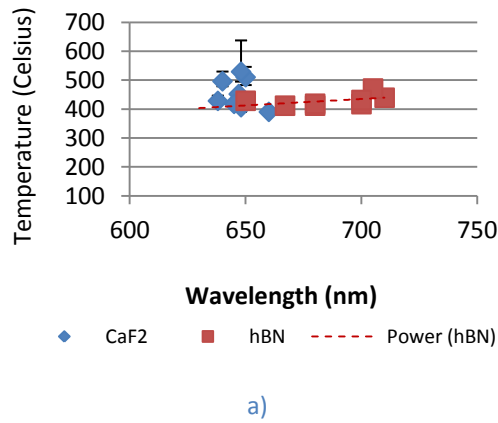


Figure 222 Measured PVD Temperature (Celsius) vs CCD detected peak wavelength (nm)

The CaF<sub>2</sub> and hBN solid lubricants demonstrate opposing behaviours with respect to finish temperature control. The CCD device was able to demonstrate that the hBN provided a stronger relationship between the movement in the finish surface temperature and the movement of the spectrum peak. This is extremely beneficial to the development of a thermo-optical control system. Figure 222 illustrates the captured wavelength of emitted light energy from the grinding chip and compared to the finish surface temperature, when using the CaF<sub>2</sub> and the hBN. The relationship between the detectable wavelength of the chip and the finish temperature was also shown against the equivalent chip thickness. This enabled a better insight into the nature of the grinding regimes. The CaF<sub>2</sub> had a restricted movement in relation to the light detection system while the hBN had a relatively stronger influence on both the movement of the wavelength and a reduction of the finish temperature.

The response from the grinding chip light intensity was extremely minimal when introducing the CaF<sub>2</sub>, as shown in Figure 223. There was no immediate interaction found between the peak of intensity and the finish surface temperatures. The intensity of the chip energy again proved more useful when introducing the hBN into the grinding zone. With respect to the feasibility of constructing an optical-thermal control system the wavelength of the chip energy appears to be the more responsive, with a clearer recognition of changes in the grinding conditions.

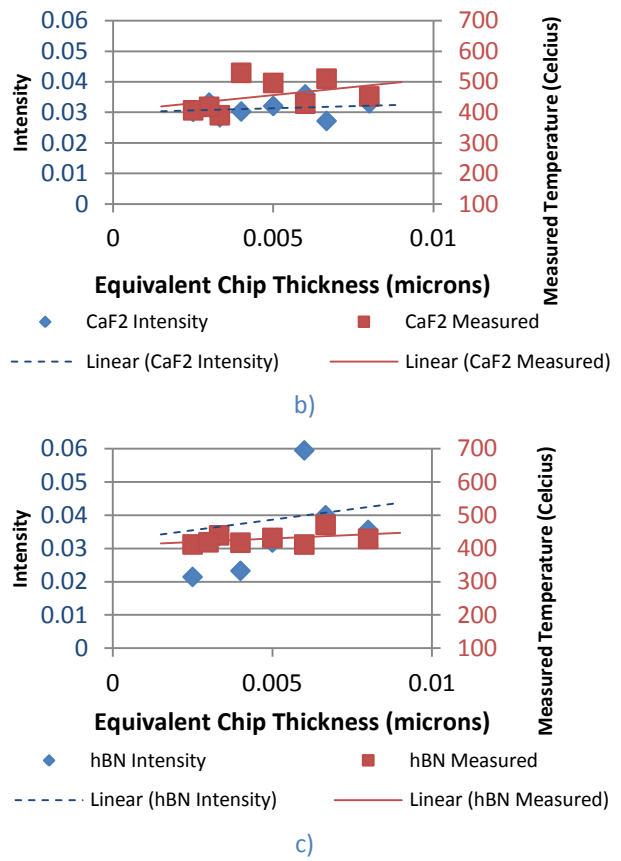
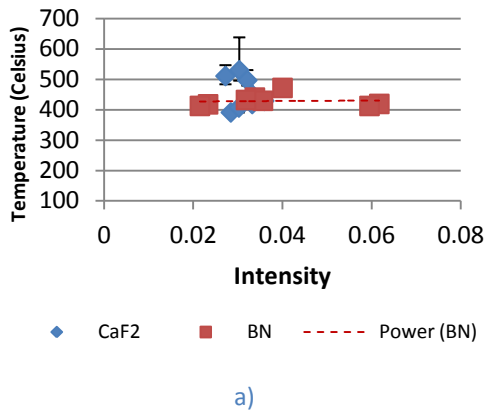


Figure 223 Intensity of the grinding sparks against the PVD measured temperature (Celsius)

---

## 6.10 Key Messages

The key messages taken from this chapter are:

- MQL Useful Flowrates were controlled throughout the Taguchi factorial trials.
- Dry dressing was unable to provide consistently open conditions of the vitrified grinding wheels. High thermal stresses forced the diamonds in the dressing wheel into a softened metal bond. The traversing movement of the dressing wheel, across the front face of the grinding wheel, endangered the dressing wheels life particularly with high levels of wheel loading.
- Baseline Minimum Quantity Lubrication (MQL) data was collected using EcoCool, water soluble semi-synthetic oil, added at concentrations of between 1% and 10% managed through the use of a Dosatron water mixture.
- Three different Solid Lubricants were introduced to the grinding process, namely; Molybdenum Disulphide ( $\text{MoS}_2$ ), Calcium Fluoride ( $\text{CaF}_2$ ), and hexagonal Boron Nitride (hBN). These materials possess tribological properties intended to reduce the source of frictional heating. The source of friction was from the grinding wheel interacting with the workpiece surface. These Solid Lubricants were in a dry powdered form and applied using MQL Useful Flowrates. Therefore the application of the Solid Lubricants was known as Minimum Quantity Solid Lubrication (MQSL).
- Molybdenum Disulphide ( $\text{MoS}_2$ ) was capable of controlling the grinding process power consumption and Specific Grinding Energies at relatively low delivery mass flow rates of 5.5 to 9.5 g/min. This was shown to produce good quality subsurface microstructure and produce acceptable levels of surface integrity of the workpiece. The lamellar layered structure of  $\text{MoS}_2$  acted as a good lubricant that enabled the Specific Grinding Energies to be controlled, thus maintaining relatively low surface temperatures. The higher flowrates of  $\text{MoS}_2$  however clogged up the grinding wheel surface as the  $\text{MoS}_2$  became compacted within the pores of the cBN wheel.
- Calcium Fluoride ( $\text{CaF}_2$ ) was found to be an unpredictable Solid Lubricant. On average the Specific Grinding Energies were about three times higher than those generated by  $\text{MoS}_2$  or EcoCool. The ranges of equivalent chip thicknesses were consistent throughout the trials. The use of  $\text{CaF}_2$  did prove encouraging at the slower infeed rates, possibly due to the cubic structure of  $\text{CaF}_2$  breaking down at temperatures above 450°C. The development of a pneumatic powder feeder was required for the  $\text{CaF}_2$  because it has a much lower mass density than  $\text{MoS}_2$ .
- Hexagonal Boron Nitride (hBN) was found to be an effective Solid Lubricant, similar to the action of  $\text{MoS}_2$ , due to its lamellar structure. The hBN offered the most encouraging results from its ability to control the workpiece temperatures providing the grinding wheel surface remained unclogged.

- 
- A 10% reduction in Specific Grinding Energy was achieved when doubling the hBN mass flowrate. A similar reduction in Specific Grinding Energy was attained through a 9% increase in the oil content of the EcoCool emulsion. Therefore an equivalent performance comparison can be suggested between the EcoCool oil and the Boron Nitride. From the grinding parameters utilised throughout the Taguchi trials a 2.5g/min increase in hBN provided an equivalent improvement to the SGE as a 1% increase in oil concentration of the EcoCool machining emulsion.
  - The use of Solid Lubricants and the resultant reduction in the quantity of machining fluid facilitated the use of an optical thermal detection system by recording light emitted from the grinding zone, more specifically from the heated chips. Differences in the electromagnetic energy spectrum captured from the emitted sparks can be identified. The level of intensity and the wavelengths was shown to vary according to the machining conditions with respect to the wheel type, the workpiece material, the speeds and feeds and the machining fluid used. This optical thermal detection system could be further developed to provide a non-destructive monitoring system to control the surface temperatures of the workpiece.
  - The MQL /MQSL concept has been successfully applied in the abrasive machining environment. A variety of Solid Lubricants has been applied directly onto the grinding wheel through the development of a MQSL delivery system. This system delivered a precise volume of solid lubricant onto the grinding wheel to be carried into the grinding zone.

These key messages, and supporting empirical data, can help to inform an assessment of the practicalities of introducing MQL and MQSL into industrial scale abrasive machining. They are carried forward to support the discussion in the next chapter.

---

## 7.0 Discussion

The aim of this research was to advance the understanding of Minimum Quantity Solid Lubrication (MQSL) in the application of abrasive machining. The key incentive was to reduce the quantity of machining fluids in order to achieve financial savings and meet increasingly stringent chemical and environmental regulatory requirements. The success of MQSL machining relies upon the ability of the lubricants to suppress the process grinding temperatures and achieve similar surface integrities to that of traditional flood or high pressure fluid delivery systems.

The partitioning of the grinding heat when grinding with solid lubricants was previously unknown. Therefore the development of the thermal model included several scenarios that adjusted the thermal properties of the grinding wheel and the machining fluid. The calculated temperatures from these scenarios were then matched against actual recorded temperatures. The accuracy of the model to predict the measured temperatures provided an insight into the movement of the thermal energy around the grinding system. The modelled scenarios were representative of the grinding parameters found when grinding with reduced flowrates of oil and water, and under dry grinding conditions. Figure 224 is an example of the modelled temperatures verses the actual measured temperatures that were determined through the empirically measured PVD isotherms and SGEs of  $\text{CaF}_2$  and hBN. The dotted line indicates where the measured temperature and the modelled temperature are equal. On initial inspection the modelled temperatures had a much wider range of values in comparison to the measured temperatures indicating instability in the grinding temperatures estimates. The adjustment of the thermal properties of the grinding wheel and solid lubricant carrying fluid however enabled the position of the modelled temperature to be fitted closer to the measured temperature.

The Specific Grinding Energies when using hBN were noted to be slightly higher than the  $\text{CaF}_2$  however the measured surface temperatures of hBN remained relatively stable. The behaviour of the hBN on the newly ground surface was seen however to improve the lubrication of the grit sliding upon the surface. Rather than encouraging the shear planes to develop in a more efficient manner as initially expected however the sliding mechanism that appears to be involved actually increases in the time duration of grit and workpiece surface interaction. Therefore the grits are in contact with the surface for a slightly longer period of time compared to before when forming the shear planes. This behaviour not only increased the energy consumed throughout the cycle but also increased the thermal conduction time period. As a result the temperature predictions for the  $\text{CaF}_2$  in the model were positioned closer to the measured surface finish temperatures when assuming that the cBN grits of the grinding wheel had a thermal conductivity value of  $240\text{W/mK}$ , while the hBN found a closer correlation when assuming  $1300\text{W/mK}$ .



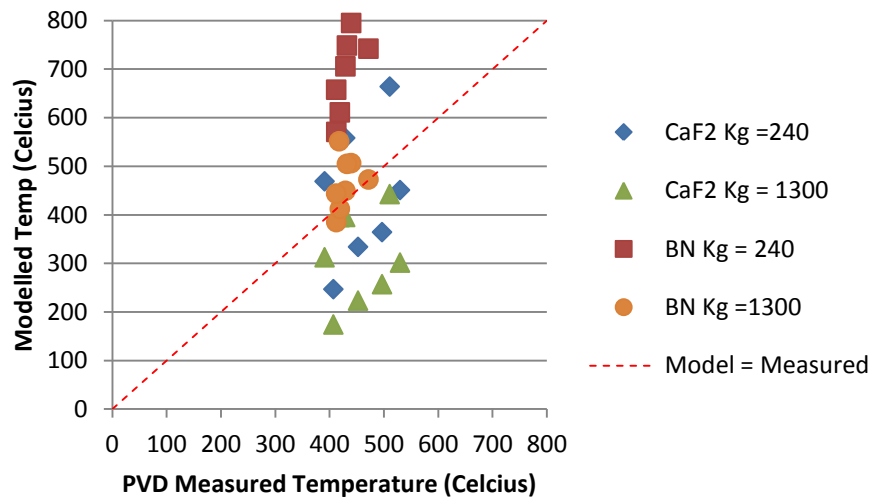


**Figure 224** PVD measured temperature vs. modelled temperature with variation in thermal conductivity of cBN wheel (heat transfer coefficient of carrying water =  $290000\text{W}/\text{m}^2\text{K}$ )

Nevertheless the increased likelihood of hBN clogging the surface of the wheel adds a further restriction to penetration of the grit into the workpiece surface and adds to the risk of elevated the Specific Grinding Energies. Figure 225 a) illustrates the downwards shift in the predicted temperatures when increasing the thermal conduction of the cBN abrasive grit. Increasing the capability of the wheel to conduct the grinding process heat away from the grinding zone reduces the finish surface temperature. The predicted temperatures using  $\text{CaF}_2$  and hBN were then fitted against the PVD measured temperatures. Figure 225 b) illustrates the most suitable combinations of the thermal conduction values of cBN against the performances of the solid lubricants (with  $\text{CaF}_2$  cBN,  $K_g = 240\text{W}/\text{m}^2\text{K}$  and with hBN,  $K_g = 1300\text{W}/\text{m}^2\text{K}$ ). This supports the argument that the SGE values are higher due to the longer contact duration of the grit upon the surface. This also encourages a higher value of thermal energy to be conducted from the workpiece surface, and as a result the hBN produces lower process temperature.

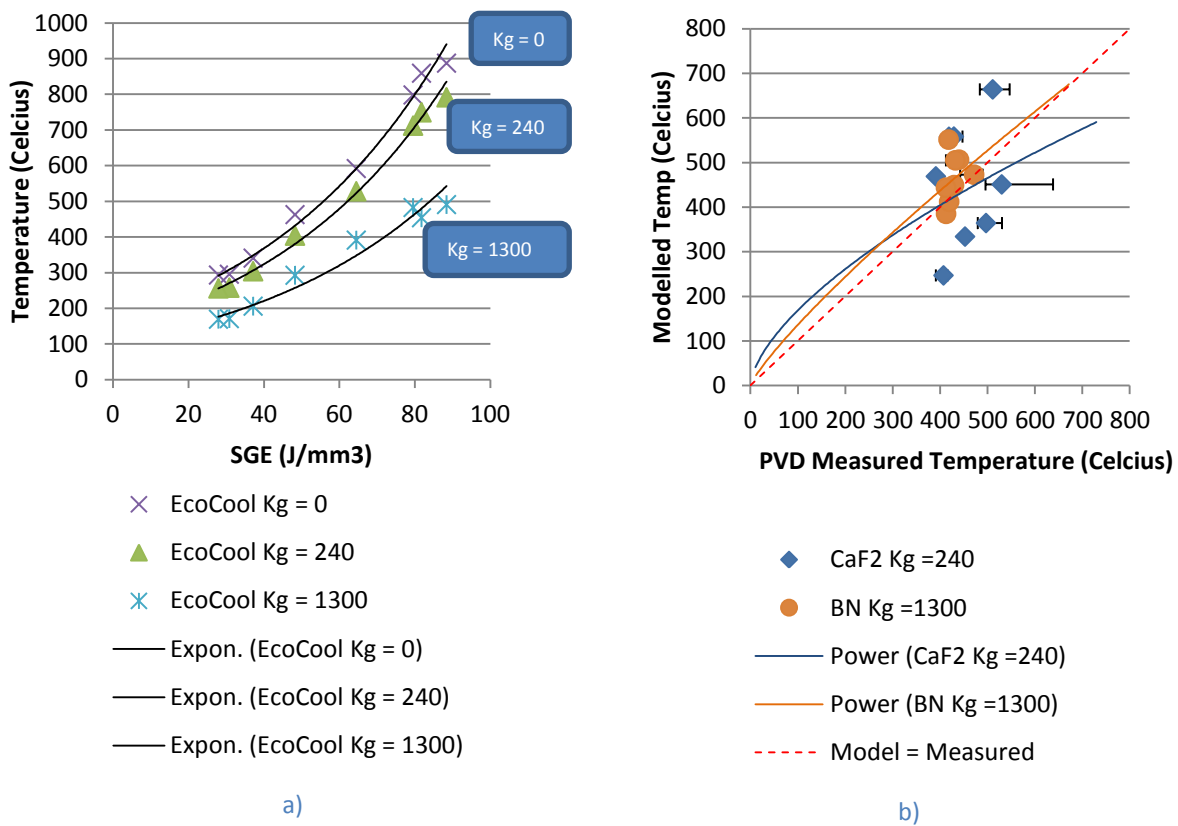


**Figure 225** a) Illustration of the variation in the model thermal property inputs, thermal conductivity values in W/mK b) PVD measured vs. modelled temperatures (with a water based carrying fluid  $h_f=290000\text{W/m}^2\text{K}$ )

The coefficient of friction of CaF<sub>2</sub> is known to reduce at elevated temperatures around 450°C. On the other hand the hBN possess extremely low coefficients of friction due to the lamella structure improving the lubricity of the grinding process due to the capability to slide more effectively. The hBN also possesses a much greater capability to conduct heat and is widely used in industry for heat sinking purposes. However it still causes a degree of clogging on the grinding wheel surface.

The various thermal property scenarios for CaF<sub>2</sub> and hBN feature in Figure 226 a) and b) respectively. The dotted lines define the two extreme thermal property conditions of dry grinding ( $h_f=0$ ) with a low thermal conduction ( $K_g=240\text{W/mK}$ ), and the use of a carrying fluid (water  $h_f=290000\text{W/m}^2\text{K}$ ) with a high conduction value ( $K_g=1300\text{W/mK}$ ). The effect of the heat transfer value of the carrying fluid ( $h_f$ ) becomes relatively insignificant at the higher values of thermal conduction. The positions of the EcoCool finish temperatures also feature in Figure 226. The PVD measured temperatures are plotted as the red pointers. These charts illustrate the general position of the SGE found when using the CaF<sub>2</sub> and hBN. Figure 226a) shows that between the ranges of 400°C to 500°C the positions of SGEs were relatively low, 30 to 80 J/mm<sup>3</sup>. The clogging of the wheel when using hBN however was the significant factor in elevating the SGE values. The hBN however can control the grinding temperatures

around 400°C to 500°C, due to a reduction in the frictional heating and a higher proportion of energy being dissipated by the wheel and by the solid lubricant.

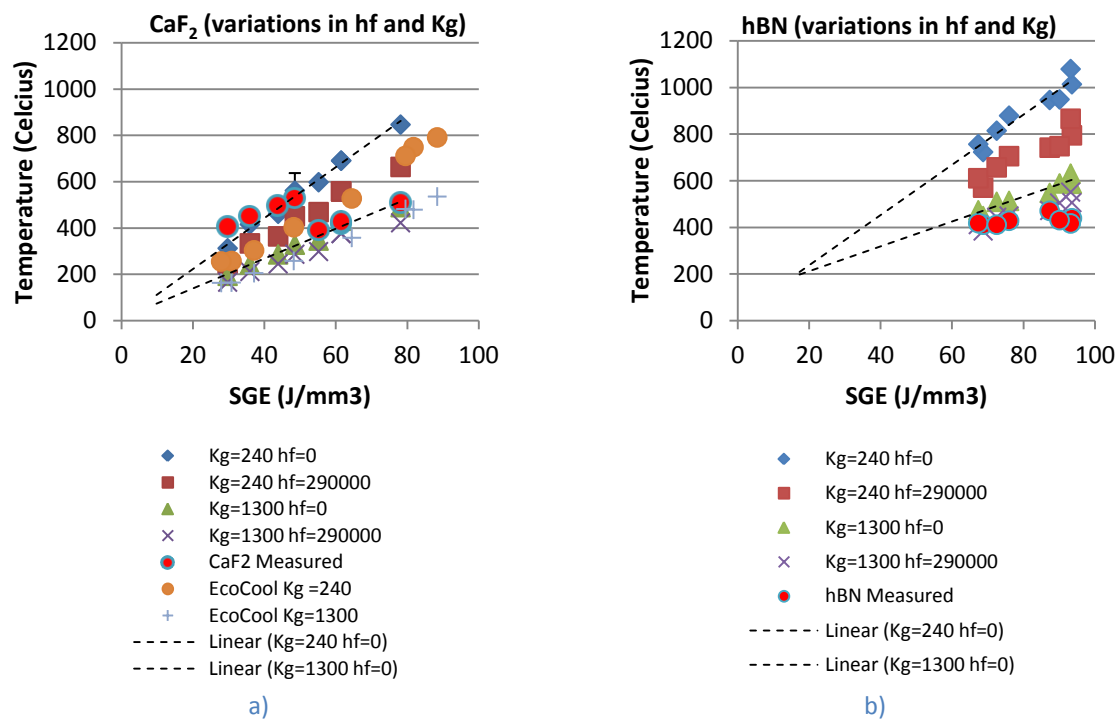


**Figure 226** Modelled temperatures with measured temperature (Celsius) when introduction of CaF<sub>2</sub> against Specific Grinding Energy (J/mm<sup>3</sup>)

Figure 227 shows the complete range of modelled and measured temperatures when introducing CaF<sub>2</sub> and hBN into the grinding zone using a cBN90 wheel and 38Mn steel workpiece. The measured temperature positions fall within the two ‘extreme’ trend lines. The use of hBN as a solid lubricant provides grinding conditions that are far less aggressive than the predicted parameters of dry grinding conditions. This indicates that the lubricant is assisting the process and that the thermal behaviour of hBN controls the finish surface temperature to a greater extent than the CaF<sub>2</sub>.

The cubic structure of the CaF<sub>2</sub> powder encourages a ‘free’ movement on the surface of the grinding wheel. This physical characteristic enables the solid lubricant to eject from the pores of the grinding wheel surface. This also enables the grinding chips to form more effectively into the surface of the grinding wheel and for the wheel to accept fresh lubricant before re-entering the grinding zone.

Recognising the influence of the thermal properties of the grinding tooling and the machining fluid on the predicted temperatures was critical in the refinement of the thermal model. The variations in the thermal conductivity and heat transfer coefficients of the solid lubricants greatly assisted in predicting the level of thermal energies when using solid lubricants. The thermal calculations are now able to account of the type of solid lubricant that is added and identify which trend line the predicted temperatures are likely to feature

upon. For example the hBN grinding conditions are more accurately predicted with a higher thermal conduction value.

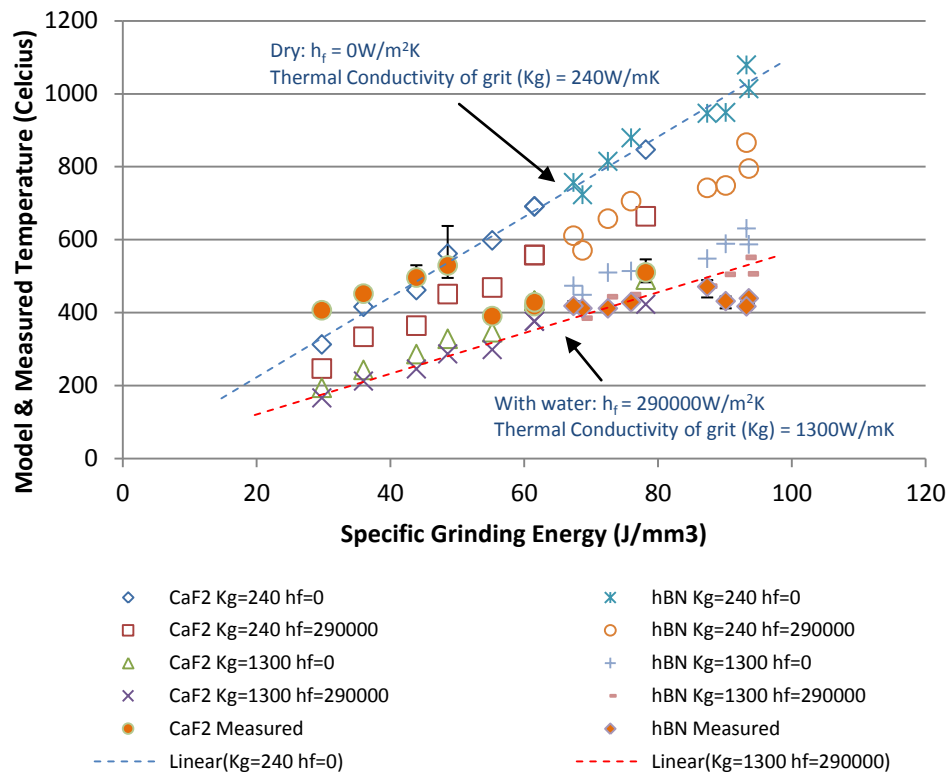


Figure 227 Temperatures measured and modelled (Celsius) when introduction of hBN against Specific Grinding Energy (J/mm<sup>3</sup>)

It was acknowledged that the depths of cuts and chip thickness values were extremely small throughout these trials. However this was necessary to guarantee the structural integrity of the grinding wheel under the reduced flowrates of the machining fluids, and without the firm appreciation of the thermal movements under dry conditions. The progression of analysis with regards to the surface integrity however showed that the solid lubrication functions in a number of modes. The lubrication is of course critical for the fine surface roughness values while the thermal conduction mechanism is of benefit towards the residual stress values and maintains the process temperatures. The thermal behaviour of the solid lubricant powders however became increasingly apparent throughout the development of the model. This characteristic can be compared to the introduction of nano-technology in the development of lubricants and cutting fluids, such as carbon nano-tubes within oils that possess high values of thermal conductivity and large surface areas for efficient thermal transfer.

The hBN was able to produce surface integrities very similar to that of the EcoCool machining emulsion. This was achieved through the careful maintenance of the grinding wheel surface through the dressing regimes and also the successful application of solid

lubrication. Therefore MQSL methods are recommended within an industrial setting providing the surface of the grinding wheel is inspected for loading.

When using the hBN as a solid lubricant the CCD detected spectral shape from the grinding sparks showed a slight relationship against the finish surface temperature. The position of the spectral shape of the chip energy shifts towards a longer wavelength with an increase of grinding finish temperature. Therefore the energy emitted from the sparks shifts the position of the spectrum peak towards the infrared region under hotter grinding conditions. This evidence suggests that the finish grinding temperatures are determinable through this non-contact optical system. The accuracy of the system however depends upon the accuracy of the system calibration and the establishment of the behaviour of the grinding thermal flows, with particular respect to the division of the grinding energy.

The relationship between the finish surface temperature and the detected spark energy was considered to be negligible when introducing the  $\text{CaF}_2$  as a lubricant. The PVD isotherm measurements identified a  $250^\circ\text{C}$  variation in temperature over the range of trial parameters, with no real movement in the wavelength position. The peak position of the spectrum curve remains consistently around 640-650nm wavelengths. The  $\text{CaF}_2$  is known to possess tribo-luminescent properties, which when sufficiently excited was expected to emit energy wavelengths around the green region of the visible spectrum of 520-570nm. The CCD device was unable to provide any evidence that the intensities and the wavelengths around this region were of any significant use and that the actual peaks were found closer to the 640-650nm region. This gave rise to the assumption that it remained to be the chip energy that was being captured by the CCD device.

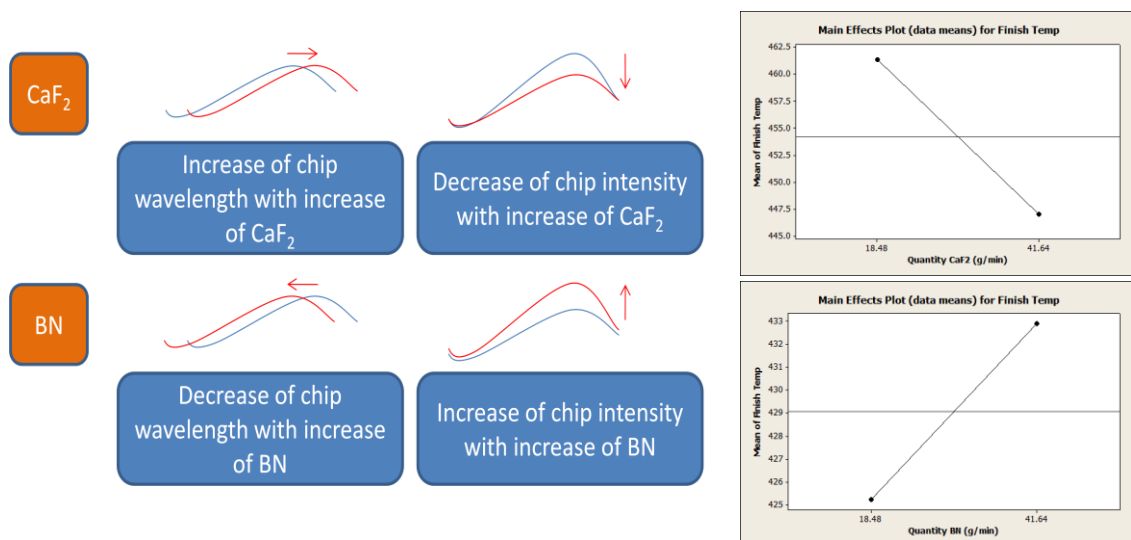


**Figure 228** Changes in the spectrum measurements when using  $\text{CaF}_2$  and hBN. The shifts in the wavelength and intensities are illustrated separately for both solid lubricant types and provide a link towards the finish surface temperature of the workpiece.

Figure 228 illustrates the pattern of movement in relation to the quantity of CaF<sub>2</sub> and hBN introduced to the grinding zone. The movement of the CaF<sub>2</sub> was found to be limited when compared to the range of surface temperatures and suggests a difficulty in determining a relationship between the two. The time period over which the chip energy was collected by the CCD device remained constant throughout the trials, as the intensity of the light detection was time dependant. Once again the hBN had a wide range of recorded intensity values in comparison to the relatively unresponsive CaF<sub>2</sub>.

Reducing the quantity of fluid that was introduced to the grinding process effected the power consumption of the grinding cycles, and therefore determined the quantity of energy available for conversion into the sliding thermal source. When using a suitably selected MQSL solid lubricant the additional machining power that was consumed through the dragging of a fluid and hydrodynamic effects in the grinding zone was seen to reduce as shown by Figure 229.

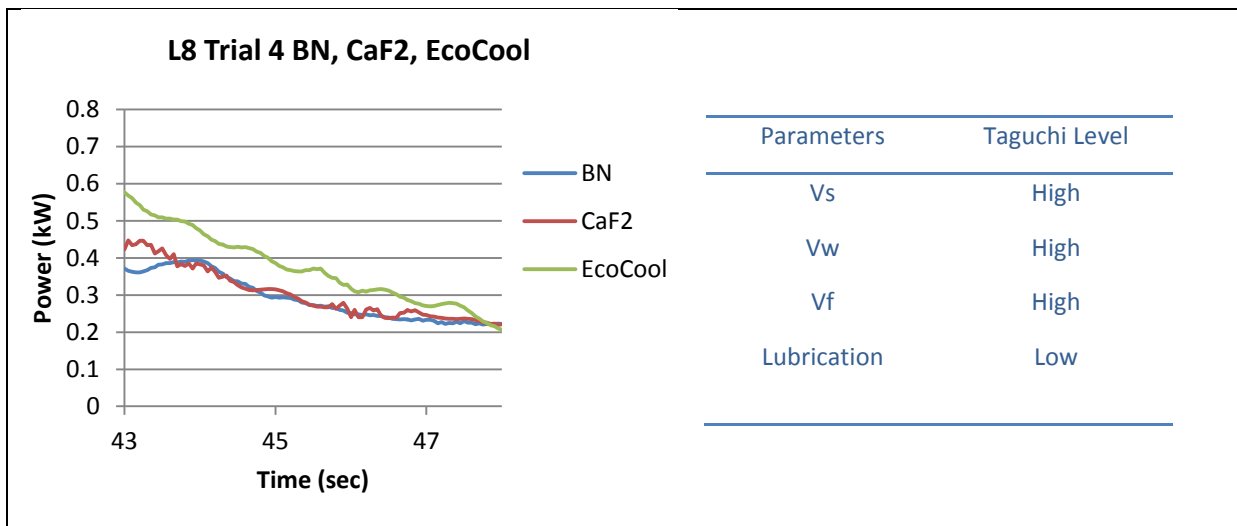


Figure 229 Reduction of power consumption by using MQSL methods of CaF<sub>2</sub> and hBN over more viscous oil based of EcoCool at the low levels of delivery.

This research however confirms that metal working fluids provide a range of functions throughout the machining process, not only for lubrication but also for the control of thermal conduction, swarf flushing and corrosion prevention. Hence, reducing the quantity of machining fluid in practice is complicated and challenging. This research mainly focused on the lubricative interaction between the grinding wheel, the workpiece and the solid lubricant. It also explored the lubrication requirements of the dressing wheel that is used to maintain the performance of the grinding wheel. It was shown that a balance must be achieved between lubrication and cooling requirements when introducing Minimum Quantity Lubrication (MQL) and MQSL techniques into the grinding zone. It was also shown that the cooling attributes of a working fluid become more important for harder materials, both regarding the interaction of the grinding wheel and diamond dressing wheel, and the interaction of the grinding wheel and the workpiece.

---

Controlling the generation and dissipation of heat is a particular challenge in MQL abrasive grinding. The research showed that the lubrication and cooling requirements when dressing the grinding wheel are equally as important compared to the operation of the grinding wheel under normal conditions. If the dressing wheel fails to dissipate under inadequately cool conditions the generated heat from the dressing process thermally softens the metal bond, and results in the diamond grits being depressed into the dresser surface. This reduces the effectiveness of the dressing wheel and can result in catastrophic failure. Thus, a development in 'dry' tooling must accommodate potentially high temperatures.

### **Comparative assessment of alternative methods and the requirement for industrial collaboration**

The control of heat in grinding, however, has long been an issue in industry scale applications with many attempts made by tool manufacturers to dissipate heat more effectively. Examples include the use of slotted grinding wheels to provide larger surface areas to enable the convection of heat and segmented wheels, thereby relieving continuous contact with the workpiece whilst promoting the ingress of a working fluid. Fluid passage ways have also been cut into the body of the grinding wheel attempt to provide thru-wheel-cooling directly to the position the grit interacts with the workpiece. These innovative solutions are used by machine builders not only to accommodate the advances in machining capabilities but also to maintain their trading position in competitive markets for machine tools. The technological development of grinding machines and the growth of exotic workpiece materials has created a much greater need for collaboration between the machine builders and the tooling developers. Therefore the pathway to the adoption of MQL methods, driven by a range of financial, regulatory and technological factors, requires continuous communication, exchange of knowledge and collaborative development amongst the key industrial agents as illustrated in Figure 230. The adoption of MQL is compatible with the concept of sustainable design and manufacturing and, given the prospect of increased real energy and material prices, can help to achieve long term competitive advantage.

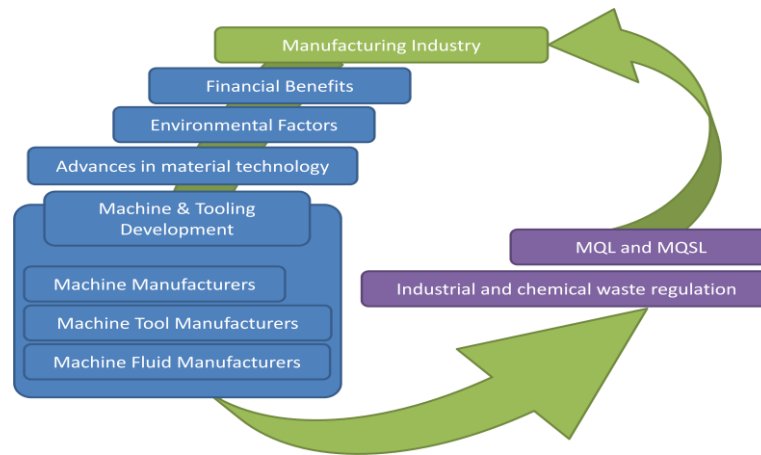


**Figure 230** The motives and interactions towards a successful implementation of MQL and MQSL into industry

### Ongoing research and technology development

The use of solid lubricants can take a number of forms, with respect to both material and application systems. Three types of solid lubricant were selected for this research; Molybdenum Disulphide ( $\text{MoS}_2$ ), Calcium Fluoride ( $\text{CaF}_2$ ) and Boron Nitride (hBN). The suitability of these lubricants was considered using a range of application methods. The lubricant was first used in its original form and subsequently was combined with alternative fluids, or doped with alternative materials and/or carrier fluids, in order to offer a degree of flexibility.

Indeed, substantial effort was involved in the design and development of the necessary tooling before any experimentation could take place. Novel lubricant feeding systems were developed to make the trials of the solid lubricant possible. This involved the design and installation of a variety of lubricant feeding mechanisms, within the SAT grinding machine environment, using mechanical, pneumatic and electrostatic principles. Accurate quantities of lubricant material were then fed with precisely controlled mass flowrates into the grinding zone.

The introduction of a graphite faced shoe nozzle provided an effective method of continuously delivering MQL and MQSL fluids under useful flowrates. This enabled the surface of the nozzle to maintain a constant height above the periphery of the grinding wheel. The geometry of the grinding wheel was replicated into the shoe nozzle by grinding into the underside of the graphite nozzle, enabling the lubricant to be applied over the width of the rotating wheel. Previous research had identified a 'useful flowrate' that is determined through the empty volume between the abrasive grits on the surface of a grinding wheel. The open pore volume was therefore assessed through microscopy measurement and con-focal imaging provided a series of topographical impressions and measurements necessary to calculate these values. Baseline 'control' measurements were gathered by using commercially available water based EcoCool machining oil under MQL conditions in order to allow the comparative assessment of the performance of the MSQs.



---

## Experimental design /controls /methods: advantages /limitations

Once the equipment was designed and installed a series of Taguchi factorial experimental designs were undertaken. These identified the significance of the four major machining parameters; the rotational speed of the grinding wheel, the rotational speed of the workpiece, the infeed speed of the plunge grind and the variation of the type and the quantity of the solid lubricant. The results from these trials were interpreted using the analysis of variance (ANOVA) technique. The power consumption from the grinding trials was recorded and a range of output characteristics were measured relating to the assessment of the surface integrity of the samples including; the microstructure, the surface roughness and the residual stresses. The Taguchi trials then provide an optimisation of the machining parameters with respect to improving the surface integrity of the workpiece.

The use of EcoCool, and therefore probably most traditional fluids, confirmed that an increase in the concentration of machining oil results in an increase in effective lubrication. An increase in oil reduces both power consumption and specific grinding energy. An important point to note is the open porous condition of the wheel as the emulsified oil is ejected after passing through the grinding zone. The free moving structure of the fluid is thought to possess a relatively large mass that is easily ejected when rotated at high grinding wheel speeds.

The first solid lubricant to be introduced to the grinding environment was MoS<sub>2</sub> with a lamella structure to encourage the efficient interaction of the tool and the workpiece. The introduction of MoS<sub>2</sub> as a solid lubricant was shown to provide some encouraging results with the MoS<sub>2</sub> showing reductions in the quantity of energy required to remove the surface of the workpiece material, known as the Specific Grinding Energy (SGE). The ability of the MoS<sub>2</sub> to reduce the SGEs at smaller chip thicknesses is of particular interest. This was the first step to determining whether cooler grinds were achievable through effective lubrication. However the MoS<sub>2</sub> does come with challenges. The powdered lubricants have a tendency to clog and load the wheel surface, which becomes more problematic if the amount of fluid is reduced or and no means of cleaning the wheel surface (scrubbing devices). The heavier concentrations of MoS<sub>2</sub> were found to compact within the grit pores of the grinding wheel and had no means of release. Under these conditions the grinding wheel was beginning to struggle in removing material from the surface of the workpiece and was observed by a rise in the consumption of machining power. This is indicative of a less effective formation of swarf or chip and is associated with a large proportion of grinding energy involved in the abrasive grits rubbing on the workpiece surface, and a clear source of thermal energy. This suggests that there is a balance to be found between the chip thickness and the inter-grit volume of the grinding wheel. The relative proportion of solid lubricant and chip thickness needs careful consideration in order to create and successfully release the chip from the workpiece surface. The porous volume of the grinding wheel

---

needs to allow the chip to form while at the same time allowing the wheel to self clean. The ability of the grinding wheel to retain its open pores between the abrasive grits is limited by a reduction of the flushing capability under the MQL regimes and increases the likelihood of increased loading and thermal damage. Therefore the maximum chip thickness and the maximum mass flowrate of solid lubricant need to be determined from the properties of the grinding wheel and workpiece in order to prevent wheel loading. These are key to establishing effective MQSL machining.

There was very little evidence of surface burn found throughout the MoS<sub>2</sub> trials. The Barkhausen Magnetic Noise scans indicated acceptable levels of residual stress which correlated well to the confirmation of a constant hardness values throughout the immediate sub surface layers. The samples that were exposed to the MoS<sub>2</sub> appeared to have a dark discolouration upon the surface. In practical applications, the next stage of manufacture would involve polishing the newly ground surfaces and polishing tools would be damaged through the contamination of MoS<sub>2</sub>, a great disadvantage. Furthermore, MoS<sub>2</sub> could create sulphides upon the surface of the steel workpiece that could cause the failure of a component through sulphide embrittlement. An alternative view was that a fusion of the solid lubricant within the surface could benefit the lifetime performance of many ground components. The SEMs analysis, captured the elemental analysis of the surface of the steel samples however, gave no conclusive evidence to suggest that the solid lubricants had reacted with the sample surface.

The second class of lubricant considered was CaF<sub>2</sub>. This was selected for its lubricity and its natural tribo-luminescent characteristic. (This was exploited at the later stages of investigation in the detection of grinding zone temperatures). However CaF<sub>2</sub> proved troublesome in comparison to MoS<sub>2</sub> because it is a lot less dense and required a redesign of the feeding mechanism in order to provide similar mass flowrates as the MoS<sub>2</sub>. The trials showed that CaF<sub>2</sub> was not quite as effective as first thought. CaF<sub>2</sub> is recognised to function more effectively as a lubricant at elevated temperatures due to the breakdown of the structure between the calcium bonds. Thermal stresses begin to weaken the ionic bonds between calcium and enable the planes to slip, that provides the lubricative action. Although a slight reduction of SGE was achieved through a higher level of delivery of 8.3 g/min of CaF<sub>2</sub>, the improvement in the grinding cycle efficiency was negligible. The general SGEs achieved by CaF<sub>2</sub> were substantially higher than the EcoCool and MoS<sub>2</sub>.

In general, the surface finish obtained with CaF<sub>2</sub> was of a lower quality when compared against the finish achieved through the use of EcoCool machining oil. The Barkhausen Noise scans indicate that the residual stresses are also leaning towards a tensile nature. CaF<sub>2</sub> however did not suffer from wheel loading problems in comparison to the lamella structured lubricants and was able to release itself from the surface of the rotating grinding wheel.

Boron Nitride was the third lubricant tested. The structure of Boron Nitride is similar to that of MoS<sub>2</sub> and graphite that provides a degree of confidence in its lubricative properties. Over the range of parameters the hBN reduces the SGE by 10J/mm<sup>3</sup> when doubling the mass flowrate from 18 g/min to 41 g/min. This range of SGE is still slightly above the EcoCool values. However, as a percentage of the reduction of SGE reduction, the quantity of hBN can be associated with the equivalent of a 1-10% increase in the oil content of the machining fluid. This helps to reduce the volume of lubrication required to achieve SGE similar to that of conventional oils.

Boron Nitride was also shown to provide stable conditions of residual stress as those seen in Figure 186. The ANOVA result indicates that lower chip thicknesses required more lubricant while larger chips needed less. This again suggests that the mechanics involved in forming a chip with solid lubricants differs from that of conventional machining fluids. The grinding wheel needs to retain its open structure in order to efficiently promote the growth of a chip. The application of solid lubricants therefore needs to provide a degree of form and function; to maintain the ability of the abrasive grit to contact the workpiece surface whilst lubricating the face of the grit in order to allow the formation of a chip. The availability of free space within the surface of a wheel to form chips dictates the quantity of lubricant that can be usefully added to the grinding process see Figure 231. As the grits move deeper into the workpiece, the lubricant occupies too much space for the successful formation of a chip. Therefore a relatively small quantity of solid lubricant within the surface of the wheel is needed to cover the flank face of the abrasive grit. This enables the chip to grow within the depth of the pore. The hBN demonstrates similar instances of wheel loading to that of MoS<sub>2</sub>. This is observed by an increase in specific grinding energy values from the lower levels of hBN mass flowrates and generally results in thermally induced damage upon the surface of the samples. When the grinding wheel began to clog with solid lubricant it was extremely difficult to promote the formation of chips and encourage the release of residue. This resulted in an undesirable quantity of the grinding wheel being lost to redressing in order to regain the original performance of the grinding wheel.

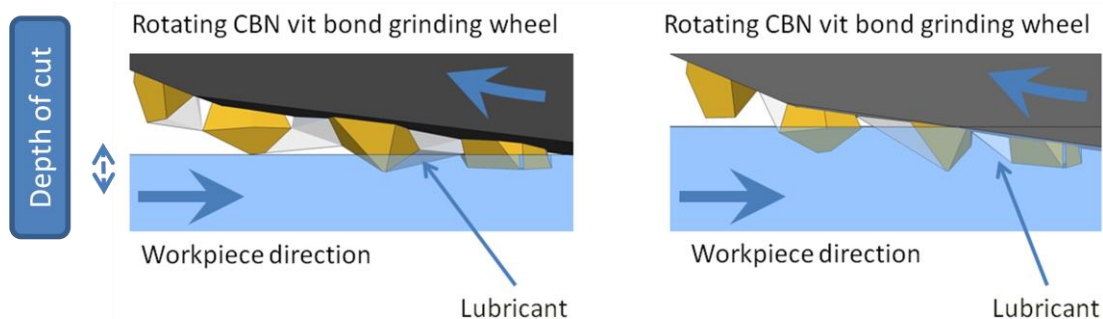


**Figure 231** The influence of chip thickness on the application of a solid lubricant within in the inter-grit space on the periphery of the wheel, with respect to identifying a balance between the delivery mass of the solid lubricant against the available remaining space for chip formation, (left image) shallow grind involving higher mass of lubricant to (right image) deeper grind less inter-grit space left for lubricant in order to efficiently form chips.

---

## Extent to which the technology can offer potential sustainable solutions

The performance of the solid lubricants were analysed in comparison to the EcoCool machining oil. Overall the lowest source of tensile stresses was produced when adding 10% oil concentration in the water based machining fluid. The use of EcoCool showed no signs of transformation in the immediate subsurface microstructure and the Barkhausen magnetic noise scans indicated acceptable levels of residual stress. On the other hand  $\text{CaF}_2$  demonstrated a considerable rise in the magnetic power levels representative of a more tensile level of residual stress. The cubic structure of the  $\text{CaF}_2$  powder was suspected to cause an increase in the specific grinding energy that indicated a degradation of the grinding conditions through a reduction of the lubricative properties of the grinding process. The Boron Nitride showed a degree of control with respect to the stress conditions due to a process involving a smoother removal of the chips from the surface. Residual stress levels associated with hBN were still not as low as the EcoCool however the stress conditions also did not significantly change over the variation in the mass flowrate of the solid lubricant. This indicates that the lower levels of hBN are able to maintain the surface integrity with a reduction in the quantity of process resources and promotes the use of MQL methods within abrasive machining.

The electrostatic powder-feed system was introduced to facilitate the precise delivery of solid lubricant delivery. The system successfully deposited a fine film of lubricant onto the surface of the workpiece and the results from the electrostatic trials proved encouraging. The powder was attracted onto the surface of the workpiece and taken into the grinding zone. The feed system was designed to function without any use of fluids that could otherwise weaken the electrostatic attraction between the powder and the workpiece. However, the dressing regime resulted in low levels of moisture remaining within the machining environment. The feeding mechanism was designed to allow the powdered lubricant to be compactly positioned directly above the grinding zone. The hopper feed was agitated by an eccentric motor to prevent the lubricant from settling and compacting within the feed lines.

Initial trials showed that the electrostatic attraction of the charged powder was able to function within the grinding environment. Specific Grinding Energy values vary with the mass flowrates of the  $\text{CaF}_2$ . The Specific Grinding Energies are shown to reduce by approximately  $20\text{J}/\text{mm}^3$  at low mass flowrates of  $\text{CaF}_2$  (6-18g/min, 0.5-1bar air pressure). An increase in the delivery mass flowrate brings with it a higher degree of air disturbance around the wheel due to higher pressure air flows. Under turbulent conditions the benefit of the added powder is lost and the SGEs rise to a value equal to that of a wheel with no added lubricants. Further increases in the delivery rates completely fill the machine with a fine dry powder. This benefits the process, but is unsafe for the operator.

---

The electrostatic field strength however was relatively weak in comparison to the forces from the movement of air generated by the abrasive machining process. Therefore adequate protection was needed to prevent unnecessary disturbance around the grinding zone. The voltages used within this research were low in comparison to commercial paint applications but were capable of delivering a fully charged dry solid lubricant material into the grinding zone without the need of a carrying body or fluid. The use of electrostatics has recently been used for MQL milling by charging oil based lubricants containing graphite. This highlights the potential benefits of electrostatics within MQL and MQSL systems if properly managed, and the lubricant itself could also be developed to possess stronger electrostatic properties.

A Charged Coupled Device (CCD) light sensor was used to identify changes in the wavelength and intensity of the emitted chip energy. The CCD device was targeted at the greatest concentration of grinding sparks after the grinding zone. The spectrum was measured over the 300-750nm range and was correlated against the finish surface temperatures. The experimental temperatures were determined through the use of Physical Vaporised Deposition (PVD) heat sensitive films that possessed low melting point properties. Isotherms develop into the depth of the ground samples when exposed to grinding heat on the finish surface. By measuring the depths of the isotherms for each of the various PVD materials the temperatures were extrapolated towards the surface.

The thermal modelling predicted finish surface temperatures without the conduction of heat through the machining fluid and provided a close parallel to the PVD determined temperatures. The outputs include the contact and finish temperature, the heat flux values and the energy partition between the chip and the workpiece. Pyrometers and thermocouples were also used as methods of temperature measurement however their operation presented problems associated with emissivity values of glowing chips and the hard-wiring of sensors respectively and so were disregarded. Originally it was intended to recognise the movement of the spectrum around 475nm wavelengths as  $\text{CaF}_2$  possesses natural tribo-luminescent properties within the blue region of the visible spectrum. The trials however detected very little variation within the spectral peaks around this region. Therefore the overall shape of the spectrum was of more significance in terms of the colour and brightness of the emitted grinding sparks. The CCD sensor showed some promising trends with respect to detecting shifting patterns in the chip electromagnetic energy. Movements towards longer wavelengths and a reduction in intensity values would be detected from the chip when lower finish surface temperatures were predicted and observed, due to the addition of effective solid lubrication and a reduction in the SGE values. Likewise, at elevated surface temperatures, the detected chip energy responded to a shortening of the peak positions wavelengths and an increase in the intensity. The behaviours of the  $\text{CaF}_2$  and hBN solid lubricants were identified with the CCD sensor, as the removal of large quantities of fluid associated with MQSL abrasive machining enabled the

---

use of the optical detection system. The higher workpiece finish surface temperatures were found with an increase in mass flowrates of  $\text{CaF}_2$  and a reduction mass flowrate of the hBN. This correlates with the general understanding of the influence of surface temperature through effective lubrication. The results from the CCD sensor investigation are encouraging and provide an important contribution to the development of a non-contact thermally adaptive machine control system. This research appreciates however the necessity of calibrating the CCD device for individual machining process that is dependent on the tooling, lubricant and workpiece materials properties.

---

## 8.0 Conclusions and Recommendations

### 8.1 Conclusions

*Objective 1: Identify the behaviour of MQL machining fluids within the abrasive machining process.*

The Taguchi experimental trials showed that the most efficient grinding conditions were achieved with a 10% concentration of Fuchs EcoCool oil added to the MQL water flowrates. Specific Grinding Energy (SGE) was reduced when increasing the lubricant properties of the MQL fluid. The microstructural analysis found no evidence of thermally induced damage in the subsurface layers of the samples exposed to higher concentrations of EcoCool, and the Barkhausen Magnetic Noise detection scans showed acceptable levels of residual stress. On the other hand the reduced concentrations of oil endangered the steel surfaces to excessive thermal loads. It is concluded that MQL methods are thought to be applicable to grinding applications providing the fluids possess properties of lubrication that are effective and are suitably directed into the grinding zone. The implications of this support an argument to reduce the quantity of machining fluid providing that sufficient lubrication is available. The knowledge attained through the completion of this objective was necessary to develop the idea of Minimum Quantity Solid Lubrication within grinding (MQSL).

*Objective 2: Develop an understanding of the implications of MQSL within abrasive machining, involving the development of suitable MQSL feeding mechanisms and compare with use of conventional fluids.*

Molybdenum Disulphide ( $\text{MoS}_2$ ), Calcium Fluoride ( $\text{CaF}_2$ ) and Boron Nitride (hBN) were applied under MQL conditions into the grinding zone. A series of lubricant delivery systems were developed to provide precise and continuous mass flowrates of solid lubricant within a series of Taguchi trials. Overall the solid lubricants did not achieve the mean Specific Grinding Energies compared to the EcoCool control fluid. Out of the solid lubricants hBN had the most significant improvement in grinding performance. This was proven by its ability to control; specific grinding energy, surface temperature and achieve good quality surface integrities. The increased effect of hBN lubrication was quantified against the variation of concentration of EcoCool in the control machining fluid. A 2.3g/min increase in hBN powder mass flowrate reduced the Specific Grinding Energy by a similar amount as that achieved from a 1% increase in EcoCool concentration, using similar MQL water flowrates, tooling, and workpiece material.

This objective was achieved in identifying the differences in the ability of grinding wheels to function between MQL and MQSL conditions. The properties of machining fluids become more prominent with respect to the capability of the wheel to self clean. The lamella



---

structured solid lubricants have a higher tendency to clog the wheel at larger chip thicknesses. The implication of this is the most efficient use of solid lubricant depends upon the tool type, the workpiece material, the capability of a wheel to convey the lubricant through the grinding cycle and finally the ability of the wheel to release the lubricant after the grinding zone. The influence of the thermal properties of the abrasive grit and the machining fluid were investigated through the development of the thermal model. The use of CaF<sub>2</sub> produced finish temperatures that were accountable through a thermal conductivity ( $K_g$ ) value of 240W/mK for the cBN grinding wheel in comparison to the hBN that implied that much more heat conduction was taking place with a value of 1300W/mK and is accountable through the high thermal conduction property of the hBN solid lubricant.

Mechanical, pneumatic and electrostatic methods were developed to deliver precise quantities of the solid lubricant. The highest delivery rates were achieved by using the pneumatic system adding the dry powder to various air pressures. The most controlled method was the electrostatic method attracting the charged solid lubricant to the surface of the workpiece. With further development the electrostatic method could prove extremely advantageous with the precise application of MQL and MQSL systems within abrasive machining.

*Objective 3: Investigate the feasibility of an optical non-invasive method of determining the surface finish temperature, by capturing the emitted energy from the grinding zone.*

The reduction in the quantity of machining fluid under MQL and MQSL methods enable an optical sensor to detect the emitted energies from the grinding process. A Charge Coupled Device (CCD) sensor was introduced into the grinding environment to capture the electromagnetic energy and identify the variations in visible spectrum with respect to the wavelength and intensity of the chip (spark) light. The shifts in spectrum patterns were correlated against experimental and modelled finish surface temperatures. The sensor recordings showed that a shortening of the wavelengths of the chip light correlated to a reduction in the finish surface temperature. Equally a reduction in the intensity of the emitted chip light resulted in instances of cooler grinding. The achievement of this objective identified that the captured spectrum bandwidth of 550nm to 700nm was of significant importance in determining the finish surface temperature. The implication of this provides a significant contribution towards the development of a non-destructive non-invasive thermal monitoring device. The optical lens was able to function within the grinding environment with a series of air jets protecting the lens from hot chips and lubricant dust.

*Objective 4: Construct, by combining the previous three objectives, a real-time grinding temperature management system*

The CCD device was proven to capture changes in the grinding process with respect to thermal behaviour however a fully automated thermally-adaptive control system was not



---

completed within the time frame of this research. The detectable optical energy of the chip is influenced by the interaction of the physical and thermal properties of the tool, workpiece and lubricant, requiring the creation of a suitable database to contain the calibrated signals for the necessary process. This database could relate the detected chip light to; the recorded grinding power, the expected finish temperatures, and to the desired surface integrity, enabling a real-time closed –loop thermal monitoring system to function. This development requires more collaboration and expertise in control systems to be fully exploited on an industrial scale.

The major contributions to knowledge are:

1. Developing the knowledge associated with applying MQL fluids within abrasive machining. A higher percentage of lubricant within MQL fluid flowrate reduces the specific grinding energies indicating that the fluid flow can also be reduced.
2. Solid lubrication was demonstrated to benefit smaller chip thicknesses. The MQSL method at smaller chip thicknesses reduced the quantity of frictional heat. At larger chip thicknesses the advantage of the solid lubricants is limited due to their behaviour within the pores of the grinding wheel. The elimination of machining fluids requires the capability to control an open surface on the grinding wheel.
3. The thermal modelling demonstrated how the solid lubricants change the frictional source of heat and the method of which the thermal energy is dissipated throughout the grinding system. The addition of an effective solid lubricant results in a longer period of sliding on the surface of the workpiece and enables a larger quantity of energy to be conducted from the finish surface.
4. The finish surface temperatures were correlated to recorded movements in the captured visible spectrum of the grinding sparks. The optical detection of grinding chip energy is a significant contribution to the development of a non-contact non-invasive temperature device. Suitable calibration of the system, and sufficient control expertise could lead to the development of a fully automated ‘thermally-adaptive abrasive machining control system’.
5. A novel use of segmented PVD films was used to determine the surface temperature from a single cylindrical plunge grind. Three types of low melting point metals were deposited onto the same surface of cylindrical discs in 120 degree segments. Upon reconstruction the sample bar was rotated by the work-head and exposed the surface to the actions of the grinding wheel. The isotherms for each trial reacted under the exact same thermal conditions providing an accurate determination of the surface temperature.
6. The introduction of an electrostatic lubricant delivery system provides an exciting direction in which to develop MQL and MQSL methods within abrasive machining. The system was proven to attract lubricant into the grinding zone and is worthy of greater development and investigation.

---

## 8.2 Recommendations

The results and conclusions drawn from this research lead to a number of recommendations for further research and development activities in order to exploit the potential of MQSL technologies, namely:

- Developments in the design of grinding tools to integrate the use of solid lubricants to promote an efficient action of the solid lubrication.
- Development of MQL and MQSL lubricants with electro-statically responsive properties to facilitate precision placement.
- Development of temperature control systems for machining parameters.

The recommendations are discussed in turn.

### 8.2.1 Tooling Development

Solid lubrication was found to have a greater effect at small chip thicknesses. On the other hand attempts to form larger chips with solid lubricants resulted in the clogging of the grinding wheel surface. This was found to occur through a combination of the compaction of the solid lubricant in the surface of the grinding wheel and a lack of machining fluid to assist in flushing out the system. Investigations in grinding wheel design should take place to enable tooling to optimise the flow and function of the solid lubricant. Tooling designs already attempt to dissipate process heat through mechanical features, and solid lubricants have already been included in the structure of the wheels. However there is an opportunity to exploit the action of solid lubrication in the pores of the surface. The shape of the grinding wheel needs to adapt towards methods of solid lubrication and dry grinding.

The Taguchi trials necessitated a repeated dressing of the wheel surface in order to return the wheel to a known topological condition. This amount of dressing obviously increased the rate of wear on the grinding wheel and would not be acceptable under industrial conditions. Trials should be undertaken with repeated plunge grinds to determine the G ratio of the tooling under MQSL machining conditions. The wheel dimensions and geometrical form should be investigated under MQSL conditions to identify the influence of the tool, workpiece, machining parameters and the lubricants.

### 8.2.2 Electrostatic Machining Lubricants

The introduction of electrostatics was proven as an innovative approach to the precise delivery of solid lubricants. The ability to direct and control the active regions of lubrication is of benefit towards achieving MQL and MQSL machining methods. Recommendations towards machining fluid and lubricant manufacturers are within the development of the lubricants themselves, and enable the lubricants to possess strengthened electrostatic properties. Improving the electrostatic nature of the lubricant would optimise the

---

performances of the electrostatic delivery, and provide a greater capability to remove and clean the grinding wheel. For example a secondary ‘target’ could be positioned after the grinding zone, to attract the solid lubricant out of the pores of the grinding wheel. This would address the problem associated with clogging, and allow the lubricant to be separated from the swarf for cleaning and recycling purposes.

### **8.2.3 Machine Design and Development**

In order to construct a fully automated thermally-adaptive control system the optically detected grinding energy requires calibration against the surface temperatures. A database containing the physical and thermal interactions between the tools, workpiece materials and the lubricants should be established to be accessed by a closed-loop NC control system. The optical system would enable the machine to ‘see’ and interpret, the condition of the grinding process. The grinding machine would then be able to automatically adapt the machining parameters or change the delivery rates of the lubricant, depending on the required surface temperature. This would greatly improve the capability to pre-determine the final surface integrities of abrasively machined parts.

Calcium Fluoride ( $\text{CaF}_2$ ) has a natural tribo-luminescent property around the blue region of the visible spectrum. This phenomenon could be potentially exploited for temperature detection. A Charged Coupled Device (CCD) sensor however failed to identify a significant shift around the region of the spectrum. Nevertheless, a CCD device captured changes in spark patterns and could, if combined with alternative thermometry methods could provide the basis for a thermo optical control system. Phosphor-doped thermal barrier coatings for example are an emerging technology designed to determine the real-time temperatures of fully functioning gas turbine blades. The addition of this technology could result in phosphorescent materials being applied to the grinding environment. The phosphorescent response created through the formation of grinding chips could enable a more responsive detection of the grinding energy and hence, the determination of surface temperature.

These recommendations have implications for researchers, tool designers, lubricant manufacturers and machine builders. The continuation of this research work highlights the need to promote the exchange of knowledge between industry and researchers. Collaborative research enables the capacity of industry to implement innovative machining methods and encourage the investment in material technology and manufacturing machine design. This is the key to the success of MQSL within abrasive machining.

---

## 9.0 References

- Batako, A. D., Rowe, W. B. and Morgan, M. N. (2005), "Temperature measurement in high efficiency deep grinding", *International Journal of Machine Tools and Manufacture*, vol. 45, no. 11, pp. 1231-1245.
- Bergeron, N. P., Hollerman, W. A., Goedeke, S. M., Hovater, M., Hubbs, W., Finchum, A., Moore, R. J., Allison, S. W. and Edwards, D. L. (2006), "Experimental evidence of triboluminescence induced by hypervelocity impact", *International Journal of Impact Engineering*, vol. 33, no. 1-12, pp. 91-99.
- Bosch Rexroth (2004), *External Gear Pumps Series F*, available at: [www.boschrexroth.com](http://www.boschrexroth.com).
- Brinksmeier, E., Aurich, J. C., Govekar, E., Heinzl, C., Hoffmeister, H. -, Klocke, F., Peters, J., Rentsch, R., Stephenson, D. J., Uhlmann, E., Weinert, K. and Wittmann, M. (2006), "Advances in Modeling and Simulation of Grinding Processes", *CIRP Annals - Manufacturing Technology*, vol. 55, no. 2, pp. 667-696.
- Brinksmeier, E., Cammett, J. T., König, W., Leskovar, P., Peters, J. and Tönshoff, H. K. (1982), "Residual Stresses — Measurement and Causes in Machining Processes", *CIRP Annals - Manufacturing Technology*, vol. 31, no. 2, pp. 491-510.
- Brinksmeier, E., Eckebrecht, J. and Buhr, H. (1994), "Improving ecological aspects of the grinding process by effective waste management", *Journal of Materials Processing Technology*, vol. 44, no. 3-4, pp. 171-178.
- Brinksmeier, E., Heinzl, C. and Wittmann, M. (1999), "Friction, Cooling and Lubrication in Grinding", *CIRP Annals - Manufacturing Technology*, vol. 48, no. 2, pp. 581-598.
- Budinski, K. G. (2007), "ASTM Guide to Friction, Wear and Erosion Testing", *ASTM International*, .
- Callister, W. D. (1997), *Materials science and engineering : an introduction*, 4th ed, Wiley, Chichester.
- Cheng, C., Phipps, D. and Alkhattar, R. M. (2005), "Treatment of spent metalworking fluids", *Water Research*, vol. 39, no. 17, pp. 4051-4063.
- Chiu, N. and Malkin, S. (1993), "Computer Simulation for Cylindrical Plunge Grinding", *CIRP Annals - Manufacturing Technology*, vol. 42, no. 1, pp. 383-387.
- Clarke, D. R. and Gentleman, M. M. (2007), "Luminescence sensing of temperatures in thermal barrier coatings", *Surface and Coatings Technology*, vol. 202, no. 4-7, pp. 681-687.
- Comley, P. (2005), *Grinding Processes and their Effects on Surface Integrity* (unpublished PhD. thesis), School of Industrial & Manufacturing Science, Cranfield University, .
- Comley, P., Corbett, J. and Cranfield University. School of Industrial and Manufacturing Science (2005), *Grinding processes and their effects on surface integrity*, .

- 
- Comley, P., Walton, I., Jin, T. and Stephenson, D. J. (2006), "A High Material Removal Rate Grinding Process for the Production of Automotive Crankshafts", *CIRP Annals - Manufacturing Technology*, vol. 55, no. 1, pp. 347-350.
- Cottingham, W. N. and Greenwood, D. A. (1987), *An introduction to nuclear physics*, Cambridge University Press.
- da Silva, L. R., Bianchi, E. C., Fusse, R. Y., Catai, R. E., França, T. V. and Aguiar, P. R. (2007), "Analysis of surface integrity for minimum quantity lubricant—MQL in grinding", *International Journal of Machine Tools and Manufacture*, vol. 47, no. 2, pp. 412-418.
- Doman, D. A., Warkentin, A. and Bauer, R. (2008), "Finite element modeling approaches in grinding", *International Journal of Machine Tools and Manufacture*, vol. In Press, Accepted Manuscript.
- Ebbrell, S., Woolley, N. H., Tridimas, Y. D., Allanson, D. R. and Rowe, W. B. (2000), "The effects of cutting fluid application methods on the grinding process", *International Journal of Machine Tools and Manufacture*, vol. 40, no. 2, pp. 209-223.
- Edwards, A. J. and Edwards, T. (2003), "Introduction to ISO 14001", in *ISO 14001 Environmental Certification Step by Step*, Butterworth-Heinemann, Oxford, pp. 9-13.
- European Union (2007), "REACH legislation", *Official Journal of the European Union*, vol. 50.
- Fuchs Lubricants (UK) Plc, (2007), *Ecocool Ultralife; New water soluble coolant technology*.
- Ganesan, M. (2001), "Analysis of Hydrodynamic Forces in Grinding", *Abrasives Magazine*, .
- George E. Totten, Steven R. Westbrook, Rajesh J. Shah (2003), *Fuels and lubricants handbook: technology, properties, performance, and testing, Volume 1*, ASTM International.
- Greeley, M. and Rajagopalan, N. (2004), "Impact of environmental contaminants on machining properties of metalworking fluids", *Tribology International*, vol. 37, no. 4, pp. 327-332.
- Griffiths, B. (2001), *Manufacturing surface technology : surface integrity and functional performance*, Penton Press, London.
- Gviniashvili, V. K., Woolley, N. H. and Rowe, W. B. (2004), "Useful coolant flowrate in grinding", *International Journal of Machine Tools and Manufacture*, vol. 44, no. 6, pp. 629-636.
- Heyes, A. L., Seefeldt, S. and Feist, J. P. (2006), "Two-colour phosphor thermometry for surface temperature measurement", *Optics & Laser Technology*, vol. 38, no. 4-6, pp. 257-265.
- Howes, T. (1990), "Assessment of the Cooling and Lubricative Properties of Grinding Fluids", *CIRP Annals - Manufacturing Technology*, vol. 39, no. 1, pp. 313-316.
- Jackson, A. (2008), *An Investigation of Useful Fluid Flow in Grinding* (unpublished PhD thesis), Liverpool John Moores University, .

- 
- Jaeger, J. C. (1942), "Moving Sources of Heat and the Temperature at Sliding Contact", *Proc. R Soc. New South Wales*, vol. 76, no. 3, pp. 203-224.
- Jin, T. and Stephenson, D. J. (Sep 2003), "International Journal of Machine Tools and Manufacture : Investigation of the heat partitioning in high efficiency deep grinding", vol. 43 (11), pp. p.1129-1134.
- Jin, T., Rowe, B. W. and McCormack, D. (2002), "Temperatures in deep grinding of finite workpieces", *International Journal of Machine Tools and Manufacture*, vol. 42, pp. 53-59.
- Jin, T. and Stephenson, D. J. (2008), "A study of the convection heat transfer coefficients of grinding fluids", *CIRP Annals - Manufacturing Technology*, vol. 57, no. 1, pp. 367-370.
- Jin, T. and Stephenson, D. J. (2006), "Heat flux distributions and convective heat transfer in deep grinding", *International Journal of Machine Tools and Manufacture*, vol. 46, no. 14, pp. 1862-1868.
- Jin, T., Rowe, W. B. and McCormack, D. (2002), "Temperatures in deep grinding of finite workpieces", *International Journal of Machine Tools and Manufacture*, vol. 42, no. 1, pp. 53-59.
- Jonassen, N. (1998), *Electrostatics*, Chapman & Hall, USA.
- Kato, T. F.,H. (1997), "Temperature Measurement of Workpiece in Surface Grinding by PVD Film Method", *Journal of Manufacturing Science and Engineering*, vol. 119.
- Kaye & Laby, N. (2010), *Tables of physical and chemical constants*, available at: <http://www.kayelaby.npl.co.uk/>.
- Khalid, A. H. and Kontis, K. (2008), "Thermographic Phosphors for High Temperature Measurements: Principles, Current State of Art and Recent Applications", *Sensors*, .
- Klocke, F., Baus, A. and Beck, T. (2000), "Coolant Induced Forces in cBN High Speed Grinding with Shoe Nozzles", *CIRP Annals - Manufacturing Technology*, vol. 49, no. 1, pp. 241-244.
- Klocke, F., Brinksmeier, E. and Weinert, K. (2005), "Capability Profile of Hard Cutting and Grinding Processes", *CIRP Annals - Manufacturing Technology*, vol. 54, no. 2, pp. 22-45.
- Klocke, F. and Eisenblätter, G. (1997), "Dry Cutting", *CIRP Annals - Manufacturing Technology*, vol. 46, no. 2, pp. 519-526.
- Koc, T. (2007), "The impact of ISO 9000 quality management systems on manufacturing", *Journal of Materials Processing Technology*, vol. 186, no. 1-3, pp. 207-213.
- Lauer-Schmaltz, H. and König, W. (1980), "Phenomenon of Wheel Loading Mechanisms in Grinding", *CIRP Annals - Manufacturing Technology*, vol. 29, no. 1, pp. 201-206.
- Lavine, A. S., Malkin, S. and Jen, T. C. (1989), "Thermal Aspects of Grinding with cBN Wheels", *CIRP Annals - Manufacturing Technology*, vol. 38, no. 1, pp. 557-560.

- 
- Malkin, S. (2007), *Grinding technology : the way things can work : theory and application of machining with abrasives*, 2nd ed, Industrial Press, New York.
- Malkin, S. and Guo, C. (2007), "Thermal Analysis of Grinding", *CIRP Annals - Manufacturing Technology*, vol. 56, no. 2, pp. 760-782.
- Malkin, S. and Joseph, N. (1975), "Minimum energy in abrasive processes", *Wear*, vol. 32, no. 1, pp. 15-23.
- Malkin, S. (1981), "Grinding Cycle Optimization", *CIRP Annals - Manufacturing Technology*, vol. 30, no. 1, pp. 223-226.
- Marinescu, I., Rowe, W. B., Dimitrov, B. and Inasaki, I. (2004), *Tribology of Abrasive Machining Processes*, William Andrew.
- Marinescu, I. D., Hitchiner, M., Uhlmann, E., Inasaki, I. and Rowe, B. W. (2006), *Handbook of Machining with Grinding Wheels*, CRC Press.
- Matweb (2008), *Online Materials Information Resource*, available at: <http://www.matweb.com/index.aspx>.
- Metzger, J. L. (1986), *Superabrasive grinding*, Butterworths, London ; Boston.
- Moorthy, V., Shaw, B. A. and Evans, J. T. (2003), "Evaluation of tempering induced changes in the hardness profile of case-carburised EN36 steel using magnetic Barkhausen noise analysis", *NDT & E International*, vol. 36, no. 1, pp. 43-49.
- Morgan, M. N., Jackson, A. R., Wu, H., Baines-Jones, V., Batako, A. and Rowe, W. B. (2008), "Optimisation of fluid application in grinding", *CIRP Annals - Manufacturing Technology*, vol. 57, no. 1, pp. 363-366.
- Nicholls, J. R., Simms, N. J., Chan, W. Y. and Evans, H. E. (2002), "Smart overlay coatings — concept and practice", *Surface and Coatings Technology*, vol. 149, no. 2-3, pp. 236-244.
- Nordson (2011), *Industrial Coating Systems*, available at: [www.nordson.com](http://www.nordson.com).
- P. Nuebert. (1937) *Device for indicating temperature distribution of hot bodies*. Anonymous Patent no. US 2,071,471.
- Perez-Benitez, J. A., Capo-Sanchez, J., Anglada-Rivera, J. and Padovese, L. R. (2008), "A study of plastic deformation around a defect using the magnetic Barkhausen noise in ASTM 36 steel", *NDT & E International*, vol. 41, no. 1, pp. 53-58.
- Rowe, G. W. (1982), "Lubricant testing for grinding operations", *Wear*, vol. 77, no. 1, pp. 73-80.
- Rowe, W.B., Pettit J.A., Boyle A., and Moruzzi J.L. (1988), "Thermal Damage in Grinding and Prediction of the Damage Threshold", *CIRP Annals - Manufacturing Technology*, vol. 37, no.1, pp. 327-330



- 
- Rowe, W. B. and Jin, T. (2001), "Temperatures in High Efficiency Deep Grinding (HEDG)", *CIRP Annals - Manufacturing Technology*, vol. 50, no. 1, pp. 205-208.
- Sawyer, W. G. and Blanchet, T. A. (1999), "Lubrication of Mo, W, and their Alloys with H<sub>2</sub>S gas admixtures to room temperature air", *Wear*, vol. 225-229, no. Part 1, pp. 581-586.
- Shaji, S. and Radhakrishnan, V. (2002), "An investigation on surface grinding using graphite as lubricant", *International Journal of Machine Tools and Manufacture*, vol. 42, pp. 733-740.
- Shaw, M. C. (1996), "Energy Conversion in Cutting and Grinding", *CIRP Annals - Manufacturing Technology*, vol. 45, no. 1, pp. 101-104.
- Shaw, M. C. (1995), "Precision Finishing", *CIRP Annals - Manufacturing Technology*, vol. 44, no. 1, pp. 343-348.
- Shaw, M. C. (2005), *Metal cutting principles*, Oxford University Press, Oxford.
- Shaw, M. C. (1996), *Principles of abrasive processing*, Clarendon Press, Oxford.
- Shionoya, S. and Yen, W. M. (1997), *Phosphor Handbook*, CRC-Press.
- Shore, P., Billing, O. and Puhasmagi, V. (2004), "A Standard Grinding Wheel Assessment Method to Support a Sophisticated Grinding Knowledge Based System", *Key Engineering Materials*, vol. 257-258, pp. 285-290.
- Skinner, S. J., Feist, J. P., Brooks, I. J. E., Seefeldt, S. and Heyes, A. L. (2008), "YAG:YSZ composites as potential thermographic phosphors for high temperature sensor applications Accepted Manuscript", *Sensors and Actuators B: Chemical*, vol. Accepted Manuscript.
- Society of Manufacturing Engineers (ed.) (1983), *Tool and Manufacturing Engineers Handbook*, THEM, USA.
- Society of Manufacturing Engineers, Dallas, D. B. and American Society of Tool and Manufacturing Engineers (1976), *Tool and manufacturing engineers handbook : a reference work for manufacturing engineers*, 3d ed, McGraw-Hill, New York.
- Sood, R., Guo, C. and Malkin, S. (2000), "Turning of Hardened Steels", *Journal of Manufacturing Processes*, vol. 2, no. 3, pp. 187-193.
- Southside Thermal Sciences (STS) Ltd. (2008), *Detection Technology*, available at: <http://www.stscience.com/technol/detection.php>.
- StressTech Group (2008), *Barkhausen Noise Analysis*, available at: [www.stresstech.fi/content/en/11501/60/60.html](http://www.stresstech.fi/content/en/11501/60/60.html).
- Sudhangshu Bose (2007), *High Temperature Coatings*, Butterworth-Heinemann.
- Suresh Kumar Reddy, N., Nouari, M. and Yang, M. (2010), "Development of electrostatic solid lubrication system for improvement in machining process performance", *International Journal of Machine Tools and Manufacture*, vol. 50, no. 9, pp. 789-797.



- 
- Tawakoli, T., Hadad, M. J. and Sadeghi, M. H. (2010), "Investigation on minimum quantity lubricant-MQL grinding of 100Cr6 hardened steel using different abrasive and coolant-lubricant types", *International Journal of Machine Tools and Manufacture*, vol. 50, no. 8, pp. 698-708.
- Tawakoli, T. (1993), *High efficiency deep grinding : technology, process planning and economic application*, Mechanical Engineering Publications, London.
- Tawakoli, T. and Azarhoushang, B. (2008), "Influence of ultrasonic vibrations on dry grinding of soft steel", *International Journal of Machine Tools and Manufacture*, vol. 48, no. 14, pp. 1585-1591.
- Tonshoff, H. K. and Brinksmeier, E. (1980), "Determination of the Mechanical and Thermal Influences on Machined Surfaces by Microhardness and Residual Stress Analysis", *CIRP Annals*, vol. 29/2, pp. 519.
- Tönshoff, H. K., Friemuth, T. and Becker, J. C. (2002), "Process Monitoring in Grinding", *CIRP Annals - Manufacturing Technology*, vol. 51, no. 2, pp. 551-571.
- Walker, D. G. and Allison, S. W. (2007), "Transient measurements using thermographic phosphors", *ISA Transactions*, vol. 46, no. 1, pp. 15-20.
- Webster, J., Brinksmeier, E., Heinzl, C., Wittmann, M. and Thoens, K. (2002), "Assessment of Grinding Fluid Effectiveness in Continuous-Dress Creep Feed Grinding", *CIRP Annals - Manufacturing Technology*, vol. 51, no. 1, pp. 235-240.
- Webster, J. and Tricard, M. (2004), "Innovations in Abrasive Products for Precision Grinding", *CIRP Annals - Manufacturing Technology*, vol. 53, no. 2, pp. 597-617.
- Webster, J. A., Cui, C., Mindek Jr., R. B. and Lindsay, R. (1995), "Grinding Fluid Application System Design", *CIRP Annals - Manufacturing Technology*, vol. 44, no. 1, pp. 333-338.
- Weinert, K., Inasaki, I., Sutherland, J. W. and Wakabayashi, T. (2004), "Dry Machining and Minimum Quantity Lubrication", *CIRP Annals - Manufacturing Technology*, vol. 53, no. 2, pp. 511-537.
- Williams, J. (2005), *Engineering tribology*, Cambridge University Press, Cambridge.
- Zapperi, S. and Durin, G. (2001), "New perspectives for the Barkhausen effect", *Computational Materials Science*, vol. 20, no. 3-4, pp. 436-442.

---

## 10.0 Publications and Abstracts

- Initial paper submitted and presented for the 7<sup>th</sup> International Conference of Manufacturing Research at The University of Warwick September 2009.
- Subsequently requested for publication within the International Journal of Advanced Manufacturing Technology, Springer ISSN [0268-3768](#)
- Submitted 4<sup>th</sup> December 2009

### Abrasive processing using Minimum Quantity Solid Lubrication (MQSL)

Morris T., Walton I., Stephenson D.J.  
Cranfield University

Research supported by EPSRC and Cranfield IMRC (Grant No. IMRC 128).

Content presented at the ICMR2009, Warwick University 8<sup>th</sup> September 2009

**Abstract** - The abrasive machining process is an energy-intensive manufacturing process where a large proportion of the process energy is converted to heat during the multiple interactions of abrasive grains against the workpiece surface. Traditionally, methods such as flood and high pressure fluid systems have been utilised to reduce to conduction of the generated heat into the workpiece, lubricate the surface assisting chip formation and encourage swarf removal.

Minimum Quantity Lubrication (MQL) methods are becoming a valid alternative within metal cutting regimes supplying only the required quantity of fluid necessary for a specific volume of material to be removed. MQL is process specific with an elevated risk of damaging the workpiece if not correctly applied and controlled. An alternative method of reducing the quantity of fluid required to achieve good cutting conditions while reducing the heat input into the workpiece is Minimum Quantity Solid Lubrication (MQSL). This method reduces the frictional forces within the contact zone, reducing the total energy necessary for chip formation and removes the effect of surface defects induced by changes in the hydrodynamic force between the wheel and workpiece during grinding.

This paper describes the development of an MQSL application system capable of delivering a controlled quantity of solid lubricant and initial trials showing the benefit of reducing the quantity of fluid into the contact zone.

Keywords: Grinding, MQSL, Solid Lubricants, cBN

- Extended abstract submitted for the HSM 2010 Metz conference titled the Electrostatic Application of MQSL in grinding.
- A paper will be written concerning the application of thermal FEA simulations to external cylindrical grinding

---

## 11.0 Key References

Batako, A. D., Rowe, W. B. and Morgan, M. N. (2005), "Temperature measurement in high efficiency deep grinding", *International Journal of Machine Tools and Manufacture*, vol. 45, no. 11, pp. 1231-1245.

Various views exist on the capability of machining fluids to aid cooling particularly at higher wheel speeds. This paper explains how the contact time between the surfaces is limited while a stiff air barrier builds upon the wheel surface preventing fluid from entering the grinding zone.

Comley, P. (2005), *Grinding Processes and their Effects on Surface Integrity* (PhD. thesis), School of Industrial & Manufacturing Science, Cranfield University.

Explains how the attainment of the desired surface integrity, form and finish can be achieved through an understanding of the creation and movement of temperature, throughout the abrasive cycle.

Jin, T. and Stephenson, D. J. (2008), "A study of the convection heat transfer coefficients of grinding fluids", *CIRP Annals - Manufacturing Technology*, vol. 57, no. 1, pp. 367-370.

Thermal modelling intends to predict the magnitude of surface temperatures. Heat partitioning is investigated for a series of grinding regimes.

Jin, T. and Stephenson, D. J. (2006), "Heat flux distributions and convective heat transfer in deep grinding", *International Journal of Machine Tools and Manufacture*, vol. 46, no. 14, pp. 1862-1868.

The majority of mechanical inputted energy is converted into heat and divided between the wheel, the workpiece, the chip, and the fluid. This paper investigates thermal modelling in comparison to thermocouple behaviour.

Kato, T. F.,H. (1997), "Temperature Measurement of Workpiece in Surface Grinding by PVD Film Method", *Journal of Manufacturing Science and Engineering*, vol. 119.

Physical Vapour Deposition (PVD) of low melting point metals provides an instantaneous reaction to the exposure of heat, in comparison to the delayed response of thermocouples. This paper describes an effective measuring technique for finding peak grinding temperatures.

Malkin, S. and Guo, C. (2007), "Thermal Analysis of Grinding", *CIRP Annals - Manufacturing Technology*, vol. 56, no. 2, pp. 760-782.

Tensile residual stresses are linked to high temperature gradients and uneven plastic deformation of the surface. These stresses can be reduced through the optimisation of the grinding parameters and providing effective cooling.

Marinescu, I., Rowe, W. B., Dimitrov, B. and Inaski, I. (2004), *Tribology of Abrasive Machining Processes*, William Andrew.

---

Abrasive machining relies upon the abrasive grit being harder than that of the workpiece material. This paper is particularly relevant to determining the wheel wear and tool life expectancy.

Morgan, M. N., Jackson, A. R., Wu, H., Baines-Jones, V., Batako, A. and Rowe, W. B. (2008), "Optimisation of fluid application in grinding", *CIRP Annals - Manufacturing Technology*, vol. 57, no. 1, pp. 363-366.

This outlines the life-cycle of machining fluids, highlighting the cost of storage and disposal necessary under recent environmental legislations. This identifies the need to establish more effective machining fluid strategies.

Roy, R. (1990), *A Primer on the Taguchi Method*, SME, Dearborn, Michigan.

This provides an explanation of statistical experimental methods. Enabling the trial parameters to be identified and assisting with the statistical analysis.

Society of Manufacturing Engineers, Dallas, D. B. and American Society of Tool and Manufacturing Engineers (1976), *Tool and manufacturing engineers handbook : a reference work for manufacturing engineers*, 3d ed, McGraw-Hill, New York.

This work provides an overview of the abrasive machining process with particular reference to high machining speeds and high specific removal rates.

Shaji, S. and Radhakrishnan, V. (2002), "An investigation on surface grinding using graphite as lubricant", *International Journal of Machine Tools and Manufacture*, vol. 42, pp. 733-740.

This work is based around the use of paste like solids and concluded that forces, specific energy and surface temperatures were actually reduced through the controlled application of solid lubricants. The surface finish was found to be dominated by the properties of the workpiece material.

T. Tawakoli, M.J. Hadad, et al. (2009), "An experimental investigation of the effects of the workpiece and grinding parameters on minimum quantity lubrication - MQL grinding", *International Journal of Machine Tools & Manufacture*, vol. 49, pp. 924-932.

This work provides evidence on the successful application of MQL within surface grinding. The series of trials reveal that the higher quality surface finishes are when machining harder materials.

Webster, J. A., Cui, C., Mindek Jr., R. B. and Lindsay, R. (1995), "Grinding Fluid Application System Design", *CIRP Annals - Manufacturing Technology*, vol. 44, no. 1, pp. 333-338.

This paper states that grinding fluids are generally accepted as being critical for the production of quality finished components. The tribological effects of grinding fluids are believed to aid in both lubrication and temperature distribution.


# Appendix A. Material Properties

As listed by Matweb 2009

## Low Alloy Steel Properties

| Physical Properties           | Metric                          | English                                 | Comments  |
|-------------------------------|---------------------------------|---|---|
| Density                       | 7.50 - 8.08 g/cc                | 0.271 - 0.292 lb/in <sup>3</sup>        | Average value: 7.85 g/cc Grade Count:1600             |
| Particle Size                 | 6.70 - 12.0 μm                  | 6.70 - 12.0 μm                          | Average value: 9.27 μm Grade Count:20                 |
| Mechanical Properties         | Metric                          | English                                 | Comments  |
| Hardness, Brinell             | 121 - 578                       | 121 - 578                               | Average value: 277 Grade Count:1321                   |
| Hardness, Knoop               | 140 - 875                       | 140 - 875                               | Average value: 310 Grade Count:1311                   |
| Hardness, Rockwell B          | 45.0 - 112                      | 45.0 - 112                              | Average value: 96.2 Grade Count:1252                  |
| Hardness, Rockwell C          | 10.0 - 66.0                     | 10.0 - 66.0                             | Average value: 30.1 Grade Count:1205                  |
| Hardness, Vickers             | 36.0 - 848                      | 36.0 - 848                              | Average value: 300 Grade Count:1323                   |
| Tensile Strength, Ultimate    | 180 - 2450 MPa                  | 26100 - 355000 psi                      | Average value: 949 MPa Grade Count:1483               |
| Tensile Strength, Yield       | 110 - 2400 MPa                  | 16000 - 347000 psi                      | Average value: 739 MPa Grade Count:1484               |
| Elongation at Break           | 0.600 - 37.0 %                  | 0.600 - 37.0 %                          | Average value: 18.5 % Grade Count:1472                |
| Elongation at Yield           | 1.00 - 40.0 %                   | 1.00 - 40.0 %                           | Average value: 16.9 % Grade Count:4                   |
| Reduction of Area             | 0.200 - 75.0 %                  | 0.200 - 75.0 %                          | Average value: 53.9 % Grade Count:613                 |
| Modulus of Elasticity         | 183 - 219 GPa                   | 26500 - 31800 ksi                       | Average value: 204 GPa Grade Count:1412               |
| Compressive Yield Strength    | 1650 - 1800 MPa                 | 239000 - 260000 psi                     | Average value: 1700 MPa Grade Count:12                |
| Bulk Modulus                  | 140 - 170 GPa                   | 20300 - 24700 ksi                       | Average value: 140 GPa Grade Count:1403               |
| Poissons Ratio                | 0.270 - 0.300                   | 0.270 - 0.300                           | Average value: 0.290 Grade Count:1407                 |
| Charpy Impact                 | 15.0 - 339 J                    | 11.1 - 250 ft-lb                        | Average value: 56.3 J Grade Count:15                  |
| Charpy Impact, Unnotched      | 39.3 - 176 J                    | 29.0 - 130 ft-lb                        | Average value: 87.9 J Grade Count:6                   |
| Izod Impact                   | 9.00 - 159 J                    | 6.64 - 117 ft-lb                        | Average value: 58.2 J Grade Count:140                 |
| Fatigue Strength              | 138 - 772 MPa                   | 20000 - 112000 psi                      | Average value: 472 MPa Grade Count:17                 |
| Fracture Toughness            | 80.9 - 143 MPa-m <sup>1/2</sup> | 73.7 - 130 ksi-in <sup>1/2</sup>        | Average value: 120 MPa-m <sup>1/2</sup> Grade Count:4 |
| Machinability                 | 40.0 - 75.0 %                   | 40.0 - 75.0 %                           | Average value: 59.8 % Grade Count:1257                |
| Shear Modulus                 | 70.0 - 84.0 GPa                 | 10200 - 12200 ksi                       | Average value: 79.8 GPa Grade Count:1453              |
| Bend Radius, Minimum          | 0.000 - 4.00 t                  | 0.000 - 4.00 t                          | Average value: 1.65 t Grade Count:101                 |
| Electrical Properties         | Metric                          | English                                 | Comments  |
| Electrical Resistivity        | 0.0000174 - 0.0000300 ohm-cm    | 0.0000174 - 0.0000300 ohm-cm            | Average value: 0.0000227 ohm-cm Grade Count:1339      |
| Thermal Properties            | Metric                          | English                                 | Comments  |
| CTE, linear                   | 10.1 - 14.9 μm/m-°C             | 5.61 - 8.28 μm/in-°F                    | Average value: 12.7 μm/m-°C Grade Count:530           |
| Specific Heat Capacity        | 0.448 - 0.669 J/g-°C            | 0.107 - 0.160 BTU/lb-°F                 | Average value: 0.475 J/g-°C Grade Count:1237          |
| Thermal Conductivity          | 25.3 - 51.9 W/m-K               | 176 - 360 BTU-in/hr-ft <sup>2</sup> -°F | Average value: 44.1 W/m-K Grade Count:1354            |
| Component Elements Properties | Metric                          | English                                 | Comments  |
| Aluminum, Al                  | 0.0100 - 1.20 %                 | 0.0100 - 1.20 %                         | Average value: 0.127 % Grade Count:69                 |
| Boron, B                      | 0.00100 - 0.00500 %             | 0.00100 - 0.00500 %                     | Average value: 0.00230 % Grade Count:211              |
| Carbon, C                     | 0.0300 - 1.29 %                 | 0.0300 - 1.29 %                         | Average value: 0.311 % Grade Count:1593               |
| Chromium, Cr                  | 0.150 - 5.50 %                  | 0.150 - 5.50 %                          | Average value: 0.742 % Grade Count:1160               |
| Cobalt, Co                    | 3.75 - 12.0 %                   | 3.75 - 12.0 %                           | Average value: 8.60 % Grade Count:50                  |
| Copper, Cu                    | 0.100 - 1.50 %                  | 0.100 - 1.50 %                          | Average value: 0.540 % Grade Count:72                 |
| Hydrogen, H                   | 0.00100 - 0.00250 %             | 0.00100 - 0.00250 %                     | Average value: 0.00200 % Grade Count:3                |
| Iron, Fe                      | 63.0 - 100 %                    | 63.0 - 100 %                            | Average value: 96.0 % Grade Count:1638                |
| Manganese, Mn                 | 0.100 - 3.00 %                  | 0.100 - 3.00 %                          | Average value: 0.803 % Grade Count:1586               |
| Molybdenum, Mo                | 0.0600 - 4.80 %                 | 0.0600 - 4.80 %                         | Average value: 0.411 % Grade Count:1203               |
| Nb + V                        | 0.0200 - 0.150 %                | 0.0200 - 0.150 %                        | Average value: 0.124 % Grade Count:5                  |
| Nickel, Ni                    | 0.200 - 18.5 %                  | 0.200 - 18.5 %                          | Average value: 2.37 % Grade Count:874                 |
| Niobium, Nb (Columbium, Cb)   | 0.00500 - 0.100 %               | 0.00500 - 0.100 %                       | Average value: 0.0426 % Grade Count:73                |
| Nitrogen, N                   | 0.00500 - 0.0300 %              | 0.00500 - 0.0300 %                      | Average value: 0.0165 % Grade Count:12                |
| Oxygen, O                     | 0.00250 - 0.100 %               | 0.00250 - 0.100 %                       | Average value: 0.0414 % Grade Count:7                 |
| Phosphorous, P                | 0.00100 - 0.250 %               | 0.00100 - 0.250 %                       | Average value: 0.0333 % Grade Count:1493              |
| Silicon, Si                   | 0.0100 - 2.00 %                 | 0.0100 - 2.00 %                         | Average value: 0.271 % Grade Count:1572               |
| Sulfur, S                     | 0.00100 - 0.250 %               | 0.00100 - 0.250 %                       | Average value: 0.0371 % Grade Count:1526              |
| Titanium, Ti                  | 0.0200 - 1.40 %                 | 0.0200 - 1.40 %                         | Average value: 0.434 % Grade Count:68                 |
| Vanadium, V                   | 0.00500 - 0.300 %               | 0.00500 - 0.300 %                       | Average value: 0.110 % Grade Count:127                |
| Zirconium, Zr                 | 0.0100 - 0.150 %                | 0.0100 - 0.150 %                        | Average value: 0.0268 % Grade Count:56                |

## AISI 1000 Series Low Alloy Steel

| Physical Properties   | Metric                      | English                           | Comments  |
|---|-----------------------------|-----------------------------------|---|
| Density   | 7.858 g/cc                  | 0.2839 lb/in <sup>3</sup>         |   |
| Mechanical Properties   | Metric                      | English                           | Comments  |
| Hardness, Brinell   | 143                         | 143                               |   |
| Hardness, Knoop   | 163                         | 163                               | Converted from Brinell hardness.                |
| Hardness, Rockwell B  | 78                          | 78                                | Converted from Brinell hardness.                |
| Hardness, Vickers   | 149                         | 149                               | Converted from Brinell hardness.                |
| Tensile Strength, Ultimate  | 490 MPa                     | 71100 psi                         |   |
| Tensile Strength, Yield   | 415 MPa                     | 60200 psi                         |   |
| Elongation at Break   | 15.0 %                      | 15.0 %                            | In 50 mm  |
| Reduction of Area   | 40.0 %                      | 40.0 %                            |   |
| Modulus of Elasticity   | 205 GPa                     | 29700 ksi                         | Typical for steel                               |
| Bulk Modulus  | 140 GPa                     | 20300 ksi                         | Typical for steel                               |
| Poissons Ratio  | 0.290                       | 0.290                             | Typical For Steel                               |
| Machinability   | 75 %                        | 75 %                              | Based on AISI 1212 steel. as 100% machinability |
| Shear Modulus   | 80.0 GPa                    | 11600 ksi                         | Typical for steel                               |
| Electrical Properties   | Metric                      | English                           | Comments  |
| Electrical Resistivity  | 0.0000169 ohm-cm            | 0.0000169 ohm-cm                  | 20°C  |
| Thermal Properties  | Metric                      | English                           | Comments  |
| CTE, linear  | 12.1 µm/m-°C                | 6.72 µin/in-°F                    |   |
|   | @Temperature 0.000 - 100 °C | @Temperature 32.0 - 212 °F        |   |
|   | 13.3 µm/m-°C                | 7.39 µin/in-°F                    |   |
|   | @Temperature 0.000 - 300 °C | @Temperature 32.0 - 572 °F        |   |
|   | 14.4 µm/m-°C                | 8.00 µin/in-°F                    |   |
|   | @Temperature 0.000 - 500 °C | @Temperature 32.0 - 932 °F        |   |
| Specific Heat Capacity  | 0.486 J/g-°C                | 0.116 BTU/lb-°F                   | 50-100°C (122-212°F)                            |
| Thermal Conductivity  | 51.9 W/m-K                  | 360 BTU-in/hr-ft <sup>2</sup> -°F | 0°C   |


## Molybdenum Disulphide MoS<sub>2</sub>

| Physical Properties    | Metric       | English                  | Comments    |
|------------------------|--------------|--------------------------|-------------|
| Density                | 5.06 g/cc    | 0.183 lb/in <sup>3</sup> |             |
| a Lattice Constant     | 3.1604 Å     | 3.1604 Å                 |             |
| b Lattice Constant     | 12.295 Å     | 12.295 Å                 |             |
| Formula Units/Cell (Z) | 2.00         | 2.00                     |             |
| Molecular Weight       | 160.07 g/mol | 160.07 g/mol             |             |
| Mechanical Properties  | Metric       | English                  | Comments    |
| Hardness, Mohs         | 1.30         | 1.30                     |             |
| Thermal Properties     | Metric       | English                  | Comments    |
| Melting Point          | 2375 °C      | 4307 °F                  |             |
| Descriptive Properties |              |                          |             |
| CAS Number             |              | 1317-33-5                |             |
| Color                  |              | Black                    |             |
| Crystal Structure      |              | Hexagonal                | Molybdenite |

## Calcium Fluoride CaF<sub>2</sub>

| Physical Properties     | Metric       | English                  | Comments             |
|-------------------------|--------------|--------------------------|----------------------|
| Density                 | 3.18 g/cc    | 0.115 lb/in <sup>3</sup> |                      |
| a Lattice Constant      | 5.4638 Å     | 5.4638 Å                 |                      |
| Formula Units/Cell (Z)  | 4.00         | 4.00                     |                      |
| Molecular Weight        | 78.075 g/mol | 78.075 g/mol             |                      |
| Mechanical Properties   | Metric       | English                  | Comments             |
| Hardness, Knoop         | 139 - 152    | 139 - 152                |                      |
| Hardness, Vickers       | 175 - 200    | 175 - 200                |                      |
| Hardness, Mohs          | 4.00         | 4.00                     |                      |
|                         | 4.00         | 4.00                     |                      |
| Abrasive Hardness       | 5.00         | 5.00                     |                      |
| Drilling Hardness       | 143          | 143                      |                      |
| Electrical Properties   | Metric       | English                  | Comments             |
| Magnetic Susceptibility | -0.0000280   | -0.0000280               | cm <sup>3</sup> /mol |
| Thermal Properties      | Metric       | English                  | Comments             |
| Heat of Fusion          | 384.2 J/g    | 165.3 BTU/lb             |                      |
| Melting Point           | 1418 °C      | 2584 °F                  |                      |
| Boiling Point           | 2533.4 °C    | 4592.1 °F                |                      |
| Optical Properties      | Metric       | English                  | Comments             |
| Refractive Index        | 1.434        | 1.434                    | n <sub>i</sub> , Na  |
| Descriptive Properties  |              |                          |                      |
| CAS Number              |              | 7789-75-5                |                      |
| Color                   |              | White                    |                      |
| Crystal Structure       |              | Cubic                    | Fluorite             |

## Boron Nitride BN

| Physical Properties  | Metric                                    | English                                    | Comments    |
|--|---|--|-------------|
| Density  | 3.49 g/cc                                 | 0.126 lb/in <sup>3</sup>                   |             |
| a Lattice Constant   | 3.615 Å                                   | 3.615 Å                                    |             |
| Mechanical Properties  | Metric                                    | English                                    | Comments    |
| Hardness, Mohs   | 10.0                                      | 10.0                                       |             |
| Electrical Properties  | Metric                                    | English                                    | Comments    |
| Electrical Resistivity  | >= 3.00e+12 ohm-cm<br>@Temperature 150 °C | >= 3.00e+12 ohm-cm<br>@Temperature 302 °F  |             |
|  | 2.00e+14 ohm-cm<br>@Temperature 23.0 °C   | 2.00e+14 ohm-cm<br>@Temperature 73.4 °F    |             |
| Dielectric Constant  | 4.08<br>@Frequency 1e+6 Hz                | 4.08<br>@Frequency 1e+6 Hz                 |             |
| Dielectric Strength  | 374 kV/mm                                 | 9500 kV/in                                 |             |
| Dissipation Factor   | 0.000340<br>@Frequency 1e+6 Hz            | 0.000340<br>@Frequency 1e+6 Hz             |             |
| Band Gap   | 4.60 eV                                   | 4.60 eV                                    |             |
| Thermal Properties   | Metric                                    | English                                    | Comments    |
| Specific Heat Capacity   | 0.793 J/g-°C                              | 0.190 BTU/lb-°F                            |             |
| Thermal Conductivity   | 20.0 W/m-K                                | 139 BTU-in/hr-ft <sup>2</sup> -°F          |             |
| Melting Point  | 3027 °C                                   | 5481 °F                                    | Approximate |
| Maximum Service Temperature, Air   | 985 °C                                    | 1810 °F                                    |             |
| Maximum Service Temperature, Inert   | 2000 °C                                   | 3630 °F                                    |             |
| Heat of Formation  | 815 kJ/mol                                | 815 kJ/mol                                 |             |
| Debye Temperature  | 1627 °C                                   | 2961 °F                                    | Approximate |
| Descriptive Properties   |   |  |             |
| Crystal Structure  | Cubic                                     | Sphalerite Structure - Space Group F(-4)3m |             |

# Grinding Machine Power Monitor

## NEW UNIVERSAL POWER CELL

Gives You Valuable Information About Machine and Process Performance by Monitoring Motor Load

- Mixture Viscosity
- Tool Condition
- Optimum Feedrate
- Pump or Fan Flow
- Beginning or End of Process
- Obstructions
- Overloads
- Loss of Load

The Universal Power Cell Senses True Motor Power—Three Phase, Variable Frequency, Single Phase or DC.



**FULLY SELF CONTAINED**  
Easy to Install  
No Current Transformers  
No Voltage Transformers

**VERSATILE**  
Works on Both Fixed and Variable Frequency Power  
ALSO: Single Phase & DC

**COMPACT**  
1 3/4" x 5 3/8" x 8"

**3 BALANCED HALL EFFECT SENSORS**

**YOU CAN ADJUST FULL SCALE TO MATCH YOUR MOTOR**

Coarse and Fine Adjustment Pots  
5HP to 150HP  
Take Extra Turns for Small Motors

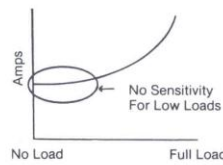
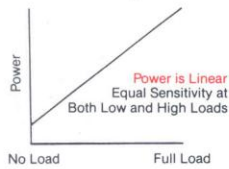
**SAMPLE VOLTAGE DIRECTLY**  
Up to 600 Volts



**BUILT-IN RESPONSE ADJUSTMENT**  
Lets you slow the Response of the Power Cell to average the readings.

**TWO ANALOG OUTPUTS**  
4-20 Milliamps  
0-10 Volts DC  
Electrically Isolated

### Why Monitor Power Instead of Just Amps?





Vydas International Marketing  
Swan House Passfield Bus Ctr  
Lynchborough Road Passfield  
Surrey GU30 7SB United Kingdom  
Tel: 01428 751822 Fax: 01428 751833 FAX 508-347-2064

TECHNOLOGY PARK  
10 PICKER ROAD  
STURBRIDGE, MA 01566  
508-347-2606



# Fuchs Water Analysis


**TECHNICAL SERVICES - LAB REPORT**  
For Internal Use Only

| <p><b>Customer</b><br/>Cranfield University<br/>-Unknown Address-</p> <p><b>Type of Product</b><br/>Water for DA</p> <p><b>Analysis</b></p> <table border="1" style="width: 100%; border-collapse: collapse;"> <thead> <tr> <th>Test</th> <th>Method</th> <th>Result</th> </tr> </thead> <tbody> <tr> <td>Appearance</td> <td></td> <td>Clear</td> </tr> <tr> <td>pH</td> <td>GA3</td> <td>7</td> </tr> <tr> <td>Total Hardness (ppm as CaCO3)</td> <td>GA45</td> <td>100</td> </tr> <tr> <td>Chlorides (PPM CL)</td> <td></td> <td>31</td> </tr> <tr> <td>Total Dissolved Solids (ppm)</td> <td>GA48</td> <td>120</td> </tr> <tr> <td>Aerobic Bacteria (Organisms/ml)</td> <td></td> <td>Nil</td> </tr> <tr> <td>Fungal Activity</td> <td></td> <td>Nil</td> </tr> </tbody> </table> <p><b>Remarks</b><br/>No remarks available</p> | Test   | Method | Result | Appearance |  | Clear | pH | GA3 | 7 | Total Hardness (ppm as CaCO3) | GA45 | 100 | Chlorides (PPM CL) |  | 31 | Total Dissolved Solids (ppm) | GA48 | 120 | Aerobic Bacteria (Organisms/ml) |  | Nil | Fungal Activity |  | Nil | <p><b>Report No:</b> T200801856<br/><b>Sampled:</b> 10 - Dec - 2008<br/><b>Received:</b> 10 - Oct - 2008</p> <p><b>Sample Taken From</b><br/>Not stated</p> |
|--|--------|--------|--------|------------|--|-------|----|-----|---|-------------------------------|------|-----|--------------------|--|----|------------------------------|------|-----|---------------------------------|--|-----|-----------------|--|-----|---|
| Test   | Method | Result |        |            |  |       |    |     |   |                               |      |     |                    |  |    |                              |      |     |                                 |  |     |                 |  |     |   |
| Appearance   |        | Clear  |        |            |  |       |    |     |   |                               |      |     |                    |  |    |                              |      |     |                                 |  |     |                 |  |     |   |
| pH   | GA3    | 7      |        |            |  |       |    |     |   |                               |      |     |                    |  |    |                              |      |     |                                 |  |     |                 |  |     |   |
| Total Hardness (ppm as CaCO3)  | GA45   | 100    |        |            |  |       |    |     |   |                               |      |     |                    |  |    |                              |      |     |                                 |  |     |                 |  |     |   |
| Chlorides (PPM CL)   |        | 31     |        |            |  |       |    |     |   |                               |      |     |                    |  |    |                              |      |     |                                 |  |     |                 |  |     |   |
| Total Dissolved Solids (ppm)   | GA48   | 120    |        |            |  |       |    |     |   |                               |      |     |                    |  |    |                              |      |     |                                 |  |     |                 |  |     |   |
| Aerobic Bacteria (Organisms/ml)  |        | Nil    |        |            |  |       |    |     |   |                               |      |     |                    |  |    |                              |      |     |                                 |  |     |                 |  |     |   |
| Fungal Activity  |        | Nil    |        |            |  |       |    |     |   |                               |      |     |                    |  |    |                              |      |     |                                 |  |     |                 |  |     |   |

**Date:** 19 - Dec - 2008 **Ref:** HANLEY/T200801856

**Signed:** M. James

**Name:** Mick James Page 1 of 1



BS EN ISO 9001 and QS 9000  
Certificate No. FM37672

The information contained herein is believed to be correct at time of publication. No warranty expressed or implied is given concerning the accuracy of the information or the suitability of the products. FUCHS reserves the right to modify and change its products and specifications without prior notice.

Hanley Plant  
New Century Street  
Hanley - Stoke on Trent  
ST1 5HU England  
Telephone +44 (0)18701 200 400  
Fax +44 (0)1782 202073  
Email contact-uk@fuchs-oil.com

Registered Office: New Century Street, Hanley, Stoke on Trent, ST1 5HU, England. Registered in England. No 300293

# Fuchs EcoCool

## (Data Sheet)

**Product INFORMATION**

**FUCHS (UK) PLC**  
New Century Street  
Hanley  
GB-Stoke-on-Trent  
Staffordshire, ST1 5HU




**ECOCOOL ULTRALIFE M**  
**Semi-synthetic water soluble cutting fluid**

**ECOCOOL ULTRALIFE**

**Advantages / Benefits**

- Semi-synthetic formulation
- Environmentally improved - does NOT contain sodium nitrite, phenols, thiazines, PTBAs or chlorinated additives
- Offers "best in class" performance in comparison to leading UK products
- Extended sump life compared to conventional fluids
- Proven to offer exceptional resistance to bacterial growth
- Developed with leading UK manufacturers
- Optimum tool life
- Good corrosion protection even at low concentrations
- Excellent lubrication to cutting operation and machine fixtures, slides etc.
- Excellent surface finish quality and improved component finish
- Excellent tramp oil rejection characteristics

**Application**

ECOCOOL ULTRALIFE M was designed for general machining and grinding on a wide variety of ferrous and non-ferrous materials including medium to high tensile steels.

**Product INFORMATION**

**FUCHS (UK) PLC**  
New Century Street  
Hanley  
GB-Stoke-on-Trent  
Staffordshire, ST1 5HU




**Machine Cleaning**

To optimize service life, the machine should be flushed thoroughly using RENOCLEAN EMC (see separate data sheet) prior to recharging with fresh fluid.

**Coolant Monitoring**

As with all modern cutting fluids, concentration control is of paramount importance. Therefore regular check by use of a refractometer is recommended for this product. It should be noted that the individual product refractometer correction factor should always be used to ensure accuracy.

**Storage**

Stable oil concentrates may be damaged by frost. Store indoors at ambient temperatures.

**Other Services**

A comprehensive range of coolant monitoring and maintenance systems are available from FUCHS Lubricants UK, incorporating coolant dispensing, recycling and disposal equipment.

**Product INFORMATION**

**FUCHS (UK) PLC**  
New Century Street  
Hanley  
GB-Stoke-on-Trent  
Staffordshire, ST1 5HU




**Typical Data (Concentrate): ECOCOOL ULTRALIFE M**

| Characteristics                     | Unit              | Test Method |
|-------------------------------------|-------------------|-------------|
| Appearance                          | Heavy amber fluid | IP160       |
| Specific gravity at 15°C            | 0.978             |             |
| Low temperature stability test -2°C | Stable            |             |

**Typical Data (Emulsion): ECOCOOL ULTRALIFE M**

| Characteristics                 | Unit       | Test Method            |
|---------------------------------|------------|------------------------|
| Appearance                      | Opalescent |                        |
| Oil value at 5%                 | 5.2        |                        |
| Corrosion flashpoint            | %          | 1.5 break point (IP28) |
| Recommended concentrations:     |            |                        |
| General machining               | %          | 5                      |
| Grinding                        | %          | 3                      |
| Refractometer correction factor |            | 1.2                    |

*Note: Refractometer Reading x Correction Factor = Actual Concentration*

For further information, please refer to our website or contact your local FUCHS representative.

For copies of research and development work, please contact your local FUCHS representative.

Health, Safety and Environment December 2007 CDUK Page 1 of 3  
Health, safety and environmental information is provided for this product in the relevant Safety Data Sheet. The provided guidance is general and should not be used as a substitute for specific safety instructions. The user should refer to the relevant Safety Data Sheet for detailed information. The user should refer to the relevant Safety Data Sheet for detailed information.

FUCHS LUBRICANTS (UK) PLC  
New Century Street, Hanley  
GB-Stoke-on-Trent, Staffordshire, ST1 5HU

Tel: +44(0)1870 202073  
Fax: +44(0)1782 202075  
Email: uk@fuchs-oil.com  
http://www.fuchs-lubricants.com

Health, Safety and Environment December 2007 CDUK Page 2 of 3  
Health, safety and environmental information is provided for this product in the relevant Safety Data Sheet. The provided guidance is general and should not be used as a substitute for specific safety instructions. The user should refer to the relevant Safety Data Sheet for detailed information. The user should refer to the relevant Safety Data Sheet for detailed information.

FUCHS LUBRICANTS (UK) PLC  
New Century Street, Hanley  
GB-Stoke-on-Trent, Staffordshire, ST1 5HU

Tel: +44(0)1870 202073  
Fax: +44(0)1782 202075  
Email: uk@fuchs-oil.com  
http://www.fuchs-lubricants.com

Health, Safety and Environment December 2007 CDUK Page 3 of 3  
Health, safety and environmental information is provided for this product in the relevant Safety Data Sheet. The provided guidance is general and should not be used as a substitute for specific safety instructions. The user should refer to the relevant Safety Data Sheet for detailed information. The user should refer to the relevant Safety Data Sheet for detailed information.

FUCHS LUBRICANTS (UK) PLC  
New Century Street, Hanley  
GB-Stoke-on-Trent, Staffordshire, ST1 5HU

Tel: +44(0)1870 202073  
Fax: +44(0)1782 202075  
Email: uk@fuchs-oil.com  
http://www.fuchs-lubricants.com

## Machining Fluid Additives and Functions

(George E. Totten, Steven R. Westbrook, Rajesh J. Shah, 2003)

| Additive Type                     | Function  | Typical Compounds   |
|-----------------------------------|---|---|
| <b>Water-based fluids</b>         |   |   |
| Alkalinity buffers/pH             | Control bacteria-derived acidity  | Amines and inorganic bases  |
| Antifoam agents                   | Prevent foam  | Silicones, silicates, and stearates   |
| Antifungal agents                 | Control fungal growth   | Sodium omadine  |
| Antimicrobials/preservatives      | Control microbial growth  | Triazines, omadine, phenol, oxazolindines, and imidazolines   |
| Metal passivators                 | Prevent staining and leaching of yellow metals                                      | Triazoles   |
| Couplers                          | Emulsion stability  | Glycols, glycol esters, and alcohols  |
| Emulsifiers                       | Emulsify organics in water  | Sodium and lithium sulfonates; poly-ethoxylated phenols, alcohols and acids; metal and amine carboxylates (soaps of fatty acids)              |
| Extreme pressure/lubricity agents | Form heat-resistant chemical films that reduce friction                             | Fatty acids, fatty amides, fatty esters, and fatty acid salts (soaps); phosphates; sulfur and chlorine containing compounds                   |
| Odor masks                        | Suppress odor   | Natural and synthetic aromatic compounds  |
| Thickeners                        | Improve viscosity   | Polyacrylate esters and glycol esters   |
| Corrosion and rust inhibitors     | Control oxidative and corrosive damage to metal surfaces and tools                  | Carboxylic acid salts, amides, and amines   |
| <b>Oil-based fluids</b>           |   |   |
| Antifoam agents                   | Prevent foam  | Silicones, polymethacrylates, and stearates   |
| Anti-misting agents               | Suppress mist formation   | Polyisobutenes and other natural and synthetic polymers   |
| Corrosion and rust inhibitors     | Control oxidative and corrosive damage to metal surfaces and tools                  | Metal sulfonates and phosphates; organic acids and esters; and triazoles  |
| Demulsifiers                      | Facilitate water separation and facilitate removal of tramp oil via skimming        | Cationic and non-ionic polymeric surfactants  |
| Dispersants                       | Prevent agglomeration of material particles that result during cutting and grinding | Polyamides and metal sulfonates   |
| Extreme pressure/lubricity agents | Form heat-resistant chemical films that reduce friction                             | Fatty acids, fatty amides, fatty esters, and fatty acid salts (soaps); phosphates; sulfur and chlorine containing compounds; basic sulfonates |
| Odor masks                        | Suppress odor   | Natural and synthetic aromatic compounds  |
| Thickeners                        | Improve viscosity   | Polyacrylate esters   |
| Solid lubricants                  | Improve film strength   | Graphite, molybdenum disulfide, Poly(tetrafluoroethylene)-PTFE (TEFLON®)  |

## Experimental Data

| Trial Name                     |      | d <sub>e</sub> (mm) | a <sub>e</sub> (mm) | v <sub>w</sub> (mm/s) | B (mm-1s-1/2) | SGE J/mm <sup>3</sup> |                  |            |            |
|--------------------------------|------|---------------------|---------------------|-----------------------|---------------|-----------------------|------------------|------------|------------|
|                                |      |                     |                     |                       |               | 30_3_09 with EcoCool  | cBN Electroplate | Vit Bond 1 | Vit Bond 2 |
| 30 09 09<br>Burnt<br>1-10% Oil | 1    | 43.75               | 0.01                | 400                   | 4.0664        | 13.5916               |                  |            |            |
|                                | 2    | 43.75               | 0.05                | 400                   | 1.2161        | 11.7683               |                  |            |            |
|                                | 1    | 43.75               | 0.01                | 650                   | 3.1900        | 7.7676                |                  |            |            |
|                                | 2    | 43.75               | 0.05                | 650                   | 0.9540        | 7.1475                |                  |            |            |
|                                | 2    | 43.75               | 0.01                | 400                   | 4.0664        | 13.0239               |                  |            |            |
|                                | 1    | 43.75               | 0.05                | 400                   | 1.2161        | 11.6210               |                  |            |            |
|                                | 2    | 43.75               | 0.01                | 650                   | 3.1900        | 7.6316                |                  |            |            |
|                                | 1    | 43.75               | 0.05                | 650                   | 0.9540        | 7.2778                |                  |            |            |
|                                | Dry  |                     | 43.75               | 0.01                  | 400           | 4.0664                |                  |            | 18.1949    |
|                                | Burn |                     | 43.75               | 0.02                  | 400           | 2.4179                |                  |            | 18.1539    |
|                                |      | 43.75               | 0.04                | 400                   | 1.4377        | 14.5787               |                  |            |            |
|                                |      | 43.75               | 0.05                | 400                   | 1.2161        | 13.7413               |                  |            |            |
|                                |      | 43.75               | 0.06                | 400                   | 1.0607        | 11.0781               |                  |            |            |
|                                |      | 43.75               | 0.08                | 400                   | 0.8549        | 10.1111               |                  |            |            |
|                                |      | 43.75               | 0.1                 | 400                   | 0.7231        | 8.4231                |                  |            |            |
| Water                          |      | 43.75               | 0.01                | 400                   | 4.0664        | 15.7630               |                  |            |            |
| Control                        |      | 43.75               | 0.05                | 400                   | 1.2161        | 1.3249                |                  |            |            |

|                     |   | d <sub>e</sub> (mm) | a <sub>e</sub> (mm) | v <sub>w</sub> (mm/s) | B (mm <sup>-1</sup> s <sup>-1/2</sup> ) | 9_7_09 with EcoCool   |  |
|---------------------|---|---------------------|---------------------|-----------------------|---|-----------------------|--|
|                     |   |                     |                     |                       |   | SGE J/mm <sup>3</sup> |  |
| 9_7_09<br>1-10% Oil | 1 | 43.75               | 0.01                | 400                   | 4.0664                                  | 42.8421               |  |
|                     | 2 | 43.75               | 0.01                | 400                   | 4.0664                                  | 31.2281               |  |
|                     | 1 | 43.75               | 0.05                | 650                   | 0.9540                                  | 7.6027                |  |
|                     | 2 | 43.75               | 0.05                | 650                   | 0.9540                                  | 7.2119                |  |
|                     | 2 | 43.75               | 0.05                | 400                   | 1.2161                                  | 18.0281               |  |
|                     | 1 | 43.75               | 0.05                | 400                   | 1.2161                                  | 12.8386               |  |
|                     | 2 | 43.75               | 0.01                | 650                   | 3.1900                                  | 21.0850               |  |
|                     | 1 | 43.75               | 0.01                | 650                   | 3.1900                                  | 25.7490               |  |

| CaF2 |      |         |                     |                     |                       |   |                       |
|------|------|---------|---------------------|---------------------|-----------------------|---|-----------------------|
| ESW1 | 1    | 55.85   | 0.0005              | 530                 | 35.5128               | ESW1                                    |                       |
|      | 2    | 55.85   | 0.0010              | 530                 | 21.1160               | 67.2158                                 |                       |
|      | 1    | 55.85   | 0.0005              | 630                 | 32.5726               | 25.3792                                 |                       |
|      | 2    | 55.85   | 0.0010              | 630                 | 19.3678               | 64.4165                                 |                       |
|      | 2    | 55.85   | 0.0005              | 530                 | 35.5128               | 55.8908                                 |                       |
|      | 1    | 55.85   | 0.0010              | 530                 | 21.1160               | 163.5353                                |                       |
|      | 2    | 55.85   | 0.0005              | 630                 | 32.5726               | 385.1049                                |                       |
|      | 1    | 55.85   | 0.0005              | 630                 | 32.5726               | 1028.3323                               |                       |
|      | 1    | 55.85   | 0.0010              | 630                 | 19.3678               | 339.4983                                |                       |
|      | ESW2 | 1       | 55.85               | 0.0005              | 530                   | 35.5128                                 |                       |
| 2    |      | 55.85   | 0.0010              | 530                 | 21.1160               | 223.4746                                |                       |
| 1    |      | 55.85   | 0.0005              | 630                 | 32.5726               | 141.7068                                |                       |
| 2    |      | 55.85   | 0.0010              | 630                 | 19.3678               | 389.8510                                |                       |
| 2    |      | 55.85   | 0.0005              | 530                 | 35.5128               | 148.4347                                |                       |
| 1    |      | 55.85   | 0.0010              | 530                 | 21.1160               | 553.5965                                |                       |
| 2    |      | 55.85   | 0.0005              | 630                 | 32.5726               | 245.2075                                |                       |
| 1    |      | 55.85   | 0.0010              | 630                 | 32.5726               | 440.9963                                |                       |
| 1    |      | 55.85   | 0.0010              | 630                 | 19.3678               | 563.8632                                |                       |
| ESW3 |      | 0       | 43.75               | 0.01                | 650                   | 3.1900                                  | ESW3                  |
|      | 0.5  | 43.75   | 0.01                | 650                 | 3.1900                | 25.38                                   |                       |
|      | 1    | 43.75   | 0.01                | 650                 | 3.1900                | 21.15                                   |                       |
|      | 1.5  | 43.75   | 0.01                | 650                 | 3.1900                | 24.63                                   |                       |
|      | 2    | 43.75   | 0.01                | 650                 | 3.1900                | 21.26                                   |                       |
|      | 2    | 43.75   | 0.01                | 650                 | 3.1900                | 25.38                                   |                       |
|      | 2.5  | 43.75   | 0.01                | 650                 | 3.1900                | 31.55                                   |                       |
|      | 3    | 43.75   | 0.01                | 650                 | 3.1900                | 24.45                                   |                       |
|      | 4    | 43.75   | 0.01                | 650                 | 3.1900                | 30.35                                   |                       |
|      | ESW5 |         | d <sub>e</sub> (mm) | a <sub>e</sub> (mm) | v <sub>w</sub> (mm/s) | B (mm <sup>-1</sup> s <sup>-1/2</sup> ) | SGE J/mm <sup>3</sup> |
|      |      | 65.1163 | 0.0005              | 500                 | 37.9936               | 146.721                                 |                       |
|      |      | 65.1163 | 0.001               | 500                 | 22.5911               | 69.5042                                 |                       |
|      |      | 65.1163 | 0.0005              | 600                 | 34.6832               | 72.8402                                 |                       |
|      |      | 65.1163 | 0.001               | 600                 | 20.6228               | 29.84                                   |                       |
|      |      | 65.1163 | 0.0005              | 500                 | 37.9936               | 695.9606                                |                       |

|  |  |         |        |     |         |  |
|--|--|---------|--------|-----|---------|--|
|  |  | 65.1163 | 0.001  | 500 | 22.5911 |  |
|  |  | 65.1163 | 0.0005 | 600 | 34.6832 |  |
|  |  | 65.1163 | 0.001  | 600 | 20.6228 |  |

| ESW6 |   |       |        |     |         |         | ESW6 |
|------|---|-------|--------|-----|---------|---------|------|
|      | 1 | 63.11 | 0.0005 | 500 | 37.6982 | 89.6161 |      |
|      | 2 | 63.11 | 0.0010 | 500 | 22.4155 | 10.5786 |      |
|      | 1 | 63.11 | 0.0005 | 600 | 34.4136 | 12.8087 |      |
|      | 2 | 63.11 | 0.0010 | 600 | 20.4624 | 19.5670 |      |
|      | 2 | 63.11 | 0.0005 | 500 | 37.6982 | 33.1593 |      |
|      | 1 | 63.11 | 0.0010 | 500 | 22.4155 | 6.9097  |      |
|      | 2 | 63.11 | 0.0005 | 600 | 34.4136 | 14.8276 |      |
|      | 1 | 63.11 | 0.0010 | 600 | 20.4624 | 9.9019  |      |

| ESW7 |   |       |        |     |         |         | ESW7 |
|------|---|-------|--------|-----|---------|---------|------|
|      | 1 | 63.11 | 0.0005 | 500 | 37.6982 | 11.8444 |      |
|      | 2 | 63.11 | 0.0010 | 500 | 22.4155 | 23.8270 |      |
|      | 1 | 63.11 | 0.0005 | 600 | 34.4136 | 28.9082 |      |
|      | 2 | 63.11 | 0.0010 | 600 | 20.4624 | 15.7719 |      |
|      | 2 | 63.11 | 0.0005 | 500 | 37.6982 | 18.7531 |      |
|      | 1 | 63.11 | 0.0010 | 500 | 22.4155 | -3.7314 |      |
|      | 2 | 63.11 | 0.0005 | 600 | 34.4136 | 26.6647 |      |
|      | 1 | 63.11 | 0.0010 | 600 | 20.4624 | 3.1899  |      |

| ESW8 |   |       |        |     |         |          | ESW8 |
|------|---|-------|--------|-----|---------|----------|------|
|      | 1 | 63.11 | 0.0005 | 500 | 37.6982 | 34.3299  |      |
|      | 2 | 63.11 | 0.0010 | 500 | 22.4155 | 22.0450  |      |
|      | 1 | 63.11 | 0.0005 | 600 | 34.4136 | 55.2320  |      |
|      | 2 | 63.11 | 0.0010 | 600 | 20.4624 | 11.1758  |      |
|      | 2 | 63.11 | 0.0005 | 500 | 37.6982 | 35.8135  |      |
|      | 1 | 63.11 | 0.0010 | 500 | 22.4155 | -14.1914 |      |
|      | 2 | 63.11 | 0.0005 | 600 | 34.4136 | 39.2584  |      |
|      | 1 | 63.11 | 0.0010 | 600 | 20.4624 | 0.9933   |      |

**EBN**

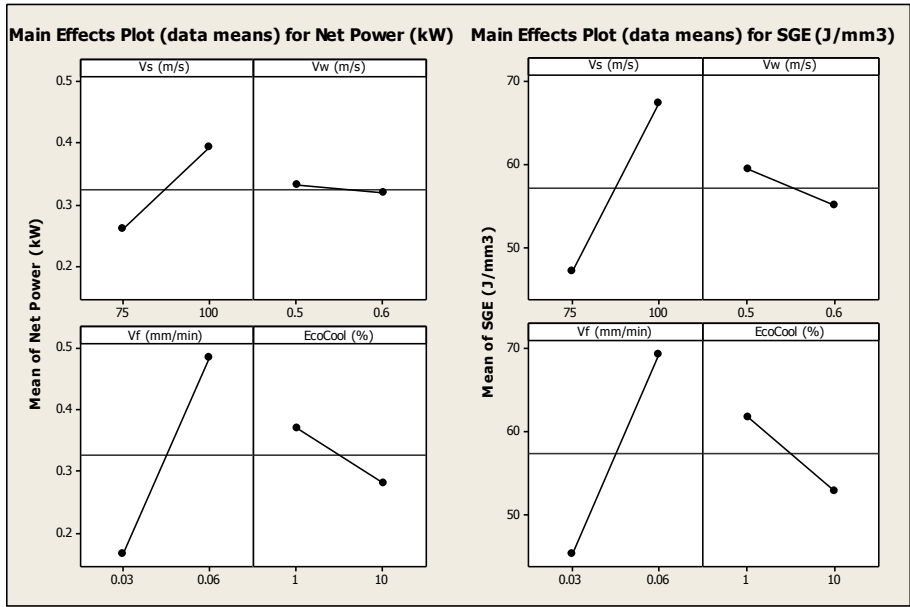
|                          |  |  |  |  |  |  |
|--------------------------|--|--|--|--|--|--|
| EBN1<br>Boron<br>Nitride |  |  |  |  |  |  |
|--------------------------|--|--|--|--|--|--|

| EBN2    |   |          |        |     |         |          | EBN2<br>SGE<br>J/mm <sup>3</sup> |
|---------|---|----------|--------|-----|---------|----------|----------------------------------|
| Boron   | 1 | 62.02219 | 0.0005 | 500 | 37.5340 | 101.8521 |                                  |
| Nitride | 2 | 62.02219 | 0.0010 | 500 | 22.3178 | 124.6824 |                                  |
|         | 1 | 62.02219 | 0.0005 | 600 | 34.2637 | 179.5127 |                                  |
|         | 2 | 62.02219 | 0.0010 | 600 | 20.3733 | 184.5637 |                                  |
|         | 2 | 62.02219 | 0.0005 | 500 | 37.5340 | 61.0088  |                                  |
|         | 1 | 62.02219 | 0.0010 | 500 | 22.3178 | 88.5525  |                                  |
|         | 2 | 62.02219 | 0.0005 | 600 | 34.2637 | 57.9367  |                                  |
|         | 1 | 62.02219 | 0.0010 | 600 | 20.3733 | 97.2513  |                                  |

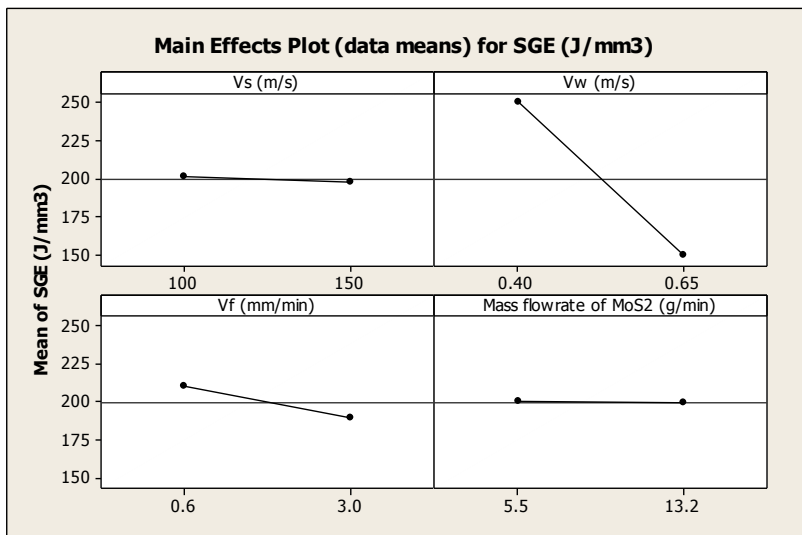
| EBN3    |   |          |        |     |         |          | EBN3<br>SGE<br>J/mm <sup>3</sup> |
|---------|---|----------|--------|-----|---------|----------|----------------------------------|
| Boron   | 1 | 62.02219 | 0.0005 | 500 | 37.5340 | 87.3698  |                                  |
| Nitride | 2 | 62.02219 | 0.0010 | 500 | 22.3178 | 81.4262  |                                  |
|         | 1 | 62.02219 | 0.0005 | 600 | 34.2637 | 95.9987  |                                  |
|         | 2 | 62.02219 | 0.0010 | 600 | 20.3733 | 116.5288 |                                  |
|         | 2 | 62.02219 | 0.0005 | 500 | 37.5340 | 23.1427  |                                  |
|         | 1 | 62.02219 | 0.0010 | 500 | 22.3178 | 72.0924  |                                  |
|         | 2 | 62.02219 | 0.0005 | 600 | 34.2637 | 109.7903 |                                  |
|         | 1 | 62.02219 | 0.0010 | 600 | 20.3733 | 112.5537 |                                  |

**EcoCool**

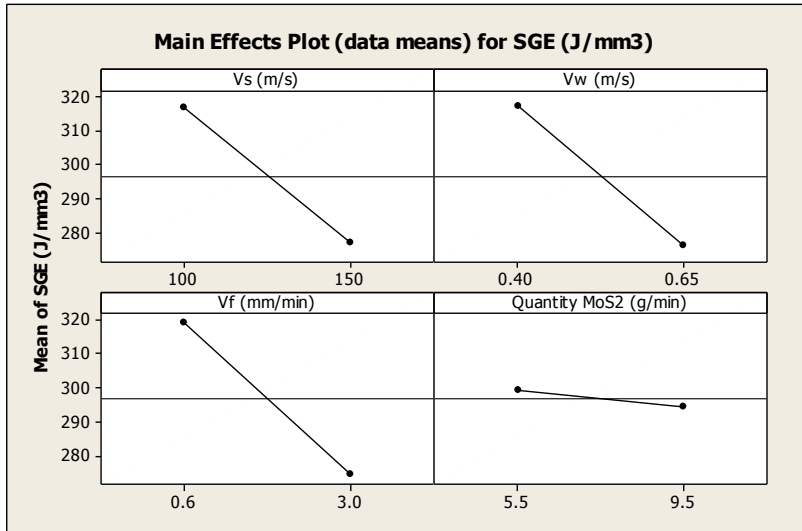
| ESW11 |   |         |        |     |         |          | 14_3_11 with EcoCool<br>SGE<br>J/mm <sup>3</sup> |
|-------|---|---------|--------|-----|---------|----------|--|
|       | 1 | 65.1163 | 0.0005 | 500 | 37.9936 | 30.8141  |  |
|       | 2 | 65.1163 | 0.0010 | 500 | 22.5911 | 81.7659  |  |
|       | 1 | 65.1163 | 0.0005 | 600 | 34.6832 | 48.2310  |  |
|       | 2 | 65.1163 | 0.0010 | 600 | 20.6228 | 27.9238  |  |
|       | 2 | 65.1163 | 0.0005 | 500 | 37.9936 | 37.1247  |  |
|       | 1 | 65.1163 | 0.0010 | 500 | 22.5911 | 88.4030  |  |
|       | 2 | 65.1163 | 0.0005 | 600 | 34.6832 | 64.4781  |  |
|       | 1 | 65.1163 | 0.0010 | 600 | 20.6228 | 79.5297  |  |
| Water |   | 65.1163 | 0.0010 | 600 | 20.6228 | 100.8121 |  |
| Dry   |   | 65.1163 | 0.0010 | 600 | 20.6228 | 140.3340 |  |



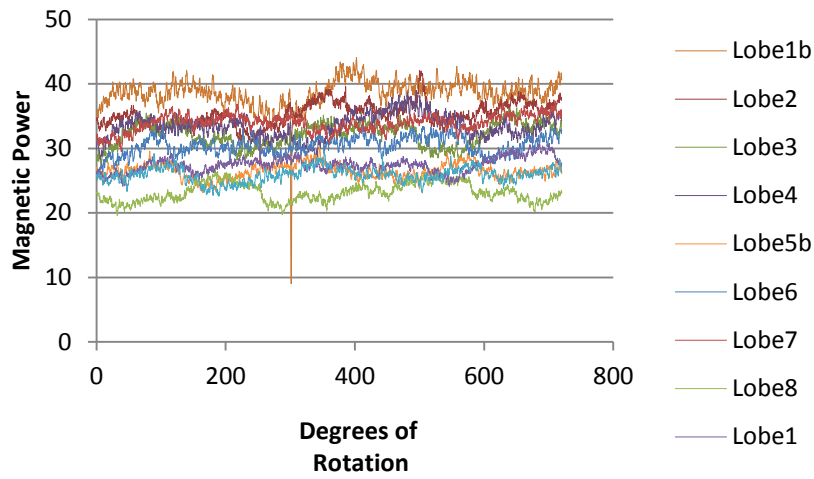
Main Effects: 1%-10% Oil Content



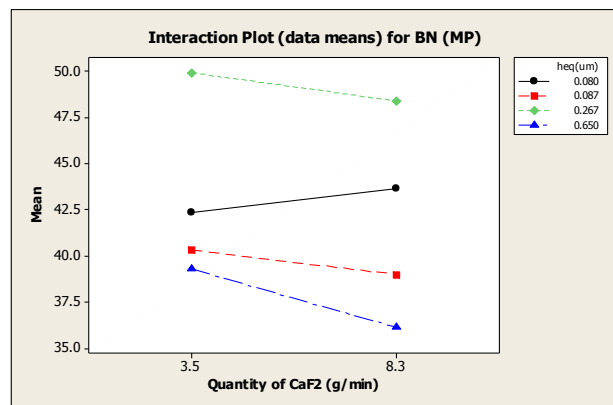
MoS2 5.5 -13.2 g/min



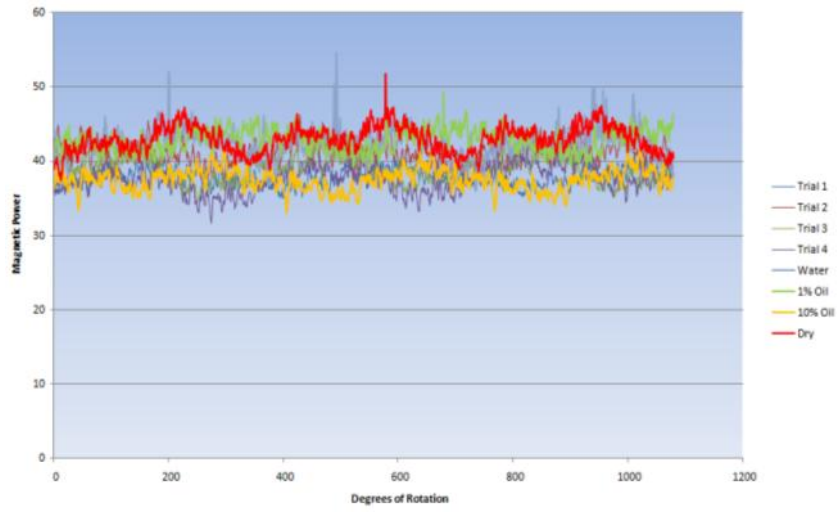
MoS2 5.5 - 9.5g/min SGE



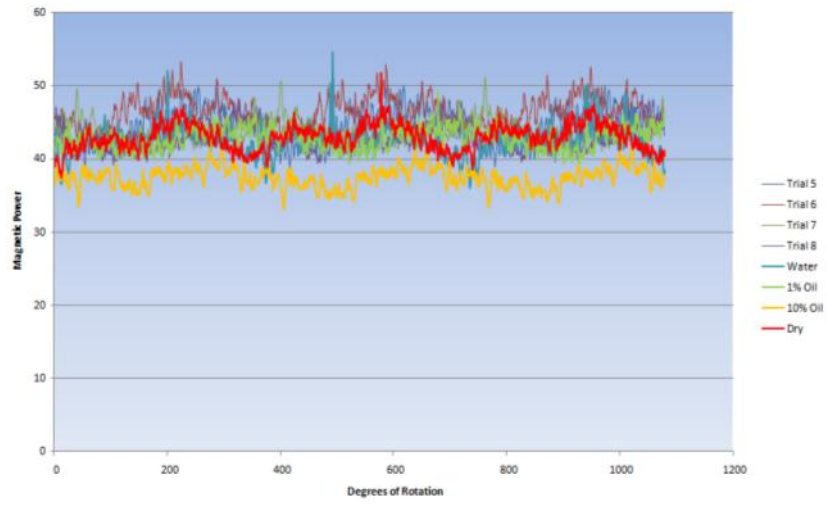
BMN ESW6 Barkhausen Noise (CaF<sub>2</sub>)



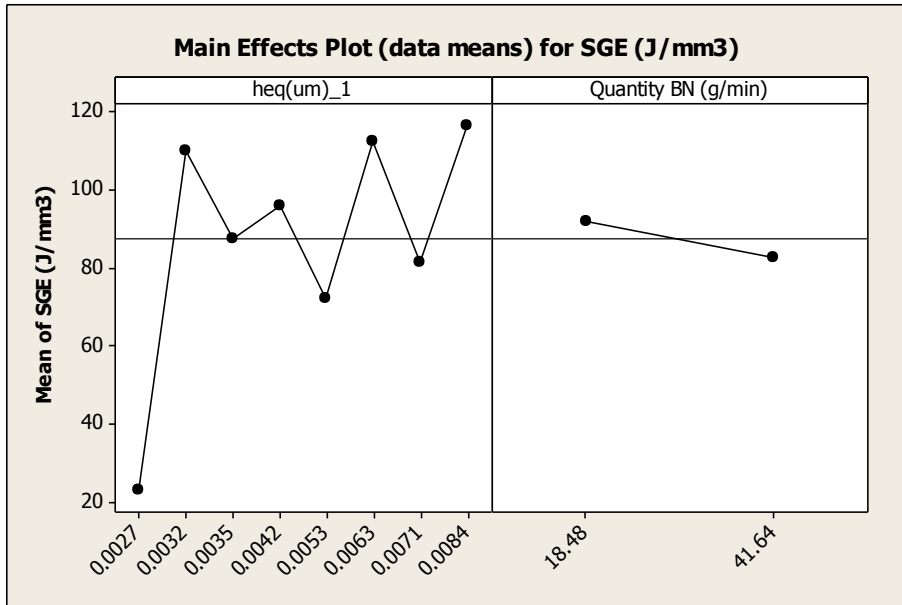
Interaction BN magnetic power CaF<sub>2</sub>(MOSL)



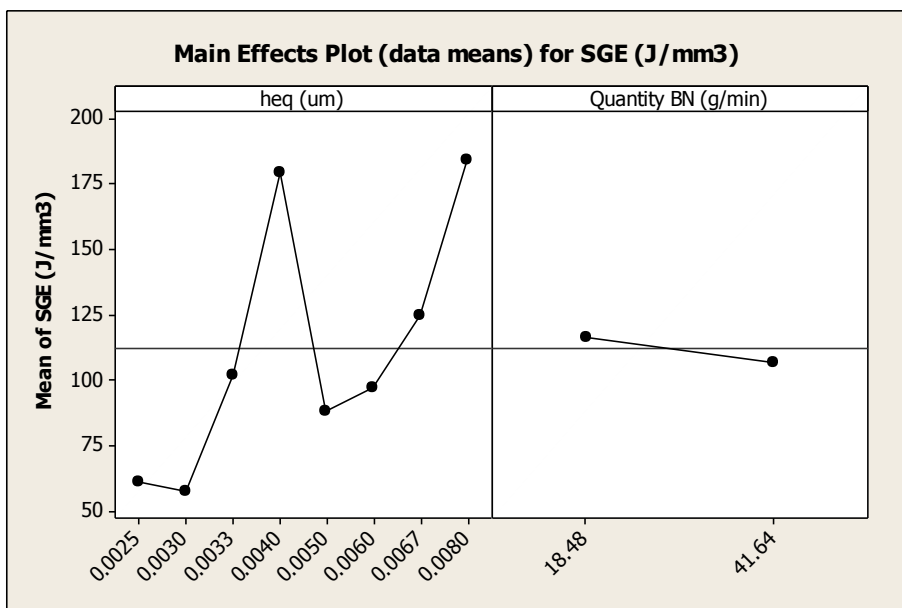
PVD2 ESW8 BN - Low Wheel Speed Vs=75m/s



PVD2 ESW8 BN - High Wheel Speed Vs=100m/s

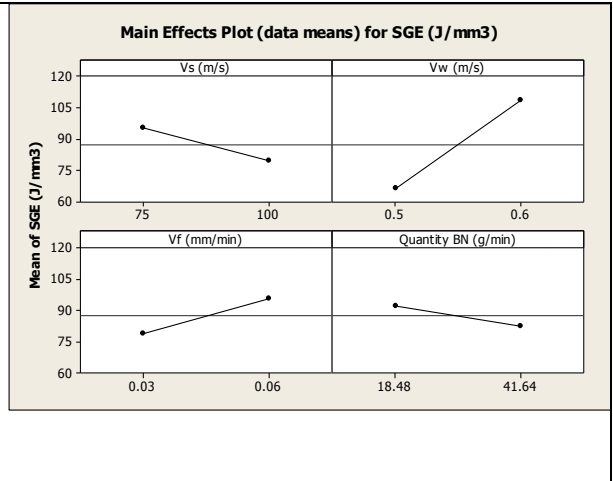
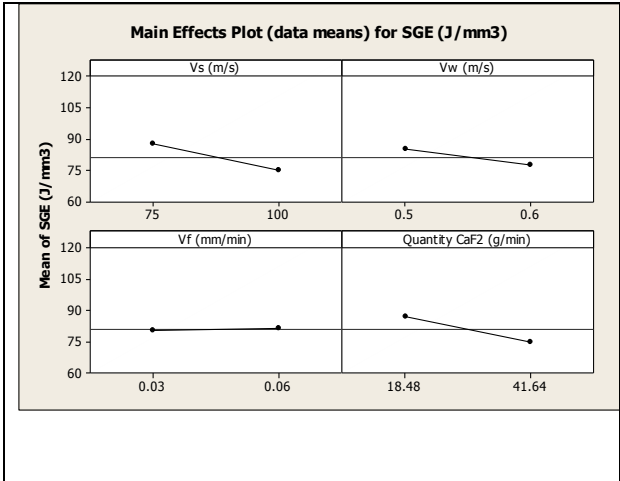
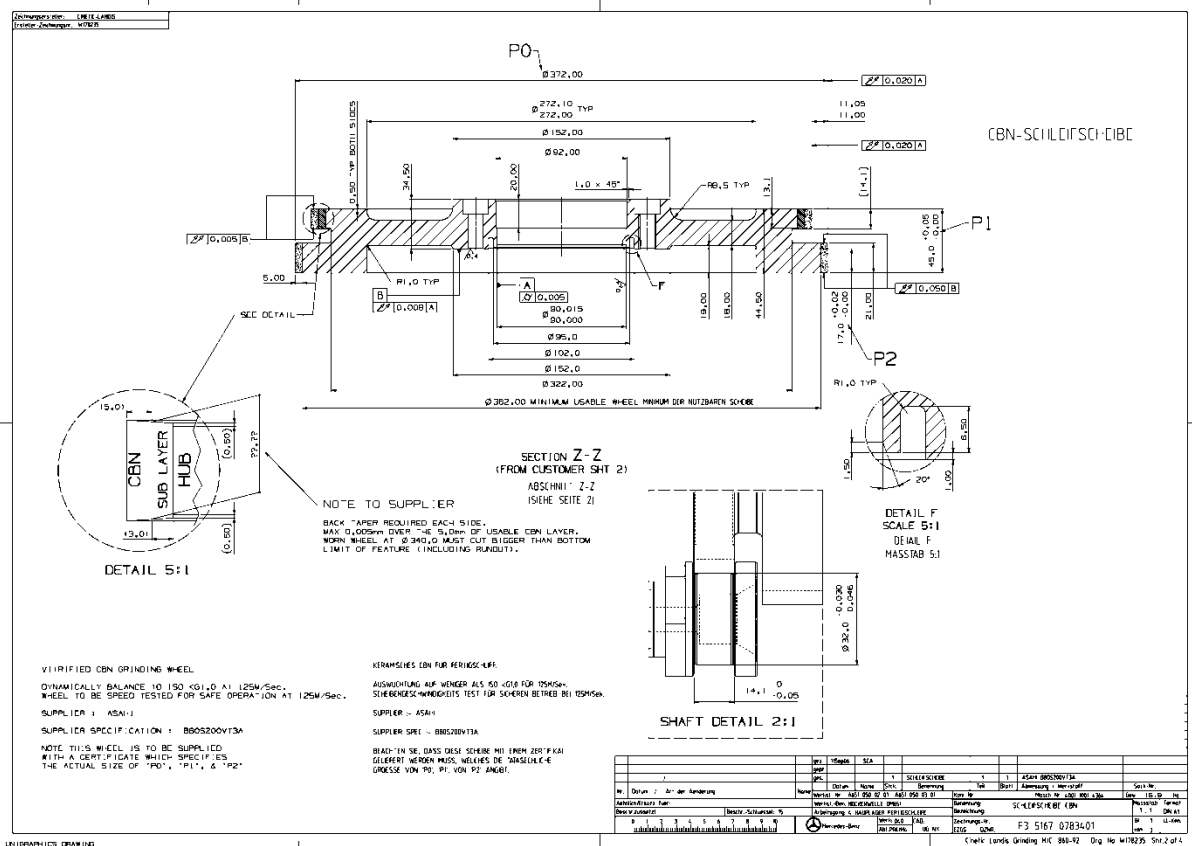
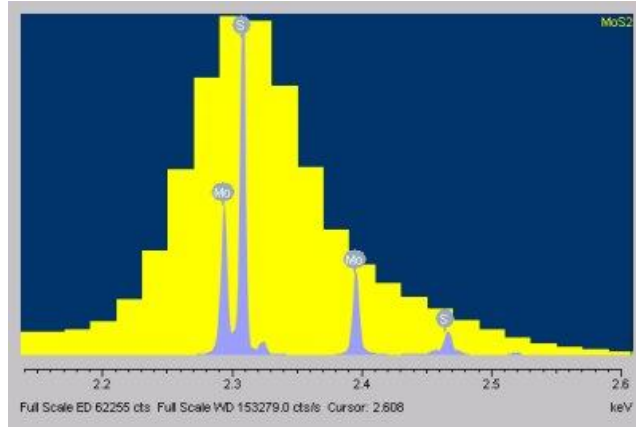


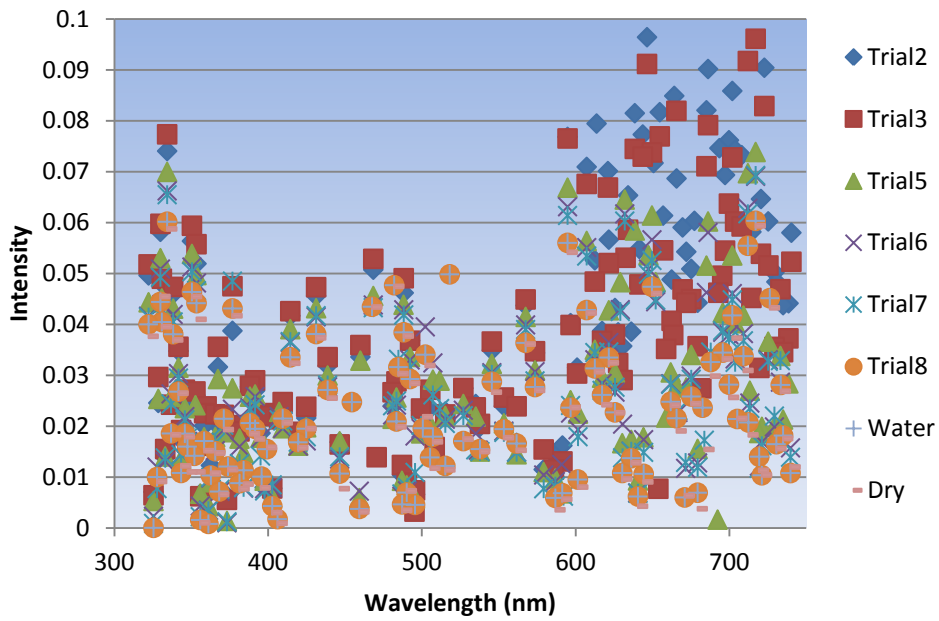
Variation of SGE with changes in heq and hBN on 38Mn steel workpiece B90 wheel



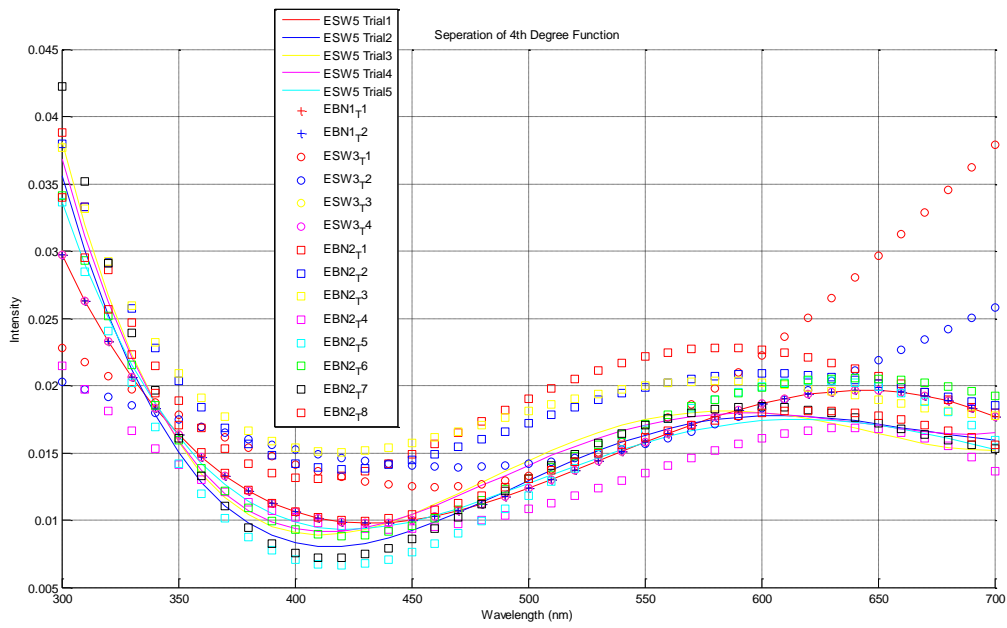
Variation of SGE with hBN 51CrV4



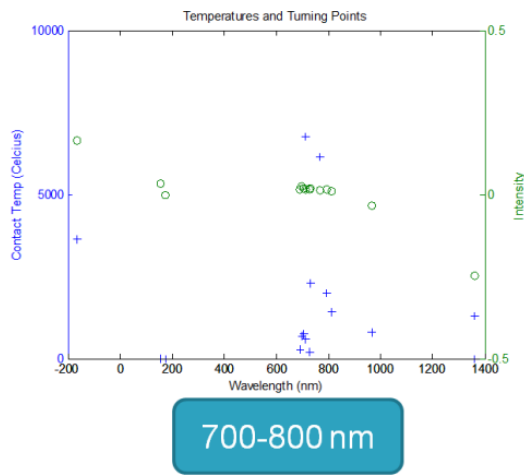
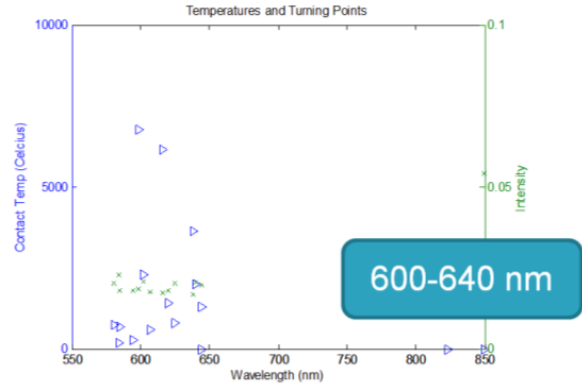
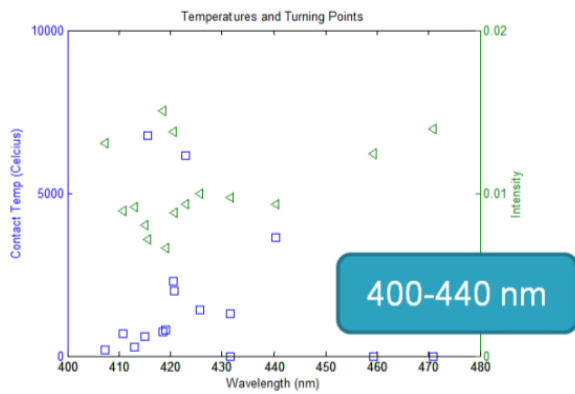




ESW11 EcoCool Light Capture



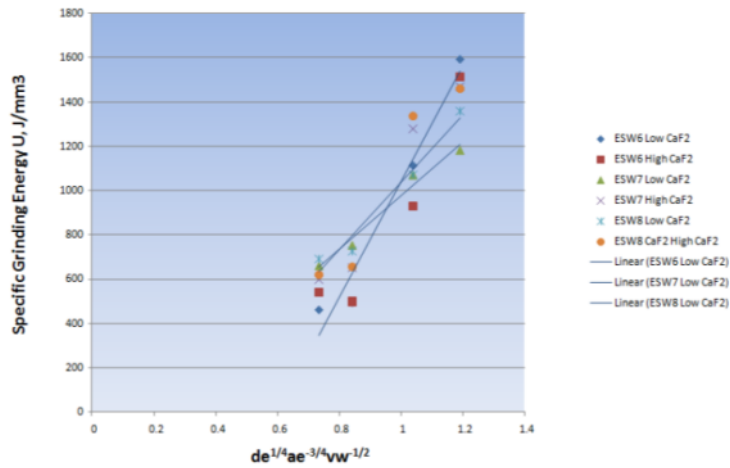
Spectral shape of captured light following a series of Taguchi trials demonstrating the differences that could be possibly linked to surface finish temperature1



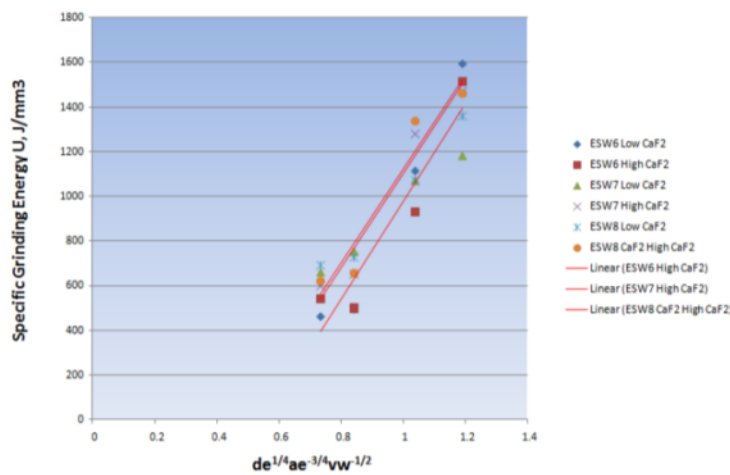
Positions of turning points of light spectral 4th degree slope interpretation identifying which wavelength provided the best indication for temperature, wavelength and light intensity positioning

Detectable changed in captured light when using CaF<sub>2</sub> and hBN as solid lubricants

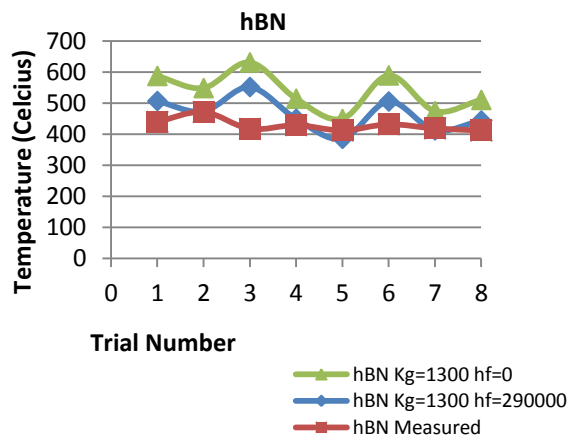
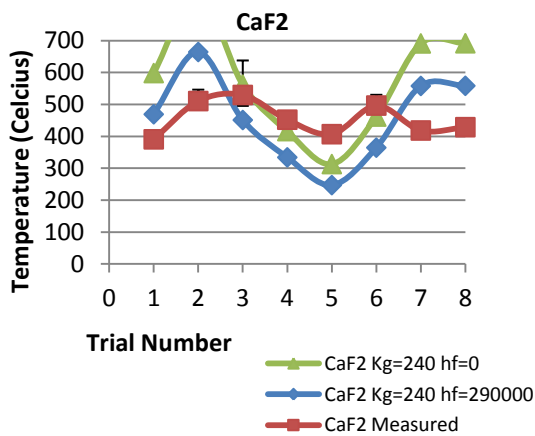
|   |  |   |
|---|--|---|
| ↑ | Increase in CaF <sub>2</sub> decreases SGE by 12J/mm <sup>3</sup> (81) | ↓ |
| ↑ | Increase in hBN decreases SGE by 9 J/mm <sup>3</sup> (87)              | ↓ |
| ↑ | Increase in CaF <sub>2</sub> decreases temp by 15 C (454)              | ↓ |
| ↑ | Increase in hBN increase in temp by 8 C (439)                          | ↑ |
| ↑ | Increase in CaF <sub>2</sub> decreases Intensity by 0.006 (0.0312)     | ↓ |
| ↑ | Increase in hBN increases Intensity by 0.004 (0.039)                   | ↑ |
| ↑ | Increase in CaF <sub>2</sub> increases wavelength by 6nm (547)         | ↑ |
| ↑ | Increase in hBN decreases wavelength 9nm (687)                         | ↓ |

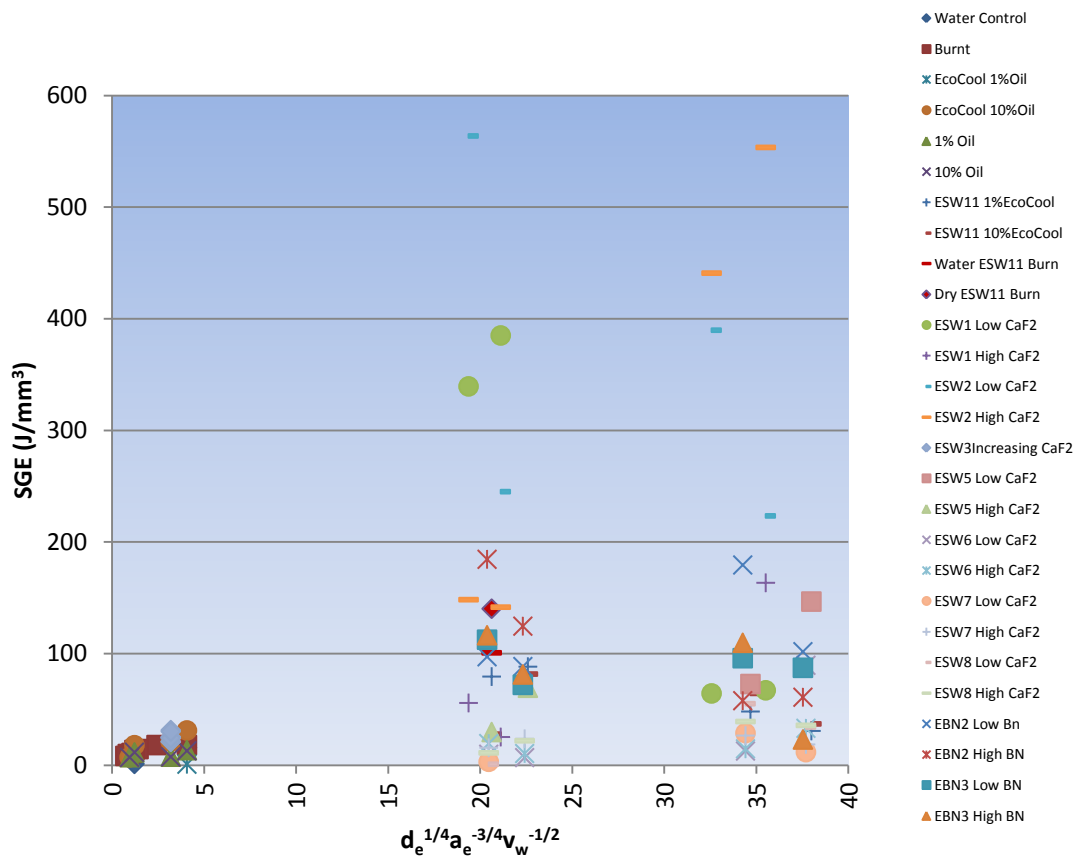


SGE vs.  $f(de,ae,vw)$  identifying the critical temperature gradient B for the lower quantity of CaF2 cases (ESW6-8)



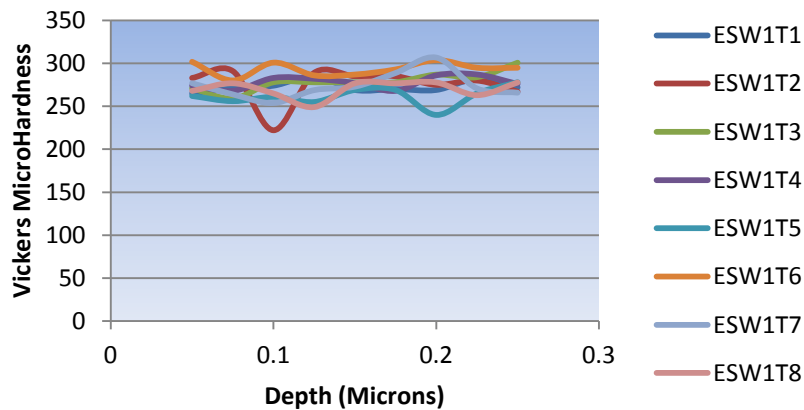
Calculation of burn threshold temperatures through relationship of SGE vs.  $f(d_e, a_e, v_w)$  (ESW6-8)



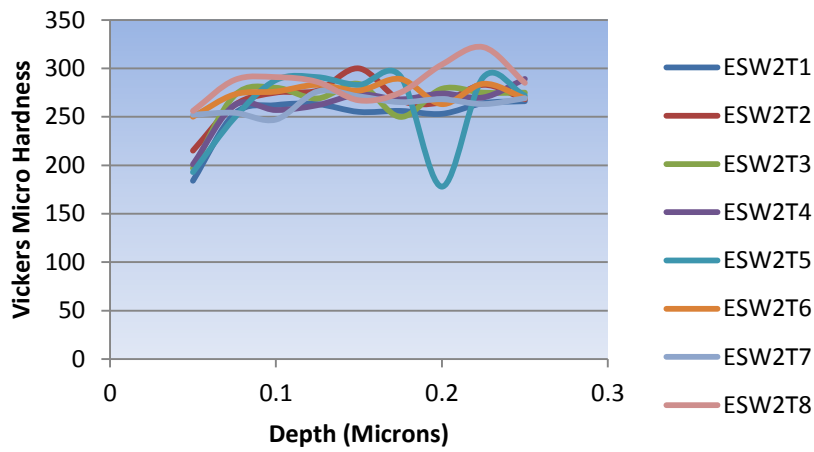


Burn Threshold Diagram - EcoCool/CaF2/hBN

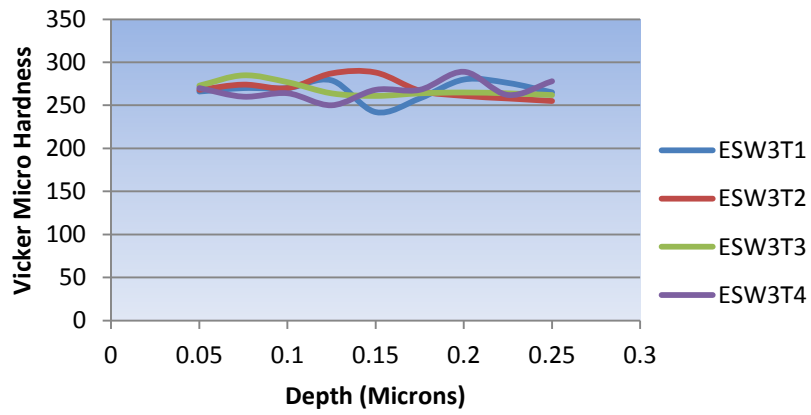
The Vickers Hardness results generally show consistent values throughout the depth of the samples. ESW3 in particular involved a steady increase in CaF2 only being delivered onto the workpiece. The surface condition was visually blackened indicating that burn had taken place. There is a degree of movement in the hardness between the depth of 1.25 microns and 2 microns suggesting that an area of softening is beginning to develop.



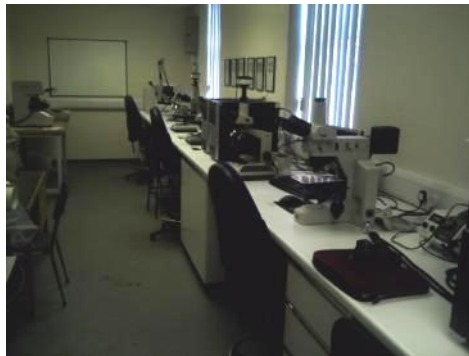
Vickers Micro Hardness CaF2 ESW1



Vickers Micro Hardness CaF<sub>2</sub> ESW2



Vickers Micro-hardness CaF<sub>2</sub> ESW3



Metallographic Laboratory including microscopes and hardness testing instrumentation

---

## Appendix B. Temperature Coding

### Matlab GUI and Temperature predictive calculations

```
function [varargout, Temps, WheelSpeed] = Temp2_12_2010(varargin)
% TEMP2_12_2010 M-file for Temp2_12_2010.fig
%   TEMP2_12_2010, by itself, creates a new TEMP2_12_2010 or raises the existing
%   singleton*.
%
%   H = TEMP2_12_2010 returns the handle to a new TEMP2_12_2010 or the handle to
%   the existing singleton*.
%
%   TEMP2_12_2010('CALLBACK', hObject, eventData, handles,...) calls the local
%   function named CALLBACK in TEMP2_12_2010.M with the given input arguments.
%
%   TEMP2_12_2010('Property','Value',...) creates a new TEMP2_12_2010 or raises the
%   existing singleton*. Starting from the left, property value pairs are
%   applied to the GUI before Temp2_12_2010_OpeningFunction gets called. An
%   unrecognized property name or invalid value makes property application
%   stop. All inputs are passed to Temp2_12_2010_OpeningFcn via
%   varargin.
%
%   *See GUI Options on GUIDE's Tools menu. Choose "GUI allows only one
%   instance to run (singleton)".
%
% See also: GUIDE, GUIDATA, GUIHANDLES

% Copyright 2002-2003 The MathWorks, Inc.

% Edit the above text to modify the response to help Temp2_12_2010

% Last Modified by GUIDE v2.5 09-Jun-2010 19:04:14

% Begin initialization code - DO NOT EDIT
gui_Singleton = 1;
gui_State = struct('gui_Name',    mfilename, ...
    'gui_Singleton',  gui_Singleton, ...
    'gui_OpeningFcn', @Temp2_12_2010_OpeningFcn, ...
    'gui_OutputFcn',  @Temp2_12_2010_OutputFcn, ...
    'gui_LayoutFcn',  [], ...
    'gui_Callback',   []);
if nargin && ischar(varargin{1})
    gui_State.gui_Callback = str2func(varargin{1});
end

if nargout
    [varargout{1:nargout}] = gui_mainfcn(gui_State, varargin{:});
else
    gui_mainfcn(gui_State, varargin{:});
end

% End initialization code - DO NOT EDIT

% --- Executes just before Temp2_12_2010 is made visible.
function Temp2_12_2010_OpeningFcn(hObject, eventdata, handles, varargin)
% This function has no output args, see OutputFcn.
```

---

```

% hObject handle to figure
% eventdata reserved - to be defined in a future version of MATLAB
% handles structure with handles and user data (see GUIDATA)
% varargin command line arguments to Temp2_12_2010 (see VARARGIN)

% Choose default command line output for Temp2_12_2010
handles.output = hObject;

% Update handles structure
guidata(hObject, handles);

% UIWAIT makes Temp2_12_2010 wait for user response (see UIRESUME)
% uiwait(handles.figure1);

% --- Outputs from this function are returned to the command line.
function [varargout, Temps, WorkSpeed] = Temp2_12_2010_OutputFcn(hObject, eventdata, handles)
% varargout cell array for returning output args (see VARARGOUT);
% hObject handle to figure
% eventdata reserved - to be defined in a future version of MATLAB
% handles structure with handles and user data (see GUIDATA)

% Get default command line output from handles structure
varargout{1} = handles.output
%varargout{2} = grindingoutput

%*****INPUTS
%*****INPUTS
%*****INPUTS

function n_Callback(hObject, eventdata, handles)
% hObject handle to n (see GCBO)
% eventdata reserved - to be defined in a future version of MATLAB
% handles structure with handles and user data (see GUIDATA)

% Hints: get(hObject, 'String') returns contents of n as text
% str2double(get(hObject, 'String')) returns contents of n as a double

n = str2double(get(hObject, 'String'))
handles.n = n
guidata(hObject, handles)

% --- Executes during object creation, after setting all properties.
function n_CreateFcn(hObject, eventdata, handles)
% hObject handle to n (see GCBO)
% eventdata reserved - to be defined in a future version of MATLAB
% handles empty - handles not created until after all CreateFcns called

% Hint: edit controls usually have a white background on Windows.
% See ISPC and COMPUTER.
if ispc
    set(hObject, 'BackgroundColor', 'white');
else
    set(hObject, 'BackgroundColor', get(0, 'defaultUicontrolBackgroundColor'));
end

%*****Material Properties*****

```



\*\*\*\*\*Material Properties\*\*\*\*\*  
\*\*\*\*\*Material Properties\*\*\*\*\*

```
% --- Executes on selection change in popupmenu1.
function popupmenu1_Callback(hObject, eventdata, handles)
% hObject    handle to popupmenu1 (see GCBO)
% eventdata  reserved - to be defined in a future version of MATLAB
% handles    structure with handles and user data (see GUIDATA)

% Hints: contents = get(hObject,'String') returns popupmenu1 contents as cell array
%        contents{get(hObject,'Value')} returns selected item from popupmenu1
%get(hObject,'string');
switch get(hObject,'value');
    case 1          % cBN
        handles.Kg=1300;      % Thermal conductivity of cBN grain ( W/mK )
    case 2          % Diamond
        handles.Kg=2000;      % Thermal conductivity of Diamond grain( W/mK )
    case 3          % AlO2
        handles.Kg=30;        % Thermal conductivity of AlO2 grain( W/mK )
    otherwise
        disp 'unknown Thermal Conductivity of grain'
end
guidata(hObject,handles);
```

```
% --- Executes during object creation, after setting all properties.
function popupmenu1_CreateFcn(hObject, eventdata, handles)
% hObject    handle to popupmenu1 (see GCBO)
% eventdata  reserved - to be defined in a future version of MATLAB
% handles    empty - handles not created until after all CreateFcns called

% Hint: popupmenu controls usually have a white background on Windows.
%        See ISPC and COMPUTER.
if ispc
    set(hObject,'BackgroundColor','white');
else
    set(hObject,'BackgroundColor',get(0,'defaultUicontrolBackgroundColor'));
end
```

```
% --- Executes on selection change in popupmenu2.
function popupmenu2_Callback(hObject, eventdata, handles)
% hObject    handle to popupmenu2 (see GCBO)
% eventdata  reserved - to be defined in a future version of MATLAB
% handles    structure with handles and user data (see GUIDATA)

% Hints: contents = get(hObject,'String') returns popupmenu2 contents as cell array
%        contents{get(hObject,'Value')} returns selected item from popupmenu2
switch get(hObject, 'value');
    case 1          % 38MnSiVS6
        handles.Cw=475;      % Specific heat of 38MnSiVS6 workpiece
        handles.Pw=7850;     % Density of 38MnSiVS6 workpiece
        handles.Kw=46.6;     % Conductivity of 38MnSiVS6 workpiece

    case 2          % 51CrV4
        handles.Cw=475;      % Specific heat of 51CrV4 workpiece
        handles.Pw=7850;     % Density of 51CrV4 workpiece
        handles.Kw=46.6;     % Conductivity of 51CrV4 workpiece

    case 3          % Low Alloy Steel
        handles.Cw=472;      % Specific heat of Low Alloy Steel workpiece
```

---

```

handles.Pw=7870;      % Density of Low Alloy Steel workpiece
handles.Kw=51.9;     % Conductivity of Low Alloy Steel workpiece

case 4               % Aluminium
handles.Cw=753;     % Specific heat of Aluminium workpiece
handles.Pw=3960;    % Density of Aluminium workpiece
handles.Kw=46;      % Conductivity of Aluminium workpiece

case 5               % Titanium
handles.Cw=530;     % Specific heat of Titanium workpiece
handles.Pw=4500;    % Density of Titanium workpiece
handles.Kw=17;      % Conductivity of Titanium workpiece

otherwise
disp ('unknown properties of workpiece')

end
guidata(hObject,handles);

% --- Executes during object creation, after setting all properties.
function popupmenu2_CreateFcn(hObject, eventdata, handles)
% hObject    handle to popupmenu2 (see GCBO)
% eventdata  reserved - to be defined in a future version of MATLAB
% handles    empty - handles not created until after all CreateFcns called

% Hint: popupmenu controls usually have a white background on Windows.
%    See ISPC and COMPUTER.
if ispc
    set(hObject,'BackgroundColor','white');
else
    set(hObject,'BackgroundColor',get(0,'defaultUicontrolBackgroundColor'));
end

% --- Executes on selection change in Fluid.
function Fluid_Callback(hObject, eventdata, handles)
% hObject    handle to Fluid (see GCBO)
% eventdata  reserved - to be defined in a future version of MATLAB
% handles    structure with handles and user data (see GUIDATA)

% Hints: contents = get(hObject,'String') returns Fluid contents as cell array
%    contents{get(hObject,'Value')} returns selected item from Fluid
switch get(hObject,'value');
case 1         % MoS2
handles.Hf=0;  % Convection coefficient of MoS2
case 2         % CaF2
handles.Hf=0;  % Convection coefficient of CaF2
case 3         % EcoCool
handles.Hf=310000; % Convection coefficient of EcoCool
case 4         % Dry
handles.Hf=0;  % Convection coefficient of Dry Machining
case 5         % Water
handles.Hf=290000; % Convection coefficient of Water

otherwise
disp 'unknown machining fluid properties'
end
guidata(hObject,handles);

% --- Executes during object creation, after setting all properties.
function Fluid_CreateFcn(hObject, eventdata, handles)

```

---

```

% hObject handle to Fluid (see GCBO)
% eventdata reserved - to be defined in a future version of MATLAB
% handles empty - handles not created until after all CreateFcns called

% Hint: popupmenu controls usually have a white background on Windows.
% See ISPC and COMPUTER.
if ispc
    set(hObject,'BackgroundColor','white');
else
    set(hObject,'BackgroundColor',get(0,'defaultUicontrolBackgroundColor'));
end

%*****RadioButtons*****
%*****RadioButtons*****
%*****RadioButtons*****

% --- Executes on button press in radiobutton1.
function radiobutton1_Callback(hObject, eventdata, handles)
% hObject handle to radiobutton1 (see GCBO)
% eventdata reserved - to be defined in a future version of MATLAB
% handles structure with handles and user data (see GUIDATA)

% Hint: get(hObject,'Value') returns toggle state of radiobutton1
if (get(hObject,'Value') == get(hObject,'Max'))
    % Radio button is selected-take appropriate action
    Ds = str2double(get(hObject,'String'))
    handles.Ds = Ds
    guidata(hObject,handles)
else
    % Radio button is not selected-take appropriate action
end

% --- Executes on button press in radiobutton2.
function radiobutton2_Callback(hObject, eventdata, handles)
% hObject handle to radiobutton2 (see GCBO)
% eventdata reserved - to be defined in a future version of MATLAB
% handles structure with handles and user data (see GUIDATA)

% Hint: get(hObject,'Value') returns toggle state of radiobutton2
if (get(hObject,'Value') == get(hObject,'Max'))
    % Radio button is selected-take appropriate action
    Ds = str2double(get(hObject,'String'))
    handles.Ds = Ds
    guidata(hObject,handles)
else
    % Radio button is not selected-take appropriate action
end

% --- Executes on button press in radiobutton3.
function radiobutton3_Callback(hObject, eventdata, handles)
% hObject handle to radiobutton3 (see GCBO)
% eventdata reserved - to be defined in a future version of MATLAB
% handles structure with handles and user data (see GUIDATA)

% Hint: get(hObject,'Value') returns toggle state of radiobutton3
if (get(hObject,'Value') == get(hObject,'Max'))
    % Radio button is selected-take appropriate action
    Ds = str2double(get(hObject,'String'))
    handles.Ds = Ds

```

---

```

    Dw = str2double(get(hObject, 'String'))
    handles.Ds = Ds
    guidata(hObject,handles)
else
    % Radio button is not selected-take appropriate action
end

% --- Executes on button press in radiobutton4.
function radiobutton4_Callback(hObject, eventdata, handles)
% hObject    handle to radiobutton4 (see GCBO)
% eventdata  reserved - to be defined in a future version of MATLAB
% handles    structure with handles and user data (see GUIDATA)

% Hint: get(hObject,'Value') returns toggle state of radiobutton4
if (get(hObject,'Value') == get(hObject,'Max'))
    % Radio button is selected-take appropriate action
else
    % Radio button is not selected-take appropriate action
end

function Ds_Callback(hObject, eventdata, handles)
% hObject    handle to Ds (see GCBO)
% eventdata  reserved - to be defined in a future version of MATLAB
% handles    structure with handles and user data (see GUIDATA)

% Hints: get(hObject,'String') returns contents of Ds as text
%       str2double(get(hObject,'String')) returns contents of Ds as a double
Ds = str2double(get(hObject, 'String'))
handles.Ds = Ds/1000
guidata(hObject,handles)

% --- Executes during object creation, after setting all properties.
function Ds_CreateFcn(hObject, eventdata, handles)
% hObject    handle to Ds (see GCBO)
% eventdata  reserved - to be defined in a future version of MATLAB
% handles    empty - handles not created until after all CreateFcns called

% Hint: edit controls usually have a white background on Windows.
%       See ISPC and COMPUTER.
if ispc
    set(hObject,'BackgroundColor','white');
else
    set(hObject,'BackgroundColor',get(0,'defaultUicontrolBackgroundColor'));
end

function Dw_Callback(hObject, eventdata, handles)
% hObject    handle to Dw (see GCBO)
% eventdata  reserved - to be defined in a future version of MATLAB
% handles    structure with handles and user data (see GUIDATA)

% Hints: get(hObject,'String') returns contents of Dw as text
%       str2double(get(hObject,'String')) returns contents of Dw as a double
Dw = str2double(get(hObject, 'String'))
handles.Dw = Dw/1000
guidata(hObject,handles)

% --- Executes during object creation, after setting all properties.
function Dw_CreateFcn(hObject, eventdata, handles)
% hObject    handle to Dw (see GCBO)

```

---

```

% eventdata reserved - to be defined in a future version of MATLAB
% handles empty - handles not created until after all CreateFcns called

% Hint: edit controls usually have a white background on Windows.
% See ISPC and COMPUTER.
if ispc
    set(hObject,'BackgroundColor','white');
else
    set(hObject,'BackgroundColor',get(0,'defaultUicontrolBackgroundColor'));
end

% --- Executes on button press in togglebutton3.
function togglebutton3_Callback(hObject, eventdata, handles)
% hObject handle to togglebutton3 (see GCBO)
% eventdata reserved - to be defined in a future version of MATLAB
% handles structure with handles and user data (see GUIDATA)

% Hint: get(hObject,'Value') returns toggle state of togglebutton3
ExtEffect = ((handles.Ds*handles.Dw)/(handles.Ds+handles.Dw))
handles.De = ExtEffect
set(handles.EffectD,'String',handles.De);
guidata(hObject,handles)

%*****Useful Flowrate*****
%*****Useful Flowrate*****
%*****Useful Flowrate*****

function Vs_Callback(hObject, eventdata, handles)
% hObject handle to Vs (see GCBO)
% eventdata reserved - to be defined in a future version of MATLAB
% handles structure with handles and user data (see GUIDATA)

% Hints: get(hObject,'String') returns contents of Vs as text
% str2double(get(hObject,'String')) returns contents of Vs as a double
Vs = str2double(get(hObject, 'String'))
handles.Vs = Vs
guidata(hObject,handles)

% --- Executes during object creation, after setting all properties.
function Vs_CreateFcn(hObject, eventdata, handles)
% hObject handle to Vs (see GCBO)
% eventdata reserved - to be defined in a future version of MATLAB
% handles empty - handles not created until after all CreateFcns called

% Hint: edit controls usually have a white background on Windows.
% See ISPC and COMPUTER.
if ispc
    set(hObject,'BackgroundColor','white');
else
    set(hObject,'BackgroundColor',get(0,'defaultUicontrolBackgroundColor'));
end

```

---

```

function b_Callback(hObject, eventdata, handles)
% hObject   handle to b (see GCBO)
% eventdata reserved - to be defined in a future version of MATLAB
% handles   structure with handles and user data (see GUIDATA)

% Hints: get(hObject,'String') returns contents of b as text
%   str2double(get(hObject,'String')) returns contents of b as a double
b = str2double(get(hObject, 'String'))
handles.b = b/1000
guidata(hObject,handles)

% --- Executes during object creation, after setting all properties.
function b_CreateFcn(hObject, eventdata, handles)
% hObject   handle to b (see GCBO)
% eventdata reserved - to be defined in a future version of MATLAB
% handles   empty - handles not created until after all CreateFcns called

% Hint: edit controls usually have a white background on Windows.
%   See ISPC and COMPUTER.
if ispc
    set(hObject,'BackgroundColor','white');
else
    set(hObject,'BackgroundColor',get(0,'defaultUicontrolBackgroundColor'));
end

function gradius_Callback(hObject, eventdata, handles)
% hObject   handle to gradius (see GCBO)
% eventdata reserved - to be defined in a future version of MATLAB
% handles   structure with handles and user data (see GUIDATA)

% Hints: get(hObject,'String') returns contents of gradius as text
%   str2double(get(hObject,'String')) returns contents of gradius as a double
gradius = str2double(get(hObject, 'String'))
handles.gradius = (gradius/2)*(1E-6)
guidata(hObject,handles)

% --- Executes during object creation, after setting all properties.
function gradius_CreateFcn(hObject, eventdata, handles)
% hObject   handle to gradius (see GCBO)
% eventdata reserved - to be defined in a future version of MATLAB
% handles   empty - handles not created until after all CreateFcns called

% Hint: edit controls usually have a white background on Windows.
%   See ISPC and COMPUTER.
if ispc
    set(hObject,'BackgroundColor','white');
else
    set(hObject,'BackgroundColor',get(0,'defaultUicontrolBackgroundColor'));
end

function porosityS_Callback(hObject, eventdata, handles)
% hObject   handle to porosityS (see GCBO)
% eventdata reserved - to be defined in a future version of MATLAB
% handles   structure with handles and user data (see GUIDATA)

% Hints: get(hObject,'String') returns contents of porosityS as text
%   str2double(get(hObject,'String')) returns contents of porosityS as a double

```

---

```

porosityS = str2double(get(hObject, 'String'))
handles.porosityS = porosityS
guidata(hObject,handles)

% --- Executes during object creation, after setting all properties.
function porosityS_CreateFcn(hObject, eventdata, handles)
% hObject    handle to porosityS (see GCBO)
% eventdata  reserved - to be defined in a future version of MATLAB
% handles    empty - handles not created until after all CreateFcns called

% Hint: edit controls usually have a white background on Windows.
%       See ISPC and COMPUTER.
if ispc
    set(hObject,'BackgroundColor','white');
else
    set(hObject,'BackgroundColor',get(0,'defaultUicontrolBackgroundColor'));
end

% --- Executes during object creation, after setting all properties.
function Quf_CreateFcn(hObject, eventdata, handles)
% hObject    handle to Quf (see GCBO)
% eventdata  reserved - to be defined in a future version of MATLAB
% handles    empty - handles not created until after all CreateFcns called

% --- Executes on button press in togglebutton2.
function togglebutton2_Callback(hObject, eventdata, handles)
% hObject    handle to togglebutton2 (see GCBO)
% eventdata  reserved - to be defined in a future version of MATLAB
% handles    structure with handles and user data (see GUIDATA)

% Hint: get(hObject,'Value') returns toggle state of togglebutton2
Useful=(handles.Vs*handles.b*handles.gradius*handles.porosityS)*1000*60
%Useful=(handles.Vs*handles.b)*(1/5)*(15.2/(handles.gradius))*1000*60

digits(2)
set(handles.Quf,'String',Useful);

%*****Variables*****
%*****Variables*****
%*****Variables*****

function ae_Callback(hObject, eventdata, handles)
% hObject    handle to ae (see GCBO)
% eventdata  reserved - to be defined in a future version of MATLAB
% handles    structure with handles and user data (see GUIDATA)

% Hints: get(hObject,'String') returns contents of ae as text
%       str2double(get(hObject,'String')) returns contents of ae as a double
ae = str2double(get(hObject, 'String'))
handles.ae = ae/1000
guidata(hObject,handles)

% --- Executes during object creation, after setting all properties.
function ae_CreateFcn(hObject, eventdata, handles)

```

---

```

% hObject handle to ae (see GCBO)
% eventdata reserved - to be defined in a future version of MATLAB
% handles empty - handles not created until after all CreateFcns called

% Hint: edit controls usually have a white background on Windows.
% See ISPC and COMPUTER.
if ispc
    set(hObject,'BackgroundColor','white');
else
    set(hObject,'BackgroundColor',get(0,'defaultUicontrolBackgroundColor'));
end

function Vw_Callback(hObject, eventdata, handles)
% hObject handle to Vw (see GCBO)
% eventdata reserved - to be defined in a future version of MATLAB
% handles structure with handles and user data (see GUIDATA)

% Hints: get(hObject,'String') returns contents of Vw as text
% str2double(get(hObject,'String')) returns contents of Vw as a double
Vw = str2double(get(hObject, 'String'))
handles.Vw = Vw
guidata(hObject,handles)

% --- Executes during object creation, after setting all properties.
function Vw_CreateFcn(hObject, eventdata, handles)
% hObject handle to Vw (see GCBO)
% eventdata reserved - to be defined in a future version of MATLAB
% handles empty - handles not created until after all CreateFcns called

% Hint: edit controls usually have a white background on Windows.
% See ISPC and COMPUTER.
if ispc
    set(hObject,'BackgroundColor','white');
else
    set(hObject,'BackgroundColor',get(0,'defaultUicontrolBackgroundColor'));
end

function Ec_Callback(hObject, eventdata, handles)
% hObject handle to Ec (see GCBO)
% eventdata reserved - to be defined in a future version of MATLAB
% handles structure with handles and user data (see GUIDATA)

% Hints: get(hObject,'String') returns contents of Ec as text
% str2double(get(hObject,'String')) returns contents of Ec as a double
Ec = str2double(get(hObject, 'String'))
handles.Ec = Ec
guidata(hObject,handles)

% --- Executes during object creation, after setting all properties.
function Ec_CreateFcn(hObject, eventdata, handles)
% hObject handle to Ec (see GCBO)
% eventdata reserved - to be defined in a future version of MATLAB
% handles empty - handles not created until after all CreateFcns called

% Hint: edit controls usually have a white background on Windows.
% See ISPC and COMPUTER.
if ispc

```



```

set(hObject,'BackgroundColor','white');
else
set(hObject,'BackgroundColor',get(0,'defaultUicontrolBackgroundColor'));
end

%*****PUSHBUTTON
%*****PUSHBUTTON
%*****PUSHBUTTON

% --- Executes on button press in Pushbutton.
function Pushbutton_Callback(hObject, eventdata, handles)
% hObject    handle to Pushbutton (see GCBO)
% eventdata  reserved - to be defined in a future version of MATLAB
% handles    structure with handles and user data (see GUIDATA)

% Hint: get(hObject,'Value') returns toggle state of Pushbutton

n=handles.n;
ae=handles.ae;
Vs=handles.Vs;
Vw=handles.Vw;
Kg=handles.Kg;
Cw=handles.Cw;
Pw=handles.Pw;
Kw=handles.Kw;
Ec=handles.Ec;
Ds=handles.Ds;
Dw=handles.Dw;
De=handles.De;
Hf=handles.Hf
guidata(hObject,handles);

Betaw=sqrt(Kw*Pw*Cw); % ( J/m2sK ) Thermal property

Alfaw=Kw/(Pw*Cw); % Thermal diffusivity
r0=1e-5; % ( m ) Grain radius
%Ds=0.350; % ( m ) wheel diameter

Lc=sqrt(ae*De); % (m) Contact length
phi=asin(ae/Lc); % (arc) Contact angle

%Hf=290000; % Convection coefficient of water

Removal=Vw*ae*1e6; % (mm3/mm.s)
L=Vw*Lc/(4*Alfaw); % Peclet number

% -----Section 1: calculate C-factor-----
Lx=L*sin(phi)/phi;

N = 100;
x = linspace(-0.1*Lx,1.1*Lx,N);
X = x;
theta = 1 : N;
for l=1:N
u=linspace(2*X(l)-2*Lx,2*X(l),N); % integrating parameter.
phix=phi+asin(phi*(2*X(l)-u)/L-sin(phi));
q2 = (n+1)*(phix./2/phi).^n;
% heat flux distribution, 0 - uniform, 1 - triangular

```

```

M=2;
%Modification
Z=-2*X(l)*tan(phi-phix/2);

    y=(1/2).*(1./cos(phix-phi)).*exp(-u.*cos(phi)+Z.*sin(phi)+(2*X(l)-u).*sin(phi).*tan(phi-phix/2))...
    .* bessell(0, sqrt(u.*u+(Z+(2*X(l)-u).*tan(phi-phix/2)).^2)).*q2.*M;
%modified Bessel functions of the second kind,
theta(l) = trapz(u,y);
end
Tmax=max(theta);

CC=Tmax*sqrt(1/L)/pi;

%-----End of section1-----

%-----section2-- calculate Tem. on the finish Surface
for l=1:N
Z=-2*X(l)*cos(phi)*sin(phi);
X(l)=X(l)*cos(phi)^2;
u=linspace(2*X(l)-2*Lx,2*X(l),N); % integrating parameter.
phix=phi+asin(phi*(2*X(l)-u)/L-sin(phi));
    q2=(n+1)*(phix./2/phi).^n;
    % heat flux distribution, 0 - uniform, 1 - triangular
M=2;
    y=(1/2).*(1./cos(phix-phi)).*exp(-u.*cos(phi)+Z.*sin(phi)+(2*X(l)-u).*sin(phi).*tan(phi-phix/2))...
    .* bessell(0, sqrt(u.*u+(Z+(2*X(l)-u).*tan(phi-phix/2)).^2)).*q2.*M;
%modified Bessel functions of the second kind,
theta(l) = trapz(u,y);
end
Tfmax=max(theta);
Frac=Tfmax/Tmax;
%-----end of section2-----

%-----Section3:calculate Rws, Hw, Hw/Rws-----
Rws=1/(1+0.97*Kg/(Betaw*sqrt(r0*Vs)));
Hw=(Betaw/CC)*sqrt(Vw/Lc);
HwRws=Hw/Rws;
%-----End of section3-----

%-----section4: Burn Threshold-----
Qt=Ec*1e9*Vw*ae/Lc; % (W/m2)

Ns=11; % grit density (1/mm2)
P=1.5; % grit distribution
m=0.8; % grit shape
alfa=(P-m)/(P+1); %
beta=P/(P+1); %
Nd=1.2*(Ns^(3/2))^beta*(Vw/Vs)*sqrt(ae/Ds)^alfa; % (1/mm2) active grit density
agmax=1000*sqrt((Vw/Vs)*sqrt(ae/Ds)/Nd); % (micron) ave chip thickness
ag=agmax/2; % chip thickness
rc=5; % (micron) corner radius of grit cutting edge
Anghalf=75-(75-60)*ag/25;
Gama=cos(Anghalf*pi/180)/(sin((90-Anghalf)*pi/2/180)*cos((90+Anghalf)*pi/2/180)); % shear strain
AlfawCh=7/4500/530; % Thermal diffusivity at chip temperature
R1=1/(1+1.328*sqrt(AlfawCh*Gama/(Vs*ag/1000000))); % heat partition to chips
Rwch=1-R1; % heat partition to work in the 'chip/work' sub-system

Tcon1=Qt/(Hw*(1/Rws+1/Rwch-1)+Hf); % contact tem, effective cooling hf>>0
Tcon2=Qt/(Hw*(1/Rws+1/Rwch-1)); % contact tem, no cooling hf=0

```

```
Tfin1=Tcon1*Frac;      % finish tem, effective cooling hf>>0
Tfin2=Tcon2*Frac;      % finish tem, no cooling hf=0

handles.Rwch=Rwch;
handles.HwRws=HwRws;
handles.Tcon1=Tcon1;
handles.Tcon2=Tcon2;
handles.Tfin1=Tfin1;
handles.Tfin2=Tfin2;
guidata(hObject,handles);

%*****OUTPUTS
%*****OUTPUTS
%*****OUTPUTS

%set(handles.Contact,'String',handles.Tcon2);
%set(handles.Finish,'String',handles.Tfin2);

set(handles.Contact,'String',handles.Tcon1);
set(handles.Finish,'String',handles.Tfin1);

set(handles.Flux,'String',handles.Rwch);
set(handles.Partition,'String',handles.HwRws);

guidata(hObject,handles);

%*****OUTPUTS
%*****OUTPUTS
%*****OUTPUTS

% --- Executes during object creation, after setting all properties.
function text15_CreateFcn(hObject, eventdata, handles)
% hObject    handle to text15 (see GCBO)
% eventdata  reserved - to be defined in a future version of MATLAB
% handles    empty - handles not created until after all CreateFcns called

% --- Executes during object creation, after setting all properties.
function text14_CreateFcn(hObject, eventdata, handles)
% hObject    handle to text14 (see GCBO)
% eventdata  reserved - to be defined in a future version of MATLAB
% handles    empty - handles not created until after all CreateFcns called

% --- Executes during object creation, after setting all properties.
function text20_CreateFcn(hObject, eventdata, handles)
% hObject    handle to text20 (see GCBO)
% eventdata  reserved - to be defined in a future version of MATLAB
% handles    empty - handles not created until after all CreateFcns called

function edit18_Callback(hObject, eventdata, handles)
% hObject    handle to edit18 (see GCBO)
```

---

```

% eventdata reserved - to be defined in a future version of MATLAB
% handles structure with handles and user data (see GUIDATA)

% Hints: get(hObject,'String') returns contents of edit18 as text
%   str2double(get(hObject,'String')) returns contents of edit18 as a double

% --- Executes during object creation, after setting all properties.
function edit18_CreateFcn(hObject, eventdata, handles)
% hObject handle to edit18 (see GCBO)
% eventdata reserved - to be defined in a future version of MATLAB
% handles empty - handles not created until after all CreateFcns called

% Hint: edit controls usually have a white background on Windows.
%   See ISPC and COMPUTER.
if ispc && isequal(get(hObject,'BackgroundColor'), get(0,'defaultUicontrolBackgroundColor'))
    set(hObject,'BackgroundColor','white');
end

function edit20_Callback(hObject, eventdata, handles)
% hObject handle to edit20 (see GCBO)
% eventdata reserved - to be defined in a future version of MATLAB
% handles structure with handles and user data (see GUIDATA)

% Hints: get(hObject,'String') returns contents of edit20 as text
%   str2double(get(hObject,'String')) returns contents of edit20 as a double

% --- Executes during object creation, after setting all properties.
function edit20_CreateFcn(hObject, eventdata, handles)
% hObject handle to edit20 (see GCBO)
% eventdata reserved - to be defined in a future version of MATLAB
% handles empty - handles not created until after all CreateFcns called

% Hint: edit controls usually have a white background on Windows.
%   See ISPC and COMPUTER.
if ispc && isequal(get(hObject,'BackgroundColor'), get(0,'defaultUicontrolBackgroundColor'))
    set(hObject,'BackgroundColor','white');
end

function edit22_Callback(hObject, eventdata, handles)
% hObject handle to edit22 (see GCBO)
% eventdata reserved - to be defined in a future version of MATLAB
% handles structure with handles and user data (see GUIDATA)

% Hints: get(hObject,'String') returns contents of edit22 as text
%   str2double(get(hObject,'String')) returns contents of edit22 as a double

% --- Executes during object creation, after setting all properties.
function edit22_CreateFcn(hObject, eventdata, handles)
% hObject handle to edit22 (see GCBO)
% eventdata reserved - to be defined in a future version of MATLAB
% handles empty - handles not created until after all CreateFcns called

% Hint: edit controls usually have a white background on Windows.
%   See ISPC and COMPUTER.

```

---

```

if ispc && isequal(get(hObject,'BackgroundColor'), get(0,'defaultUicontrolBackgroundColor'))
    set(hObject,'BackgroundColor','white');
end

```

```

function edit23_Callback(hObject, eventdata, handles)
% hObject    handle to edit23 (see GCBO)
% eventdata  reserved - to be defined in a future version of MATLAB
% handles    structure with handles and user data (see GUIDATA)

% Hints: get(hObject,'String') returns contents of edit23 as text
%       str2double(get(hObject,'String')) returns contents of edit23 as a double

```

```

% --- Executes during object creation, after setting all properties.
function edit23_CreateFcn(hObject, eventdata, handles)
% hObject    handle to edit23 (see GCBO)
% eventdata  reserved - to be defined in a future version of MATLAB
% handles    empty - handles not created until after all CreateFcns called

% Hint: edit controls usually have a white background on Windows.
%       See ISPC and COMPUTER.
if ispc && isequal(get(hObject,'BackgroundColor'), get(0,'defaultUicontrolBackgroundColor'))
    set(hObject,'BackgroundColor','white');
end

```

```

% --- Executes on selection change in Xaxis.
function Xaxis_Callback(hObject, eventdata, handles)
% hObject    handle to Xaxis (see GCBO)
% eventdata  reserved - to be defined in a future version of MATLAB
% handles    structure with handles and user data (see GUIDATA)

% Hints: contents = get(hObject,'String') returns Xaxis contents as cell array
%       contents{get(hObject,'Value')} returns selected item from Xaxis

```

```

Vs=handles.Vs;
Ec=handles.Ec;
Tfin2=handles.Tfin2;
Rwch=handles.Rwch;

```

```

switch get(hObject,'value');
    case 1          %Specific Grind Energy (SGE)
        handles.xaxis=1%Ec
    case 2          %Finish Temperatures
        handles.xaxis=2%Temps
    case 3          %Heat Flux
        handles.xaxis=3%Rwch
    case 4          %Wheel Speed
        handles.xaxis=4%Vs

    otherwise
        disp 'unknown axis'
end
%xaxis
guidata(hObject,handles);

```

```

% --- Executes during object creation, after setting all properties.
function Xaxis_CreateFcn(hObject, eventdata, handles)

```

---

```

% hObject handle to Xaxis (see GCBO)
% eventdata reserved - to be defined in a future version of MATLAB
% handles empty - handles not created until after all CreateFcns called

% Hint: popupmenu controls usually have a white background on Windows.
% See ISPC and COMPUTER.
if ispc && isequal(get(hObject,'BackgroundColor'), get(0,'defaultUicontrolBackgroundColor'))
    set(hObject,'BackgroundColor','white');
end

```

```

% --- Executes on selection change in Yaxis.
function Yaxis_Callback(hObject, eventdata, handles)
% hObject handle to Yaxis (see GCBO)
% eventdata reserved - to be defined in a future version of MATLAB
% handles structure with handles and user data (see GUIDATA)

% Hints: contents = get(hObject,'String') returns Yaxis contents as cell array
% contents{get(hObject,'Value')} returns selected item from Yaxis

```

```

Vs=handles.Vs;
Ec=handles.Ec;
Tfin2=handles.Tfin2;
Rwch=handles.Rwch;

switch get(hObject,'value');
    case 1 %Specific Grind Energy (SGE)
        handles.yaxis=1%Ec
    case 2 %Finish Temperatures
        handles.yaxis=2%Temps
    case 3 %Heat Flux
        handles.yaxis=3%Rwch
    case 4 %Wheel Speed
        handles.yaxis=4%Vs

    otherwise
        disp 'unknown axis'
end
guidata(hObject,handles);

```

```

% --- Executes during object creation, after setting all properties.
function Yaxis_CreateFcn(hObject, eventdata, handles)
% hObject handle to Yaxis (see GCBO)

% eventdata reserved - to be defined in a future version of MATLAB
% handles empty - handles not created until after all CreateFcns called

% Hint: popupmenu controls usually have a white background on Windows.
% See ISPC and COMPUTER.
if ispc && isequal(get(hObject,'BackgroundColor'), get(0,'defaultUicontrolBackgroundColor'))
    set(hObject,'BackgroundColor','white');
end

```

```

% --- Executes on selection change in Zaxis.
function Zaxis_Callback(hObject, eventdata, handles)
% hObject handle to Zaxis (see GCBO)
% eventdata reserved - to be defined in a future version of MATLAB
% handles structure with handles and user data (see GUIDATA)

```

---

```

% Hints: contents = get(hObject,'String') returns Zaxis contents as cell array
%   contents{get(hObject,'Value')} returns selected item from Zaxis

switch get(hObject,'value');
    case 1
        handles.zaxis=1%3D Contours
    case 2
        handles.zaxis=2%HeatFlux
    case 3
        handles.zaxis=3%Temperatures

        otherwise
            disp 'unknown axis'
end
guidata(hObject,handles);

% --- Executes during object creation, after setting all properties.
function Zaxis_CreateFcn(hObject, eventdata, handles)
% hObject   handle to Zaxis (see GCBO)
% eventdata reserved - to be defined in a future version of MATLAB
% handles   empty - handles not created until after all CreateFcns called

% Hint: popmenu controls usually have a white background on Windows.
%   See ISPC and COMPUTER.
if ispc && isequal(get(hObject,'BackgroundColor'), get(0,'defaultUicontrolBackgroundColor'))
    set(hObject,'BackgroundColor','white');
end

function edit24_Callback(hObject, eventdata, handles)
% hObject   handle to edit24 (see GCBO)
% eventdata reserved - to be defined in a future version of MATLAB
% handles   structure with handles and user data (see GUIDATA)

% Hints: get(hObject,'String') returns contents of edit24 as text
%   str2double(get(hObject,'String')) returns contents of edit24 as a double

% --- Executes during object creation, after setting all properties.
function edit24_CreateFcn(hObject, eventdata, handles)
% hObject   handle to edit24 (see GCBO)
% eventdata reserved - to be defined in a future version of MATLAB
% handles   empty - handles not created until after all CreateFcns called

% Hint: edit controls usually have a white background on Windows.
%   See ISPC and COMPUTER.
if ispc && isequal(get(hObject,'BackgroundColor'), get(0,'defaultUicontrolBackgroundColor'))
    set(hObject,'BackgroundColor','white');
end

function edit25_Callback(hObject, eventdata, handles)
% hObject   handle to edit25 (see GCBO)
% eventdata reserved - to be defined in a future version of MATLAB
% handles   structure with handles and user data (see GUIDATA)

% Hints: get(hObject,'String') returns contents of edit25 as text
%   str2double(get(hObject,'String')) returns contents of edit25 as a double

```

---

```

% --- Executes during object creation, after setting all properties.
function edit25_CreateFcn(hObject, eventdata, handles)
% hObject    handle to edit25 (see GCBO)
% eventdata  reserved - to be defined in a future version of MATLAB
% handles    empty - handles not created until after all CreateFcns called

% Hint: edit controls usually have a white background on Windows.
%   See ISPC and COMPUTER.
if ispc && isequal(get(hObject,'BackgroundColor'), get(0,'defaultUicontrolBackgroundColor'))
    set(hObject,'BackgroundColor','white');
end

```

```

% --- Executes on selection change in popupmenu8.
function popupmenu8_Callback(hObject, eventdata, handles)
% hObject    handle to popupmenu8 (see GCBO)
% eventdata  reserved - to be defined in a future version of MATLAB
% handles    structure with handles and user data (see GUIDATA)

% Hints: contents = get(hObject,'String') returns popupmenu8 contents as cell array
%   contents{get(hObject,'Value')} returns selected item from popupmenu8

```

```

% --- Executes during object creation, after setting all properties.
function popupmenu8_CreateFcn(hObject, eventdata, handles)
% hObject    handle to popupmenu8 (see GCBO)
% eventdata  reserved - to be defined in a future version of MATLAB
% handles    empty - handles not created until after all CreateFcns called

% Hint: popupmenu controls usually have a white background on Windows.
%   See ISPC and COMPUTER.
if ispc
    set(hObject,'BackgroundColor','white');
else
    set(hObject,'BackgroundColor',get(0,'defaultUicontrolBackgroundColor'));
end

```

```

% --- Executes on button press in togglebutton5.
function togglebutton5_Callback(hObject, eventdata, handles)
% hObject    handle to togglebutton5 (see GCBO)
% eventdata  reserved - to be defined in a future version of MATLAB
% handles    structure with handles and user data (see GUIDATA)

% Hint: get(hObject,'Value') returns toggle state of togglebutton5

```

```

% --- Executes on button press in togglebutton4.
function togglebutton4_Callback(hObject, eventdata, handles)
% hObject    handle to togglebutton4 (see GCBO)
% eventdata  reserved - to be defined in a future version of MATLAB
% handles    structure with handles and user data (see GUIDATA)

% Hint: get(hObject,'Value') returns toggle state of togglebutton4
n=handles.n;
ae=handles.ae;
Vs=handles.Vs;
Vw=handles.Vw;

```



---

```

Kg=handles.Kg;
Cw=handles.Cw;
Pw=handles.Pw;
Kw=handles.Kw;
Ec=handles.Ec;
%handles.xaxis;
%handles.yaxis;
%handles.zaxis;
guidata(hObject,handles)

xaxis=handles.xaxis
yaxis=handles.yaxis
zaxis=handles.zaxis

if (xaxis == 1) %X-axis Selector - SGE
    %then select y-axis

    if (yaxis == 1) %Temperature

        [Tcon2,Tfin2,Vs,Temps]=SGEloop(n,ae,Vs,Vw,Kg,Cw,Pw,Kw,Ec);
        fh = figure( );

        hold on
        handles.Temps=Temps
        guidata(hObject,handles)

        x=Temps(:,1);
        y1=Temps(:,2);
        y2=Temps(:,3);
        y3=Temps(:,4);
        y4=Temps(:,5);

        %x1=ESW1(2,:);
        %y5=ESW1(3,:);

        plot(x,y1,'r',x,y2,'b',x,y3,'r',x,y4,'b')
        xlabel('Specific Grinding Energy (J/mm3)')
        ylabel('Temperature (Degrees C)')
        title('SGE vs Temperatures');
        legend('Tcon1','Tcon2','Tfin1','Tfin2')
        grid on
    end
    %i=0
    %for i=(1:1:5)
    % x2=XX(14,i)
    % y5=XX(5,i)
    % plot(x2,y5,'r+')
    % end

    %i=0
    %for i=(20:1:27)
    % x2=XX(14,i)
    % y5=XX(5,i)
    % plot(x2,y5,'b+')
    % end
    % hold off

if (yaxis == 2)
[Tcon2,Tfin2,Vs,Temps]=SGEloop(n,ae,Vs,Vw,Kg,Cw,Pw,Kw,Ec);

```

```

fh = figure( );
x=Temps(:,1);
y=Temps(:,6);

plot(x,y,'r')
xlabel('Specific Grinding Energy (J/mm3)')
ylabel('Heat Flux (W/mm2)')
title('SGE vs Heat Flux');
legend('Heat Flux (W/mm2)')
grid on
Temps
end
end

if (xaxis == 2) %X-axis Selector - Wheel Speed
%then select y-axis
%[WheelSpeed] = Speedloop(n,ae,Vs,Vw,Kg,Cw,Pw,Kw,Ec)
[WheelSpeed]=Speedloop(n,ae,Vs,Vw,Kg,Cw,Pw,Kw,Ec)
if (yaxis == 1)
fh = figure( );
x=WheelSpeed(:,1);
y1=WheelSpeed(:,3);
y2=WheelSpeed(:,4);
y3=WheelSpeed(:,5);
y4=WheelSpeed(:,6);

plot(x,y1,'r',x,y2,'b',x,y3,'r',x,y4,'b')
xlabel('Wheel Speed (Vs - m/s)')
ylabel('Temperature (Degrees C)')
title('Wheel Speed vs Temperatures');
legend('Tcon1','Tcon2','Tfin1','Tfin2')
grid on

end
if (yaxis == 2) %Heat Flux

fh = figure( );
x=WheelSpeed(:,1);
y1=WheelSpeed(:,7);
y2=WheelSpeed(:,8);

plot(x,y1,'r',x,y2,'r-')
xlabel('Wheel Speed (Vs - m/s)')
ylabel('Heat Flux (W/mm2)')
title('Wheel Speed vs Heat Flux');
legend('Heat Flux (W/mm2)','Chip/Workpiece Partition')
grid on
WheelSpeed;
end
end

if (xaxis == 3) %X-axis Selector - Chip Thickness
%then select y-axis
[WheelSpeed] = Speedloop(n,ae,Vs,Vw,Kg,Cw,Pw,Kw,Ec) ;

if (yaxis == 1) %Temperatures
fh = figure( );
hold on
x=WheelSpeed(2:20,9);
y1=WheelSpeed(2:20,3);

```

---

```

y2=WheelSpeed(2:20,4);
y3=WheelSpeed(2:20,5);
y4=WheelSpeed(2:20,6);

plot(x,y1,'r',x,y2,'b',x,y3,'r',x,y4,'b')
xlabel('Equivalent Chip Thickness (um)')
ylabel('Temperature (Degrees C)')
title('Equivalent Chip Thickness vs Temperatures');
legend('Tcon1','Tcon2','Tfin1','Tfin2')
grid on

%i=0
%for i=(1:1:5)
% x2=XX(16,i)
% y5=XX(5,i)
% plot(x2,y5,'r+')

%i=0
%for i=(20:1:27)
% x2=XX(16,i)
% y5=XX(5,i)
% plot(x2,y5,'b+')
%hold off

end
if (yaxis == 2) %Heat Flux

fh = figure( );
x=WheelSpeed(2:20,9);
y1=WheelSpeed(2:20,7);
y2=WheelSpeed(2:20,8);

plot(x,y1,'r',x,y2,'r--')
xlabel('Equivalent Chip Thickness (um)')
ylabel('Heat Flux (W/mm2)')
title('Equivalent Chip Thickness vs Heat Flux');
legend('Heat Flux (W/mm2)','Chip/Workpiece Partition')
grid on
WheelSpeed;
end
if (yaxis == 3) %WheelSpeed

fh = figure( );
x=WheelSpeed(2:20,9);
y=WheelSpeed(2:20,1);

plot(x,y,'r')
xlabel('Equivalent Chip Thickness (um)')
ylabel('Wheelspeed (m/s)')
title('Equivalent Chip Thickness heq vs Vs');
legend('heq = ae*Vw/Vs = Qw/Vs')
grid on
WheelSpeed;
end
end

%handles.output=set(handles.Temps)

```

---

```
%Special Case - 3D
if (zaxis == 3)
    [Tcon2,Tfin2,Vs,Temps]=SGEloop(n,ae,Vs,Vw,Kg,Cw,Pw,Kw,Ec);
    fh = figure( );
    x=Temps(2:12,1);
    y=Temps(2:12,8);
    z1=Temps(2:12,2);
    z2=Temps(2:12,3);
    z3=Temps(2:12,4);
    z4=Temps(2:12,5);

    plot(x,y,z1,x,y,z2,x,y,z3,x,y,z4)
    xlabel('Specific Grinding Energy (J/mm3)')
    ylabel('Equivalent Chip Thickness (um)')
    zlabel('Temperature (C)')
    title('SGE vs Heq vs Temperature');
    legend('Contact Temp1','Contact Temp2','Finish Temp1','Finish Temp2')
    grid on
    Temps
end
```

---

## Ansys Batch File for geometry creation

1.

```
/prep7
btol,1e-10

lvsel,all
lvdele,all,,1

wheelrad=175
partrad=23
cutwidth=2
feedrate=0.00001 !(m/s)
partrot=0.005 !(1/s)
rotstep=10 !(°)
lnpolygon=200
finish
!~SATIN,'cylinder','sat','.\macros','SOLIDS,0

/AUX15
!*
IOPTN,IGES,NODEFEAT
IOPTN,MERGE,YES
IOPTN,SOLID,YES
IOPTN,SMALL,YES
IOPTN,GTOLER,DEFA
IGESIN,'SampleBar3','igs','C:\Documents and Settings\c110683\My Documents\Ansys2\'
VPLOT
!*

/prep7

VSEL,S,LOC,z,0,-10,1
vplot

|*****

*Do,alpha,0,270,rotstep
raddist=partrad-feedrate/partrot*alpha/360
*afun,deg
deltax=cos(alpha)*(wheelrad+raddist)
deltay=sin(alpha)*(wheelrad+raddist)

/AUX15
!*
IOPTN,IGES,NODEFEAT
IOPTN,MERGE,YES
IOPTN,SOLID,YES
IOPTN,SMALL,YES
IOPTN,GTOLER,DEFA
IGESIN,'largerXY350Wheel2','igs','C:\Documents and Settings\c110683\My Documents\Ansys2\'
VPLOT
!*

/prep7
VGEN,,all,,,-deltax,,,,1
VGEN,,all,,,deltay,,,,1
VGEN,,all,,,,,cutwidth,,1
```

vsel,all  
VSEL,S,LOC,X,-deltax-20,-deltax+20  
VSEL,r,LOC,y,deltay-20,deltay+20

csys,1  
VSEL,a,LOC,X,0,10,0  
csys,0

vptn,all

vsel,all  
VSEL,S,LOC,X,-deltax-120,-deltax+120  
VSEL,r,LOC,y,deltay-120,deltay+120  
vdele,all,,,1

\*ENDDO  
|\*\*\*\*\*

### 3.

/prep7  
btol,1e-10

lvsel,all  
lvdele,all,,,1

wheelrad=175  
partrad=25  
cutwidth=2  
feedrate=0.00001 !(m/s)  
partrot=0.005 !(1/s)  
rotstep=10 !(°)

volumc=36

Inpolygon=200  
!finish  
!~SATIN,'cylinder','sat','.\macros\','SOLIDS,0

/AUX15  
!\*  
IOPTN,IGES,NODEFEAT  
IOPTN,MERGE,YES  
IOPTN,SOLID,YES  
IOPTN,SMALL,YES  
IOPTN,GTOLER, DEFA  
IGESIN,'SampleBar3','igs','Z:\Ansys\Ansys2'  
VPLOT  
!\*  
/prep7

VSEL,S,LOC,z,0,-10,1  
vplot

```

!*****

*Do,alpha,0,360,rotstep
raddist=partrad-feedrate/partrot*alpha/360
*afun,deg
deltax=cos(alpha)*(wheelrad+raddist)
deltay=sin(alpha)*(wheelrad+raddist)

/AUX15
!*
IOPTN,IGES,NODEFEAT
IOPTN,MERGE,YES
IOPTN,SOLID,YES
IOPTN,SMALL,YES
IOPTN,GTOLER,DEFA
IGESIN,'largerXY350Wheel2','igs','Z:\Ansys\Ansys2'
VPLOT
!*

/prep7
VGEN,,all,,,-deltax,,,,,1
VGEN,,all,,,deltay,,,,,1
VGEN,,all,,,,,cutwidth,,,1

vsel,all
VSEL,S,LOC,X,-deltax-20,-deltax+20
VSEL,r,LOC,y,deltay-20,deltay+20

csys,1
VSEL,a,LOC,X,0,10,0
csys,0

vptn,all

vsel,all
VSEL,S,LOC,X,-deltax-120,-deltax+120
VSEL,r,LOC,y,deltay-120,deltay+120
vdele,all,,,1

*ENDDO

VSEL,S,LOC,x,-100,-50,1
vplot
vdele,all,,,1

ALLSEL,ALL
/TRLCY,VOLU,0.5,ALL,,,
VPLOT

/PNUM,VOLU,1

/REPLOT
!*****

```

4.

ASEL, R, LOC, Z, 13

csys,1  
ASEL,S,1,partrad,rotstep

ASEL,S,LOC,Y,shight  
ASEL,R,LOC,Z,0,-woc  
ASEL,R,LOC,X,0,stepw  
VSLA,R

vsel,u,,,VOLCOUNT(volumc+1,1,1)  
\*GET,VOLCOUNT(1,1,1),VOLU,,NUM,MAX, , , ,  
ASLV,S  
ASEL,U,LOC,Z,0  
ASEL,U,LOC,Z,-woc  
ASEL,U,LOC,Y,shight  
ASEL,U,LOC,X,0

\*DO,runloc,2,volumc,1  
VSLA,S  
Vsel,u,,,VOLCOUNT(runloc-1,1,1)  
vsel,u,,,VOLCOUNT(volumc+1,1,1)  
  
\*GET,VOLCOUNT(runloc,1,1),VOLU,,NUM,MAX, , , ,  
ASLV,S  
Vsel,s,,,VOLCOUNT(runloc-1,1,1)  
ASLV,U

ASEL,U,LOC,Z,0  
ASEL,U,LOC,Z,-woc  
ASEL,U,LOC,Y,shight  
ASEL,U,LOC,X,0

ASEL,U,LOC,X,slenght  
\*ENDDO  
\*set,runloc,

\*DO,runloc,1,volumc,1           !saves current wheel x position for each volume created  
VOLCOUNT(runloc,2,1)=-sqrt(whrad\*whrad-(whrad-doc)\*(whrad-doc))+runloc\*stepw  
\*ENDDO  
\*set,runloc,

ALLSEL,ALL  
Vplot

|\*\*\*\*\*

5.

/sol  
lvolumc=36

\*DIM,volcount,ARRAY,volumc+1,3,1, , ,

rotstep=0  
partrad=23  
alpha=rotstep



```

doc=0.5
woc=13
whrad=175

lstepw=rotstep+1
lslenght=0.115
lshight=0.044

csys,0
ASEL,S,LOC,x,0
VSLA,S

*GET,VOLCOUNT(volumc+1,1,1),VOLU,,NUM,MAX,,,
vsel,all

vplot
vsel,u,,,volcount(volumc+1,1,1)          !unselect main body
lvplot

!* *****

*DO,rota,1,volumc,1

csys,1
rotstep=10
rotloc=rotstep*rota

lvsel,u,,,volcount(volumc+1,1,1)
lvplot

/prep7
asel,s,loc,x,23.0,24.0          !,24.999          !rotation x position in radial coordinate system
aplot
asel,r,loc,z,1,-14          !
aplot
asel,r,loc,y,rotloc-0.5,rotloc-12  !+7,rotstep+12          !rotational y position in radial coordinate system
aplot
vsla,r
vplot

*GET,VOLCOUNT(rota,1,1),VOLU,,NUM,MAX,,,
VOLCOUNT(rota,2,1)=rota
VOLCOUNT(rota,3,1)=rotloc

vsel,all
vsel,u,,,volcount(volumc+1,1,1)
vsel,u,,,volcount(rota,1,1)
vplot

*ENDDO

!*set,rota,
!*DO,rota,1,volumc,1
!*enddo

|*****

```

6.

/POST1

```
ALLSEL,ALL
*DO,bdurchl,1,nofnod,1
DNSOL,bdurchl,TEMP,,nodtemp(bdurchl,1,1),,,,,,
*ENDDO
*set,bdurchl,
```

!\*\*\*\*\*

7.

/POST1

```
ALLSEL,ALL
SET,LAST
*GET,resultsn,ACTIVE, ,SET,LSTP
*VGET,cnodtemp,NODE, ,TEMP,,,,,2
*VGET,nodtemp,NODE, ,TEMP,,,,,2
*GET,nofnod,'PARM',CNODTEMP,DIM,X

*Do,cresult,resultsn-1,1,-1
SET,cresult,LAST,1,
step=cresult !displays step number in console
*set,step,
*VGET,cnodtemp,NODE, ,TEMP,,,,,2
*DO,adurchl,1,nofnod,1
*IF,cnodtemp(adurchl,1,1),gt,nodtemp(adurchl,1,1),then
nodtemp(adurchl,1,1)=cnodtemp(adurchl,1,1)
*ENDIF
*ENDDO
*ENDDO
*set,cresult,
```

!\*\*\*\*\*

---

## Appendix C. Phosphor Thermometry

This section outlines the definition of phosphorescence, explaining the principles behind phosphor thermometry, central to the purpose of this research, with the intention to include phosphor thermometry within the abrasive machining environment.

The word *Phosphor* comes from the Greek meaning 'light bearer'. Records show that Vincentinus Casciarolo of Bologna, Italy, an alchemist living in the 17<sup>th</sup> Century found a stone at the foot of a volcano which emitted red light in the dark after exposure to sun light. The 'Bolognian stone' as it is now known turns out to be Barite ( $BaSO_4$ ) which turns out to be a host for phosphor materials (Shionoya and Yen, 1997) Galileo Galilei is reported to have commented on the Bolognian Stone saying 'It must be explained how it happens that the light is conceived into the stone, and is given back after some time, as in childbirth'

Luminescence is the natural phenomenon involving energy emission from materials through the medium of light, *Lumen* meaning light in Latin. Excluding energy release through means of combustion or blackbody radiation many species of bacteria, insect, fungi, and ocean born creatures possess the ability to produce light. A great example of this occurrence is the distinctive light produced from glow worms and fire flies, ultimately defining their names.

Luminescence is defined as; 'the promotion of electrons into higher energy states with subsequent emission of light'. (George Stokes)

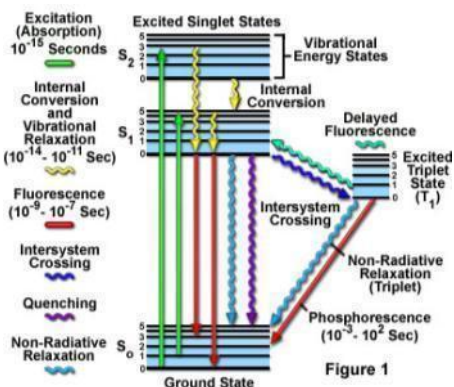
There are various types of luminescence, known as a 'cold light' as heat is not necessarily the source of energy emission, principally defined by the exciting energy source, i.e. a mechanical action resulting in the lifting of electrons into a higher energy state is known as Mechanico-luminescence. Others include Electro-, Chemi-, Bio-, Radio-, Tribo-, Fracto-, Sono- and Cathode- (Bergeron et al., 2006).

If the source of excitation happens to be light energy then the subsequent luminescence is termed Photoluminescence which is the principle method utilised within phosphor thermometry.

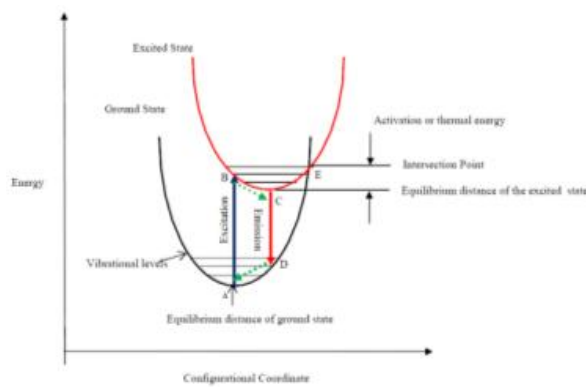
### Electron Energy Levels

An extremely useful illustration of these energy states is depicted in what is known as the Jablonski diagram, see illustration below. The elevation of an electron to a higher state however is only a temporary response and ultimately electrons will naturally find their way back down to the ground state. The ground state is the only stable state. The Jablonski diagram neatly illustrates the many paths that an electron may take to find its way back down to the ground divided between non-radiative and radiative relaxation.

Not only can an electron be promoted to a higher energy state with the absorption of energy, known as Singlet States, but there are also spin orientations for the electron orbit at an atomic level, known as Triplet States.



a)



b)

Phosphorescence states of electrons.

a) Jablonski Energy Diagram showing excited states of electrons b) Configuration Diagram

An electron with extra electronic energy is known as a phonon (Quantum Physics goes deeper into the definitions and behaviour of particles such as bosons, fermions and Maxwell’s equations however for this overview it is not particularly beneficial). The movement of phonons depends upon the various possible routes of relaxation to ground. Phonons release their temporary energy predominantly through non-radiative methods, followed then by the radiative methods. Figure 47 b) demonstrate the configuration diagram showing the interaction between energy states and consequential relaxation paths.

The electron population of the energy states can be equated to the intensity of the radiative energy by;

$$\frac{I_1}{I_2} = \frac{n_1}{n_2} = e^{-\left(\frac{\Delta E}{k_B T}\right)} \quad \text{Equation 45}$$

Where  $n_1$  and  $n_2$  are the upper and lower energy states respectively,  $\Delta E$  the energy gap,  $T$  the temperature in Kelvin,  $k_B$  the Boltzmann constant and  $I_1$  and  $I_2$  the relative intensities {{88 Heyes,A.L. 2006}}.

Vibration relaxation releases the additional energy resulting in the emission of heat. Depending on how close the electronic energy of an electron is to various levels an electron has the ability to jump down releasing the energy potential through vibrational means. Temperature itself is defined by molecular vibration i.e. a body exposed to a heat source will result in the increase of molecular vibrational movement hence the increase of the bodies energy, similarly for when excited phonons vibrate down to ground state resulting in a body temperature rise indicating a release of energy.

---

Quenching is a form of relaxation where the increased electron energy is transferred to adjacent molecules searching for a state of equilibrium. The probability of quenching can be increased through the manipulation of the surrounding environment with quench-able molecules willing to accept additional electrons i.e. oxygen

Fluorescence is a form of radiative relaxation originating from the singlet energy level. Relaxing of electrons from the singlet states occurs simultaneously with the excitation of the source light. Fluorescence will cease to radiate if the source energy is removed. According to Stokes Shift the resulting wavelength will be longer than the excitation source which can be detected through the resulting light spectrum.

$$dE = h\nu = \frac{hc}{\lambda} \quad \text{Equation 46}$$

Intersystem crossing involves the movement between singlet and triplet states ultimately defined by the spinning of electrons, with the triplet state generally being the least probable state to occur. Electron spin is more likely to occur with atoms of a larger size and of a particular molecular structure, and intersystem crossing is therefore encouraged through the combination of particular molecules able to reach the triplet state. Relaxation is still needed to reach the ground state, either through further non-radiative transition (including the likelihood of more intersystem crossing back into the singlet state) or the conversion of the phonon into a photon and releasing energy as a radiation, otherwise known as phosphorescence.

Phosphorescence is the radiative release of energy as a photon from the triplet state. The wavelength of the photon is longer than that of fluorescence as well as the longer response time due needed to spin the electron into the triplet state. The opportunity exists however where the triplet electron can relax back to the singlet form before radiating off as fluorescence. In this instance the time response will be similar to the delay of phosphorescence however the wavelength will be similar to fluorescence. Hence the name – delayed fluorescence.

Skinner et al. state that the increased life cycle of phosphorescence involves the increased length of time that the higher electron states are exposed to the surrounding environment (Skinner et al., 2008). The longer exposure directly affects the nature of the phosphorescent emission, with temperature being a major factor to any environment leading to the use of phosphors as indicators of temperature.

Host materials doped with a heavy molecular element form the basis of phosphor thermometry. Generally the materials used within phosphor thermometry consist of ceramics doped with lanthanides (rare earth ions). (Heyes et al., 2006)The possible combination is extensive and the operating environment needs to be considered before the selection is made i.e. ceramic based hosts are preferred for higher working temperatures.

Ceramics in particular are currently being developed as Thermal Barrier Coatings for gas turbine blades (Sudhangshu Bose, 2007) typical examples of host materials include:

Typical host materials for thermal barrier coatings

|                             |                                     |
|-----------------------------|-------------------------------------|
| Yttrium garnets             | $Y_3AlGa$ , YAG                     |
| Yttrium oxides              | $Y_2O_3$                            |
| Yttrium/Lutetium phosphates | $YPO_4$ , $LuPO_4$                  |
| Oxysulfides                 | $La_2O_2S$ , $Gd_2O_2S$ , $Y_2O_2S$ |
| Vanadates                   | $VO_3$ , $VO_4$ , $V_2O_7$          |

Typical doping rare earth ions used as activating atoms

|            |    |
|------------|----|
| Europium   | Eu |
| Dysprosium | Dy |
| Neodymium  | Nd |

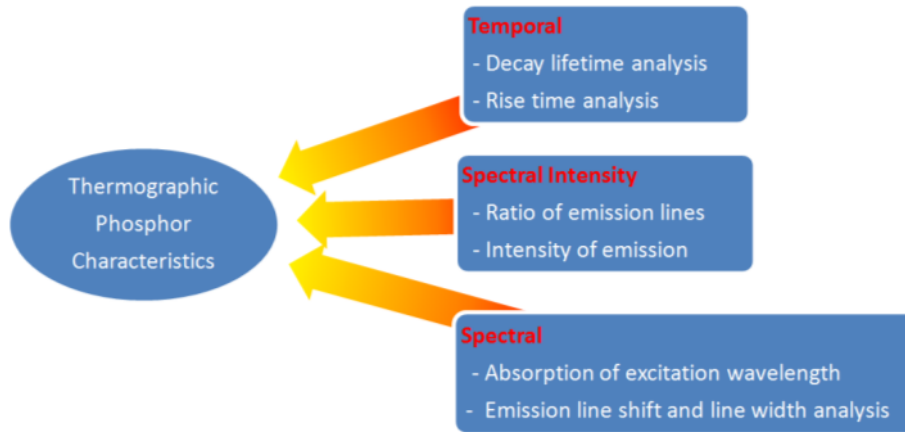
Each element features a unique set of energy levels which can be detected through the use of spectrometry. Generally the heavier the nucleus the more excited states exist (Cottingham and Greenwood, 1987). A source of energy can have its radiation captured and determined through the particular bands of energy wavelengths and the elemental construction can be established. As mentioned before Fluorescence and Phosphorescence are both radiative sources of energy however due to the distinctive forms of singlet and triplet forms the wavelengths are significantly different (Clarke and Gentleman, 2007) .

### Temperature measurement

Following the principles of phosphorescence it is only natural to progress into the valuable and detectable behaviours found when exposing phosphors to differing temperatures.

The relation between light energy and temperature has long been studied from the early days of Neubert (P. Nuebert. (1937)) were a loss from fluorescent lamps was noted along with an increase of temperature. Since then the development of thermographic phosphors has pursued providing us with not only probe type temperature detectable instruments but also the possibility of remote surface temperature analysis by introducing phosphor doped barriers and paints (Nicholls et al., 2002).

Phosphor decay time, emission frequency and line width, and intensity are all temperature dependent and can theoretically be used in thermometry, with decay time being the most reliable (Walker and Allison, 2007). The figure below highlights the detectable effects when exposing thermographic phosphors to temperature.



Description of response modes from thermographic phosphors

This research predominantly focuses on phosphor decay detection. The successful implementation of phosphor decay analysis within gas turbine engines demonstrates the functionality of this remote temperature system within an aggressive environment and since grinding represents an extremely aggressive environment this provides some confidence in the approach.

The decay time of phosphors varies immensely from nanoseconds to hours. Therefore for effective detectable behaviour within a system a phosphor needs to possess a decay life time smaller than that of any transient temperatures. Radiative and Non-radiative relaxations are mutually exclusive expressed as;

$$\lambda = \frac{1}{\tau} = k_r + k_{nr} \quad \text{Equation 47}$$

The radiative rate ( $k_r$ ) is temperature independent and can be considered as a constant. However the non-radiative ( $k_{nr}$ ) relaxation becomes highly temperature dependent after the quenching temperature. Probability of radiative emissions:

$$P_r = \frac{k_r}{k_r + k_{nr}} \quad \text{Equation 48}$$

Probability of non-radiative emissions:

$$P_{nr} = \frac{k_{nr}}{k_r + k_{nr}} \quad \text{Equation 49}$$

Therefore as the temperature increases the decay rate through non-radiative means ( $k_{nr}$ ) also increases. For steady state temperatures the decay time can be expressed as:

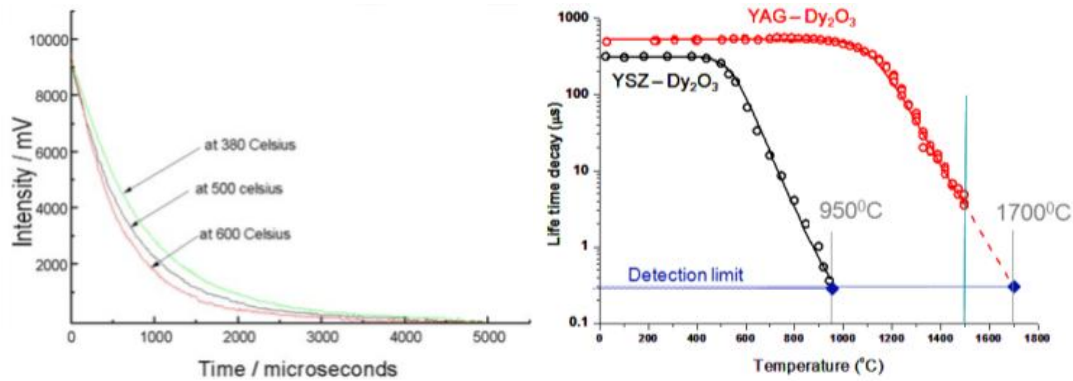
$$I(t) = I_0 \exp\left(-\frac{t}{\tau}\right) \quad \text{Equation 50}$$

Where;

$I_0$  Initial intensity (at  $t = 0$ )

$\tau$  Decay time

The illustration below demonstrates the method of tracing back temperature from the phosphorescent behaviour of a phosphor doped host material. Depending on the environment and temperature range expected suitable combinations of phosphors can be developed for optimum performance. When placed upon a log scale the temperature, from the exposed phosphor, can be easily determined from the decay lifetime. However prior calibration and temperature behaviour particular to the phosphor dope and host needs to be determined from experimental study.



Effect of temperature on phosphorescent intensity and decay  
(Southside Thermal Sciences (STS) Ltd., 2008)

High energy pulsed UV light produced through various laser sources are excellent methods of exciting phosphors into their higher energy states; Nd:YAG lasers, Q switched diode pumped solid state (DPSS) lasers, and Excimer lasers. The pulse strength and wavelengths can be tuned in order to promote the necessary excitation of the selected phosphor, allowing the optimum performance for a temperature measuring system. UV LEDs are also available but as of yet have only been included in low temperature application. They are continuing to offer increased controllability and in certain instances are replacing previous laser sources.





The End